# CONTROLLING MICROPOROUS AND MESOPOROUS DOMAINS IN ZEOLITE CRYSTALLIZATION

by

Aseem Chawla

A dissertation submitted to the Department of Chemical and Biomolecular Engineering,

in partial fulfillment of the requirements for the degree of

Doctor of Philosophy

in Chemical Engineering

Chair of Committee: Dr. Jeffrey D. Rimer

Committee Member: Dr. Lars C. Grabow

Committee Member: Dr. Jeremy Palmer

Committee Member: Dr. Allan J. Jacobson

Committee Member: Dr. Daniel A. Evans

University of Houston

May 2020

# ACKNOWLEDGEMENTS

First and foremost, I would like to express my sincere gratitude to my advisor Dr. Jeffrey Rimer for his endless support and guidance over the past five years. Jeff has been a phenomenal mentor and one of the most brilliant people I have ever met. It has been an incredible experience to learn from someone with such an insightful approach to both conducting and communicating science. His invaluable mentorship has shaped me into the researcher and presenter that I am today.

I am very grateful to the members of my dissertation committee Drs. Lars Grabow, Jeremy Palmer, Allan Jacobson, and Daniel Evans for their wonderful ideas, feedback, and inspiring discussions throughout all these years. I also had the privilege to collaborate with fantastic researchers. This dissertation would not have been possible without their intellectual contributions. More specifically, I would like to acknowledge Dr. Jeremy Palmer and Dr. R. John Clark for their critical contributions that significantly enriched our work on surfactant templating of zeolites. In addition, most of the projects discussed in this dissertation were done in collaboration with Dr. Javier Garcia Martinez and Dr. Noemi Linares. I am greatly indebted to them for their help, discussions, and brilliant insights into different aspects of projects. Javier's enthusiasm and passion for science is contagious and has been an inspiration for me. I would also like to thank my undergraduate research advisors Drs. Aniruddha B. Pandit, Murari Prasad, and Yogesh C. Sharma for their constant encouragement. The time spent in their labs was the primary reason why I decided to pursue a career in research.

I would like to express my special appreciation to all Rimer group members for their help and support during my time at the University of Houston. I am extremely grateful to the friendly atmosphere the whole group provided and I cannot thank them enough. I will always remember all the group events, lunches, and fun activities we have done together over the past years. I am especially thankful for having the opportunity to work with Dr. Rui Li, Rishabh Jain, Thuy Le, and

James Sutjianto who directly contributed to various projects related to this dissertation. I will forever be grateful to former group members Drs. Rui Li, Manjesh Kumar, and Madhuresh Choudhary for the helpful discussions and training me on various characterization techniques during the initial stages of my graduate career.

Apart from this, I consider myself lucky and blessed to have the friendship of Priyanka Arora, Ankur Agarwal, Dr. Pritpal Singh Dhillon, Dr. Shobhit Mishra, and Dr. Pushpesh Sharma who were my support system and helped me survive graduate school. Last but not the least, I would like to express my deepest gratitude to my parents and my sister for their unconditional love and support. There are no words to express the sacrifices they have made over the years to help me endure through difficult times. This dissertation would not have been possible without their support and motivation. I would like to dedicate this dissertation to my family and teachers.

# ABSTRACT

Zeolites are crystalline microporous aluminosilicates with confined cages and channels of molecular dimensions, that are utilized in a wide variety of commercial applications ranging from catalysis and ion-exchange to separations and drug delivery. Despite their commercial relevance, fundamental mechanism(s) that govern the nucleation and growth of zeolites are not well understood. The lack of molecular level understanding often prohibits *a priori* selection of synthesis conditions to predictively control the physicochemical properties of zeolites. This dissertation focusses on establishing improved fundamental understanding of zeolite crystallization, and to use that knowledge in developing facile and inexpensive routes to tune the porous architecture, active site distribution, size, and morphology of zeolites.

Surfactant templating has emerged as one of the most effective and versatile strategies for the construction of well-defined porous architectures in zeolites. Here, we have explored the dual roles of the cationic surfactant cetyltrimethylammonium (CTA) as an organic structure-directing agent (OSDA) and as a mesostructuring agent in the rational design of two commercial zeolites (ZSM-5 and USY). Our findings reveal that the selection of OSDA has a significant impact on the kinetics of ZSM-5 crystallization, as well as the physicochemical properties of ZSM-5 crystals. In addition to OSDA design, the development of mesoporosity in zeolites has been a long-standing goal in catalysis to alleviate the diffusion limitations imposed by micropores. One area of research that has garnered considerable interest, yet is not fully understood, is the rearrangement of zeolite crystals post-synthesis to accommodate mesoporosity. Here, we will also report *in situ* observations of intracrystalline mesoporosity in USY zeolite assisted by CTA using atomic force microscopy. Our findings capture the structural, morphological, and textural evolution of initially rough crystals to smooth crystals with a uniform distribution of mesopores.

Although surfactants offer significant advantages over conventional organics, they are not heavily commercialized since they are irrecoverable due to post synthesis calcination. To this end,

we have developed a more rational approach employing seeds as a unique tool to synthesize hierarchical ZSM-5 with intergrown nanosheets in an organic-free media. We demonstrate nonclassical pathways of ZSM-5 crystallization involving the nucleation of crystals at the external surface of amorphous precursor particles.

One of the critical challenges in elucidating the mechanism(s) of nucleation and growth in zeolites is the lack of available techniques that can monitor the amorphous-to-crystal transformation with sufficient spatiotemporal resolution. Here, we have developed an elemental mapping method employing FE-SEM-EDX as a versatile tool to characterize morphological and compositional properties of precursors during the crystallization of five commercial zeolites. Time-resolved *ex situ* elemental mapping images of extracted solids during several stages of zeolite crystallization reveal that a sufficient disparity in the chemical composition (e.g., alkali metal content) between amorphous precursors and crystals can be exploited for tracking the early stages of zeolite crystallization, locating where it happens, and resolving residual amorphous material among crystalline domains. Given the ubiquitous presence of amorphous precursors during nonclassical crystallization, we expect that elemental mapping may prove valuable for understanding and tracking the growth of other zeolites and minerals.

# Table of Contents

# List of Tables

# List of Figures

# Chapter 1

# Prior Work on Zeolite Crystal Engineering and Growth Mechanisms

## 1.1 Introduction

Zeolites are crystalline microporous materials that often belong but are not limited to the category of aluminosilicates. The term “zeolite” was first coined by Swedish mineralogist A.F. Cronstedt in 1756 due to his observation that mineral stilbite gave off steam during heating.[1] Cronstedt, therefore, combined the Greek words *zein* (to boil) and *lithos* (rock) to form the word zeolite.[2] Despite their unique porous structure and properties, zeolites were largely ignored by the scientific community for 200 years. The two centuries after the Cronstedt’s discovery, the only zeolites which were known were natural in origin, found predominantly in basaltic rocks as large single crystals. In 1943, Barrer's pioneering work[3,4] in synthesis and adsorption led to the discovery of first synthetic zeolites. Earlier researchers attempted the synthesis of zeolites by replicating the geological conditions of natural zeolites, where the aluminosilicates were made to react with mixtures of potassium and barium hydroxides at high temperature (170-200 °C) and autogenous pressure. To extend the utility of zeolites in large scale industrial processes, Union Carbide researchers Milton, Breck, and Flanigen began an exploratory program of zeolite synthesis which led to the discovery of commercially relevant zeolites A, X, and Y.[5,6] Zeolites A and X (LTA and FAU types, respectively) displayed exceptional adsorption properties and were employed by Union Carbide for a number of applications including xylene separation, olefin separation, $CO_2$ removal, and drying among others.[3] Most of the separation applications exploited the unique property of zeolites to act as molecular sieves owing to their uniform pore size, thus allowing to distinguish molecules based on size.[7] Moreover, the initial discoveries of zeolites were limited to low Si/Al ratio with high ion exchange capacity which led to their largest application as detergent builders. Zeolite market size as detergent builders is expected to reach US$ 2 billion by 2028.[8]

One of the most significant milestones in zeolite science was achieved in 1962 when zeolite Y (FAU type) was tested as a catalyst for fluid catalytic cracking applications.[9,10] The advent of zeolites as catalysts revolutionized the refining and petrochemical industry and brought many disruptive changes to these fields. The high activity, superior selectivity to gasoline, and longer lifetime as compared to amorphous silica and alumina significantly reduced the capital requirement of the refining industry.[10] The breakthroughs of the early 1960s triggered a new discipline in catalysis, materials science, separations, and organic chemistry. Since then there has been rapid growth in the field which is evident by the vast number of zeolite structures reported till date. There are currently over 240 known zeolite framework types, each assigned a three-letter code by the International Zeolite Association (IZA).

The molecular structure of zeolites is composed of $TO_4$ tetrahedra (where T = Si, Al, Ge, Zn, and Sn, among others) that are primary building units connected through the corner-sharing of oxygen atoms to form 3D frameworks **(Figure 1.1A)** that encompass pores of molecular dimension occupied by ions and water molecules. It should be noted that the channels/cages of zeolites are large enough to allow the movement of guest species. The crystal structure of zeolites is typically categorized into primary building units (PBUs), secondary building units (SBUs), and composite building units (CBUs) **(Figure 1.1B)**.[11] The PBUs are the $TO_4$ tetrahedra which combine with adjacent tetrahedra to form a specific arrangement of rings and chains referred to as SBUs. The most common SBUs contain n-membered rings (where n = 4, 5, 6, 8, and 10, among others corresponding to the number of T atoms). Recently, zeolites with 20-rings have been reported.[12] On the other hand, CBUs are more complex species that are constructed by connecting SBUs of different sizes. Zeolites frequently comprise of cages, double rings, and alpha cavities as CBUs. In certain instances, CBUs can help predict the relationship between different framework types.[13,14] Cages are typically defined as polyhedrons whose largest rings exclude the movement of molecules larger than water. Zeolites are porous on a molecular level owing to the unique arrangement of

interlinked channels and cages with a pore size typically less than 1 nm.[15] Therefore, zeolites belong to the category of microporous materials. According to IUPAC classification, porous materials can be divided into three categories depending on their pore size: (a) microporous materials are those materials which have pore size less than 2 nm, (b) mesoporous materials have pore size between 2-50 nm, and (c) macroporous materials exhibit pore diameters greater than 50 nm. Zeolites are comprised of channels with sizes determined by different pore topologies, which can range from small (8 membered-ring (MR), ~4 Å) to large (12 MR, ~7.4 Å).[16] Recently, new structures with extra-large pore openings **(Figure 1.1C)** have been synthesized ranging from 14 MR to 30 MR[17] with the potential of accommodating large guest molecules. These channels form multi-dimensional topology **(Figure 1.1D)** depending upon their interconnectivity such as unconnected pores (1D), pores connected in a plane (2D), or pores connected to every other pore in the crystal (3D). The porous architecture of zeolites is responsible for shape selectivity that can be controlled by the transition state or restricted movement of reactant and product molecules through the pores.[18-20]

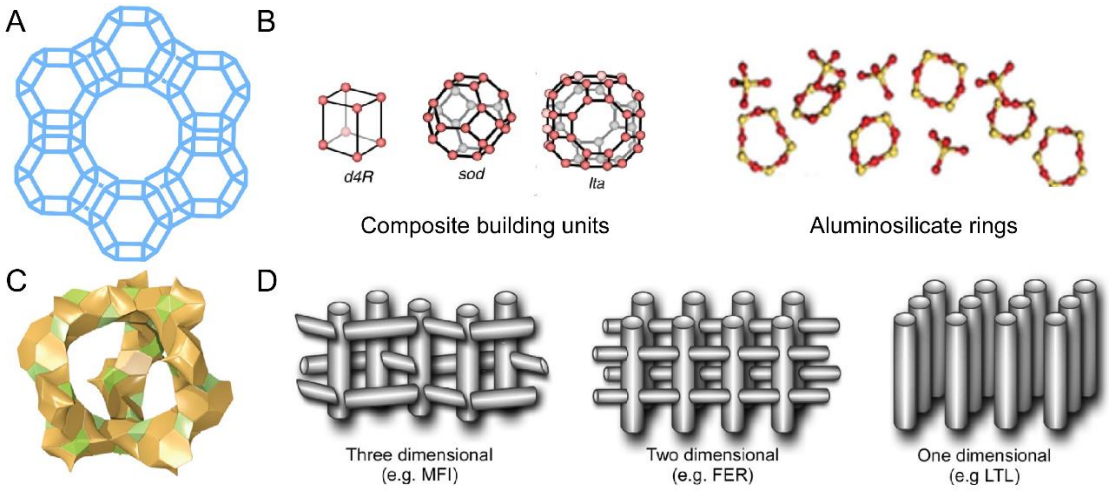


**Figure 1.1 (A)** Schematic representation of faujasite (FAU) zeolite framework. **(B)** Examples of common building units and secondary building units (aluminosilicate rings). **(C)** Extra-large pore zeolite defined by three 30 MR windows.[17] **(D)** Illustration of interconnecting channels extending in 1, 2, and 3-dimensional networks.

In 1967, Mobil researchers were the first to use organic cations in zeolite synthesis mixtures to control the chemical composition of aluminosilicate zeolites from Si/Al ratio = 1 to infinity. This represents one of the major achievements in the field of zeolite science since the low charge to size ratio of organic molecules enabled the synthesis of high silica zeolites with high hydrothermal stability. The incorporation of tetrahedral aluminum in zeolite framework creates a negative charge that is counterbalanced by extra-framework cationic species, which can range from protons and metals to metal-oxo species.[21-23] The exchangeable extra-framework positively charged species act as active sites for a wide range of catalysis and adsorption applications. Recent investigations focused on the incorporation of heteroatoms other than aluminum have resulted in the development of zeolites with diverse catalytic properties and novel topologies. For example, several groups have explored the possibility of framework incorporation by elements such as gallium, iron, silver, zinc, tin, titanium, and germanium.[24-26] The extremely wide range of heteroatoms and extra-framework species result in an enormously broad array of catalytic applications including redox catalysis, Lewis and Brønsted acid catalysis.[27-29]

## 1.2 Applications of zeolites

### 1.2.1 Catalysis

The application of zeolites as catalysts in the refining and petrochemical industries is regarded as one of the major accomplishments of the 20$^{th}$ century.[10] The current efficiency of petrochemical and refining processes can be largely attributed to the high surface area, durability, strong acidity, shape selectivity, and high hydrothermal stability of zeolite catalysts.[2,9] Zeolites as catalysts account for 28% of the world zeolite market.[30] Fluid catalytic cracking (FCC) is by far the largest use of zeolite catalysts wherein zeolite USY (FAU type) is typically employed to produce most of the world's gasoline as well as a significant fraction of propylene for the polymer industry. FCC is a major process in the petroleum refining industry which allows for the cracking of high molecular weight crude oil to lighter and more useful products such as diesel, gasoline, and olefins.

Recent approaches to engineer efficient FCC catalysts are focused on tuning the porous architecture, addition of rare-earth metals, and altering the amount of extra-framework aluminum leading to an overall improvement in product selectivity and activity.[31] Moreover, significant advances have been made over the past few decades to modify the properties of ZSM-5 zeolite (MFI type), which is typically added as an additive to tune the gasoline octane.[32] In addition to FCC, hydrocracking (HC) is another key conversion process in a modern refinery.[33] HC is mainly used to produce clean fuels (i.e., low aromatics and low sulfur content) by the addition of hydrogen to the feed with the help of a bifunctional catalyst containing highly dealuminated USY zeolites.[34] There have been advancements in the hydrocracking process such as Mobil's Octgain process[9], which removes a significant amount of sulfur in gasoline without impacting its octane content. Although the largest application of zeolite catalysts is found in HC and FCC, there are several critical processes in the refining and petrochemical industries that employ zeolites for other reactions, such as alkylation, reforming, isomerization, and dewaxing.[30] In (petro)chemical industries, the key examples of zeolite-based catalytic processes are isomerization of xylene, production of both ethylbenzenes and cumene.[30]

One of the more active areas of zeolite catalysis is the production of chemicals using renewable feedstock **(Figure 1.2),** wherein the overall goal is to develop sustainable routes to fulfill future societal needs. The main challenge of these transformations is the oxygen-rich nature of biomass- derived molecules.[35] Lewis acid zeolites that contain multifunctional active sites such as Ga, Sn, Ti, and Zr have emerged as versatile catalytic materials owing to their unique hydrophobicity.[36] Although Lewis acid zeolites have demonstrated excellent catalytic performance, industrial production of biofuels is still in its infancy. The obstacles needed to be overcome for successful commercialization include scalability, reusability, and stability of zeolite catalysts for these applications.[37,38]

Another emerging application of zeolite catalysts is the treatment of exhaust gases from mobile or stationary sources. These gases include NOx and CO where the selective catalytic reduction (SCR) of NOx by $NH_3$ using Fe and Cu ion-exchanged small pore zeolites has been extensively studied over the past three decades.[39] The discoveries of Cu-SSZ-13 and Cu-SAPO-34 (both CHA type) has spurred research by several groups to develop zeolite-based SCR processes.[40] These zeolites exhibit high NOx conversion and superior $N_2$ selectivity. Moreover, Cu-exchanged small pore zeolites have extremely high hydrothermal stability which is critical in a practical vehicle exhaust environment. Despite extensive research on Cu-zeolites, there are remaining issues that need to be resolved, especially with regard to low-temperature reduction of NOx. As such, this active area of research presents many opportunities to develop commercially viable NOx reduction technologies that can operate at low temperature.

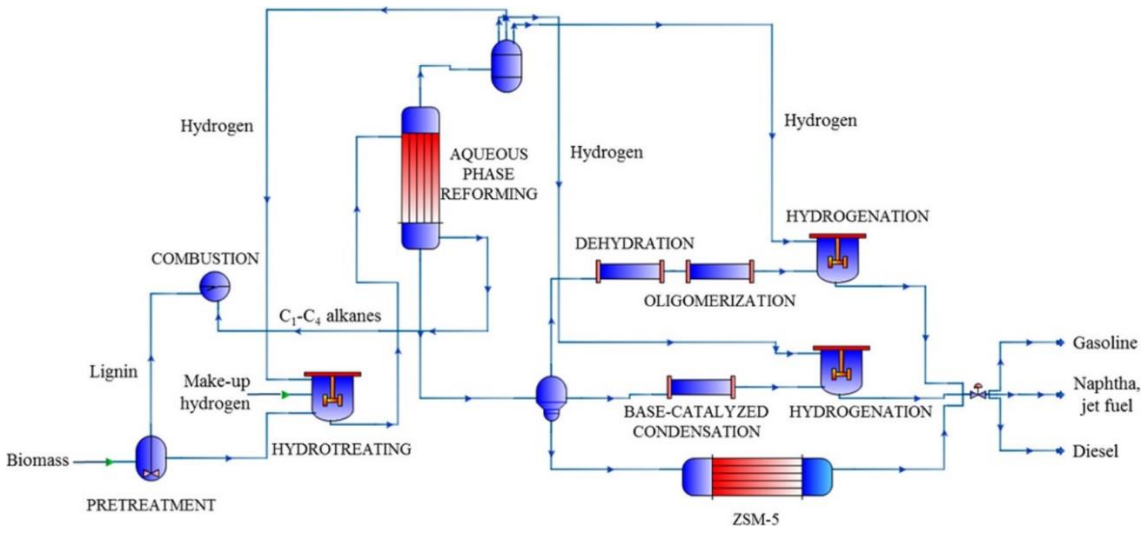


**Figure 1.2** Major operations in a bio reforming process showing the emerging applications of zeolite-based catalysts.[41]

Zeolite-based catalysts have also found applications in the conversion of methanol to valuable hydrocarbons (e.g., gasoline, olefins and aromatics) broadly referred to as methanol-to-hydrocarbons (MTH) processes.[42,43] MTH is a critical process for the production of fuel and olefins that utilizes alternative carbon sources such as coal, biomass, and natural gas.[44] Mobil

commercialized the first methanol-to-gasoline process in 1985 based on natural gas with a capacity of 14500 barrels per day. Despite its early commercialization, there has been a considerable interest from both academia and industry to improve the performance of zeolite catalysts as well as to develop a mechanistic understanding of the catalytic conversion of methanol to value added chemicals.[45] Zeolites SAPO-34 and ZSM-5 are commercial catalysts frequently employed to produce olefins and higher hydrocarbons, respectively. Recent studies have shown that other zeolite frameworks, such as ZSM-22, ZSM-11, IM-5, TNU-9, and UZM-5, can also be used to tune product selectivity.[43,46] Therefore, crystal engineering of zeolite catalysts still remains an active area of research to establish structure-performance relationships with an overall goal of ensuring the long term stability and high yield of desired products. [47]

### 1.2.2 Adsorption and separations

Zeolite membranes have been demonstrated to be viable alternatives to energy-intensive industrial separations owing to their unique pore architectures and shape-selective properties.[48] Several zeolite frameworks have been tested for the fabrication of membranes including zeolite A, mordenite, ferrierite, ZSM-11, ZSM-5, SAPO-34, chabazite, and a few other zeolites;[49] however, to date only zeolite A membranes have been commercialized for the dehydration of solvents. It is worth pointing out that research teams at Nanjing and Dalian have played a vital role in establishing over 50 plants to dehydrate solvents in the chemical and pharmaceutical industry using zeolite A membranes.[50,51] Despite significant progress in the fabrication of supported thin layer zeolite membranes, there are still no industrial processes employing zeolite membranes for the separation of gases such as xylene or butene isomers.[52] Typical challenges for the industrial implementation of zeolite membranes include the high cost of supported zeolite membranes, scale-up, and lack of fundamental understanding of growth mechanism(s) of zeolites. The ability to rationally design zeolite membranes at a commercial scale requires fundamental knowledge regarding the nucleation and growth of zeolites. Recent advances over the past decade have led to a number of breakthroughs

that provided unique insights into the elusive mechanism of zeolite crystallization[53] and development of methods for the manipulation of crystal size and morphology.[54-57] An accumulation of progress and recent discoveries have set a foundation for what will undoubtedly lead to new applications in the future. For example, the potential applications for zeolite membranes could include separation of $CO_2/CH_4$, $H_2/CH_4$, xylene isomers, and $N_2/O_2$, among others.[49,58,59]

### 1.2.3 Ion exchange

Natural and synthetic zeolites are one of the most important ion-exchange materials. Channels and cages of zeolite structure can accommodate a variety of cations including $Na^+$, $K^+$, $Ca^{2+}$, and $Ba^{2+}$, among others due to negatively-charged aluminosilicate framework.[11] In addition to alkali and alkaline earth metals, large molecules such as ammonia, water, and nitrate ions can reside inside the pores and channels of zeolites. The ion-exchange is a reversible process, thereby making zeolites useful materials for heavy metals removal, dust filters, and medical applications.[60] The largest application of zeolites is in detergency due to their exceptional selectivity for $Ca^{2+}$ and $Mg^{2+}$ over $Na^+$.[61] It is estimated that the global zeolite detergent market is valued at US$ 1.8 billion in 2018 and is expected to reach US$ 2 billion by 2028. Although several zeolite frameworks have been tested as water softeners, zeolite A is typically used for commercial applications in conjugation with zeolite X. Recent studies have also claimed zeolite P (GIS type) to be more effective than zeolite A for detergent builders. In addition to water softeners, the remarkable ion-exchange properties of zeolites have also found applications in the removal of radioactive components such as $^{90}Sr^{2+}$ and $^{137}Cs^+$ from nuclear waste.[62] Natural zeolites, such as chabazite and clinoptilolite, have attracted significant interest recently due to their low cost and high abundance for the treatment of radioactive waste.[62] Another major application is the treatment of municipal and agricultural wastewater, wherein both natural and synthetic zeolites have been tested for the removal of ammonia and ammonium.[63] Examples include zeolite W (MER type), zeolite F (KFI type), and clinoptilolite. Recent trends are now emerging that demonstrate zeolites ion-exchanged

with inexpensive transition metals are ideal materials for antimicrobial applications.[64] For example, $Ag^+$ ion-exchanged zeolite X exhibits superior kinetics and efficacy in inhibiting *methicillin-resistant Staphylococcus aureus* (MRSA).[64] Ion-exchange properties of zeolites can be exploited for a variety of biochemical processes and have the potential to facilitate significant advances in biology, medicine, and the pharmaceutical industry in the near future.[65]

## 1.3 Crystal engineering of zeolites

The physicochemical properties of zeolite catalysts such as size, morphology, surface roughness, pore architecture, acidity, and topology can significantly impact their performance in a variety of reactions (i.e., catalyst activity, selectivity, and lifetime). Herein, the application of crystal engineering to manipulate the physicochemical properties of zeolites is discussed.

### 1.3.1 Engineering crystal size and shape

Catalytic reactions over porous materials predominantly occur within the interior of the catalyst particle; therefore, compared to nonporous catalysts, there is a fundamental difference in the approach taken to tailor the size and shape of porous catalysts to control internal diffusion – a property that can influence on-stream lifetime and selectivity. The impact of internal diffusion within porous catalysts is commonly illustrated by a plot of the effectiveness factor $\eta$ versus the Thiele modulus $\phi$.[66] A decrease in catalyst size shifts the performance of the material to lower values of $\phi$ and higher values of $\eta$, which reduces diffusion limitations. This, in turn, reduces the rate of carbon accumulation (i.e., coking) that is a frequent culprit of catalyst deactivation. Among the known zeolite structures, on the order of 20 are used as commercial catalysts owing to factors associated with the cost and complexity of large-scale synthesis.[67] Fewer than ca. 20 framework types have been synthesized with sizes less than 100 nm.[68] Typical challenges of these syntheses include low yield, the required use of expensive organics, post-synthesis aggregation, and issues with scale up.[69] A survey of zeolite literature shows that changes in synthesis conditions can have

a significant impact on the properties of zeolite crystals. These parameters include (but are not limited to) the selection of silicon and aluminum sources, the use of inorganic and/or organic structure-directing agents (SDAs), reaction temperature, and the molar composition of reagents. For example, Mintova and coworkers showed that low temperature aging **(Figure 1.3A)**[70] and the mixing of reagents at low temperature[71] **(Figure 1.3B)** is critical to control (alumino)silicate polymerization and achieve ultrasmall (10 – 100 nm) zeolite crystals. Guidelines for selecting synthesis parameters *a priori* to achieve a desired property are generally lacking due to the complexity of zeolite crystallization.[53] Indeed, zeolite synthesis is more of an art than a science, despite significant efforts from multiple groups to shift the field towards the latter. To this end, this active area of research presents many opportunities to develop new synthesis methods and elucidate structure-property relationships.

One method to produce relatively monodisperse zeolite crystals is hard templating. Colloidal crystal templating is utilized to synthesize 3-dimensional ordered macroporous/mesoporous (3Dom) materials, also known as inverse opals. Design strategies for a range of 3Dom materials and their use in catalytic applications is highlighted in a review article by Stein.[72] Challenges in 3Dom synthesis involve defect minimization, morphology control, and the identification of templates that can be removed efficiently and/or add additional functionality. The interconnected network of pores and adaptable functionalization of 3Dom materials make them attractive structures for catalytic applications. Tsapatsis and coworkers used this approach to synthesize uniform silicalite-1 (MFI) crystals with tunable size (< 50 nm) in carbon templates **(Figure 1.3C).**[73] This approach has been used by others to synthesize a broader set of zeolites, which have been tested in a range of catalytic reactions.[74,75]

A versatile method to tailor the anisotropic rates of zeolite crystallization is through the use of growth modifiers (ZSMs), which are economically beneficial in that they can be recovered and potentially recycled. Rimer and coworkers introduced ZGMs [57] by posing a classical mode of action

wherein modifiers bind to sites (kinks, steps, terraces) on specific crystal surfaces and impede the addition of solute to adjacent sites; however, the fact that zeolites grow via a combination of classical (i.e., monomer-by-monomer addition) and nonclassical pathways involving a wide variety

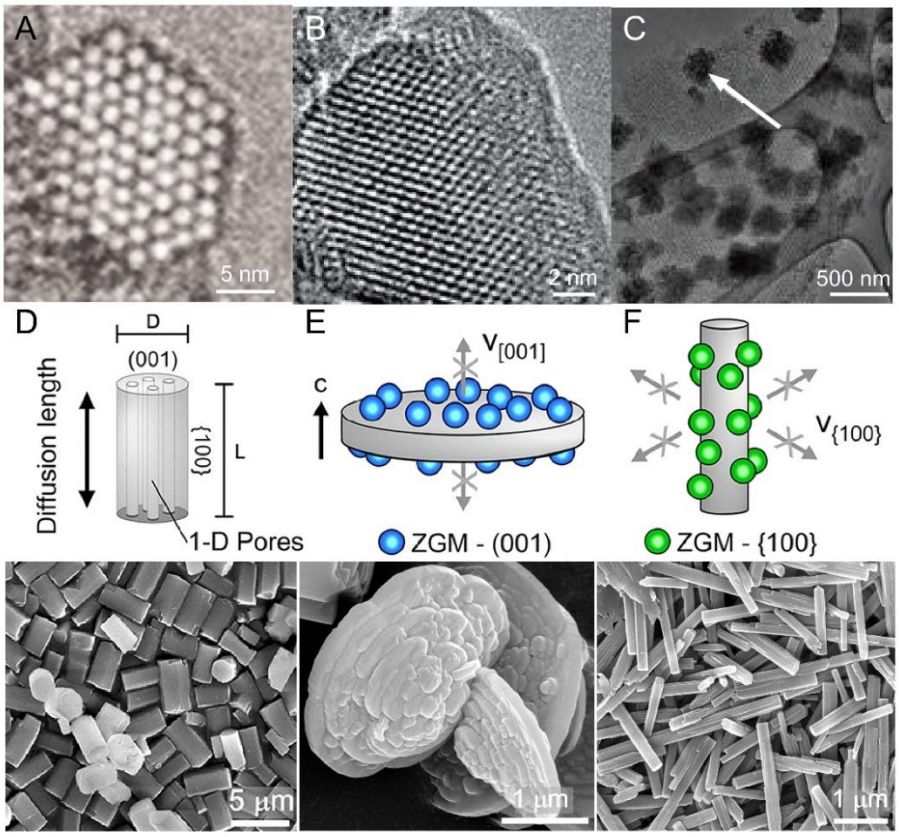


**Figure 1.3 (A–C)** Transmission electron micrographs of various zeolite nanocrystals. **(A)** EMT[76] **(B)** FAU[71] **(C)** MFI[74] **(D–F)** Examples of zeolite L (LTL) morphology in the presence of modifiers.[54]

of precursors, calls into question the exact role(s) of ZGMs in zeolite nucleation and growth.[77] Rimer[54,56,78] and others[79-82] have demonstrated the impact of modifiers on a range of zeolite frameworks that include LTL, MFI, MOR, MTW, TON, and CHA. Studies of silicalite-1 revealed that polyamines reduce the [010] dimension of crystals, which is the principal direction for internal diffusion.[56] Effective modifiers of LTL include alcohols, which are capable of reducing the diffusion path length by more than a factor of three **(Figure 1.3D,E).**[54] Studies of CHA (SSZ-13) reveal that ZGMs operate as colloidal stabilizers to either prevent or promote the aggregation of

amorphous precursors, thus allowing for crystal size to be selectively tuned over three orders of magnitude (0.1 – 10 μm).[78] A general rule of thumb for selecting modifiers in crystallization is that macromolecules, such as polymers, tend to be more effective than smaller molecules (e.g., their respective monomers). Examples include the use of Poly diallyl dimethyl ammonium chloride (PDDAC) in zeolite L synthesis, which leads to a dramatic increase in crystal length-to-width aspect ratio **(Figure 1.3F)**.

### 1.3.2 Design of organic structure-directing agents

The most common use of organics in zeolite synthesis is as SDAs, which are molecules with a size and shape that is commensurate with the geometry of zeolite channels/pores. SDAs facilitate the formation of pores to which they are occluded during crystallization. In addition to directing the formation of the crystal structure, organic SDAs can also have a significant impact on crystal morphology.[83,84] Ryoo and coworkers[85] introduced the use of surfactant-like SDAs (e.g., di- and triquaternary ammonium-type surfactants) to generate unilamallar ZSM-5 comprised of randomly-stacked 2-dimensional (2D) nanosheets **(Figure 1.4A-C)** that exhibit mesoporosity **(Figure 1.5A)**. Novel SDAs have been used by Ryoo and others to generate a wide range of 2D zeolite structures (e.g., MFI, MWW, BEA, MTW, and MRE).[85-87]

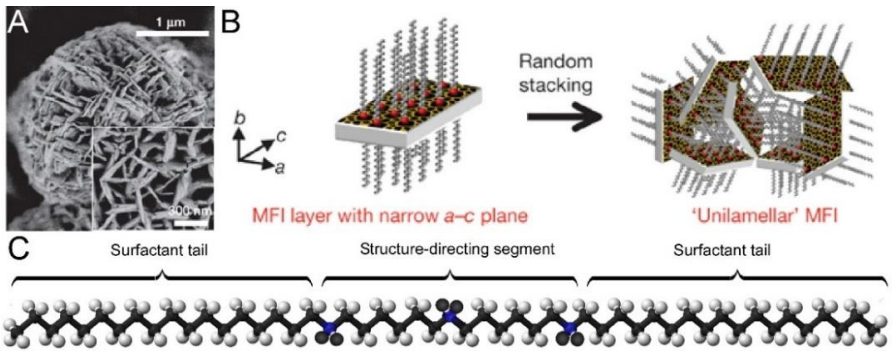


**Figure 1.4 (A-B)** Unilamellar ZSM-5 (MFI) zeolite nanosheets with approximately 2-nm thickness prepared with di-quaternary ammonium-type surfactant (not shown).[88] **(C)** Illustration of the dual-porogenic surfactant family $C_{18}H_{37}–N^{+}(CH_3)_2–C_6H_{12}–N^{+}(CH_3)_2–C_6H_{12}–N^{+}(CH_3)_2–C_{18}H_{37}(Br^{-})_3$.[86]

It has been shown that phosphonium-based SDAs and molecular analogues of tetrapropylammonium, a common SDA for zeolite MFI, can generate MFI crystals as self-pillared nanosheets with mesoporosity **(Figure 1.5B,C)**[66], crystals with sequential intergrowths **(Figure 1.5D)**[89], and other unique morphologies with reduced internal diffusion path length.[90] There has been a surge in research efforts to design 2D materials; however, this topic dates back 30 years beginning with the delamination of layered zeolites. Materials such as MWW (or MCM-22, ERB-1, UCB-1)[91,92] can be delaminated to thin sheets of ca. 2.5 nm thickness with extremely high external surface area. This process involves the swelling of layers with an organic (e.g., surfactant) followed by sonication to disperse individual sheets. Nanosheets have been demonstrated to exhibit higher selectivity [93] and markedly longer lifetime [85] than their commercial analogues. Prior studies have shown that unilamellar ZSM-5 can be exfoliated into single sheets via a top down approach [59] using a similar methodology as MWW. More recently, a study of purely siliceous MFI (silicalite-1) introduced a bottom up approach to generate 2D sheets **(Figure 1.5E)** using ca. 30nm MFI seeds in the presence of bis-1,5-(tripropyl ammonium) pentamethylene diiodide as the SDA.[58]

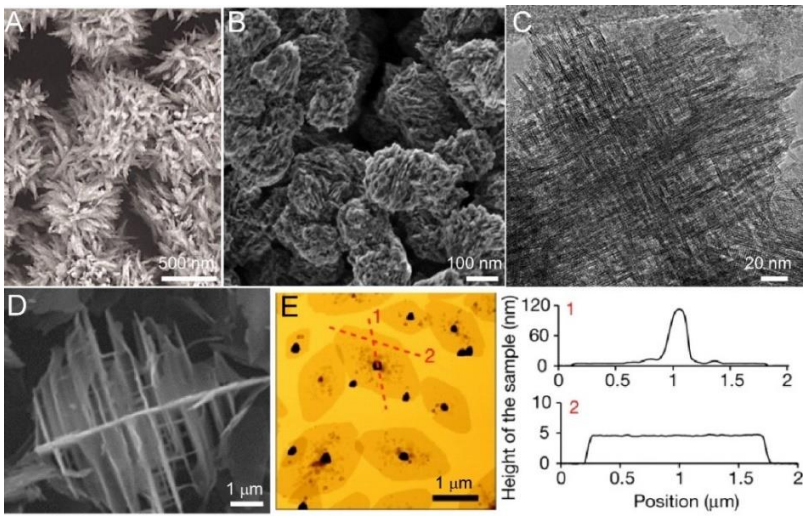


**Figure 1.5 (A)** Mesoporous aggregates synthesized using dual-porogenic surfactants.[86] **(B-C)** Self-pillared pentasil (SPP) zeolite crystals prepared with tetrabutylphosphonium.[66] **(D)** Sequentially intergrown ZSM-5 crystals.[94] **(E)** Silicalite-1 nanosheets with atomic force microscopy height profiles shown to the right.[58]

A common theme of organic structure-directing agent (OSDA) design is the synergistic combination of modeling and experiments. There are several examples where computational screening of OSDAs have generated the crystal structure that was predicted *a priori*. Deem and coworkers developed a computational method to generate a large library of synthesizable OSDAs.[95] Once these compounds were generated, the criteria for reducing the number of viable candidates in each library was based on their hydrothermal stability and overall compatibility (e.g., rigidity and interaction energy) with the target zeolite framework.[95]

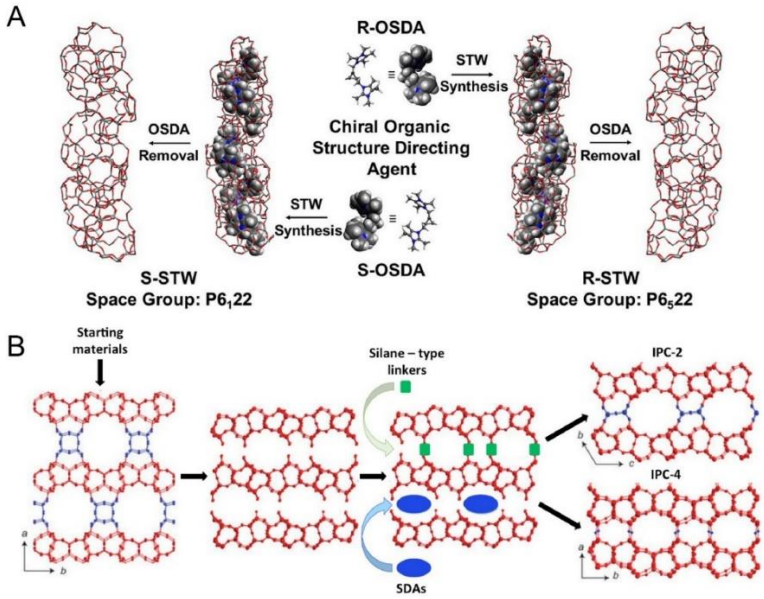


**Figure 1.6 (A)** Graphical rendering of R- and S-STW zeolites prepared with chiral R- and S-OSDA, respectively.[98] **(B)** Illustration of the ADOR (assembly, disassembly, organization, and reassembly) process for the synthesis of novel zeolites.[99,100]

Proof of concept studies were conducted by Zones, Davis, and coworkers wherein *de novo* OSDA compounds identified through computational design were first synthesized and then used to generate zeolite structures, such as SFW (SSZ-52), which were difficult to obtain via conventional routes.[96] This method of predicting OSDAs for a particular zeolite structure is not always successful, but advancements in this area of research have markedly shifted current trial and error methods to those that are more predictive or rational. In some cases, OSDAs have been generated by modifications to organics in existing databases. For example, Corma and coworkers identified

phosphazene-based OSDAs through computer-guided design that produce boggsite (BOG), a natural zeolite that had never been made synthetically. They showed that a basic building block can be combined in various oligomer configurations to generate different structure-directing agents. The design of OSDAs has been integral to the synthesis of chiral zeolites. Prior attempts to produce an enantiomerically pure zeolite from an achiral OSDA have proven to be ineffective [97]; however, Davis and coworkers showed that the use of chiral OSDAs can successfully lead to pure R or S zeolite enantiomers[98] wherein the criteria for chiral OSDA design is based on two factors: (i) there must be a large difference between the computed stabilization energy of a chiral OSDA in both zeolite enantiomers to ensure that the product is of a single enantiomorph; and (ii) the OSDA must possess sufficient hydrothermal stability to withstand the synthesis conditions of the targeted zeolite. For example, it was shown that R- and S-OSDAs produce R- and S-STW zeolites, respectively **(Figure 1.6A)**. These STW materials were tested as catalysts and showed enhanced enantioselectivity of epoxide ring-opening reactions and chiral butanol adsorption, thereby illustrating that zeolite enantiomers have potential applications in highly selective separation and reaction processes.

In recent years, top down approaches have been explored as alternative (and potentially more facile) routes to generate 2D zeolites. One method introduced by Čejka, Morris, and coworkers is known as the ADOR process (where ADOR = assembly, disassembly, organization and reassembly). In brief, the steps involved in this process begin with the identification of a parent germanosilicate zeolite (e.g.,, UTL), which is first synthesized, followed by the disassembly of the zeolite via the breakage of bonds to generate single layers. As shown in **Figure 1.6B**, the zeolite layers organize by switching out different composite building units that connect the layers (e.g., double four-ring, D4R, or single four ring, S4R) and reassembling the layers into new frameworks with different pore aperture (e.g., OKO or PCR).[101] This method allows for the synthesis of a new class of materials that are referred to as IPC-n (with n = 2, 4, 6, 7, 9, and 10). The ADOR process

has potential to produce a library of structures with variable pore size and geometries.[100] An alternative top down approach to convert UTL zeotype into a siliceous structure of different topology (e.g.,, COK-14) is the *inverse sigma transformation*, which uses post-synthesis mineral acid treatment to selectively remove composite building units followed by calcination and leaching of Ge to reform broken bonds.[102]

Corma and coworkers have used computational simulations of transition states for a particular reaction within the pores of a zeolite to guide the selection of an appropriate structure for catalytic reactions (i.e., reverse engineering the catalyst to improve reaction selectivity). To this end, density functional theory (DFT) was used to evaluate transition state (TS) stabilization **(Figure 1.7A)** for select reactions in confined cages/channels of zeolites with disparate pore networks.[103] This principle, termed "molecular recognition pattern," can be viewed as a rudimentary analogue to the lock and key mechanism in enzymatic catalysis wherein the geometric complementarity of the TS and the confined pore reduces energetic pathways to a desired product.[104] In order to ensure that the zeolite can lower the activation energy of the TS, OSDAs of similar size and structure (i.e., TS mimics) are selected for the synthesis **(Figure 1.7A,B)**.

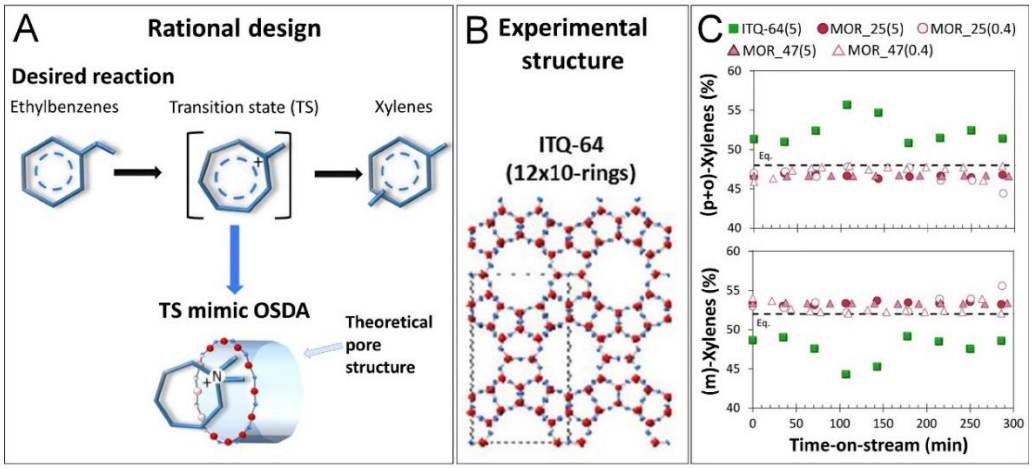


**Figure 1.7 (A–C)** The molecular recognition pattern approach wherein an OSDA is computationally selected to match the transition state **(A)** to produce a zeolite (ITQ-64) with optimal confinement **(B)**. **(C)** Comparison of ITQ-64 (green symbols) with common zeolite catalysts in the production of xylene isomers.[103]

Corma and coworkers verified this concept through screening the suitability of existing zeolites and predicting their selectivity for reactions (e.g., xylene production, **Figure 1.7C**) based on the calculated stability of the respective TS in the zeolite framework. Their study constitutes a major step toward designing customizable OSDAs and corresponding zeolite catalysts for specific reactions. As such, this method can be used to streamline catalyst selection and circumvent Edisonian approaches in zeolite synthesis.

### 1.3.3 Engineering porous architecture

A common objective in zeolite catalyst design is the reduction of internal diffusion limitations imposed by small micropores (typically <1nm) and long diffusion path lengths in crystals that negatively impact catalyst performance. Approaches to address these problems include (i) the synthesis of zeolites with extra-large pores (> 12-membered ring aperture)[17], (ii) reduction of crystal size (as previously discussed), and (iii) introduction of mesopores (so-called *hierarchical zeolites*)[74,105,106]. Zeolites with extra-large pores can be used for reactions of large molecules that are unable to diffuse into conventional zeolites; however, synthesis of extra-large zeolites requires expensive OSDAs and often relies on the incorporation of heteroatoms (e.g., Ge) that are less acidic than Al.[17] An alternative to engineering hierarchical zeolites is the creation of mesopores[107], which has been shown to enhance catalyst performance in reactions such as methanol to hydrocarbon (MTH), alkylation, isomerization, cracking, and condensation.[108] Methods used to synthesize mesoporous zeolites can be classified as either *bottom up* or *top down*.

Bottom up approaches involve the use of either hard or soft templates. Hard templates include carbon nanotubes or nanofibers, ordered mesoporous carbons, non-ordered carbon aerogels or mesoporous carbons, pyrolyzed wood or carbonized rice husk, $CaCO_3$ nanoparticles, and polystyrene (and other polymeric) microspheres. Soft templating is associated with the use of cationic surfactants, mesoscopic cationic polymers, silylated polymers or surfactants, polymeric aerogels, and others (e.g., starch and bacteria). A third category is the generation of disordered

stacks (or aggregates) of crystals that result from the synthesis of 2D zeolites (refer to **Figure 1.5**). Lastly, the "zeolitization" of mesoporous materials (i.e., conversion of the amorphous walls of mesoporous materials into zeolites) can be used to synthesize hierarchical zeolites. One differentiating factor of bottom up approaches is that the chemical composition (Si/Al ratio) of the final hierarchical material is similar to that of the parent zeolite in the absence of template; however, the use of expensive templates and/or the multiple steps involved with zeolite extraction from organic/inorganic matrices pose challenges for commercial processes.[109]

Top down methods are associated with the removal of either silicon or aluminum from the zeolite framework post-synthesis. Dealumination is one of the most extensively used techniques for generating zeolite catalysts, such as the conversion of zeolite Y to ultrastable Y (USY). The removal of framework Al can be accomplished by acid leaching or steam treatment. An undesirable outcome of these processes is a change in Si/Al ratio and a concomitant increase in extra-framework Al relative to the parent zeolite, which alters the acidic properties of dealuminated zeolites.[109,110] Moreover, de Jong and coworkers[111] found that the mesoporosity generated by steaming, or steaming followed by acid leaching, leads to cavities on the exterior surfaces of zeolites without penetrating into the interior. Low interconnectivity and minimal depth of mesopores have spurred efforts to identify alternative routes, such as desilication[112,113]. In the latter approach, an alkaline medium is used to selectively remove Si from the framework. The concentration and spatial positioning of Al in the framework are critical factors influencing silica dissolution [113]. For instance, Groen and coworkers [113] have demonstrated for ZSM-5 that Si/Al = 25 – 50 is an optimal range for desilication. Similar studies have been extended to other frameworks such as MTW, MOR, BEA, AST, FER, MWW, IFR, STF, CHA, FAU, TON, and TUN [114]. Garcia Martinez and coworkers introduced a surfactant-templated approach that is performed in mild conditions (i.e., low temperature and low alkalinity) compared to desilication methods[115,116]. They demonstrated that surfactants, such as cetyltrimethylammonium (CTA), introduce uniform mesopores **(Figure 1.8A-**

**C)** in various zeolites, e.g., FAU, MOR, and MFI. Additional advantages of this technique over others is the preservation of zeolite structure without significant alteration of composition (i.e., Si/Al ratio). An alternative approach introduced by Valtchev and coworkers [55] uses $NH_4F$ to selectively target defect sites and etch both Si and Al at similar rates, which also preserves the Si/Al ratio (in contrast to less controlled treatment with other acids/bases).

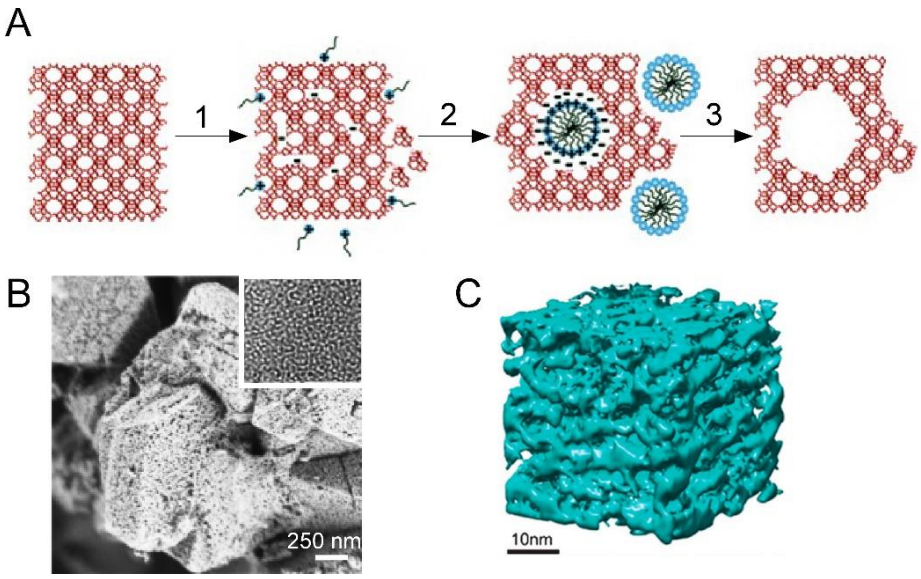


**Figure 1.8 (A)** The mechanism of mesopore formation is illustrated as three stages during surfactant templating.[117] **(B)** Mesoporous FAU prepared by postsynthesis treatment with CTA surfactant (inset: HRTEM image).[117] **(C)** 3D morphology of mesoporous FAU obtained from electron tomography.[118]

### 1.3.4 Introducing catalytic diversity in zeolites

Metal occlusion within zeolite pores can be accomplished through post-synthesis processes involving either wetness impregnation or solution ion exchange provided that the metal (or hydrated metal) is sufficiently small to diffuse through the channels and pore windows of zeolite catalysts. The metal cations can serve as Lewis acid sites for reactions, such as Cu-exchanged zeolites (e.g., CHA, LTA, etc.) for SCR of NOx with $NH_3$.[28,119] Some reactions rely on the incorporation of metal nanoparticles (or clusters), such as Pt-LTL catalysts used in Chevron Aromax and UOP Platforming processes.[120] Attempts to introduce atomic single metal sites have proven to be nontrivial. Examples include the work by Gates and coworkers who prepared single

site Pt in K-LTL[121] and Rh in dealuminated zeolite Y **(Figure 1.9A)**[122], and confirmed the monodispersity of these single sites by EXAFS, $^{13}C$ NMR and other techniques.[123,124] These mononuclear metal sites supported on zeolites combine the advantages of heterogeneous and homogeneous molecular catalysts; however, challenges still exist in synthesizing and controlling the dispersion of metals in microporous materials. To this end, continued efforts to verify the existence of atomic metals in the support (zeolite) are needed to accompany studies aimed at elucidating the catalytic activity of these sites.[125]

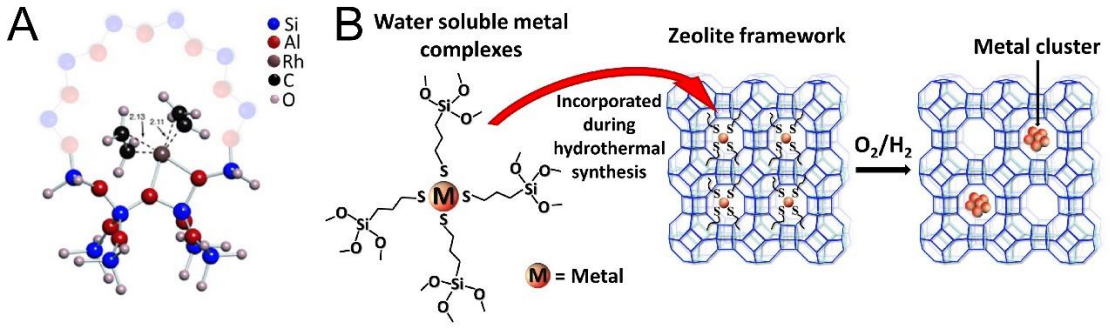


**Figure 1.9 (A)** Single metal site rhodium (brown) bonded to an aluminum (red) of zeolite FAU.[124] **(B)** Mechanism of metal occlusion in which the water-soluble metal complexes get incorporated into the zeolite framework and form metal clusters.[126]

The occlusion of metals in zeolites can reduce the effects of sintering and sulfur poisoning that are associated with catalyst deactivation. In cases where the desired metal to be occluded is either too large for post-synthesis treatment or is highly susceptible to sintering during post-synthesis calcination, an alternative approach is required. A novel method was proposed by Choi, Iglesias, and coworkers[127,128] to incorporate monodisperse, single metal atoms and/or nanoclusters of large metals within zeolite frameworks (e.g., LTA) by enclosing the metal atoms/clusters in ligands (e.g., mercaptosilane[126]). In this approach, metal reduction is averted during zeolite synthesis and enables the occlusion of metal complexes into zeolite pores as they form **(Figure 1.9B)** owing to the interaction between the ligands and zeolite precursors and/or composite building units. After zeolite synthesis is complete, the metals are isolated from the ligands during typical post-synthesis calcination. It was shown that metal-occluded zeolites exhibit reduced sintering and

improved thermal stability, along with the added benefit of shape and size selectivity in various reactions (e.g., alkanol oxidative dehydrogenation and CO oxidation).[126] However, high temperature synthesis for some zeolite frameworks can lead to early ligand decomposition, rendering this method ineffective. In this regard, Zones, Iglesias, and coworkers have further developed a protocol of zeolite interconversion, based on well-known methods[67] of converting metastable zeolites with large pores (e.g., BEA or FAU) to more thermodynamically stable structures with medium-sized pores (e.g., MFI) wherein the metal is first encapsulated within a parent framework at milder synthesis conditions (lower temperature); and then during the interzeolite conversion the metal is occluded within the pores of the daughter structure.[129] Corma and coworkers devised another procedure for Pt single atom and cluster (1 – 2 nm) occlusion in siliceous MCM-22 by incorporating the metal during the swelling stage of MWW 2D layer transformation into 3D structures.[130]

### 1.3.5 Tuning Al siting and distribution

The trajectory of zeolite catalyst design has shifted over the past decades from the microscopic level (e.g., crystal size and morphology) to the atomic level, wherein biasing the insertion of Al at specific tetrahedral sites has emerged as an area of significant interest in heterogeneous catalysis.[22] Advancements in this area are the result of rapid progress in high precision synthesis,[131,132] development of computation models to validate and/or guide experiments,[22,133-135] and the use of state-of-the-art characterization methods[136] to investigate Al siting and proximity. Early studies probing the impact of aluminum content on zeolite catalysis proposed that protons compensating Al atoms located at different lattice sites behave similarly in catalytic reactions, thereby suggesting that zeolites catalyze reactions predominantly by their shape selective properties.[137] This observation seems to agree with the calculations of deprotonation energies (DPE) derived from density functional theory (DFT) models, which demonstrate that acid strength is independent of Al siting.[138-140] The catalytic diversity of zeolites, however, is attributed

to van der Walls (vdW) stabilization that derives from confinement effects in nano-sized channels and cages. The relative contribution of Brønsted acidity and vdW interactions remains a subject of debate.

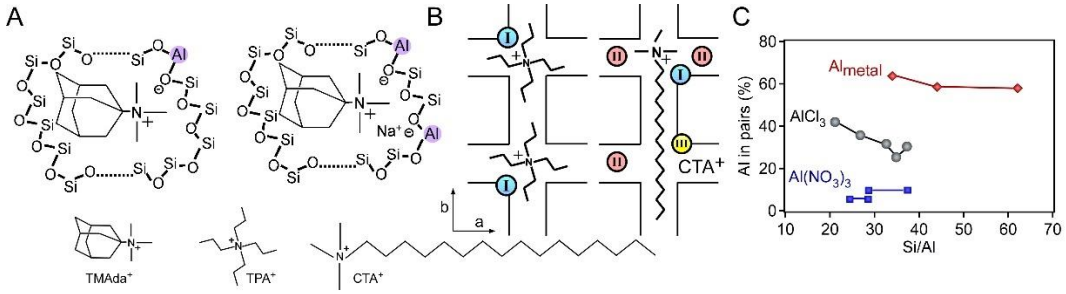


**Figure 1.10 (A)** Schematic of Al organization in CHA structure which forms isolated Al in the presence of $TMAda^+$ or paired Al in the presence of $TMAda^+$ and $Na^+$.[21] **(B)** Schematic of Al siting in ZSM-5 channels and intersection.[141] **(C)** Effects of aluminum source on the proportion of paired aluminum sites in the ZSM-5 framework.[142]

The spatial distribution of Al sites in zeolite frameworks is not always random, but can be manipulated by the judicious control of synthesis conditions that include (but are not limited to) structure-directing agents,[143-148] silicon source,[132,142,149] aluminum source,[142,149] heteroatom incorporation (e.g., B and Ge),[150] seeding (or accompanying interzeolite transformations),[151-154] and gel composition.[155] Structure-directing agents (SDAs) typically contain positively charged functional groups which can interact with anionic $[AlO_2]^-$ sites, thereby impacting Al siting in zeolite frameworks.[23] Several groups have explored the possibility of altering both proximity and siting of Al in several structures by varying the charge-density of SDAs. For example, Gounder and coworkers[21] have reported on the effects of relative ratios of organic (N,N,N-trimethyl-1-admantylammonium) and inorganic ($Na^+$) cations to influence the arrangement of paired and isolated Al **(Figure 1.10A)** in SSZ-13 (**CHA**). Rimer and coworkers[141] demonstrated that cooperative effects of organic molecules, such as cetyltrimethylammonium ($CTA^+$) or tetrapropylammomium ($TPA^+$), and inorganic cations (e.g., $Na^+$ or $K^+$) can be exploited to direct Al positioning in ZSM-5 (**MFI**) to either channel (straight and sinusoidal) or their intersections **(Figure 1.10B)**. Similar studies have been extended to other frameworks, such as FER,[144,145] IFR,[148]

and MEL,[156] among others. One method to tailor Al siting among different lattice sites is through the selected combination of silicon and aluminum sources. Dědeček and coworkers[157] employed this approach to show that the use of colloidal silica can enrich acid sites in sinusoidal and straight channels of ZSM-5, whereas switching the silicon source to tetraethylorthosilicate (TEOS) selectively places Al at channel intersections. The same group also hypothesized that the choice of aluminum source **(Figure 1.10C)** can impact the fraction of paired Al sites in the following order: $Al(OH)_3$ > $AlCl_3$ > $AlPO_4$ > $Al(NO_3)_3$.[142] The aluminum distribution can also be regulated by introducing heteroatoms, such as B or Ge, into synthesis gels owing to the competition between Al and heteroatoms to occupy distinct lattice sites in the framework. Indeed, it has been demonstrated that the variation of heteroatom-to-Al ratio in synthesis mixtures can impart unique distributions of acid sites in a number of zeolites, including MCM-22 (**MWW**),[158] ZSM-5,[150] and ZSM-11 (**MEL**).[159] An alternative strategy involving interzeolite transformations was reported by Yokoi and coworkers[151] who showed that CHA zeolites crystallized from faujasite (**FAU**) as a parent zeolite results in a higher proportion of $Q^4$(2Al) compared to CHA synthesized directly from amorphous reagents. Analogous approaches have been used by Dusselier and coworkers[152] to alter paired Al sites in CHA, which reportedly alters the speciation of Lewis acids (e.g. Fe) for partial oxidation of methane. Lastly, the systematic adjustment of synthesis parameters (e.g., temperature) can spatially bias Al positioning.[155] Similar effects were demonstrated by Rimer, Okubo and coworkers[160] who successfully synthesized a highly siliceous FAU zeolite (HOU-3) with biased Al siting by simultaneously varying the alkalinity and water content of the starting gel. Using a combination of solid state NMR and theoretical calculations, this study verified that $Q^4$(nAl)Si speciation corresponds to low energy configurations.

Numerous studies have demonstrated that the ability to selectively place Al at specific locations in the zeolite catalyst can significantly impact the activity, stability, and selectivity for a wide variety of reactions. Examples include methanol dehydration,[161] cracking,[162,163]

carbonylation,[164] methanol-to-hydrocarbons (MTH),[156,158,165-167] oligomerization,[168] and methane oxidation,[169,170] among others. Dědeček and coworkers[157] determined the consequence of Al proximity in ZSM-5 zeolites on the product yields in 1-butene cracking **(Figure 1.11A and B)**. They showed that a higher fraction of paired Al atoms enhances the hydrogen transfer reaction, which subsequently leads to the formation of aromatics **(Figure 1.11A)**.

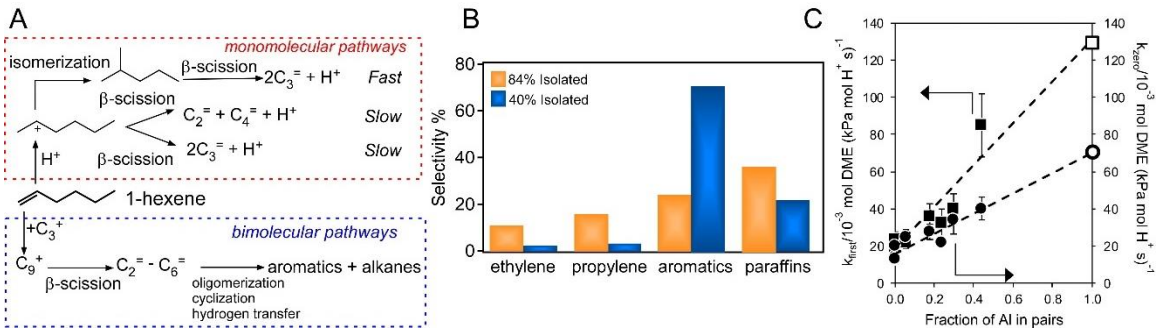


**Figure 1.11 (A)** Distinct pathways for mono- and bimolecular cracking of 1-hexene in ZSM-5.[150] **(B)** Impact of Al distribution on the cracking of 1-hexene over ZSM-5 with 84% isolated Al sites (red) and 40% isolated sites (blue).[157] **(C)** Zero order (circles) and first order rate constants (squares) for methanol dehydration in the CHA zeolites.[161]

In contrast, ZSM-5 samples with isolated Al arrangements promotes cracking with enhanced light olefins selectivity. Similar effects have been observed in methanol dehydration to dimethyl ether (DME), which is the first step in the MTH reaction. For example, Gounder and coworkers[161] showed that both zero-order and first-order rate constants increase with increasing proportion of paired Al sites **(Figure 1.11C)**. They attributed the increase in rate constants to a transition in the mechanism from an associative to dissociative pathway. Grabow and coworkers[171] employed periodic DFT to show that the location of Brønsted acids at different tetrahedral (T) sites within ZSM-5 channels (straight, sinusoidal, and intersections) can significantly influence the kinetics of DME formation, resulting in a broad temperature range (ca. 300 K) where the dominant pathway switches from associative to dissociative. The potential for variations in Al siting among different ZSM-5 catalysts may explain why there are conflicting claims in literature regarding the dominant reaction mechanism. Carbonylation of DME is another probe reaction which is used to

indirectly identify the location of acid sites in select zeolites. Iglesia and coworkers[172,173] have observed a direct correlation between carbonylation rates and Al sites within the 8-membered ring side pockets of mordenite (**MOR**). Using a similar methodology, Davis and coworkers[164] evaluated the impact of Al distribution in ferrierite (**FER**) on catalytic behavior. Control of framework Al siting can also markedly alter the dual cycle mechanism of MTH reactions. For example, Wang[165] and others[29,31,38-40] have proposed that acid sites located at the channel intersections of ZSM-5 promote the aromatic cycle (with increased coke formation), whereas it is suggested that Al in the narrower channels favors the olefin cycle. Provided that ZSM-5 catalysts can be synthesized with biased Al siting, the judicious distribution of acid sites can lead to enhanced selectivity and/or stability. The controlled location of Brønsted acids can also impact reactions involving Lewis acids, which are often placed in close proximity to Al sites as extra-framework species (i.e., ions, metals, or oxides). For example, Cu- and Fe-exchanged SSZ-13 zeolites have attracted significant interest over the years for either emission catalysis or methane activation applications. The speciation of extra-framework Cu or Fe,[174] which are active sites for the selective catalytic reduction (SCR) of nitrogen oxides (NOx)[175], can be manipulated by altering the proportion of paired/isolated Al sites in the zeolite framework. Specifically, paired Al sites can compensate $Cu^{2+}$ ions while isolated Al sites exchange $[CuOH]^{+}$ ions.[176] For the direct conversion of methane, Roman-Leshkov and coworkers[170] have demonstrated that a dimeric motif $[Cu\text{-}O\text{-}Cu]^{2+}$ associated with paired Al sites is the primary active site responsible for partial methane oxidation.

A long-standing challenge in developing structure-performance relationships in zeolite catalysis has been the inability to fully characterize Al siting. In recent years, there have been a number of advancements in the development of analytical tools[177] to quantify Al distributions and proximity with greater accuracy. Magic Angle Spinning-Nuclear Magnetic Resonance (MAS-NMR) spectroscopy of both $^{29}Si$ and $^{27}Al$ in combination with DFT calculations[178-180] **(Figure 1.12A)** is typically employed to probe $Q^4$(nAl)Si speciation and averaged Al-O-Si bond angles,

respectively. These synergistic analyses have enabled the identification of Al sites in a number of zeolites, such as ferrierite, ZSM-5, MCM-22, and ZSM-11, among others; however recent studies have shown that it is often nontrivial to obtain quantitative information solely from NMR data. For instance, Dědeček and coworkers[132] have shown that Al proximity can lead to $^{27}$Al isotropic chemical shifts up to 4 ppm, which can be misinterpreted as distinct crystallographic sites leading to controversial interpretations. Alternative techniques employing X-rays can be particularly useful owing to their large penetration depth for atomic level characterization. For example, Lercher and coworkers[181] used extended X-ray absorption fine structure (EXAFS) analysis in combination with DFT-trained molecular dynamics simulations to demonstrate the preferential occupancy of Al in zeolite beta (**BEA**). Moreover, van Bokhoven and coworkers[182,183] have developed an X-ray standing wave technique and X-ray emission spectroscopy to determine the distribution of Al (with atomic level resolution) in a natural zeolite (scolecite) and synthetic ferrierite, respectively. In general, X-ray diffraction methods are not sensitive enough to distinguish aluminum from silicon in the framework due to their similar scattering length density; however Pérez-Pariente and coworkers[144,145] have reported Rietveld refinement of synchrotron X-ray diffraction patterns to elucidate the location of organic SDAs within the channels/cages of zeolites, which directly influence Al occupancy. They showed that organic molecules capable of forming hydrogen bonds with framework oxygen atoms are the most likely to demonstrate this effect. Rimer and coworkers[184] used a combination of techniques, including synchrotron X-ray diffraction, molecular modeling, and solid-state two-dimensional NMR, to show that SDAs influence Al siting in mordenite. Weckhuysen and coworkers[185] developed a powerful atom probe tomography tool **(Figure 1.12B)** wherein three-dimensional element distribution maps of thin needle-shaped samples (ca. 100 nm) can be generated with exceptional spatial resolution (0.1 to 1 nm) using focused ion beam (FIB) milling. This technique can provide unique insights into the effects of harsh reaction conditions (e.g., steaming) on the dealumination and migration of Al atoms within zeolite pores. Alternatively, titration methods have been adopted in numerous studies to quantitatively

characterize the proportion of paired and isolated sites in zeolite frameworks. Several groups[131,142,150,179] have proposed that paired aluminum arrangements can be titrated by divalent metal cations (e.g., $Co^{2+}/Cu^{2+}$), whereas isolated sites compensate monovalent cations (e.g., $H^{+}/Na^{+}$). The adsorption of divalent metal cations is often combined with UV-visible spectroscopy. An analogous approach involves the use of a probe reaction, such as methanol dehydration or alkane cracking (i.e., constraint index),[143,180,186] to deduce Al arrangements.

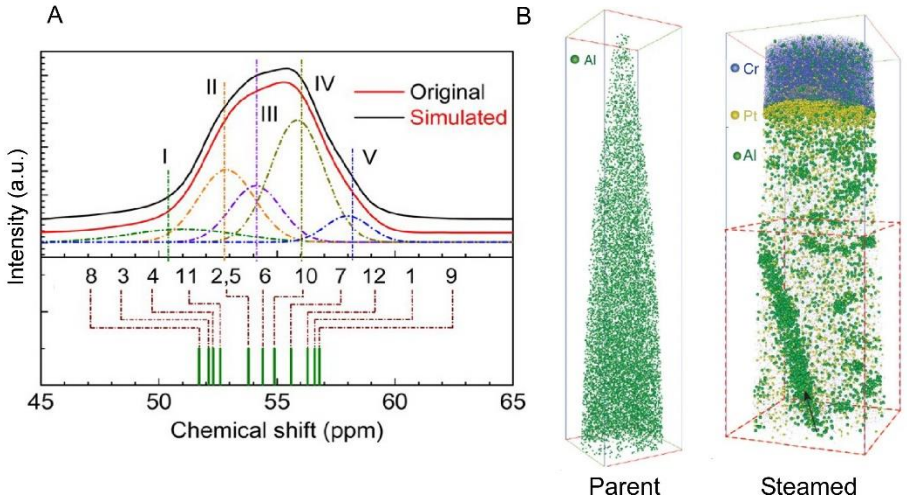


**Figure 1.12 (A)** Deconvolution of experimental (red) and calculated (black) $^{27}Al$ MAS NMR spectrum for orthorhombic ZSM-5 with 12 distinct T-sites.[165] **(B)** Comparison of 3D atom distribution maps of Al within a parent ZSM-5 zeolite and steam-treated zeolite using atom probe tomography.[185]

## 1.4 Mechanism(s) of zeolite crystallization

One of the most significant challenges to synthesize theoretical zeolite catalysts is overcoming the lack of fundamental knowledge of the crystal growth mechanism. In other words, if one wishes to design a material, it is critical to know the pathways that can be manipulated to alter the final product. This task is nontrivial owing to the large variety of precursors present in the synthesis mixtures of zeolites. Here a brief overview of our current understanding regarding the mechanism(s) of crystallization of zeolites is presented.

### 1.4.1 Nucleation

The molecular-level details governing the formation of first nuclei and their subsequent transformation to zeolite crystals are not well understood.[187] Amongst 245 known zeolite structures, mechanistic studies have only been done on a few zeolites leaving many fundamental questions unanswered. Zeolite synthesis often involves the formation of precursors which can range in complexity from primary particles (ca. 1-6 nm)[188,189] to amorphous gels.[190,191] There is consensus within the zeolite community that zeolite nucleation does not follow classical nucleation theory (CNT) wherein clusters of critical size form by the association of monomers.[192] In contrast, it has been argued by multiple groups that during the pre-nucleation stage primary amorphous phase formed by the initial mixing of silica and alumina sources transforms into secondary amorphous phase with evolved size, shape, and microstructure assisted by either room temperature aging or hydrothermal treatment.[193] Zeolite precursors are highly heterogeneous both in terms of size and composition, wherein they contain networks of aluminosilicate polymers with a significant fraction of solvent or colloidal aggregates often termed as worm-like particles (WLPs) in the literature.[187,194,195] It is extremely challenging to probe the microstructure of the amorphous precursor phase; however, calorimetry and colloidal stability experiments by Rimer and coworkers[196] have demonstrated that precursors exhibit some level of local ordering before nucleation. The presence of amorphous precursors is ubiquitous in zeolite synthesis mixtures which suggests a two-step mechanism of nucleation postulated for other materials such as proteins, colloids, and biominerals.[197-199] There are two distinct hypotheses regarding the roles of amorphous precursors in zeolite nucleation: (i) precursors can either act as a substrate for heterogeneous nucleation; and/or (ii) precursors can provide local regions of high supersaturation, thereby impacting the energetic barriers for nucleation.[55,200] Multiple groups have shown that the spatial origin of nucleation can either be inside the amorphous precursors[200] or at the exterior surface of the particles[191,201] **(Figure 1.13)**. The former mechanism has been reported for zeolite frameworks such as LTA[200], whereas the latter mechanism has been proposed for zeolites such as FAU[202],

EMT[201], and ANA[203]. Valtchev and coworkers[204,205] have shown that nucleation of zeolite LTA occurs at the solid/liquid interface wherein significant exchange of Si and Al species is needed through a solution mediated pathway of crystallization. Similar findings have been reported by the groups of Rimer[206] and Subotic on zeolite LTL and MFI[195] respectively. Conversely, Serrano and coworkers and others have reported solid-state transformations for a number of zeolites such as TS-1, TS-2, ZSM-5, ANA, and TS-beta.[207-209] It must be emphasized here that it is highly unlikely for the solid to reach specific chemical compositions critical for zeolite nucleation without the exchange of species between solid and liquid phases.

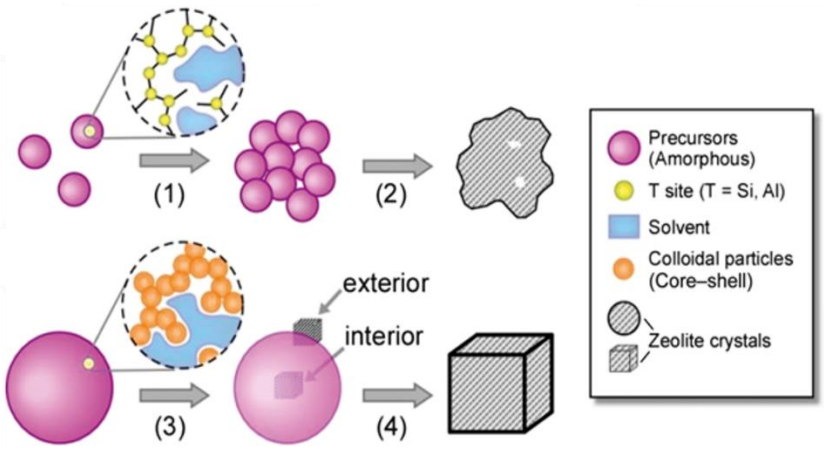


**Figure 1.13** Putative mechanisms of zeolite nucleation involving the formation of amorphous aggregates which serve as sites for heterogeneous nucleation either on the exterior surface or within the interior.[187]

In contrast to gel-based zeolite syntheses, there is relatively more information in the literature regarding zeolite nucleation in clear solutions (i.e., sols) owing to their facile characterization by *in situ* techniques such as scattering and microscopy. Silicalite-1 (MFI type) zeolite remains a subject of study by several groups since the growth solutions are clear and ideal for mechanistic studies. Amorphous precursors of silicalite-1, which range in size from 1-6 nm,[188,189,210] evolve during the induction period, yet they lack long-range order. The exact microstructure of precursors is relatively unknown; however, both experimental and computational studies have shown that nanoparticles exhibit a core-shell structure where the OSDA

tetrapropylammonium ($TPA^+$) forms a shell around the hydrated amorphous silica.[211-213] Tsapatsis and coworkers used cryo-TEM analysis[189] to track the evolution of nanoparticles at room temperature. The experiments revealed a unique mode of crystallization wherein precursors form aggregates that over time undergo complete crystallization (while maintaining the same morphology as the original aggregate), suggesting oriented aggregation as a major pathway for crystallization.[188] Moreover, several computational studies[214,215] have attempted to examine the formation of rings or CBUs during the polymerization of aluminosilicate clusters as potential growth units for crystallization; however, there has not been any direct experimental evidence to support this viewpoint. To this end, characterizing the role of precursors in zeolite nucleation remains an active area of research and significant advances in characterization techniques and modeling methods over the past years could provide a first molecular-level description of zeolite nucleation in the near future.

### 1.4.2 Zeolite growth

There are two schools of thought describing the growth mechanism(s) of zeolites: (i) the classical view of growth involving the addition of monomers from the solution to the crystal surface, and (ii) non-classical pathways which involve the incorporation of precursors more complex than a monomer ranging from oligomers and clusters to nanocrystals and amorphous gel-like particles **(Figure 1.14)**.[77] The Kossel model is often used to illustrate the distinct sites for the attachment of monomers: steps, kinks, and terraces.[216] Among these three sites, kinks are more energetically favorable as compared to steps and edges due to three bonds formed between a monomer and the crystal surface, whereas steps and terraces only lead to two bonds and a single bond, respectively. The driving force for crystal growth is proportional to supersaturation, which can be manipulated by varying the pressure, temperature, pH, and chemical nature of the solvent.[217] Classical crystal growth typically involves the generation of two-dimensional layers and spreading by the addition of monomers to the crystal surface.[217] Another route by which crystals can grow is

spiral growth which usually operates at low supersaturation and leads to the formation of growth hillocks emerging from a spiral dislocation.[218] At high supersaturation, adhesive type growth dominates leading to a rough surface topography (i.e., kinetic roughening). The advent of surface sensitive techniques such as atomic force microscopy (AFM), interferometry, and confocal microscopy has led to unique insights on the mechanism(s) of crystal growth for a number of zeolites and zeotypes such as LTA[218], FAU[220], LTL[221], MFI[222], SAV[223], and CHA[224]. Notably, Anderson and coworkers[220,221,223,225] showed the formation of steps and terraces on fully crystalline LTA, MER, FAU, and MFI and concluded that birth and spread is the dominant pathway for zeolite growth. The same group also reported that spiral growth is the preferential mode of growth for zeotypes such as STA-7[223] and zinc phosphate SOD[226]. It must be noted that most of the studies in the literature employ *ex situ* techniques to probe the crystallization mechanism of zeolites, which is subject to controversial interpretations since the mechanistic insights are limited when interpreting *ex situ* data. As such, if one wishes to obtain definitive evidence of crystallization pathway(s), techniques capable of investigating the dynamic sequence of events on crystal surfaces with molecular-level resolution are highly desired. To this end, Rimer and coworkers developed a unique *in situ* AFM tool to capture the zeolite surface growth in solvothermal conditions with exceptional spatiotemporal resolution.

In situ AFM studies on silicalite-1 revealed that crystal growth occurs by both molecular addition and nanoparticle attachment.[53] The first *in situ* demonstration of silicalite-1 surface growth identified novel pathways of crystallization involving 3-dimensional nucleation and island growth. These findings were in direct contrast with the layer-by-layer growth mechanism proposed for other zeolites using *ex situ* data. Recently, Rimer and coworkers extended the applicability of the technique to a more challenging system: zeolite A (or LTA).[218] The growth solutions of zeolite A are opaque due to the presence of bulk amorphous precursors. In the case of zeolite A, diverse precursors were identified contributing to surface growth ranging from monomers and oligomers

to nanocrystals and gel-like islands **(Figure 1.14)**. These studies are part of a growing discipline focused on crystallization by particle attachment (CPA) where the list of materials that are believed (or known) to grow by these complex pathways is rapidly expanding. Examples include metal oxides, biominerals, and proteins, among others.[227-229] Moreover, a systematic analysis of intermediate stages during the crystallization of zeolites LTL[206], MFI[195], MTW[230,231], and CHA[78] by *ex situ* electron microscopy has provided important pieces of evidence of crystals embedded in the deposits of amorphous precursors, indicative of CPA as a predominant pathway of crystallization.

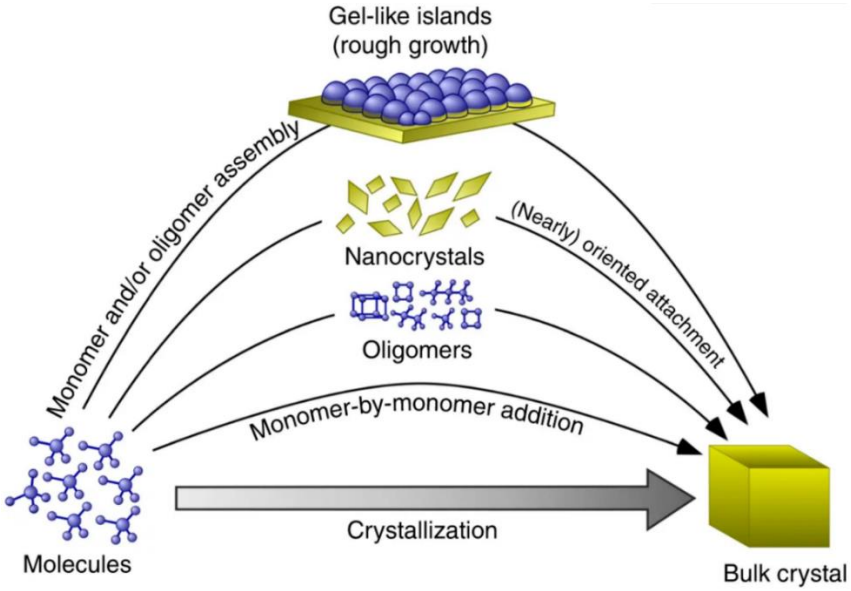


**Figure 1.14** Illustration of distinct growth mechanisms of zeolite crystallization involving either classical or nonclassical pathways. The former involves monomer-by-monomer addition while the latter involves the incorporation of precursors more complex than a monomer.[232]

Few studies have also explored the possibility to switch the growth pathway from nonclassical to classical for a desired application. For instance, Rimer and coworkers[78] have shown that a slight adjustment in the synthesis conditions, such as temperature, can result in faceted cubic crystals during SSZ-13 crystallization, suggesting a classical pathway is a prominent mode of growth. In addition to synthesis parameters, manipulation of organic molecules employed as either

growth modifiers or structure-directing agents is another viable approach to selectively control classical and nonclassical pathways of zeolite growth as recently demonstrated by the group of Tsapatsis.[233] Collectively, these observations highlight the complexity of zeolite synthesis in that growth occurs by multiple pathways involving a wide variety of potential growth units. As such, this active area of research presents opportunities for future studies to better understand the relative contributions of these pathways to generate superior zeolites for a wide range of applications.

## 1.5 Dissertation outline

The physicochemical properties of zeolite catalysts such as acidity, porous architecture, size, roughness, and crystal morphology can significantly alter their performance for a wide variety of reactions. As previously mentioned, fewer than 25 framework types are used in commercial applications. There are two major challenges associated with optimizing and/or expanding this list of materials for industrial applications. The first is the development of more streamlined routes to reduce the cost of zeolite synthesis. The second one is the lack of fundamental knowledge regarding the crystallization mechanism(s) of zeolites which often prohibits the control of zeolite properties. This dissertation focuses on three critical elements of zeolite catalyst design: (i) investigating the principles of surfactant templating to tune the properties of two zeolites (MFI and FAU) that are used in commercial applications that include catalysis, adsorption, and separations among others; (ii) developing organic-free routes for the fabrication of hierarchical zeolites to improve the performance of zeolites particularly in stability, lifetime, and activity using an economically feasible seed assisted approach; and (iii) developing techniques that are capable of monitoring complex mechanism(s) of zeolite crystallization with sufficient spatiotemporal resolution.

Surfactant templating has emerged as one of the most effective and versatile strategies for the construction of well-defined porous architectures in zeolites. Despite tremendous efforts by multiple groups to elucidate the mechanisms of surfactant templating in zeolite synthesis, these pathways are not well understood. In Chapter 2, we highlight the roles of surfactant

cetyltrimethylammonium (CTA) as an SDA in the design of ZSM-5 zeolites. Our findings reveal that the selection of inorganic/organic SDA combinations has a significant impact on the kinetics of ZSM-5 crystallization, as well as the properties of the resulting crystals. Using a combination of experiments and molecular modeling, we show that we can achieve smaller crystals (ca. 600 nm) in a similar time (< 24 h) as conventional syntheses. In Chapter 3, we discuss the roles of CTA as a mesostructuring agent to alleviate the diffusion limitations imposed by the micropores of USY zeolite (FAU type). We present *in situ* observations of intracrystalline mesoporosity generation in USY using AFM. Our findings capture in real time the structural, morphological, and textural evolution of initially rough crystals to smooth crystals with a uniform distribution of mesopores. In Chapter 4, we further expand our discussion to introduce an economically feasible method to synthesize hierarchical self-pillared pentasil (SPP) zeolites with intergrown nanosheets using a seed-assisted route. Our findings reveal nonclassical pathways of SPP crystallization. We also present the effects of various parameters such as seed structure, chemical composition, temperature, and time on the properties of SPP zeolites.

The ability to generate zeolites with well-defined and diverse physicochemical properties is dependent upon the fundamental understanding of crystallization pathways. There are a wide range of precursors that can serve as growth units during crystallization. One of the critical questions regarding precursor assembly pertains to the microstructure and physical state of amorphous particles as they evolve. In Chapter 5, we discuss the heterogeneity and physical state of amorphous bulk precursors encountered in the synthesis of various framework types. Our findings show that the majority of the zeolite synthesis mixtures are prepared in such a manner that will never lead to the formation of gels owing to the incomplete dissolution of the silicon source. Another major challenge in elucidating the assembly, microstructure, and mechanism(s) by which precursors are involved in crystallization is the lack of available techniques that are capable of monitoring amorphous-to-crystal transformations with sufficient spatiotemporal resolution. In

Chapter 6, we propose an elemental mapping method employing Field Emission Scanning Electron Microscopy with Energy Dispersive X-ray spectroscopy (FE-SEM-EDX) as a versatile tool to characterize morphological and compositional properties of precursors during the crystallization of five commercial zeolites (MER, MFI, MOR, TON, and LTL). The dissertation ends with a brief section summarizing the findings in this dissertation, providing an overview of future directions, and offering perspectives to further develop zeolite catalysts for a wide range of applications.

# Chapter 2

# Cooperative Effects of Inorganic and Organic Structure-Directing Agents in ZSM-5 Crystallization

## 2.1 Motivation

Zeolites are crystalline microporous aluminosilicates with unique properties, such as tunable acidity and exceptional (hydro)thermal stability, which are utilized in commercial processes ranging from ion-exchange and adsorption to catalysis and separations.[60,234-236] In this chapter we focus on the synthesis of ZSM-5 (MFI framework type), which is heavily used in catalytic applications that include (but are not limited to) reforming,[237] isomerization,[238] hydrocracking,[239] biomass conversion,[240] and methanol to hydrocarbon (MTH) reactions.[42] The MFI framework is comprised of 3-dimensional (3D) pore network consisting of intersecting straight and sinusoidal channels (ca. 5.6 Å diameter). Among the approximate 240 known zeolite structures, the vast majority are synthesized in the presence of an organic structure-directing agent (OSDA),[241] which is a molecule with a size and geometry similar to the channels or cages of zeolites; therefore, OSDAs facilitate pore formation, alter the kinetics of crystallization, and (in some instances) direct the incorporation of Al at specific tetrahedral sites within the crystal lattice.[21] It is possible to synthesize ZSM-5 in the absence of an OSDA using sodium ions.[242,243] as inorganic structure-directing agents; however, the products of OSDA-free synthesis contain a significant amount of Al (i.e., Si/Al < 20). In order to achieve higher Si content, which is often desirable for catalytic applications, an OSDA must be used in the growth mixture.

The most common OSDA for zeolite MFI is tetrapropylammonium (TPA).[55,56] Prior literature contains examples of other OSDAs, such as triethylbutylammonium bromide (TEBA),[244] dimers and trimers of TPA,[90,245] amines (e.g., triethanol amime[246] and ethyelene diamine[244]), and alcohols (e.g., 1,6-hexanediol[247] and tetrabutyl alcohol[248]). Ryoo and coworkers reported the use of

dual-porogenic surfactants containing mono quaternary ammonium groups to synthesize MFI nanosheets of several unit cell thickness.[88] Other groups have also established that under appropriate conditions the surfactant cetyltrimethylammonium (CTA) can act as an OSDA for MFI crystallization.[249-251] Prior studies have explored the use of CTA for alternative purposes, including its use as a crystal growth modifier to alter zeolite habit,[78] as a mesoporogen,[252] as a swelling agent in the preparation of 2-dimensional nanosheets from layered zeolites,[59,92,253-255] and in post-synthesis treatment to induce mesoporosity.[256-259] Few studies have explored the use of CTA strictly as an OSDA in zeolite synthesis as well as methods to optimize the physicochemical properties of ZSM-5 crystals produced by this OSDA. Examples include the work from Okubo and coworkers[249] that introduced CTA-directed MFI synthesis, as well as a recent paper by Hensen and coworkers[251] that highlighted the role of dual inorganic/organic structure-directing agents (SDAs). Interestingly, molecular analogues of CTA, such as tetramethylammonium (TMA) and its structural derivatives, do not direct the formation of MFI, but act as OSDAs for other zeolite structures (e.g., CAN, ERI, GIS, GME, LTA, LTN, MAZ, PHI, and SOD).[260-265] This suggests that the hydrophobic tail of CTA (**Figure 2.1)** is instrumental in its role as a structure-directing agent for MFI.

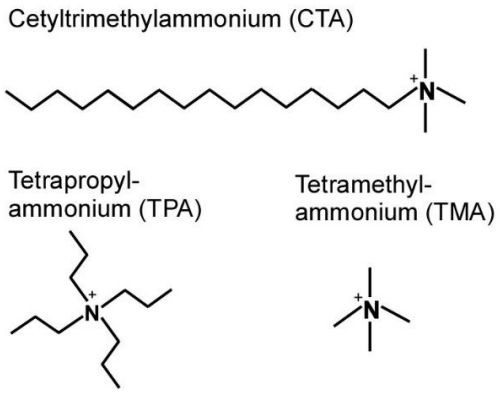


**Figure 2.1** Molecular structures of organic structure-directing agents.

Alkali and alkaline earth metals are common inorganic structure-directing agents (SDAs) in zeolite synthesis [1] and are also found in a majority of natural zeolites.[63] Inorganic SDAs function as extra-framework cations and have the ability to increase the rate of crystallization. For instance,

Davis and coworkers observed a seven-fold increase in the rate of MTW crystallization in the presence of alkali metals.[266] Prior studies have categorized the effects of inorganic SDAs on the basis of their ability to either promote or disrupt hydrogen bonding of water molecules around the cation, with subsequent displacement by (alumino)silicate species leading to the formation of nuclei.[267] Notably, Li and Na ions are referred to as structure formers, while K, Rb, and Cs are structure breakers owing to their large ionic radius. In general, the rate of crystallization is reduced or enhanced in the presence of structure breakers or formers, respectively;[268] however, it is not well understood how or why certain inorganic SDAs selectively promote the formation of a particular zeolite framework type, and how cations work in concert with organics to alter the kinetics of zeolite crystallization.

Herein, we investigate the effects of dual inorganic and organic SDAs on the synthesis of ZSM-5 through integrated experimental and molecular modeling studies. Comparisons are made using CTA and TPA as organic SDAs in combination with various alkali metals as the inorganic SDAs. Our findings reveal that the selection of specific organic/inorganic SDA combinations has a direct impact on the kinetics of MFI crystallization. Moreover, our findings indicate that SDA combinations influence the physicochemical properties of ZSM-5, which includes crystal size, morphology, and the number and/or spatial distribution of aluminum in the MFI framework. Time-resolved analysis of zeolite nucleation and crystal growth indicate a synergistic effect of organic and inorganic cations on MFI formation.

## 2.2 Results and Discussion

### 2.2.1 MFI synthesis with organic and inorganic ion pairings.

Here we investigate various combinations of inorganic and organic ions in ZSM-5 synthesis using two commonly reported SDAs for MFI – tetrapropylammonium (TPA) and Na – and two less commonly reported SDAs – cetyltrimethylammonium (CTA) and K. Beginning with studies of CTA, scanning electron micrographs reveal the formation of ca. 1.3 μm ZSM-5 crystals

in the presence of K (Figure 2.2A). In the presence of Na we observe ca. 650 nm crystals (Figure 2.2B), which is a factor of 3 less than those reported in prior studies of CTA-directed MFI crystallization.[249] The ability to produce small ZSM-5 crystals is associated, in part, to the SDA pairings. In addition, our findings indicate that crystal size is attributed to the use of colloidal silica compared to alternative silicon sources, such as tetraethylorthosilicate (TEOS). For instance, we prepared a ZSM-5 growth mixture with the same composition and switched from colloidal silica to TEOS. The resulting crystals (shown in Figure 2.9A) were approximately three times larger, which highlights the importance of Si source selection in MFI synthesis.

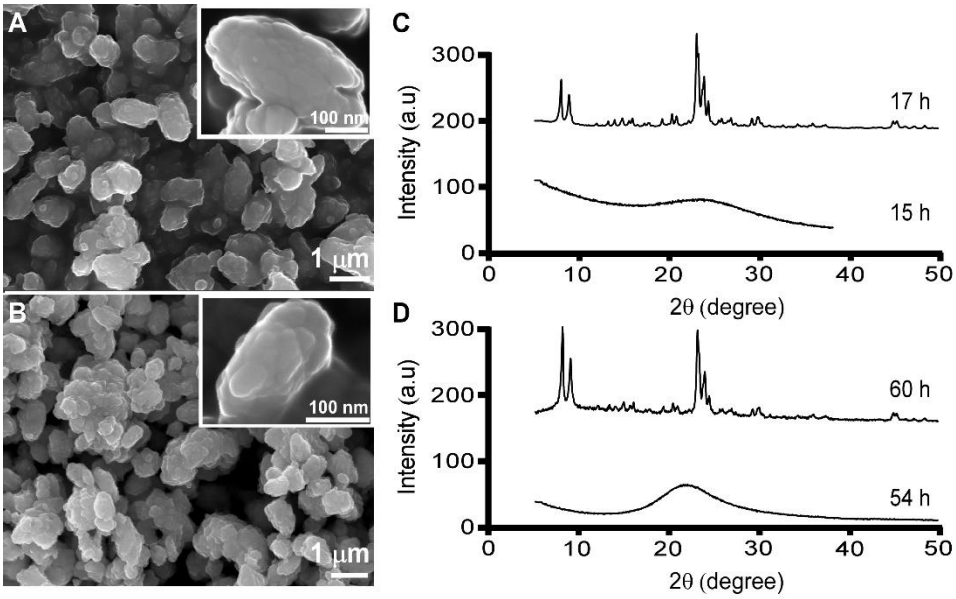


**Figure 2.2** Scanning electron micrographs of ZSM-5 crystals synthesized with CTA as the OSDA in the presence of **(A)** potassium and **(B)** sodium cations. Powder X-ray diffraction patterns of solids extracted from ZSM-5 syntheses (at specified times) in the presence of **(C)** potassium and **(D)** sodium cations.

Meng et al. reported that combinations of CTA and K resulted in the formation of MFI, whereas solutions of CTA and Na did not produce crystals under the conditions tested.[251] Here, we report that both SDA combinations result in MFI formation, with shorter crystallization times for solutions containing K. Notably, time-resolved powder X-ray diffraction (XRD) analysis of samples containing both CTA and K reveal that crystallization is complete within 17 h of

hydrothermal treatment (**Figure 2.2C)**. We observed that the combination of CTA and Na results in MFI crystals after longer heating time (ca. 60 h), as shown in (**Figure 2.2D)**. It should be noted that our experiments were performed at 160 °C compared to 140 °C in the study by Meng et al., which seems to indicate that crystals will form if given sufficient time to nucleate and grow. If true, this suggests that MFI crystallization potentially occurs in solutions containing CTA/Na at lower temperature with adequate heating time (i.e., > 10 days at 140 °C).

The synergy observed in the combination of CTA and K is quite unexpected given that K is reported in literature to either slow MFI crystallization or suppress its formation.[268] For instance, organic-free syntheses of ZSM-5 are possible using Na as an inorganic structure-directing agent (SDA),[243] but to our knowledge MFI cannot form in the presence of K as the only SDA. Conversely, K is known to direct the formation of many other zeolite frameworks (e.g., LTL, TON, and MER, among others).[43,54,206,269] A systematic analysis of MFI growth mixture containing CTA and varying ratios of K and Na reveal that there is a three-fold reduction in the induction time **(Figure 2.3A)** when switching from mixtures of CTA with Na to those with K. It should be noted that the reported induction times are an overestimation given that we use the first appearance of Bragg peaks in powder XRD patterns of extracted solids to estimate the onset of nucleation (i.e., peaks in XRD patterns appear once there is ca. 3% crystalline material in the sample).[270] By comparison we tested ZSM-5 synthesis using combinations of TPA and alkali metals and observed an opposite trend. Crystallization of ZSM-5 in the presence of Na is complete within ca. 24 h of hydrothermal treatment **(Figure A9)**, whereas the combination of TPA and K yields a partially amorphous product **(Figure 2.3B)**. Scanning electron micrographs of products extracted after 24 h of heating also reveal dramatic differences in crystal morphology **(Figure 2.3B)**, which was not observed in samples prepared with CTA. For instance, growth mixtures containing TPA and K result in the formation of hexagonal crystals (ca. 6 μm) with residual amorphous precursors **(Figure 2.3B, arrow)** clearly visible.

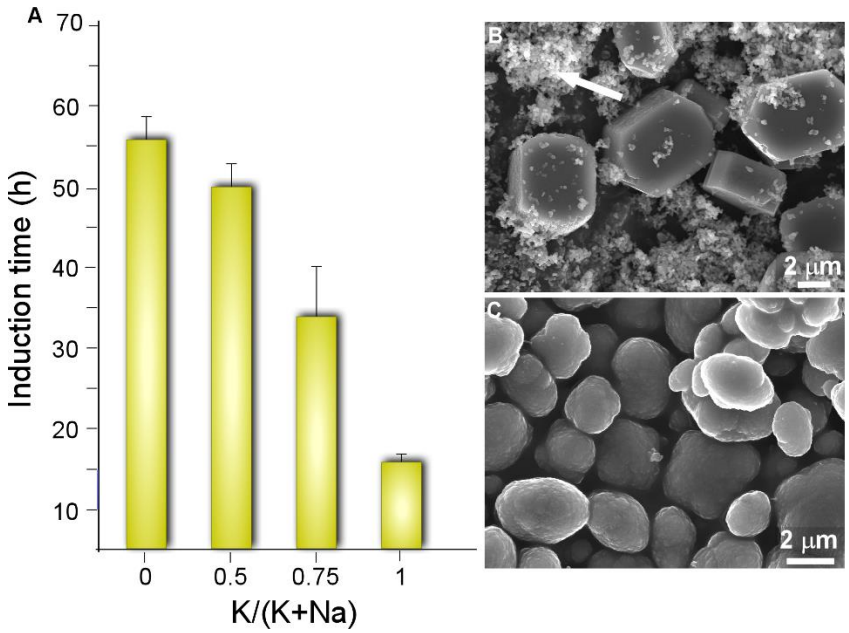


**Figure 2.3 (A)** Approximate induction times as a function of inorganic SDA content in ZSM-5 growth mixtures. Scanning electron micrographs of ZSM-5 crystals synthesized with TPA as the OSDA in the presence of **(B)** potassium and **(C)** sodium.

SEM images of crystals prepared with TPA and Na reveal an ellipsoidal morphology (Figure 2.3C) with smaller size (ca. 3 μm). The increased crystallization time for solutions containing K is qualitatively consistent with reports of MFI synthesis in literature. The ability of K to reduce crystallization time is only observed with CTA; therefore, our findings indicate that organic/inorganic SDA pairings do not follow identical trends but are dependent upon the selected combination. The molecular mechanism(s) governing the cooperative effects of inorganic/organic SDA combinations is not well understood.

### 2.2.2 TPA and CTA occlusion in MFI pores.

We also used MD to locate regions within the MFI framework where the OSDAs (TPA and CTA) become preferentially occluded during synthesis. Favorable conformations were identified by computing the stabilization energy $E_s$ for each OSDA in an MFI framework consisting of 36 unit cells (3×3×4) (see Methods). Modeling such a large system was necessary to avoid spurious self-interactions when inserting CTA, which is more than 2 nm in length in its fully

extended conformation. To minimize the computational cost of the simulations, conformational sampling was performed using only a single OSDA molecule. The results from these simulations, however, were found to be qualitatively consistent with limited sets of calculations performed using higher OSDA loadings (i.e., 1 and 2 OSDAs per unit cell).

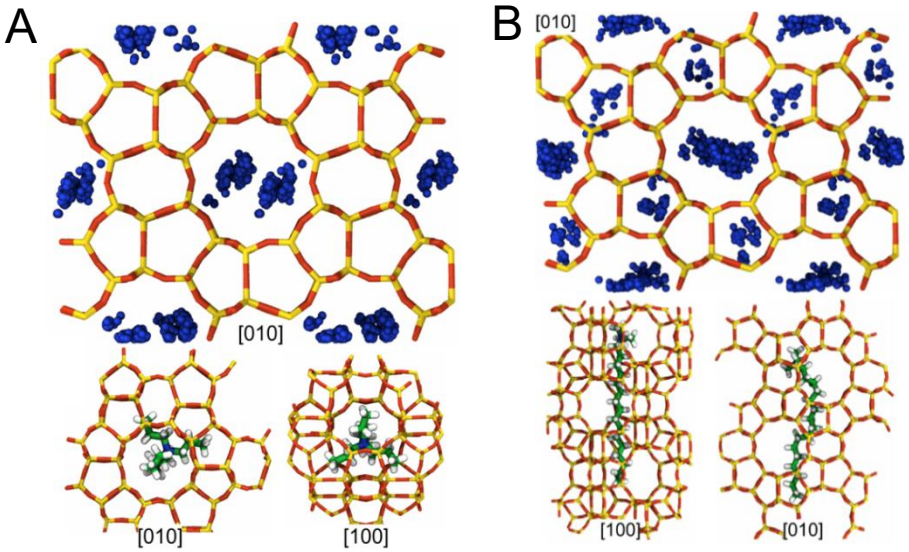


**Figure 2.4** Energetically favorable conformations for **(A)** TPA+ and **(B)** CTA+ in the MFI framework identified using MD. Blue beads indicate characteristic positions of the N atoms on SDAs for energetically favorable conformations.

The simulations predict that TPA preferentially occupies MFI's large pores located at the junctions where the straight and sinusoidal channels in the framework intersect **(Figure 2.4A)**. These pores are ~0.7 nm in diameter, which is similar to the size of TPA (min/max dimensions: ~0.65/0.91 nm). TPA adopts conformations inside these pores in which its N center sits near pore's middle and its bulky propyl groups extend into the adjoining channels **(Figure 2.4A)**. These favorable conformations significantly enhance the stability of the MFI framework ($E_s$ ~ -530 kJ/mol). Further, they are in excellent agreement with the TPA conformations deduced from nuclear magnetic resonance and X-ray diffraction measurements and predicted in other computational studies of MFI.[271-274] By contrast, conformations in which the N center of TPA is located inside the straight or sinusoidal channels result in unfavorable steric interactions that

destabilize the MFI framework (i.e., $E_s > 0$). Hence, the simulations suggest that TPA is too large to become occluded in other regions within the framework. Whereas TPA molecules can only be accommodated in MFI's large pores, there are at least two distinct conformations accessible to CTA, which has a chain-like structure (min/max dimensions: ~0.3/2.3 nm).

In the first conformation, CTA occupies a straight channel with its trimethylammonium head group extending into one of MFI's large pores **(Figure 2.4B)**. In the second conformation, CTA's backbone bends to allow it to occupy a sinusoidal channel **(Figure 2.4B)**. While both conformations are favorable ($E_s$ ~ -575 and -500 kJ/mol, respectively), the former leads to greater framework stability and thus will be energetically preferred. Nevertheless, the similar magnitude of the stabilization energies suggest that CTA may be occluded in both conformations during zeolite synthesis. Although, to our knowledge, no prior computational studies have been performed to examine CTA occlusion in MFI. The first conformation is remarkably similar to those that have been previously posited on the basis of steric considerations.[249,250] The second conformation, however, has not been previously hypothesized, which is likely due to the fact that it involves a complex rearrangement of CTA's backbone structure.

### 2.2.3 Impact of SDA pairings on Si/Al ratio.

The inorganic and organic SDAs in this study are both capable of becoming extra-framework cations to counterbalance negatively-charged framework Al sites. The occlusion of TPA cations in MFI can direct Al siting at channel intersections, whereas Na has the capability of directing Al siting in straight and sinusoidal channels.[180] It is postulated that Al siting in MFI[147] and other frameworks[21,275] is biased to particular tetrahedral sites, wherein the choice of organic and/or inorganic cations can alter Al distributions.[143] Motivated by past studies of Al distribution, we examined the molar Si/Al ratio of ZSM-5 crystals prepared with various SDA pairings **(Figure 2.5)**.

To study the spatial distribution of Al, we used a combination of electron dispersive X-ray (EDX) spectroscopy and X-ray photoelectron spectroscopy (XPS). The former probes greater depths of particles, thereby assessing the bulk Si/Al, whereas XPS is a surface-sensitive technique with a shorter penetration depth that assesses the outer rim of zeolite crystals. Numerous studies have reported aluminum zoning in ZSM-5 crystals, which refers to a gradient in Si/Al (high to low Al content) from the outer rim of the crystal to its interior.[277-279] The presence of an Al-rich rim has been observed for ZSM-5 crystals synthesized in the presence of TPA, whereas it is postulated that OSDA-free syntheses lead to a more homogenous Al distribution. This is seemingly true for ZSM-5 crystals prepared with a combination of TPA and K, which is aluminum zoned **(Figure 2.5)**.

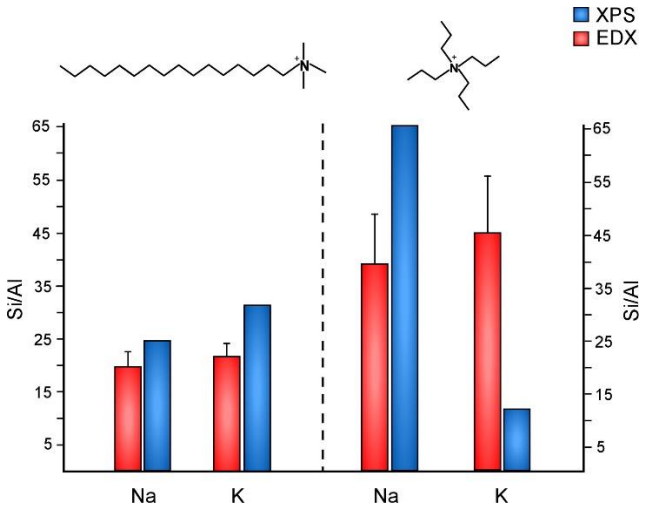


**Figure 2.5** Elemental analysis of ZSM-5 samples using EDX (red) and XPS (blue) to measure the Si/Al molar ratio. ZSM-5 crystals were prepared using CTA (left) and TPA (right) as OSDAs in the presence of either sodium or potassium.

Interestingly, synthesis mixtures containing TPA and Na resulted in the opposite trend: crystals with a Si-rich exterior and a more aluminous interior. Combinations of CTA and alkali metals resulted in more homogenous Al distributions (i.e., similar Si/Al measurements by XPS and EDX), with a small degree of silicon zoning. It is evident from this study that the judicious selection of SDA combinations has a marked influence on the spatial distribution of Al sites in the MFI framework.

As shown in **(Figure 2.5)**, EDX analysis reveals that the Si/Al of TPA-MFI crystals is approximately two-times higher than CTA-MFI crystals. This indicates that specific SDA combinations are capable of altering the degree of Al incorporation in framework sites; however, measurements of occluded organic by TGA reveal a relatively constant number of molecules per unit cell (labelled Z) for all SDA combinations: Z = 2.4, 2.2, 2.9, and 2.5 for CTA/K, CTA/Na, TPA/K, and TPA/Na, respectively.

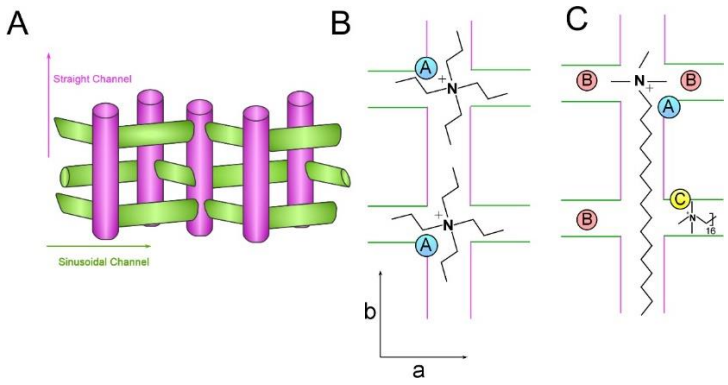


**Figure 2.6 (A)** Schematic of the straight and sinusoidal channels of MFI oriented along the b- and a-directions, respectively. **(B and C)** Idealized packing arrangements of TPA **(B)** and CTA **(C)** in ZSM-5 framework based on MD simulations

The inorganic and organic SDAs compensate the negative charge of framework Al, although it is not evident from our studies how Al is distributed within the straight and sinusoidal pores of the crystal structure **(Figure 2.6A)**. Moreover, it is understood that SDAs can stabilize defect sites (i.e., deprotonated siloxy groups), which is not explicitly considered in this discussion. Schematics of SDA occlusion in the pores of MFI are depicted in **Figure 2.6 B and C**. In the idealized rending of SDA occupancy, we postulate that TPA places a single Al site at the intersection of straight and sinusoidal channels (i.e., "A" site in **Figure 2.6B**). It could be argued on the basis of steric constraints that the propyl groups of TPA extending into adjoining channels reduce the likelihood of alkali metals occupying Al sites in close proximity of the organic.

Conversely, molecular modeling of CTA occlusion in MFI **(Figure 2.4B)** revealed an energetic preference for its alignment with the straight channel (analogous to assumptions in prior literature[251]). This allows for Al siting at channel intersections near the tetraalkylammonium (head) group of CTA (i.e., "A" site in **Figure 2.6C**). We postulate that the short methyl groups of CTA are less prohibitive for alkali metals to direct Al siting in vacancies or in close proximity of the head groups (sites "B" in **Figure 2.6C**). CTA may also direct Al siting within the channels (e.g., illustrated as site- "C" for a sinusoidal channel in **Figure 2.6C**). It should be emphasized that the scenarios illustrated in **Figure 2.6** are merely suggestive, and do not reflect direct evidence of Al siting; however, the hypothesized sequence of Al positions is qualitatively consistent with the nearly two-fold difference in Si/Al of CTA- and TPA-MFI samples.

### 2.2.4 Putative effects of SDA pairings on MFI nucleation.

Meng et al.[251] reported a relatively short timeframe of MFI crystallization in the presence of CTA and K, which they attributed to the kinetics of silica dissolution. This is consistent with studies in literature showing that silica dissolves more rapidly in alkaline solutions of K compared to those of Na.[280] Here, we confirmed this phenomenon using solutions similar to those of ZSM-5 synthesis, but in the absence of alumina. Alkaline solutions were prepared with colloidal silica (LUDOX AS-40) using the molar composition 20 $SiO_2$: 0.2 MOH: 1030 $H_2O$ (with M = K and Na). The temporal reduction in the hydrodynamic diameter of silica particles was measured *ex situ* by dynamic light scattering (DLS) using a previously reported protocol.[191] The results for KOH and NaOH are shown in **Figure 2.7A** and **A11**, respectively. The hydrodynamic diameter of colloidal silica decreases linearly with time. A monotonic increase in the slope, or rate of dissolution, is observed with an increase in temperature. It was noted that once the silica particles reach ca. 91% of their original size, dissolution ceases and the particle size remains constant (dashed line in **Figure 2.7A**). This indicates that the solution is saturated (i.e., silica solubility). In synthesis mixtures the presence of alumina forms a shell surrounding silica particles that reduces the rate of

dissolution.[281] It is also expected that the adsorption of OSDAs would impact precursor dissolution; however, the kinetic data in **Figure 2.7** indicates that the rate of silica dissolution at the actual synthesis temperature should be 500 – 1000 times faster (i.e., on the order of seconds). Given that the timescale of zeolite nucleation is on the order of hours, it is reasonable to argue that dissolution is not the rate determining step in MFI crystallization. An Arrhenius plot in **Figure 2.7B** confirms that silica dissolves more rapidly in KOH compared to NaOH, but the apparent activation energy of dissolution is approximately equal for both alkali metals. We propose that differences in dissolution cannot account for the relatively short time of MFI crystallization by CTA/K.

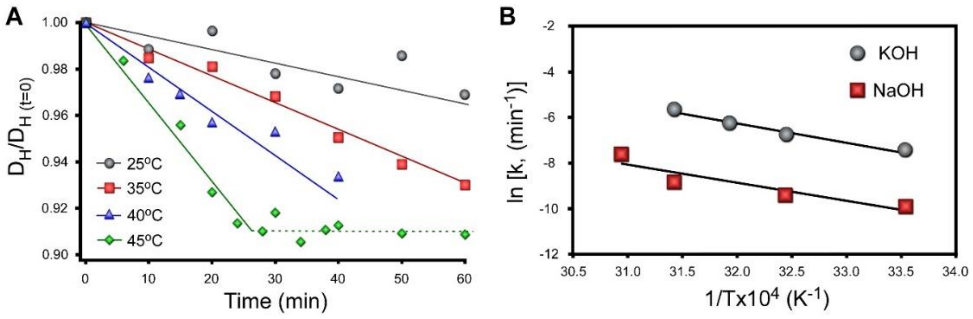


**Figure 2.7 (A)** Ex situ DLS measurements of silica dissolution in Al-free solutions. **(B)** Arrhenius plot of silica dissolution in NaOH (red) and KOH (grey). The apparent activation energies of dissolution are $E_A$ = 66 and 69 kJ/mol for NaOH and KOH, respectively.

Indeed, if a short induction time was attributed to faster silica dissolution, we would anticipate similar outcomes for growth mixtures containing TPA/K, which we did not observe. The cooperative interactions between organic and inorganic SDAs that lead to significant differences in crystal nucleation and growth times, as well as the final crystal size and morphology, are not well understood. SDA combinations could potentially impact MFI growth by influencing the formation of composite building units, altering the solvation of (alumino)silicate species in solution and/or at crystal interfaces, which can subsequently influence monomer or oligomer addition to growing crystals, or display favorable packing configurations within the pores of MFI crystals.

Elucidating the nature of cooperative SDA interactions is a topic that requires further analysis by concerted modeling and experimental efforts to identify their mechanism(s) of action.

A common characteristic of zeolite growth mixtures is the presence of amorphous precursors, which can range in size from small nanoparticles[53,233] to micron-sized agglomerates that are often referred to as *worm-like particles* (WLPs).[78,206,282] During hydrothermal treatment, precursors evolve in size, composition, and/or microstructure, eventually reaching a steady state at a time that generally coincides with the end of the induction period. During crystal growth the population of precursors gradually reduces, and in many instances precursors are implicated in nonclassical pathways of growth, referred to as crystallization by particle attachment (or CPA).[283] Prior studies of zeolites, such as zeolite L (LTL), revealed an apparent correlation between the final size of evolved precursors and crystallization time. Notably, the slower the rate of crystallization, the larger the average size of evolved precursors.[206] In this study of ZSM-5 we observe similar trends. In **Figure 2.8** we report the size of precursors at early and later stages of crystallization for all four SDA combinations. When evaluating the differences in precursor size (from smallest to largest), we obtain the following order: TPA/Na < CTA/K < TPA/K < CTA/Na. This sequence matches the order of crystallization time, which is 15, 17, 48, and 60 h, respectively, which indicates that SDA combinations leading to faster crystallization (i.e., TPA/Na and CTA/K) provide less time for precursors to evolve. Similar observations for zeolite LTL have been reported when using modifiers (e.g., peptoids) that inhibit nucleation and allow more time for precursors to evolve.[284]

A comparison of ZSM-5 induction and crystal growth times are provided in Table 1 for various combinations of inorganic and organic SDAs with the addition of two alkali metals, Li and Cs. The induction time is estimated as the onset of Bragg peaks in powder XRD patterns **(Figure 2.2, A9, and A10)** where it is recognized that nucleation begins slightly before this point and may continue beyond it based on prior observations in literature.[206,247] For estimates of crystal growth times we use a combination of powder XRD patterns and SEM images **(Figure A12)** to confirm

that all amorphous precursors have been consumed (which is difficult to determine from XRD alone).

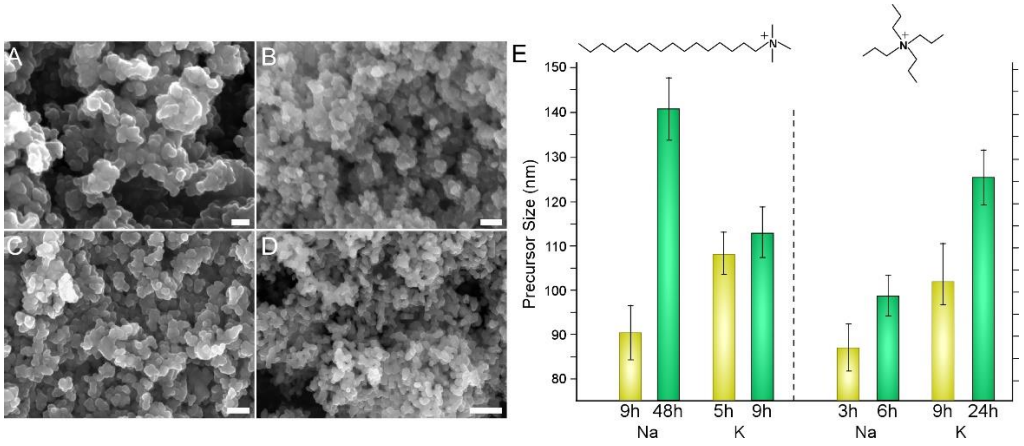


**Figure 2.8 (A – D)** SEM images of samples prepared with CTA in the presence of **(A)** Na and **(C)** K. These images are compared to samples prepared with TPA in the presence of **(B)** Na and **(D)** K. Scale bars equal 500 nm. **(E)** Average precursor size at short (yellow) and long (green) heating times using various SDAs

Comparison of natural zeolites and prior literature of OSDA-free zeolite synthesis reveals that Li can direct structures such as EDI, ABW, EMT, FAU, and ANA,[285] whereas Cs can direct the formation of TON, RHO, CHA, LTA, and ANA.[285,286] In this study we found that combinations of CTA with either Li or Cs results in amorphous products. Conversely, MFI crystallization occurs in the presence of TPA with each alkali metal tested. The induction times for syntheses with Li and Cs are ca.12 h, which is longer than those of Na and K; however, there is a substantial difference in the crystal growth times. Specifically, K and Cs have much longer growth times as compared to Li and Na, which is qualitatively consistent with the structure forming and structure breaking effects observed for different cations reported in literature.[267,268] One notable difference between TPA and CTA is the amphiphilic nature of the latter that can lead to micelle formation at sufficiently high concentration. CTA is one of the most extensively studied surfactants, and in the presence of alkali metals it has been reported[287] that when introducing Na salts to an aqueous CTA solution (0.1 M CTA), the dissociation enthalpy of the salts is an order of magnitude higher than that measured in water. Similar studies for K salts reveal that the relative increase in enthalpy (from

water to a CTA solution) is much less,[287] which is inconsistent with the Hofmeister series that is used to explain differences in alkali salt dissociation in water and the potential influence of alkali metals on the critical micelle concentration of surfactants.[287] To this end, we performed DLS measurements of CTA dissolved in KOH and NaOH solutions at room temperature (using the exact concentration of MFI synthesis, but without the addition of silica and alumina sources) to test the effect of alkali metals on CTA micellization. The scattering counts of the NaOH mixture was 1.5-times higher than that of KOH at 25 °C, indicating a higher concentration of CTA micelles in the former; however, the counts were insufficient to obtain reliable hydrodynamic diameters.

**Table 2.1** Comparison of ZSM-5 induction and crystal growth times.

| | Induction Time (h) | | Crystal Growth (h) | |
|---|---|---|---|---|
| Alkali Metal | TPA | CTA[b] | TPA | CTA |
| Li | 9 -12 | -----[a] | < 12 | -----[a] |
| K | 3 – 6 | 15-17 | > 21 | < 2 |
| Na | 3 – 6 | 54 –60 | < 21 | < 6 |
| Cs | 9 – 12 | -----[a] | > 60 | -----[a] |

[a] Amorphous products (after 5 days of heating); [b] ZSM-5 can be prepared using only TPA or only Na, but we were unable to prepare crystals with only CTA.

It is also expected that the critical micelle concentration at 160 °C (i.e., the actual synthesis condition) will be different.[288] Nevertheless, Na is a more effective promoter of CTA micellization than K, which may offer some insight into the latter's ability to increase the rate of MFI crystallization. If the interaction between organic and inorganic cations is indeed critical, this would also suggest that the effective TPA/Na combination is due to less favorable interactions between TPA and Na ions (relative to the interactions of TPA with other alkali metals).

### 2.2.5 Generation of mesoporosity by CTA.

The most common uses of CTA in zeolite synthesis are associated with its role as a mesoporogen,[116,252] as a post-synthesis agent to generate mesoporosity,[289] or a swelling agent to generate 2-dimensional zeolites from layered structures.[253] To this end, we performed textural

analysis of MFI samples prepared with CTA and observed a type IV isotherm **(Figure 2.9A, *i*)** that indicates the presence of mesoporosity.

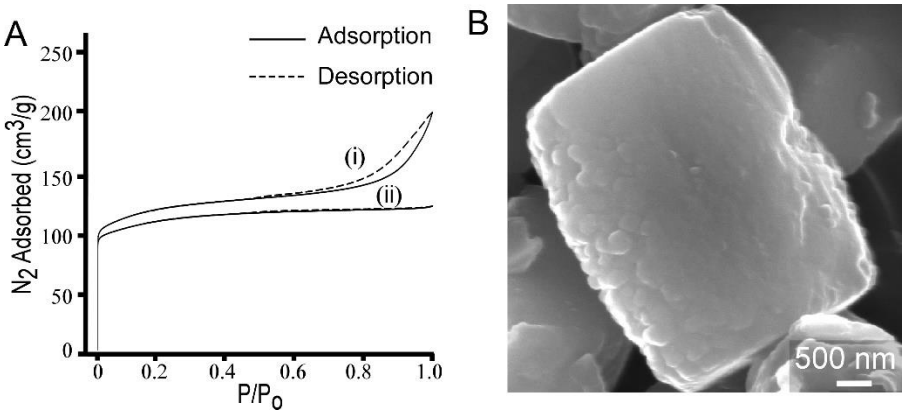


**Figure 2.9 (A)** $N_2$ physisorption isotherms of ZSM-5 crystals synthesized with CTA using two different silica sources: (i) LUDOX AS-30; and (ii) TEOS. **(B)** Scanning electron micrograph of a ZSM-5 crystal synthesized using TEOS.

The t-plot external surface area contribution to the total surface area is 31% (or 139 $m^2/g$) of the measured surface area of crystals. The shape of the adsorption/desorption curve suggests that mesopores are likely formed by nanocrystal aggregation, which is qualitatively consistent with SEM images in **Figure 2.2.** Interestingly, when we switch silicon sources from LUDOX AS-30, which was used for all previous syntheses, to tetraethylorthosilicate (TEOS), we observed several notable differences in the crystalline product. Crystals prepared using TEOS exhibit a type 1 isotherm (**Figure 2.9A, *ii*)** which is a characteristic of microporous materials without evidence of mesoporosity.

Nitrogen adsorption measurements reveal that crystals prepared with TEOS have lower surface area (**Table C2**). TEOS also leads to a 3-fold increase in crystal size (ca. 3 μm), as shown in **Figure 2.9B**. Moreover, elemental analysis reveals that crystals prepared with TEOS have much higher silicon content (i.e., the Si/Al increases from 17 to 53). Overall, our parametric examination of MFI crystallization reveals that the physicochemical properties of ZSM-5 crystals can be tailored through the judicious selection of SDA combinations, synthesis conditions, and reagent sources.

## 2.3 Conclusions

In summary, we have shown that CTA can be an effective SDA for ZSM-5 crystallization based on its ability to generate sub-micron particles in a period of time that is equivalent to more conventional SDAs, such as TPA. We have shown that CTA-directed growth of MFI crystals leads to a more uniform distribution of aluminium throughout the particle, which may be explained by computational simulations showing that CTA can access both straight and sinusoidal channels, unlike TPA that resides strictly at the intersection of the channels.

Investigation of organic and inorganic SDA combinations reveals a cooperative effect between two positively-charge species that act as both structure-directing agents and extraframework cations. We observe that pairings of CTA/K and TPA/Na result in the fastest crystallization times, suggesting these combinations have a synergistic effect on ZSM-5 growth that is unique to the selection of SDAs. The ability of dual SDAs to alter the physicochemical properties of zeolite crystallization is a potentially useful approach to rational design. Moreover, the relatively low cost and high market availability of CTA makes it a promising candidate for commercial production of ZSM-5.

## 2.4 Material and Methods

### 2.4.1 Materials

The following chemicals were purchased from Sigma-Aldrich (St. Louis, MO): LUDOX AS-30 (30 wt % suspension in water), LUDOX AS-40 (40 wt % suspension in water), tetraethylorthosilicate (TEOS, 98%), potassium hydroxide (85% pellets), aluminum sulfate hydrate (98%, 14-18 $H_2O$, calculated as 18 $H_2O$), hexadecyltrimethylammonium bromide (CTAB, BioXtra, ≥99%), tetrapropylammonium bromide (TPABr, 98%), and tetramethylammonium bromide (TMABr, 98%). Additional reagents used for the synthesis of ZSM-5 include sodium hydroxide (98% pellets, MACRON Fine Chemicals), lithium hydroxide (anhydrous 98%, Alfa Aesar), and

cesium hydroxide (50% w/w aq. soln., Alfa Aesar). Deionized (DI) water used in all experiments was purified with an Aqua Solutions RODI-C-12A purification system (18.2 MΩ). All reagents were used as received without further purification.

### 2.4.2 Crystallization of MFI Zeolite

ZSM-5 crystals were synthesized from a growth mixture with a molar composition of 2 OSDA: 11.9 $M_2O$: $Al_2O_3$: 90 $SiO_2$: 3588 $H_2O$ (OSDA = CTAB or TPABr; M = K and/or Na). Aqueous solutions of potassium hydroxide (0.33 g in 1.44 g of DI water) and aluminum sulfate (0.14 g in 1.44 g of DI water) were mixed with 5.76 g of water, and LUDOX AS-30 solution (3.76 g in 2.13 g of DI water) was added under vigorous stirring. AS-30 was used as the nominal silicon source unless otherwise stated. The resulting mixture was stirred for ca. 20 h at room temperature (referred to as aging). After aging, the OSDA (e.g., 0.1515 g CTAB) was added and the solution was left to stir for another 2 h at room temperature. The growth mixture (ca. 10 g) was then placed in a Teflon lined stainless steel acid digestion bomb (Parr Instruments) and was heated under rotation (30 rpm) and autogenous pressure in a Thermo Fisher Precision Premium 3050 Series gravity oven. The nominal time and temperature for ZSM-5 synthesis was 3 days at 160 °C. For X-ray and microscopy analyses, the particulates in the growth mixture (amorphous and/or crystalline) were isolated as a white powder by centrifugation (Beckman Coulter Avanti® J-E series high-speed centrifuge) at 13,000 rpm for 45 min. The solid was washed with DI water to remove the supernatant and the centrifuge/washing step was repeated a second time. The resulting solid was dried at ambient conditions. During the preparation of microscopy samples, the solid was dispersed in DI water and an aliquot of the suspension was placed on a glass slide and dried overnight. Crystals on the glass slide were transferred to SEM sample holders (Ted Pella) by gently pressing the glass slide on the carbon tape.

### 2.4.3 Materials Characterization

Powder X-ray diffraction (XRD) patterns of as made samples were collected on a Siemens D5000 X-ray diffractometer using a Cu Kα source (40 kV, 30 mA). Scanning electron microscopy (SEM) images were obtained with a LEO 1525 FEG system operated at 15 kV and a 5 mm working distance. All SEM samples were coated with a thin carbon layer (ca. 30nm) prior to imaging. Textural analysis was performed with a Micromeritics ASAP 2020 instrument using N2 as a probe gas for physisorption at an incremental dosing rate of 3 m3/g STP and an analysis bath temperature of 77 K. Prior to analysis, samples were calcined at 550 ℃ for 6 h under flow of compressed air at 100 $cm^3$/min. The surface area was calculated from BET analysis selecting the initial low pressure points with a correlation coefficient greater than 0.999. The weight percentage of occluded organics in ZSM-5 samples were assessed by thermogravimetric analysis (TGA) using a TA instruments Q50 model and N2 as the carrier gas at a flow rate of 100 mL/min. The temperature was ramped up to 800 ℃ at the rate of 1 ℃/min with an isothermal dwell time of 10 min. X-ray photoelectron spectroscopy (XPS) data were collected by a Physical Electronics Model 5700 XPS instrument. A monochromatic Al Kα X-ray source (1486.6 eV) was used with the power of 350 W. All spectra were obtained once reaching a vacuum of $5\times10^{-9}$ torr or better. Elemental analysis of samples was conducted by energy dispersive X-ray (EDX) spectroscopy using a JEOL SM-31010/METEK EDAX system at 15 kV and 15 mm working distance. Dynamic light scattering (DLS) measurements were performed on a Brookhaven Instruments BI-200SM machine equipped with a TurboCorr Digital Correlator, a red HeNe laser diode (30mW, 637 nm), and a decalin bath that was filtered to remove dust. The liquid sample cell was regulated at 25°C with a Polyscience digital temperature controller. Samples were prepared by diluting zeolite growth mixtures in pre-filtered DI water (0.45-μm nylon syringe filter, Pall Life Sciences) to achieve reasonable scattering counts (>20,000 count-sec-1). At least three measurements were performed per sample. Autocorrelation functions were collected over a 2 min timeframe and the hydrodynamic diameter DH was analyzed by the method of cumulants to assess particle size distribution. Silica dissolution experiments were

performed by adding colloidal silica to metal hydroxide solutions (pH = 12) in the absence of aluminum. Solutions were separated into different vials and heated at specified temperatures in a Julabo ED-5M/B water bath. Vials were removed at periodic times and immersed in ice to cool down to room temperature before performing DLS analysis.

### 2.4.4 Molecular Modeling

Molecular dynamics (MD) simulations were performed with GROMACS 4.6.7 [290] to identify energetically favorable conformations of the OSDA molecules (*i.e.*, CTA and TPA) within the MFI framework. The structure of MFI was modeled using the atomic positions and lattice parameters from the IZA database. Interactions between zeolite framework atoms (Si and O) were described the ClayFF potential,[291] whereas TPA and CTA were modeled using the generalized AMBER force field.[292] Standard Lorentz-Berthelot combining rules were employed to determine the potential parameters for modeling van der Waals interactions between the SDAs and zeolite framework.[293] Van der Waals and real-space Coulombic interactions were truncated using a cutoff of 0.9 nm, and the particle mesh Ewald method[293] was used to treat long-range electrostatics. Parameters for the Ewald summation were chosen to ensure a relative error of less than $10^{-5}$ in the calculated energy. The equations of motion were integrated using a velocity-Verlet scheme with a 2 fs time step.[293] A Bussi-Parrinello velocity-rescaling thermostat[294] was used to maintain temperature, and constant pressure conditions were imposed using a Parrinello-Rahman barostat.[295] A relaxation time constant of 2 ps was used for the both the thermostat and barostat.

Energetically favorable conformations for the OSDAs were sampled using a three-step procedure. In the first step, OSDA molecules were inserted into the zeolite framework. To avoid trapping the systems in high-energy conformations, the insertions were performed gradually using an alchemical transformation procedure[296] in which the OSDAs were converted from an ideal gas to fully interacting molecules over the course of a 500 ps canonical ensemble MD simulation at 300 K. The details of this procedure follow those described by Kim et al.[297]. In the second step, the

configurational energy of the system (OSDAs + zeolite framework) was minimized using the conjugate gradient algorithm. Minimization was stopped when the maximum pair-wise force fell below a threshold of 5 kJ/mol/nm. Finally, in the third step, the energy-minimized configuration was used to initialize a ns-long isothermal-isobaric ensemble MD simulation at 300 K and 0 bar. The last half of each MD trajectory was used to evaluate the average energy for the system $\langle U_{sys} \rangle$ and the stabilization energy[95,96] $E_s \equiv \langle U_{sys} \rangle - \langle U_{zeo} \rangle - n\langle U_{SDA} \rangle$, where $n$ is the number of SDA molecules in the system, and $\langle U_{SDA} \rangle$ and $\langle U_{zeo} \rangle$ are average energies computed for a single SDA molecule and the empty zeolite framework, respectively. Previous computational investigations have shown that $E_s$ computed a similar manner is a good descriptor for identifying novel OSDAs to stabilize otherwise thermodynamically unstable zeolite polymorphs. [95,96] For the purpose of this study, $E_s$ was used to identify energetically favorable arrangements of OSDAs that enhance the MFI framework stability. The three steps above were repeated to evaluate $E_s$ for ~$10^3$ different conformations for each OSDA; favorable conformations with $E_s < 0$ were kept for further analysis.

# Chapter 3

# Time-Resolved Dynamics of Intracrystalline Mesoporosity Generation in Zeolite USY

## 3.1 Motivation

For more than 25 years the surfactant-templating approach has been employed to facilitate the mesostructuration of different materials through supramolecular self-assembly of surfactants.[298] Since the first publication regarding the surfactant-templating route for mesoporous silica,[299] the number of studies reporting the preparation of nanostructured mesoporous solids via supramolecular templating has been continuously increasing and expanding to more diverse inorganic, organic/inorganic hybrid, and organic solid materials.[300-305] More recently, the surfactant-templating approach has also been extended to the synthesis of hierarchical zeolites in which the surfactant can be used to generate intracrystalline mesoporosity in the structure of these microporous materials.[306] Among the different procedures developed to generate secondary porosity within zeolites,[47,99,307-310] surfactant-templating in alkaline media allows for the incorporation of mesoporosity with tailored dimensions, while simultaneously maintaining the strong acidity and hydrothermal stability of the original zeolite.[117,141,311-313] The structure of surfactant-templated zeolites has been resolved by a combination of advanced gas adsorption, rotation electron diffraction (RED), and electron tomography (ET), which unambiguously confirmed the presence of intracrystalline mesoporosity within the zeolites.[118,314] The simplicity, low cost, and versatility of this procedure to generate hierarchical zeolites has led to its commercialization and use as an FCC catalyst in several refineries to more efficiently produce liquid fuels while reducing $CO_2$ emissions.[117] The most plausible mechanism for the formation of these surfactant-templated zeolites relies on the crystal reconstruction of the zeolite that occurs through multiple processes: (i) the diffusion of cationic surfactants to the interior of the zeolites

attracted by the negatively charged silicon tetrahedra formed by the opening of Si-O-Si bonds by hydroxide ions; (ii) the self-assembly of the surfactant molecules into micelles within the zeolite structure; and (iii) the expansion of the zeolite crystals in order to accommodate the formed mesoporosity.[315]

Recently, we reported the first time-resolved study of the development of mesoporosity in zeolites through surfactant-templating by *in situ* synchrotron XRD.[289] By combining these measurements with a number of *ex situ* techniques, we were able to determine the apparent activation energy of the development of mesoporosity in USY by surfactant-templating, which is in the same order of magnitude (30 – 65 kJ $mol^{-1}$) to those involved in the crystallization of zeolites.[316] Additionally, the use of a time-resolved technique, such as liquid-cell transmission electron microscopy (Liq-TEM), rendered the first *in situ* real time visualization of this process.[289] Due to the presence of liquid water and the silicon nitride windows of the TEM sample cell, the incident-wave amplitude was attenuated, reducing the resolution, which hampered the visualization of features below 5 nm. This limitation prevented the visualization of the development of surfactant-templated mesoporosity, which was confirmed *posteriori* by HR-TEM. Collective experiments revealed two interesting phenomena of this process: the disappearance of the secondary broad mesoporosity (20-30 nm) of the parent USY zeolite, and the preservation of the crystal, which does not dissolve during the process.[289]

In this study we directly visualized the surface reconstruction of zeolite USY using atomic force microscopy (AFM), which is a widely used technique that is capable of capturing dynamic events of crystal surfaces at near molecular resolution. AFM has proven especially useful for examining the crystallization of zeolites and metal-organic frameworks (MOFs) that include LTA,[317] MFI,[53,233] LTL,[221] SAV,[223] FAU,[220] CHA,[224] MOF-5,[220] and HKUST-1,[318] among others.[53,220,221,223,233,317] Rimer and coworkers[317] recently demonstrated the use of *in situ* AFM to illustrate the diverse precursors involved in the crystallization of zeolite LTA ranging from

monomers and oligomers to nanocrystals and gel-like islands. Weckhuysen and coworkers[318] employed *in situ* AFM to elucidate the nucleation and growth mechanisms of MOF thin films; however, to the best of our knowledge, AFM has never been used to study the formation of intracrystalline mesoporosity in zeolites.

Here, we use AFM to systematically examine the generation of mesoporosity in USY zeolites by surfactant-templating. This technique allows for the *in situ* visualization of individual crystals to elucidate processes related to the mesostructuring of zeolites, including both the formation of mesoporosity and the disappearance of the broad porosity present in the original USY. Bulk characterization techniques, such as $N_2$ adsorption, $^{27}$Al NMR and XRD, were used to confirm the uniformity of mesopores throughout the zeolite (i.e., surface and interior). Ultramicrotomed slices of the zeolite mesostructured at different times were examined by TEM to monitor mesoporosity development throughout the zeolite crystals and to relate these observations with the phenomena studied on the surface by AFM. Collectively, these findings reveal low energy barriers and short timescales for the facile restructuring of zeolite USY.

## 3.2 Results and Discussion

We used *in situ* AFM to monitor the evolution of surface features on USY crystals (Zeolyst CBV 780) during mesostructuring. The size of as received USY crystals is 600 – 800 nm **(Figure B1)**, which is comparatively smaller than single crystals typically used for AFM analyses. This required a multi-tiered approach to locate appropriate surfaces for *in situ* imaging wherein the sample was first imaged with a large scan size (e.g., 5 x 5 $\mu m^2$ area, **Figure B1**), followed by a progressive reduction in scan size to encompass a single USY crystal. The imaged surface is often located within an agglomerate of multiple crystals, as shown in **Figure 3.1A**. Only surfaces oriented flat relative to the plane of imaging were selected for analysis. The surfaces of USY samples are comprised of protrusions **(Figures 3.1B-D and B2)** ranging in height from 1 to 6 nm and width

from 20 to 40 nm **(Figure 3.1C)**, noting that the width of protrusions is an overestimate due to the curvature of AFM tips (ca. 20 nm). Interestingly, the rough topography of USY crystals is consistent with the defects reported in literature using techniques such as TEM and nitrogen physisorption.[289,319] These features are induced by steaming and acid treatments carried out by the supplier to remove aluminum from the framework, thereby converting zeolite HY to USY.[319]

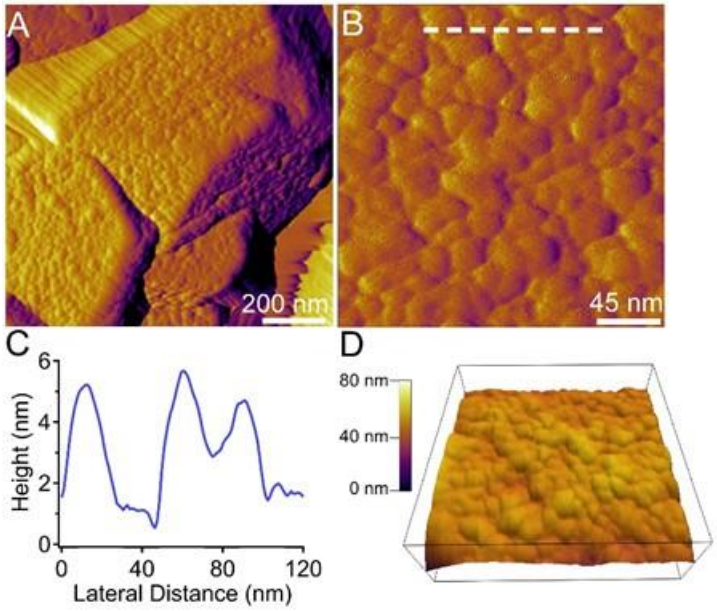


**Figure 3.1 (A and B)** AFM images of as received USY (CBV 780, FAU type) in amplitude mode revealing rough surface protrusions. **(C)** Height profile along the dashed line in panel B showing a representative topography of untreated crystals. **(D)** 3-dimensional image of the surface depicted in panel B.

Mesostructuring was performed at room temperature using a mild basic solution (62.5 mM NaOH) containing 68.6 mM surfactant (solution S2). Upon introduction of this solution to the AFM liquid cell, we observed a smoothening of crystal surfaces within the first 30 min of scanning. This is evident in time-resolved AFM images **(Figure 3.2A – C)**, which show a temporal reduction in the heights of rough features initially present on the crystal surface. **Figure 3.2C** depicts changes in the root mean square (RMS) area roughness of the crystal surface obtained from measurements of multiple 500 × 500 $nm^2$ scan areas. The disappearance of the rough islands (convex protrusions), which are one type of USY surface defect, results in the reduction of RMS roughness. It is worth

noting that rapid fluctuations in surface features during the first 30 min of treatment can give a false impression of non-monotonic smoothening. Tracking pore size before and after exposure to solution S2 reveals a progressive decrease in the average pore diameter **(Figure 3.2D)** with a concomitant narrowing of the pore size distribution, as expected due to the ability of the surfactant to direct the formation of uniform mesopores. It is important to note that USY surfaces begin reconstructing and forming mesopores within the first minutes of exposure to the solution, which is qualitatively consistent with $N_2$ physisorption and TEM results (see **Figures 3.6 and 3.7**) showing that large pores in as received USY crystals (i.e., the byproduct of steam treatment) disappear during surfactant treatment.

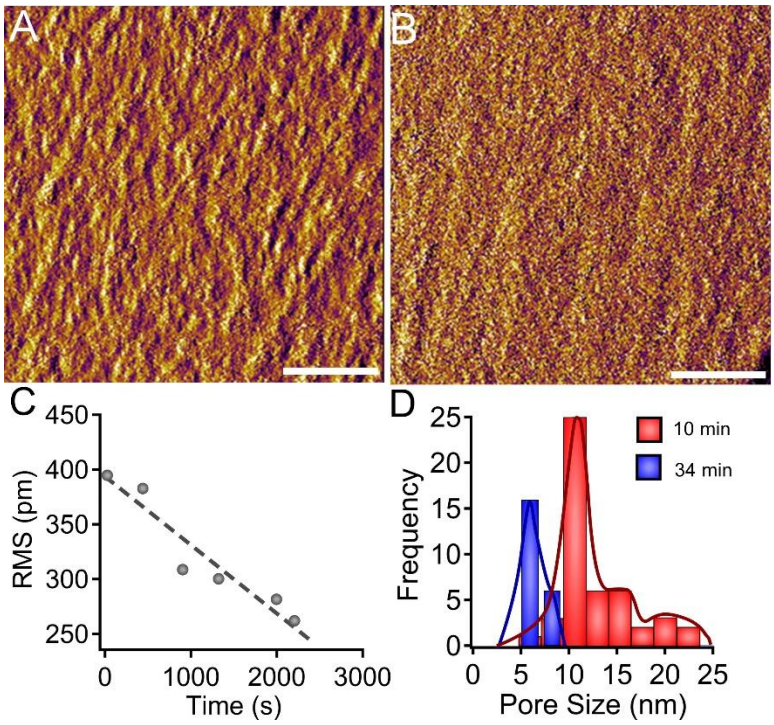


**Figure 3.2 (A and B)** Time-resolved *in situ* AFM amplitude mode images of a USY crystal treated with solution S2 after **(A)** 10 min and **(B)** 34 min of continuous scanning. Scale bars are equal to 100 nm. **(C)** Temporal reduction in the root mean square (RMS) roughness of scanned areas. **(D)** Statistical analysis of mesopore sizes that were measured on a single USY sample after 10 min (red) and 34 min (blue) of treatment.

Here we report a rapid reconstruction of surface defects during mesostructuring. We begin with an analysis of 3-dimensional (3D) islands, or convex protrusions, analogous to those observed

in Figures 1 and 2. Exposure of USY crystal surfaces to solution S2 results in a temporal reduction in the height of 3D islands (arrow in **Figure 3.3A**) that occurs in parallel with the emergence of new mesopores (callout in **Figure 3.3B**). The height profiles along the dashed line in each micrograph of **Figure 3.3** reveal a temporal healing of convex protrusions wherein the defect height decreases by a factor of two within 6 min of imaging **(Figure 3.3D)**. In order to confirm that the disappearance of 3D islands was representative of the entire sample, and not a local effect of the AFM tip, we collected AFM images of different crystal surfaces at periodic times during treatment **(Figures B4 and B5)**.

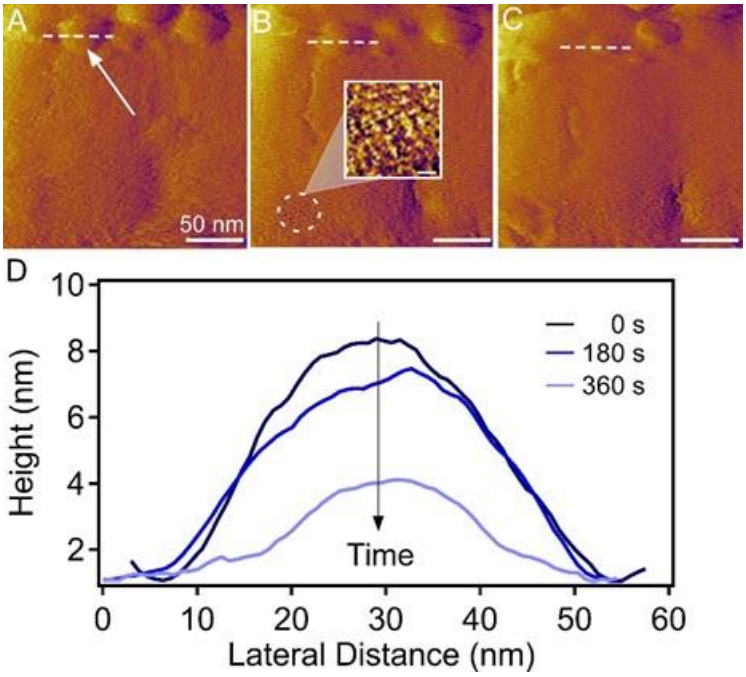


**Figure 3.3 (A – C)** Temporal changes of the same USY crystal surface after 4 h of treatment in solution S2. scale bar equals 10 nm. Images were collected in ca. 180 s intervals during continuous scanning. **(D)** Height profiles along the dashed white lines reveal a monotonic decrease in the height of islands (convex protrusions).

The collection of images corroborated the general trend observed in **Figure 3.3**, thus indicating that surface reconstruction results in the progressive disappearance of convex topographies. These observations also confirm that the surface phenomena and underlying crystal reconstruction that occurs during surfactant-templating have low energy barriers, as previously

measured by *in situ* X-ray diffraction and gas adsorption.[316] In addition to convex protrusions, AFM measurements reveal the annealing of two additional types of defects: macrosteps and concave pits **(Figure 3.4A)**. The presence of large steps (ca. 30 nm height) is evident on several USY samples **(Figure 3.4B and C)**. Mesostructuring results in the annealing of these surface features to render the interface more level, as indicated in height profiles during periodic imaging times **(Figure 3.4D)**. We also observe numerous concave cavities (or pits) on USY crystal surfaces **(Figures 3.4E and B3)**. *In situ* AFM measurements reveal that the latter features are healed by surfactant treatment and the morphology of pits changes from a circular to ellipsoid shape **(Figure 3.4E and F)**. Height profiles of a single pit **(Figure 3.4G)** reveal that these concave defects become shallower with prolonged exposure to solution S2. Indeed, there is a 4-fold reduction in pit height after 43 min of mesostructuring. To once again confirm that this healing effect caused by the treatment with the surfactant was not attributed to the movement of the AFM tip during continuous imaging, we tracked the evolution of several crystal surfaces **(Figures B7 and B8)** and observed a similar transition to more level interfaces laden with uniformly-sized mesopores. Low magnification AFM images of USY crystals after a 6-h treatment **(Figure B10)** further shows that the final USY crystal surface is devoid of any defects. The ability of surfactant to heal the defects of USY crystals is consistent with time-resolved *ex situ* $N_2$ physisorption data and TEM images **(Figures 3.6 and 3.7, respectively)**, and with our previous results for a for a less severely steamed CBV720 USY zeolite as published elsewhere.[289,315] High resolution AFM images of USY crystal surfaces treated with surfactant for 60 min reveal a homogenous distribution of mesopores **(Figure 3.5A and B)**. Quantitative analysis of mesopores over multiple crystal surfaces shows two distinct pore size distributions with an average pore size of 7 nm. The height plot of a typical mesopore **(Figure 3.5C)** reveals a lateral dimension (pore diameter) of 7 nm, whereas the depth of mesopores cannot be accurately determined by AFM owing to the relatively large curvature of the AFM tip; however, TEM images of ultramicrotomed samples (see **Figure 3.7**) reveal that mesopores are interconnected and penetrate deep into the crystals.

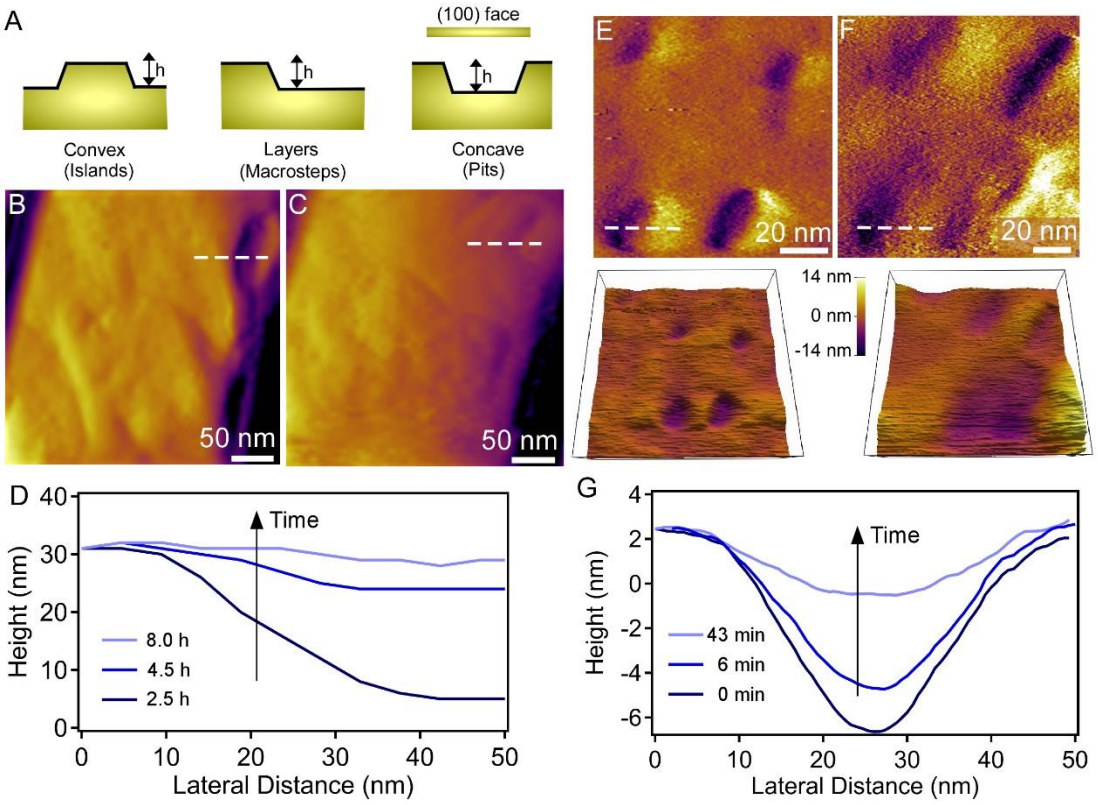


**Figure 3.4 (A)** Schematics of three types of surface defects analyzed by AFM. **(B and C)** AFM amplitude mode images show the presence of **(B)** an initial macrostep (white dashed line) and **(C)** the same area after 8 h treatment with solution. **(D)** Height profiles along the white dashed lines at various imaging times. **(E – G)** Measurements of a separate USY crystal showing the healing of etch pits.

It is also important to note that the lateral pore size distribution from AFM images is slightly higher than calculated from alternative techniques such as TEM and $N_2$ physisorption **(Figure 3.5D)** due to the geometry of the AFM tip. However, the mesopore size distribution obtained by AFM is consistent with other techniques; and the same conclusion can be drawn when analyzing a sample after 6 h of treatment *ex situ* **(Figure B6)** where AFM images show a homogenous distribution of mesopores with similar pore sizes as those measured *in situ*.

This AFM study provides important evidence for the processes of surfactant-mediated zeolite surface reconstruction to produce uniform mesopores. To confirm that this mesoporosity generation and crystal reconstruction also occur in the interior of the crystal, samples prepared *ex*

*situ* under similar conditions were thoroughly characterized. The changes in the textural properties of the zeolite during the surfactant-templating process were evaluated by $N_2$ physisorption **(Figure 3.6A and Table B1)** and TEM analyses **(Figure 3.7)** of solids prepared at different times. Additionally, milder (S1) and harsher (S3) alkaline solutions were used to investigate how the kinetics of mesopore formation depends upon the base concentration. In agreement to what has been observed by AFM, the parent USY zeolite is comprised of large mesopores as a result of steaming and acid treatment[319] that contribute to the initial porosity, as can be deduced by the increasing amount of nitrogen adsorbed in the high relative pressure range ($P/P_0 > 0.8$).

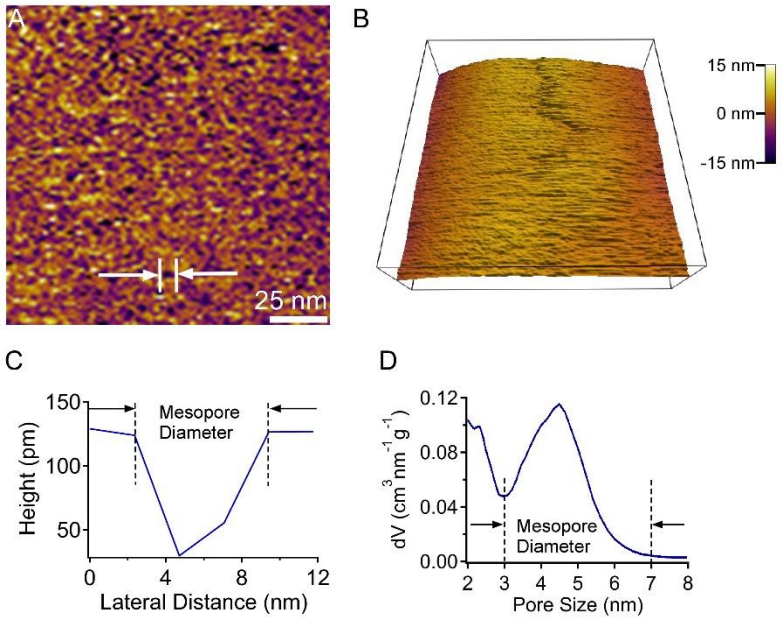


**Figure 3.5 (A)** High resolution AFM amplitude mode image and **(B)** corresponding 3-D rendering showing the uniform distribution of mesopores. **(C)** Height profile of the feature denoted in panel A (double white arrow) showing the diameter of a representative mesopore. **(D)** NL-DFT pore size distribution of mesostructured USY.

Moreover, the isotherm of as received USY presents a hysteresis loop and some cavitation due to the presence of mesopores embedded in the zeolite that are only accessible through micropores.[320] As the mesostructuring process develops, extracted solids display surfactant-templated mesopores from the first moments of treatment **(Figure 3.6B)**, which increase in population with time until reaching a plateau (circles in **Figure 3.6C**). The mesoporosity generated

by the surfactant-templating treatment evolves to generate very narrow pore size distributions with an average pore diameter ca. 4 nm, as corresponds to the use of CTAB as a surfactant **(Figure 3.6B)**. A second effect of surfactant-templating process, similar to what was has been previously reported for USY,[289] is the disappearance of the larger porosity of the original zeolite, as evidenced by the plateau in the high relative pressure region of the $N_2$ adsorption isotherms obtained at longer treatment times (triangles in **Figure 3.6C**). This is indicative of zeolite restructuring during the creation of new mesopores.[289,315] The kinetics of the incorporation as well as the amount of mesoporosity introduced depends on the concentration of the base during the treatment. For instance, the mesoporosity of the zeolite increases by factors of 1.6, 2.3, and 3.5 in the first 30 min of treatment using solutions S1 (38 mM NaOH), S2 (62.5 mM NaOH), and S3 (94 mM NaOH). It is worth noting that the incorporation of mesoporosity in CBV 780, under the conditions and time of treatment used in this study, has a negligible effect on the microporosity of these materials (see **Figure B11**). As shown in **Figure 3.6C**, the evolution of the volume of micropores barely shows a very slight decrease in their microporosity with the time of treatment.

Extensive TEM analysis of ultramicrotomed zeolites after different treatment times was carried out to further confirm the mesostructuring of entire crystals, in addition to surface restructuring observed by AFM. Statistical analysis of the development of mesoporosity was performed by studying at least 50 crystals of every sample (see **Figures 3.7 and B12**). TEM images of the parent zeolite shows the presence of large mesopores due to steaming **(Figure 3.7A)**, which is consistent with the continuous uptake of $N_2$ at 77 K at $P/P_0 > 0$. At early stages of treatment, two types of porosity can be observed in the TEM micrographs: the original large porosity and the uniform, smaller mesopores due to surfactant-templating **(Figure 3.7B)**. As the mesostructuring evolves, the surfactant-templated mesopores develop in a homogenous manner through the whole crystal, as evidenced in micrographs after 2 h of treatment in solution S2 **(Figure 3.7C)**, where no preferential sites for the development of mesoporosity can be observed. At longer treatment times,

TEM images show the homogenous distribution of mesoporosity throughout the crystalline zeolites **(Figure 3.7D–F)**. In agreement with $N_2$ physisorption, TEM images of samples treated with solutions S1, S2, and S3 reveal that the amount of mesoporosity incorporated depends on the alkalinity of the medium (**Figure 3.7D, E, and F**, respectively).

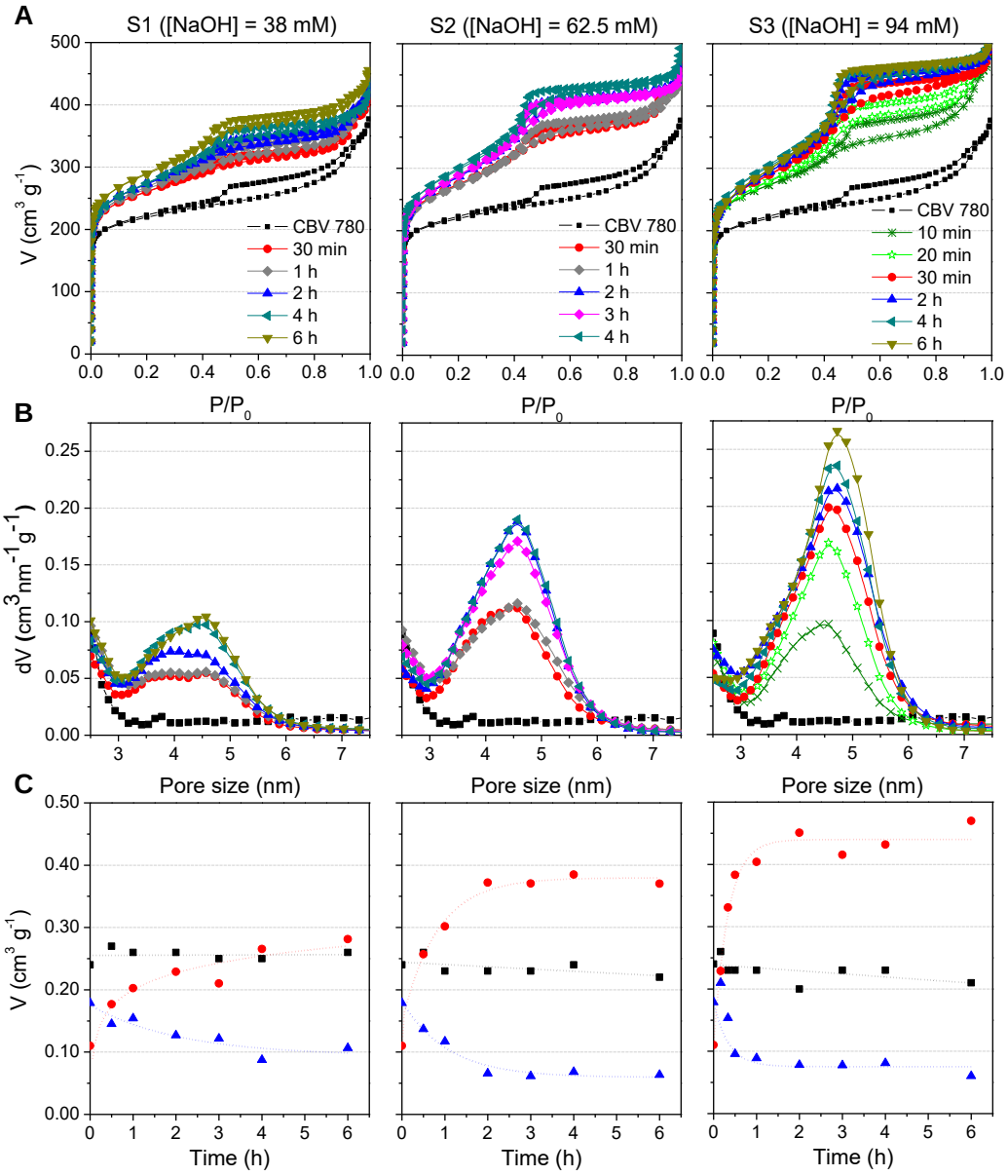


**Figure 3.6** **(A)** $N_2$ physisorption isotherms for USY zeolites prepared using different base concentrations and treatment times. **(B)** NL-DFT pore size distribution of corresponding samples. **(C)** Changes in the volume of micropores (black square), surfactant-templated mesopores (red circle), and large mesopores (blue triangle).

The disappearance of the larger initial porosity while the surfactant-templated mesoporosity develops is clearly observed in these images; however, the different kinetics shown by $N_2$ physisorption are also observed by TEM. For samples treated with solutions S2 and S3 the large mesoporosity completely disappears after 6 h of treatment (see **Figure 3.7E and F**); and for the sample prepared with a lower base concentration (S1), TEM images show only a fraction of the original large mesoporosity after the same time of treatment **(Figure 3.7D)**. In all cases, the intracrystalline nature of the mesoporosity was confirmed by the crystal lattice observed at higher resolution (see for example **Figure 3.7G**) and by digitally analyzing micrographs of ultramicrotomed samples. For example, we show in **Figure 3.7G–I** the TEM images and corresponding digital analyses (insets) of ultramicrotomed samples after 1 h of treatment with solution S2. The direct observation of mesoporosity (through the halo presented in the Fast Fourier Transformed (FFT) of each region) and crystallinity (responsible for the spots in the FFT) in the ultramicrotomed slices of surfactant-templated zeolites is strong evidence for the presence intracrystalline mesoporosity in the interior of the zeolite crystals. These results obtained for CBV 780 are consistent with our previously reported work about the intracrystalline nature of the mesoporosity introduced in CBV 720 using the same method, which has been proved by a combination of techniques, including electron tomography (ET).[118,289,315]

It is important to note that the mesostructuring of zeolite USY does not involve the filling of its large pre-existing mesopores. First, we have previously demonstrated that zeolites without initial mesoporosity, such as NaY, can be mesostructured with surfactants.[23] Second, the volume of mesoporosity introduced can be significantly higher than the pre-existent porosity (i.e., 0.29 $cm^3\ g^{-1}$ initially compared to 0.45 $cm^3\ g^{-1}$ after surfactant-templating treatment with S2); and third, the surfactant-templated mesoporosity introduced with surfactant occurs throughout the entire crystal, as evidenced by extensive TEM studies **(Figure 3.7)**. The mesostructuring process can be incomplete with insufficient treatment time, or a low quantity of NaOH is used. In partially

mesostructured zeolites, the unconverted areas are zeolitic (microporous) domains, as recently described by Galarneau and coworkers.[321]

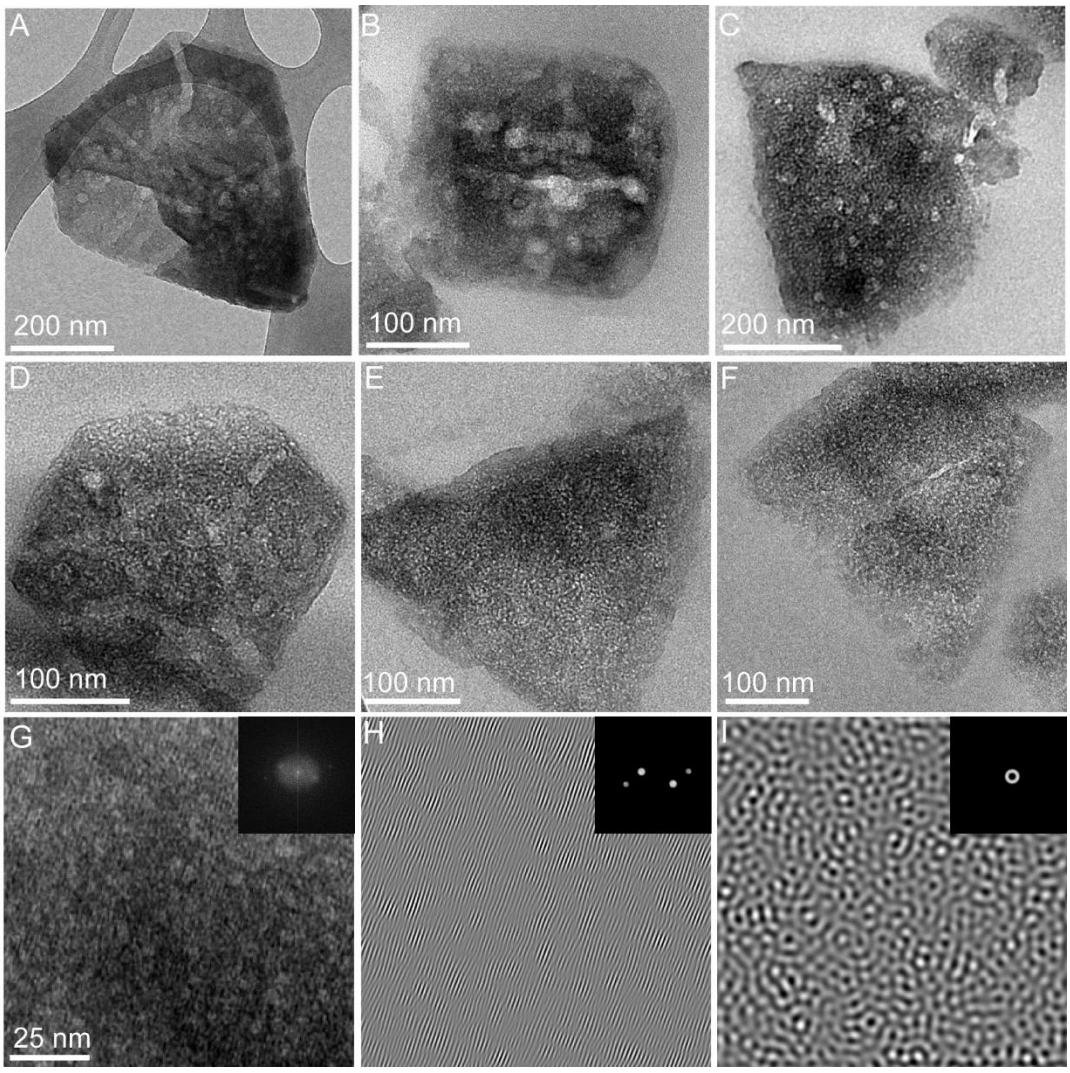


**Figure 3.7** TEM images of **(A)** as received USY and after **(B)** 30 min and **(C)** 2 h of surfactant treatment. Representative images for samples treated in different alkaline solutions: **(D)** S1, **(E)** S2, and **(F)** S3. **(G)** TEM micrograph of an ultramicrotomed slice of a sample treated using solution S2. The inset shows its corresponding FFT. **(H-I)** Reconstruction of the crystalline phase and mesopore distance by FFT.

On the other hand, if the treatment is excessive (e.g., high pH), a fraction of the zeolite can be dissolved and an amorphous mesoporous phase is formed **(Figure B13)**, as reported by García-Martínez and coworkers[306] and recently confirmed independently.[321] Therefore, it is critically important to judiciously select the mesostructuring conditions to produce high quality surfactant-

templated zeolites and to avoid the formation of spurious phases. For severely steamed zeolites (e.g. CBV 780), it is also important to mention that these samples contain some heterogeneity in composition as not all the crystals are equally dealuminated during the preparation of USY. The population of crystals with lower aluminum content are easier to treat by surfactant templating and, consequently, show higher degree of mesoporosity **(Figure B14)**.

The preservation of the crystalline structure of the zeolite after the mesostructuring process was confirmed by X-ray diffraction. The diffraction patterns of parent USY and the highly mesoporous sample treated for 6 h with solution S2 **(Figure B9)** show intense peaks associated to the FAU structure even after the incorporation of a large amount of mesoporosity (0.37 $cm^3\ g^{-1}$). However, if the same treatment is performed to USY zeolite in the absence of CTAB (i.e., using only alkaline NaOH solutions), the crystalline structure of the zeolite is totally lost and the resultant powder XRD patterns indicate an amorphous product, which confirms that CTAB adds a level of protection that prevents a crystal-to-amorphous transformation.[315] Additional evidence of crystal reconstruction during surfactant-templating process was obtained by $^{27}Al$ NMR and elemental analysis (ICP). The NMR spectrum of the original USY sample **(Figure 3.8)** shows two bands around 60 and 0 ppm that correspond to Al in tetrahedral (Al(IV)) and octahedral (Al(VI)) coordination environments, respectively.[322,323] The band at around 0 ppm disappears completely during the treatment (even for short treatment times), indicating the elimination of the octahedral Al (i.e., extra-framework species). Interestingly, ICP measurements of extracted reaction liquids after various treatment times do not show any leaching of Al, thereby suggesting that the removal of octahedral Al leads to its the re-insertion of extra-framework Al into the zeolite framework (as it has been observed in different studies for zeolites treated with alkaline solutions).[324-326]

Moreover, deconvolution of the peak associated with tetrahedral Al further results in two contributions, Al(IV)a and Al(IV)b. The Al(IV)a species is assigned to tetra-coordinated Al atoms in the framework (charge-balanced by protons),[323] whereas the attribution of Al(IV)b is more

challenging. In zeolites, this band can be due to distorted tetra-coordinated Al species[327] or to framework Al atoms interacting with cationic species present outside the network.[328] On the basis that surfactant-templating treatment causes a slight increase of the Al(IV)b contribution, we hypothesize this signal is related to the interaction of the framework Al with $CTA^+$ cations and to the subsequent distortion of the tetrahedral coordination.

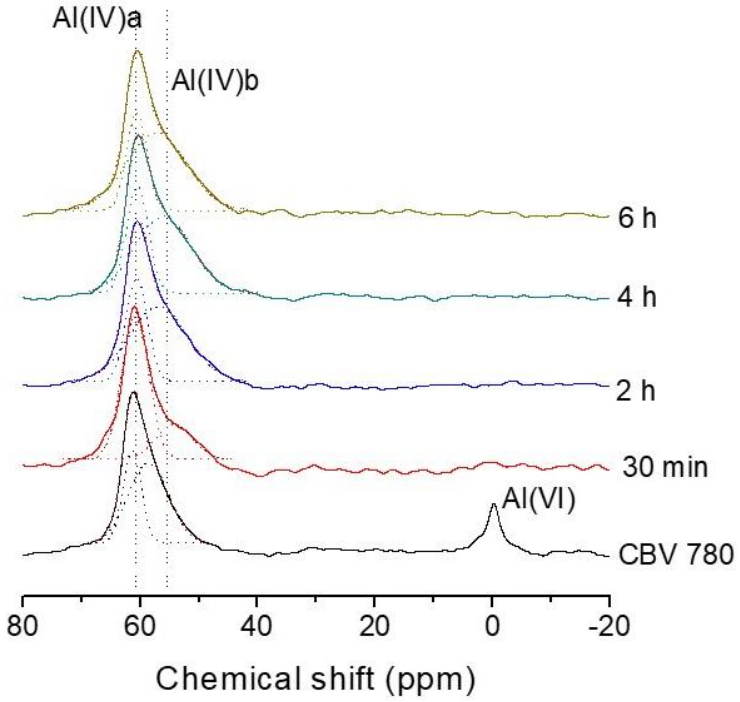


**Figure 3.8** $^{27}$Al NMR spectra of the parent USY zeolite (CBV 780) and surfactant-templated zeolites treated with solution S2 and different reaction times spanning from 30 min to 6 h. The dotted lines show the deconvolution of the individual bands.

## 3.3 Conclusions

In summary, we have been able to directly observe the development of mesoporosity in USY through surfactant-templating by the use of AFM. In a time-resolved manner, we have observed how the defects present in USY, which are produced by the supplier by a combination of steaming and acid washes, are removed while narrower surfactant-templated mesoporosity develops. Interestingly, these processes occur rapidly at room temperature to produce a final product with uniformly-distributed mesopores throughout the entire crystal. Molecular level details

of the crystal reconstruction during surfactant-templating are not fully understood. Nevertheless, this study provides additional evidence that zeolite crystals do not dissolve to produce mesoporosity. Indeed, elemental analysis of the liquids post-treatment reveals the negligible presence of soluble species, while ca. 100% of the solids are recovered at any given time of the surfactant-templating process. Extensive *in situ* microscopy confirmed that zeolite USY does not dissolve during the surfactant-templating treatment, although short-scale breaking and reconstruction of the zeolite framework is necessary for the generation of intracrystalline mesoporosity. The use of additional techniques such as $N_2$ adsorption, TEM of ultramicrotomed samples, powder XRD, and $^{27}Al$ NMR have confirmed that the surface phenomena observed by AFM is consistent with changes occurring throughout the entire crystal. Collectively, these techniques provide new and unequivocal insights that confirm surfactant templating is a facile and efficient method to induce reconstruction of the crystal, the healing of defects, the reinsertion of extra-framework Al, and the disappearance of large mesoporosity towards the generation of optimal FAU-type zeolites for catalytic applications.

## 3.4 Material and Methods

### 3.4.1 Materials

USY zeolite (CBV780 with a Si/Al molar ratio of 40 as indicated by the supplier) was purchased from Zeolyst. Hexadecyltrimethylammonium bromide (CTAB) (98%) was purchased from Sigma-Aldrich. Sodium hydroxide (98% pellets) was supplied by MACRON Fine Chemicals. Deionized (DI) water was prepared using an Aqua Solutions RODI-C-12A purification system (18.2 MΩ). All reagents were used as received without further purification.

### 3.4.2 Preparation of treatment solution

The basic surfactant solution used for in situ AFM experiments was prepared by mixing the required quantity of all components to yield a solution with molar composition 1 NaOH:1.08 CTAB:888 $H_2O$. In order to obtain a 62.5 mM NaOH solution, NaOH (0.20 g) was added to DI

water (80 g) and mixed in a polypropylene (PP) bottle. Thereafter, CTAB (2 g) was added to this mixture and continuously stirred for 15 min at 40 °C to obtain a clear solution. The PP bottle was then heated in a Thermo-Fisher Precision Premium 3050 Series gravity oven at 90 °C for 1 day and was quenched to room temperature (RT). Herein, this solution is referred to as S2.

### 3.4.3 Scanning probe microscopy

All AFM measurements were performed on an Asylum Research Cypher ES instrument (Santa Barbara, CA) equipped with a liquid sample cell. Zeolite USY crystals were firmly placed on a 15-mm specimen disk (Ted Pella, Inc.) using quickset Loctite epoxy (Henkel Corporation) that was cured in an oven at 50 °C for 24 h. The sample was then removed from the oven and cooled to room temperature in air. The specimen disk was rinsed with DI water to remove loosely bound crystals and dried under inert argon gas to remove dust. The sample was then placed in a closed AFM liquid cell and images were collected using a Cr/Au-coated silicon nitride cantilever (Olympus TR800PSA) with a spring constant of 0.57 N $m^{-1}$. The crystal substrate was first scanned in air to locate a desired imaging area. Solution S2 was then introduced into the AFM cell by a syringe and the system was left to equilibrate at RT for ca. 30 min. During in situ measurements, solution S2 was continuously supplied to the liquid cell using a syringe pump (Razel Scientific Instruments, Model R100-E) at a rate of 2 $cm^3$ $min^{-1}$. AFM images were collected in tapping mode to minimize tip–substrate contact using at a scan rate of 1 – 8 Hz and 256 lines per scan.

### 3.4.4 *Ex-situ* characterization of samples

The morphology of the mesoporous materials was investigated by transmission electron microscopy (TEM) using a JEM-2010 microscope (JEOL, 200 kV, 0.14 nm of resolution). Selected samples were embedded in a Spurr resin, cured, and cut into slices 80 nm thin using a RMC-MTXL ultramicrotome (Boeckeler Instruments, Tucson, AZ). These slices were then placed on a grid to study the interior of the zeolite crystals by TEM. Digital analysis of TEM micrographs was performed using Gatam DigitalMicrographTM 1.80.70 for GMS 1.8. Porous texture was

characterized by $N_2$ gas adsorption/desorption at 77 K in a Quadrasorb-Kr/MP apparatus from Quantachrome Instruments. The samples were previously degassed for 4 h at 250 ºC at $5x10^{-5}$ bars. Adsorption data were analyzed using the software QuadraWin™ (version 6.0) of Quantachrome Instruments. Cumulative pore volumes and pore-size distribution curves were calculated using a density functional theory method (NL-DFT adsorption branch model) from the adsorption branch of the isotherms, as described elsewhere.[329] From the cumulative pore volume determined by NL-DFT, the micropore volume was obtained at a pore size of 2 nm; the mesopore volume was calculated by subtracting the micropore volume from the pore volume at a pore size of 8 nm (to discard the large mesoporosity due to the steaming present in the original USY); and the large mesopore volume was obtained by subtracting the micropore and mesopore volume from the total pore volume obtained at a relative pressure ($P/P_0$) of 0.95. X-ray diffraction (XRD) patterns were collected on a Seifert XRD 3003 TT (Bragg–Brentano geometry) powder diffractometer using Cu Kα radiation (λ = 1.54056 Å) at a scanning velocity of 0.05º $min^{-1}$ in the 5º<2θ<50º range. Solid state NMR analyses were carried out in a 500 MHz Bruker Avance III HD Spectrometer using the pulse program ZG. The samples were spun at a rate of 4 kHz and the $^{27}Al$ NMR spectra were obtained with a relaxation delay of 5 s and 2048 scans. Inductively coupled plasma optical emission spectrometry (ICP-OES) analyses of the liquid mixtures after the surfactant-templating treatment were performed using a Perkin Elmer spectrometer (Optima 4300 DV model).

### 3.4.5 *Ex-situ* treatment of samples

The preparation of surfactant-templated mesoporous zeolites *ex situ* was carried out by first dissolving CTAB (0.5 g) in 40 mL of 62.5 mM NaOH (S2 solution). To this mixture was added 1 g of CBV 780 zeolite and the resultant slurry was stirred at RT for 1 min. The surfactant-templating process was performed under static conditions by allowing the zeolite to remain in contact with the alkaline surfactant solution for a set amount of time at RT. Solutions of varying NaOH concentration, ranging from 38 mM (solution S1) to 94 mM (solution S3), were also prepared to

evaluate the influence of pH on the quality of hierarchical zeolites and the kinetics of mesostructuring. Calcination of the samples was carried out under the flow of dry air at 823 K for 5 h (2 K $min^{-1}$).

# Chapter 4

# Seed-Assisted Crystallization of Self-Pillared Pentasil Zeolites

## 4.1 Motivation

A common objective in zeolite design is the reduction of the diffusion limitations imposed by their narrow micropores (typically <1 nm) and long diffusion path lengths in large crystals that negatively impact performance for a wide range of applications.[108,330] These mass transport limitations may increase the probability of coking (i.e., carbonaceous deposits leading to deactivation), thus affecting the overall catalyst lifetime.[43,44] Approaches to address these limitations include (but are not limited to) the synthesis of zeolites with extra-large pores[17], reduction of crystal size[70,331], and/or hierarchical zeolites that possess high surface areas through the introduction of mesopores and/or the generation of highly branched (or intergrown) morphologies.[94,245,332-336]

Synthesis strategies for the production of ultra-small crystals are non-trivial and often require the use of complex organics.[47,184,337] Among the more successful approaches has been the design of hierarchical zeolites, which can improve the performance of zeolites in a variety of catalytic processes, including alkylation, transalkylation, isomerization, cracking, methanol to hydrocarbon (MTH), and condensation reactions.[108,330] Methods used to synthesize hierarchical zeolites can be broadly classified into two categories: bottom-up and top-down approaches.[117] The bottom-up approach includes the use of hard and soft templates, e.g., zeolites are crystallized over the surface of carbonaceous or polymeric templates, and then templates are removed by calcination, leaving a zeolite with additional mesoporosity.[338,339] Alternatively, dual porogenic surfactants have been used in select cases.[89,340] Top-down approaches include desilication or dealumination, i.e., the removal of silicon or aluminum atoms from the zeolite framework by alkaline or acid treatments that lead to an additional level of porosity in the zeolite.[113,341,342]

Hierarchical zeolites with multiple rotated intergrowths have received significant attention in recent years. Ryoo and coworkers[85,86,332] utilized a diquaternary ammonium-type surfactant to obtain unilamellar ZSM-5 (MFI) nanosheets and hexagonally ordered mesoporous molecular sieves.[86,88] They found these zeolites are better catalysts in MTH reactions as well as liquid phase reactions (e.g., Friedel-crafts alkylation and acylation). Using a similar methodology, Che and coworkers[334,336] utilized π– π interactions of amphiphilic surfactants for the preparation of single-crystalline ordered MFI nanosheets. Tsapatsis and coworkers[66] used a phosphonium-based organic molecule to generate MFI crystals as self-pillared pentasil (SPP) nanosheets in a 'house-of-cards' arrangement.[343 344] One of the underlying similarities in all of these studies is the need for complex or unconventional organic structure-directing agents, which imposes restrictions on the potential for commercialization. For instance, a disadvantage of using organics is the necessity for their removal by calcination post-synthesis, which is both inefficient and costly, and in some cases, the removal of organics can lead to partial structural collapse.[88,334]

In recent years, Cejka, Morris, and coworkers[345,346] introduced a facile top-down synthesis approach to facilitate the formation of two-dimensional zeolites using an ADOR (assembly, disassembly, organization, and reassembly) process wherein parent germanosilicate zeolite is first synthesized and then disassembled to form single layers which further undergoes reassembly to form distinct zeolite frameworks with unique pore apertures. This methodology has led to the discovery of several novel zeolite frameworks with exceptional pore topologies. Tsapatsis and coworkers[66] hypothesized that in case of hierarchical SPP materials, the connectivity between the MFI nanosheets is achieved by the presence of MEL at the intersections acting as a 4-fold symmetric connector. Recently, Tsapatsis and coworkers[347] successfully confirmed their hypothesis by directly imaging the intersections to show that MEL connectors (or junctions) linking two MFI nanosheets generate 90° rotational intergrowths leading to the formation of the house of card like structures. Interestingly, Schwieger and coworkers[348] and others[349,350] also reported FAU

hierarchical crystals with similarly rotated intergrowths with EMT found to be involved in the branching process. Thus, it is possible that controlling these intergrowths can lead to new pathways for synthesizing hierarchical structures without using organics.

In this chapter we employ a seed-assisted method, which has proven to be useful in zeolite syntheses to decrease/eliminate organics.[14,351] The use of seeds can also reduce crystallization times and can tailor the physicochemical properties of zeolite crystals, such as size, morphology, and the number and siting of aluminum;[352] however, the role of seeds in the zeolite crystallization mechanism(s) remains elusive.[353] In this chapter, we demonstrate how seed-assisted processes offer a novel route to synthesize hierarchical SPP zeolites with intergrown nanosheets in the absence of organics. Our findings reveal nonclassical pathways of SPP formation involving the heterogeneous nucleation of crystals at the exterior surfaces of amorphous precursor particles. We also explore the effects of various parameters such as seed structure and chemical composition, synthesis temperature, and crystallization time on the physicochemical properties of SPP zeolites. In order to elucidate the structure-performance relationships, we tested hierarchical SPP catalysts using MTH as a benchmark reaction and show that the hierarchical material exhibits improved catalytic stability in comparison to ZSM-5 crystals prepared by conventional synthesis.

## 4.2 Results and Discussion

Here we present a unique bottom-up synthesis approach of generating hierarchical self-pillared pentasil (SPP) crystals in organic-free media. Motivated by reports[66,347] that MEL functions as a junction to facilitated branching in SPP materials, we explored the possibility of generating hierarchical SPP-like materials by introducing calcined silicalite-2 (MEL) as seeds into a zeolite growth mixture that does not contain any organic (i.e., using $Na^+$ as the sole structure-directing agent). Silicalite-2 crystals **(Figure C1)** employed as seeds exhibit a spheroidal morphology with sizes of 5-10 μm **(Figure 4.1B)**. Time-resolved analysis of solids extracted from synthesis mixtures

using powder X-ray diffraction (XRD) patterns reveal an incomplete dissolution of silicalite-2 seeds during room temperature aging; however, Bragg peaks corresponding to MEL-type seeds **(Figure 4.1A)** disappear around 24 h of hydrothermal treatment at 150° C, which seems to indicate the dissolution of seeds (noting that XRD is unable to detect crystals that are present in quantities less than 3 wt%).[201,204]

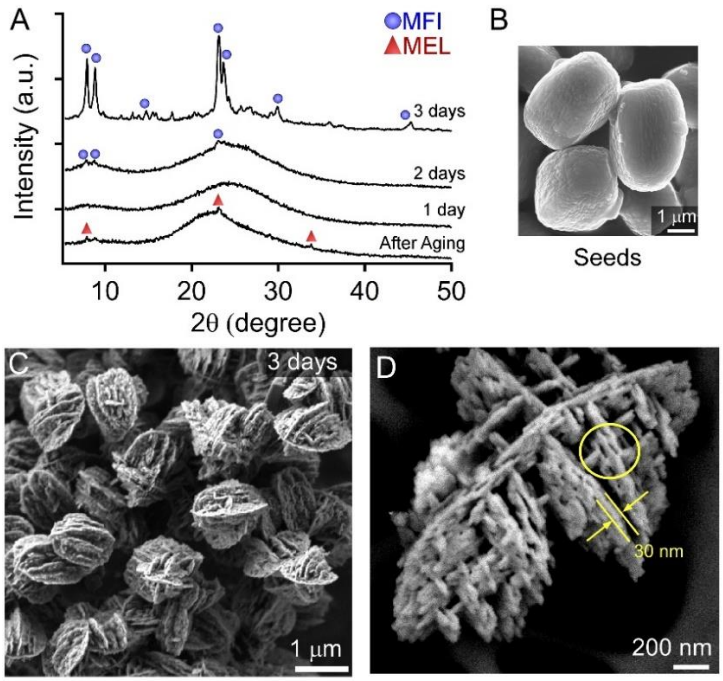


**Figure 4.1** (**A**) XRD patterns of samples extracted from growth solution S1 containing for periodic times. (**B**) SEM image of silicalite-2 seeds synthesized from growth solution S2 (**C**) SEM image of the ZSM-5 product after 3 days of seeded growth. (**D**) High magnification image revealing ZSM-5 nanosheets of thickness ca. 30 nm and mesopores (yellow circle).

Indeed, FE-SEM micrographs of solids extracted after 24 h show the remnants of seeds **(Figure C2)** that have undergone either partial dissolution or amorphization. Interestingly, a phase with a predominantly MFI framework type (ZSM-5) nucleates **(Figure 4.1A)** within 2 days with the near completion crystallization observed after ~3 days. **Figure 4.1 C and D** show the high-resolution FE-SEM micrographs of the product revealing a remarkable house-of-card like morphology of interconnected nanosheets comprising ZSM-5 (MFI) nanosheets with an average

thickness of 30 nm that are arranged as intergrowths. The interstitial spacing between SPP nanosheets leads to a hierarchical porous architecture consisting of a wide variety of pore size distributions ranging from micropores to macropores. This observation is consistent with the $N_2$ adsorption isotherms **(Figure C3)** demonstrating a large uptake at relative pressure below 0.2, the presence of a hysteresis loop at intermediate relative pressures, and a slight uptake at high relative pressure that is attributed to the presence of micro-, meso-, and macroporosity, respectively. To our knowledge, this is the first example of a hierarchical SPP-like zeolite synthesized without the use of an organic.

To investigate the structure of SPP nanosheets, we performed high-resolution transmission electron microscopy (HRTEM). Images of single particles reveals the presence of numerous nano-sized (20 – 100 nm) crystallites **(Figure 4.2A),** which is qualitatively consistent with previous studies of MFI-type materials showing crystallization by particle attachment.[53] Analysis of the selected area electron diffraction (SAED) patterns **(Figure 4.2B)** acquired for the entire SPP particle corroborate the single-crystalline nature of the sample (likely the superposition of scattering from the (010) and (100) planes). The scattering pattern **(Figure C4)** indicates that the individual nano-sized features on each nanosheet of SPP particles are aligned in equal crystallographic registry. To further confirm crystal orientation, we embedded SPP crystals in a spurr resin and studied thin sections of ultramicrotomed zeolite. HRTEM images and the corresponding FFT analysis show that the straight channels along the [010] axis are oriented perpendicular to the surface of nanosheets **(Figure 4.2C)**. A higher magnification image showing two nano-sized features on a single nanosheet lattice fringes **(Figure 4.2D)** confirms their crystallinity and equal registry, where the orientation was corroborated by overlaying the framework structure of MFI along b-axis on the HRTEM image **(Figure C7)**.

We postulate that the 90-degree angles between intergrowths is facilitated by MEL junctions at the intersections of MFI nanosheets, which was confirmed for SPP materials prepared

by Tsapatsis and coworkers.[347] It should be noted that it is challenging to resolve MEL segments in TEM images, while their net quantity is likely too little to be observed in powder XRD patterns. Prior studies[347] have reported that these MEL junctions can lead to the elongation of electron diffraction spots, such as (102) and (104), in SAED patterns; however, we did not observe any noticeable broadening of diffraction spots for our SPP crystals.

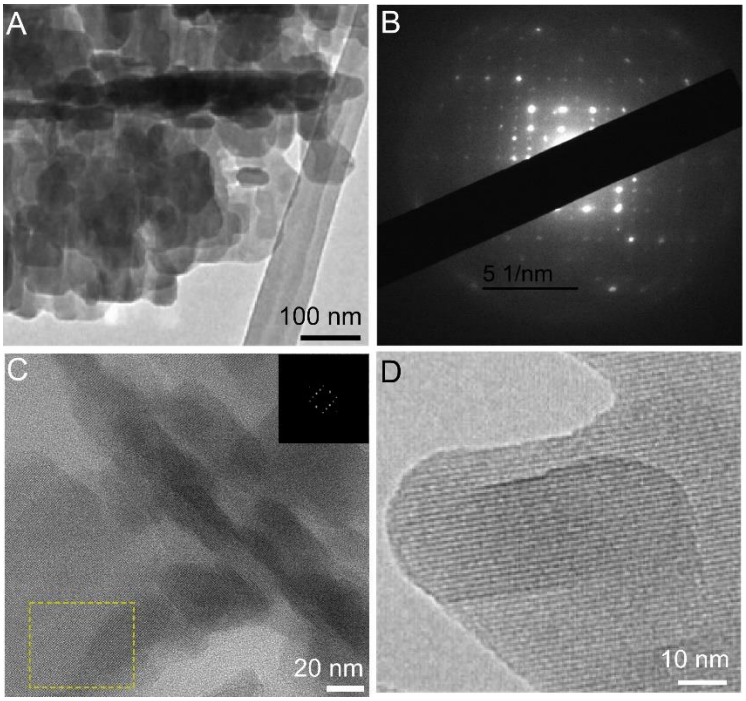


**Figure 4.2** **(A)** TEM image of a SPP crystal showing the individual sheets composed of nanoparticle aggregates. **(B)** Electron diffraction patterns of a hierarchical crystal showing the single-crystalline nature of the particles. **(C)** TEM image of SPP zeolite with corresponding FFT reconstructed electron diffraction pattern (inset). **(D)** TEM image (dashed box in C) showing distinct lattice fringes.

Time-resolved FE-SEM images of solids extracted at several stages of growth were obtained to elucidate the mechanism of hierarchical zeolite crystallization. At early synthesis times (e.g., 1 day) where the powder XRD pattern lacks distinct MFI-type Bragg peaks **(Figure 4.1A)**, solids are predominantly amorphous precursors **(Figure 4.3A)**; however, close inspection shows the evidence of plate-like features that resemble the nanosheets of SPP crystals **(Figure 4.3A)** decorating the surfaces of precursors. SAED patterns of individual plate-like particles **(Figure C10)**

confirm that these are MFI-type crystals nucleating on the external surface of amorphous particles. Images of solids after longer heating time reveal the progressive consumption of amorphous precursors in favor of an increasing density of SPP crystals. The hierarchical pillared structures emerge from the surface of precursors **(Figure 4.3B-E)**, eventually becoming individual crystals that are arranged in aggregates, seemingly clustered around the original site of nucleation. These findings indicate heterogeneous nucleation, indicative of a two-step process that deviates from classical nucleation theory.[283,354] **Figure 4.3F** illustrates the putative mechanism of hierarchical SPP crystallization wherein the external surface of amorphous precursors (depicted in grey) serves as a heterogeneous site for nucleation. It is likely that the precursor-solvent interface provides localized regions of high supersaturations that can lower the energetic barriers for the nucleating platelets (depicted in yellow). The molecular-level details regarding the microstructure of amorphous precursors and their putative roles in the growth of SPP crystals are not well understood. Hierarchical structures are only obtained in the presence of seeds; thus, we hypothesize that partially dissolved fragments of silicalite-2 (MEL) seeds, either in the form of oligomers or composite building units, preserve some unknown 'memory' of the original crystal. These dissolved species may facilitate nucleation; however, we believe the remnants of the MEL structure facilitate branching (i.e., promoting the formation of junctions) that leads to self-pillaring.

FE-SEM images show the presence of spherical protrusions on the surfaces of SPP crystals **(Figure 4.3C)**, which agrees with prior studies of silicalite-1 (siliceous MFI)[53] showing that crystal growth occurs by a combination of processes: (i) classical pathways involving the addition of soluble monomeric species formed during the dissolution of amorphous precursors; and (ii) nonclassical pathways involving the attachment of amorphous precursors (i.e., nanoparticles) through CPA[355] followed by a disorder-to-order transition where precursors are incorporated into the underlying crystal structure. Multiple indicators of nonclassical growth can be gleaned from

the spheroidal protrusions captured on FE-SEM images of solids extracted during intermediate stages of crystallization as evidence for growth by CPA.[78,206]

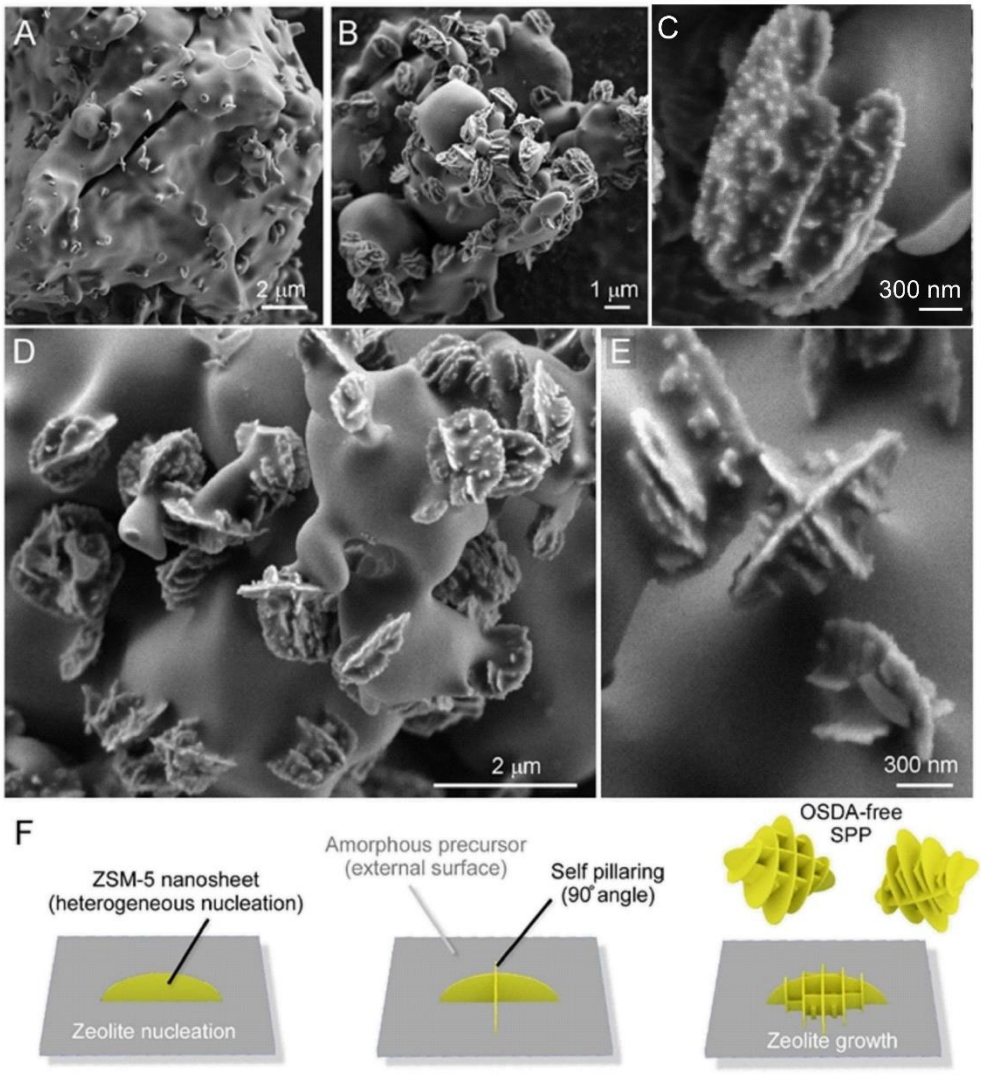


**Figure 4.3 (A – C)** FE-SEM images of solids extracted from growth solution S1 after **(A)** 1, **(B)** 2, and **(C)** 3 days of heating. **(D and E)** High magnification images of solids after 2 days of heating capture the emergence and self-pillaring of hierarchical SPP crystals from the surfaces of amorphous precursors. **(F)** Idealized schematic of heterogeneous nucleation and growth of SPP zeolite on amorphous particles.

In most zeolite syntheses, nucleation is far too rapid to capture using *ex situ* microscopy, which has led to uncertainty regarding the site(s) for nucleation. This is particularly true for MFI-type zeolite where prior studies of silicalite-1 have had to alter synthesis conditions, such as reduce

the temperature, in order to significantly extend the timescales of crystallization (i.e., on the order of one year) to capture before/after images of nucleation.[188,189] Here, we provide what are arguably the most detailed images of heterogeneous nucleation and confirm that SPP crystals originate on exterior surfaces of amorphous precursors (consistent with our earlier hypotheses for zeolites FAU and LTA where we argued that energetic barriers for nucleation are much higher within the interior of amorphous particles compared to the exterior surfaces of precursors).[191]

The SPP sample is fully crystalline **(Figure 4.4A)** after 3 days of synthesis; however, continued heating leads to an interzeolite transformation **(Figure 4.4B)** from SPP (MFI/MEL) to mordenite (MOR). Comparison of the powder XRD patterns **(Figure C6)** extracted from seeded growth mixtures at periodic heating times reveals a progressive decrease in the fraction of MFI phase in favor of an increasing fraction of MOR. After 10 days of heating, the product contains MOR as the majority component **(Figure C6)** with a minor fraction of MFI. High-resolution FE-SEM micrographs **(Figure 4.4C)** of samples after 4 days of heating, corresponding to the first appearance of mordenite peaks in the XRD patterns, show rod-shaped particles emerging from the center of SPP aggregates. As the MFI-to-MOR transformation proceeds, there is a visible decrease in the population of SPP crystals with a concomitant increase in the size of mordenite crystals **(Figure 4.4D)**. Samples extracted at longer times **(Figure 4.4D)** when the MFI-to-MOR transformation is nearly complete (i.e., 10 days) contain only traces of the original SPP material and aggregation of rod-shaped particles which are most likely mordenite crystals.[352,356,357]

Prior studies have shown that interzeolite transformations tend to occur in the order of increasing framework density[191,285,358] (consistent with thermodynamic measurements of purely siliceous zeolites);[356,359] however, we recently showed evidence for MFI-to-MOR transformations where we postulated that changes in the Si/Al ratio of the growth solution, as inferred by a shift in the composition of MFI (Si/Al = 16) and MOR (Si/Al = 6) crystals, alters the thermodynamic driving force **(Figure C5)** for this transformation.[356] This finding is consistent with a recent

machine learning study by Gómez-Bombarelli and coworkers[13] who demonstrated multiple examples of transformations with decreasing framework density.

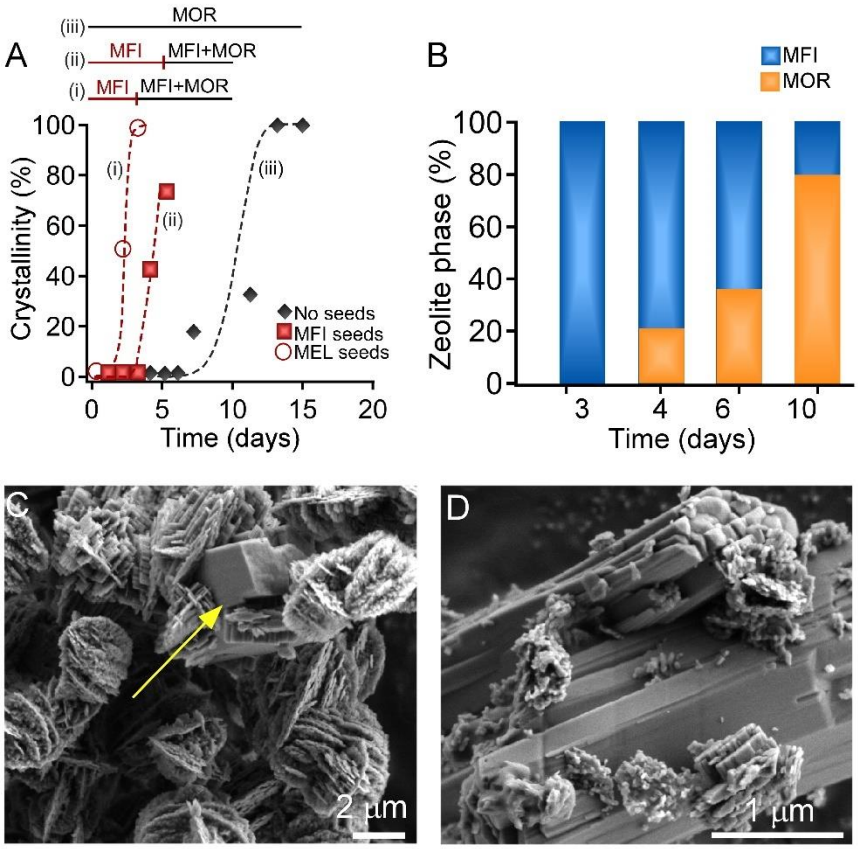


**Figure 4.4 (A)** Percent crystallinity as a function of synthesis time measured from powder X-ray diffraction patterns**. (B)** Extended synthesis time reveals an interzeolite transformation from MFI-to-MOR **(C)** SEM images of crystals extracted after 4 days and after **(D)** 10 days showing aggregated rod-shaped crystals with traces of original SPP material.

It is widely reported that the presence of seeds can significantly impact the kinetics of nucleation wherein seeds tend to enhance crystallization rates resulting in shorter synthesis time and smaller crystals.[14,353,360,361] To this end, there is a four-fold increase in the induction time when switching from a synthesis mixture with silicalite-2 seeds to one containing no seeds **(Figure 4.4A)**. Interestingly, non-seeded syntheses result in the formation of mordenite crystals with different size and morphology **(Figure C13)** which is not surprising given that mordenite is commonly prepared in organic-free media with $Na^+$ as the sole structure-directly agent. Here, we examined the impact

of seed selection by testing a series of pentasil crystals: ZSM-11 (aluminosilicate MEL), silicalite-1 (siliceous MFI), and ZSM-5 (aluminosilicate MFI). In the case of ZSM-5 seeds **(Figure 4.4A and Figure C8)**, we observed that the time period for crystallization is extended to approximately 5 days; however, the sample never reaches full crystallinity **(Figure C8)** before observing the onset of a MFI-to-MOR transformation. Analysis of samples after 5 days of heating reveal that the product is a SPP crystal **(Figure 4.5A-C)** with similar hierarchical features, but with slightly thicker nanosheets (ca. 65 nm). FE-SEM images of solids extracted from growth mixtures using ZSM-5 seeds revealed a similar crystallization mechanism with SPP crystals emerging form the surfaces of amorphous precursors **(Figure 4.5A)**. **Figure 4.5B** captures for what appears to be an onset of nucleation at the exterior of amorphous precursor. This observation reveals that the memory of dissolved MEL seeds is not a prerequisite for SPP formation; however, the longer timescale for crystallization and the inability to achieve a fully-crystalline SPP product using ZSM-5 seeds likely reflects the ability of MEL-type seeds to facilitate the formation of the hierarchical zeolite. For instance, we observe a dramatic decrease (ca. 20%) in the total surface area when switching from silicalite-2 seeds to ZSM-5 **(Table C1)**.

Interestingly, we observe a dramatic difference in the morphology and textural properties of crystals when substituting ZSM-5 seeds with silicalite-1 **(Figure 4.5D-F)**, which is its siliceous isostructure (i.e., Si/Al ratio = ∞, analogous to silicalite-2)**.** Silicalite-1 seeds yield a fully crystalline ZSM-5 product within 3 days of heating **(Figure C9)**, which is much faster than seeded growth using ZSM-5 seeds. This disparity in crystallization kinetics can be explained by the fact that seeds with a higher Si/Al ratio dissolve faster in alkaline solution, consistent with trends in ZSM-5 dissolution reported by Groen and coworkers.[107,113,341] The combination of FE-SEM **(Figure 4.5D)** and HRTEM **(Figure 4.5E)** capture heterogeneous nucleation at the exterior surface of precursor particles where the crystals generated from silicalite-1 seeds are less fractal in nature,

but contain many of the same features (e.g., nanosheets with spheroidal protrusions), compared to those produced from silicalite-2 seeds.

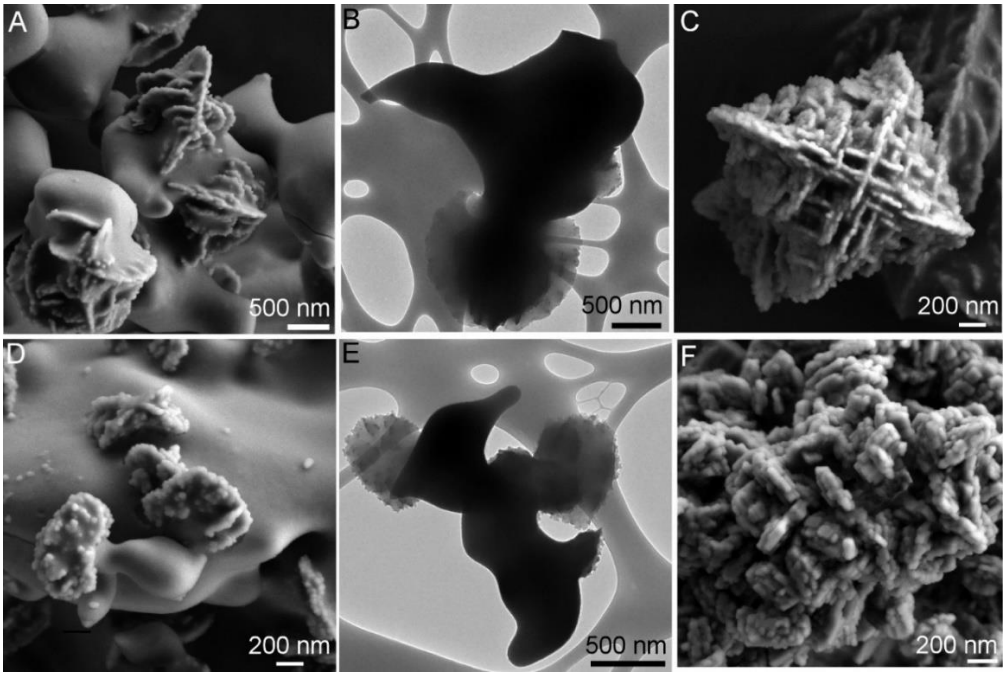


**Figure 4.5 (A)** FE-SEM image and **(B)** HRTEM image of solids from growth solution S3 after 3 days of heating. **(C)** FE-SEM image of solids extracted after 5 days of heating (**D**) FE-SEM image and **(E)** HRTEM image of solids extracted from growth solution S4. (**F**) FE-SEM image of a crystal extracted after 3 days of heating.

A key difference in silicalite-1 seeded growth is the generation of a ZSM-5 product that resembles a dense aggregate of nanocrystals **(Figure 4.5F)** lacking the distinct hierarchy of pores **(Figure C12)** that are characteristic of SPP zeolites. Indeed, there is a two-fold reduction in mesoporous volume determined using $N_2$ physisorption for silicalite-1 seeded solution as compared to ZSM-5 seeded growth **(Table C1).** Contrary to the observed trends for MFI seeded growth solutions, the timeframe for the formation of hierarchical SPP crystals doesn't depend on the framework composition of MEL seeds. For example, comparisons of time-resolved powder X-ray diffraction patterns **(Figure C14)** confirms that kinetics of crystallization for ZSM-11 and silicalite-2 seeded growth mixtures are nearly identical.

To further characterize SPP crystals synthesized with silicalite-2 seeds, we tested structure-performance relationships of catalysts using methanol-to-hydrocarbons (MTH) as a model reaction. Conventional ZSM-5 (ca. 1 μm) was prepared as a benchmark material; and all zeolites were ion-exchanged with $NH_4^+$ and calcined according to established protocols[362] to achieve H-form catalysts. MTH reactions were performed at sub-complete methanol conversion to quantify differences in activity and selectivity. Prior studies have demonstrated that hierarchical zeolites typically exhibit longer catalyst lifetime owing to the reduced diffusion limitations that enable slower buildup of carbonaceous deposits (i.e., coke), which is a frequent culprit in catalyst deactivation.[108,330,335,363]

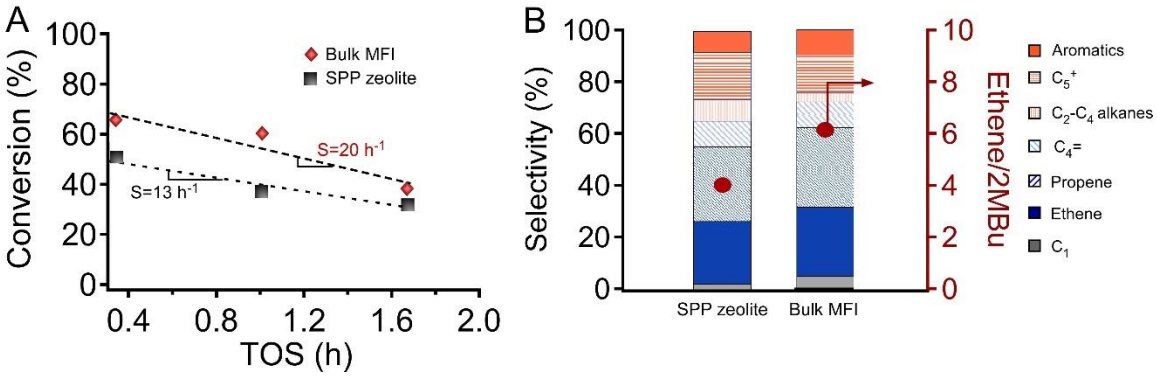


**Figure 4.6 (A)** Plots of sub-complete methanol conversion in the MTH reaction for H-SPP and H-ZSM-5 catalysts using WHSV = 27 and 60 $h^{-1}$ respectively. **(B)** Selectivities of effluent hydrocarbons (histograms, left axis) and ethylene to 2MBu ratio (circles, right axis).

In **Figure 4.6A** we compare methanol conversion with time on stream (TOS) and show that the hierarchical SPP crystals exhibit a nearly 2-fold reduction **(Figure 4.6A)** in the rate of catalyst deactivation as compared to conventional ZSM-5. The acid site density and framework aluminum were quantified by $NH_3$ TPD and $^{27}Al$ NMR respectively **(Figure C11)**. According to the $NH_3$ TPD analyses **(Table C1)**, all SPP materials exhibit similar very similar acid site density with the exception of bulk MFI, which has a slightly lower value. A comparison of the selectivity of both catalysts **(Figure 4.6B)** reveals a stark difference. Bhan and coworkers[364-366] proposed the use of the ethene-to-2MBu ratio as a descriptor to indirectly access the propagation of aromatic and

olefin cycle of hydrocarbon pool mechanism (where 2-MBu = 2-methylbutane and 2-methyl-2butene). It has been demonstrated that major products resulting from olefin-based cycle are propene, alkanes, and higher olefins, whereas in the aromatic based cycle a series of methylation and dealkylation reactions occur leading to ethene as one of the major products. Therefore, a higher ethene-to-2MBu ratio indicates an enhanced propagation of the aromatic cycle. We observe that the SPP zeolite promotes olefin-based cycle **(Figure 4.6B)**, consistent with trends of decreasing pentasil (ZSM-5 or ZSM-11) size in literature.[365,367]

## 4.3 Conclusions

In summary, we have demonstrated here for the first time an organic-free route to prepare hierarchical SPP zeolites using a seed-assisted approach. Time-resolved *ex situ* imaging of samples revealed unprecedented insight into the early stages of crystallization, capturing images of nucleation where SPP crystals emerge from the surfaces of amorphous precursors and grow via a nonclassical pathway of crystallization. Our findings of heterogeneous nucleation of SPP crystals agree with the premise that energetic barriers for nucleation can be significantly higher within the interior of precursors. The judicious selection of seed structure and chemical composition is a unique and facile method to tailor the physicochemical properties of SPP crystals. Interestingly, the preparation of hierarchical SPP crystals is seemingly connected with the ability of MEL fragments (i.e., the products of seed dissolution) to effectively bridge MFI nanosheets, thereby directing the organization of intergrown nanosheets with complex hierarchical architecture. The unique porous structure coupled with the reduced diffusion path length of nanosheets results in a higher performance catalysts, which was verified in MTH reactions showing that the SPP material exhibits reduced rates of coke formation and shift the product selectivities in comparison to a conventional ZSM-5 zeolite.

The organic-free synthesis of hierarchical SPP zeolites opens exciting prospects for both fundamental studies and large-scale applications. We expect seed-assisted synthesis may prove to

be broadly applicable to other zeolite frameworks and related crystalline porous materials. Moreover, this facile and cost-effective approach is likely to be easily scalable for a variety of applications ranging from catalysis to the development of thin films for membranes and nanoscale devices. Our findings also offer new insights into the complex mechanism(s) governing the crystallization of SPP zeolites and are potentially applicable to other minerals that crystallize via nonclassical routes.

## 4.4 Material and Methods

### 4.4.1 Materials

The following chemicals for zeolite synthesis were purchased from Sigma Aldrich: LUDOX AS-40 (40 wt% suspension in water), tetraethylorthosilicate (TEOS, ≥ 99.5%), sodium aluminate (57.1% $Al_2O_3$ and 37.2% $Na_2O$), 1,8-diaminooctane (DAO, 98%), tetrapropylammonium bromide (TPABr, 98%). Additional chemicals purchased from Alfa Aesar included sodium hydroxide (98% pellets) and tetrabutylammonium hydroxide (TBAOH, 40%). All reagents were used as received without further purification. Deionized (DI) water used in all experiments was purified with an Aqua Solutions RODI-C-12A purification system (18.2 MΩ).

### 4.4.2 Synthesis of Seed Crystals

MEL seeds with Si/Al ratios of ∞ (silicalite-2) and 33 (ZSM-11) were synthesized with organic structure-directing agents (OSDAs) TBAOH and DAO, respectively, according to previously reported protocols[368,369]. For samples with a crystal Si/Al ratio of 16, the synthesis involved the addition of $NaAlO_2$ to a NaOH solution followed by additions of TEOS and TBAOH to obtain a final molar composition of 20 TBAOH: 4 $Na_2O$: 100 $SiO_2$: 2.5 $Al_2O_3$: 3000 $H_2O$. The solution was aged for 2 h at room temperature and transferred to a 23 mL Teflon-lined stainless steel acid digestion bomb (Parr Instruments), which was placed in a Thermo Scientific gravity convection oven and heated at 160°C for 1 day.

MFI seed crystals with Si/Al ratios of ∞ (silicalite-1) and 14 (ZSM-5) were synthesized with TPABr and without OSDA, respectively, according to previously reported protocols[370,371]. Seeds were calcined in a Thermo Fisher Lindberg Blue furnace at 550°C for 10 h (with temperature ramping rate of 1 °C $min^{-1}$) under the constant flow of compressed air (Matheson Tri-Gas) at 100 mL $min^{-1}$ before application.

### 4.4.3 Seeded Zeolite Synthesis

Seed-assisted syntheses were carried out by first adding sodium aluminate to an aqueous NaOH solution followed by the addition of LUDOX AS-40 to obtain the molar ratios listed in Table 1. The nominal amount of seeds used in experiments was 10 wt% unless mentioned otherwise. The growth solution was aged at room temperature for ca. 24 h and subsequently transferred to a 23 mL acid digestion bomb. Hydrothermal treatment was carried out in an oven at temperatures spanning from 130 to 170°C under autogenous pressure. Solids extracted after select time intervals were isolated from the mother liquor by two cycles of centrifugation and washing with DI water, followed by drying in an oven at 60°C.

### 4.4.4 Characterization of samples

Powder X-ray diffraction (XRD) patterns of dried solids were collected on a Rigaku SmartLab diffractometer with a Cu Kα source (40kV, 30mA). Scanning electron microscopy (SEM) images were obtained using a Zeiss Leo 1525 instrument equipped with FEG at 10 kV. All samples were carbon coated (layer thickness ~ 30 nm) prior to imaging to reduce charging. The size of the crystals was measured from multiple SEM images of a single batch. Elemental analysis was performed by electron dispersive X-ray (EDX) spectroscopy. EDX spectra were collected using a JEOL SM-31010/METEK EDAX system at 15kV and a 15mm working distance. The morphology of the crystals was also investigated by transmission electron microscopy (TEM) using a JEM-2010 microscope (JEOL, 200 kV, 0.14 nm of resolution). Selected samples were embedded in a Spurr resin, cured, and cut into slices 80 nm thin using a RMC-MTXL ultramicrotome

(Boeckeler Instruments, Tucson, AZ). These slices were then placed on a grid to study the interior of the zeolite crystals by TEM. Digital analysis of TEM micrographs was performed using Gatam DigitalMicrographTM 1.80.70 for GMS 1.8. Textural analysis was performed with a Micromeritics ASAP 2020 instrument using $N_2$ as a probe gas for physisorption at an incremental dosing rate of 3 $m^3$ $g^{-1}$ STP and an analysis bath temperature of 77 K. Prior to analysis, samples were calcined at 550 °C for 6 h under flow of compressed air at 100 $cm^3$ $min^{-1}$. The surface area was calculated from BET analysis selecting the initial low pressure points with a correlation coefficient greater than 0.999. The cumulative pore volumes and pore-size distribution curves were calculated using a density functional theory method (NL-DFT adsorption branch model) from the adsorption branch of the isotherms, as described elsewhere.[329] From the cumulative pore volume determined by NL-DFT, the micropore volume was obtained at a pore size of 2 nm; the mesopore volume was calculated by subtracting the micropore volume from the pore volume at a pore size of 8 nm (to discard the large mesoporosity due to the steaming present in the original USY); and the large mesopore volume was obtained by subtracting the micropore and mesopore volume from the total pore volume obtained at a relative pressure ($P/P_0$) of 0.95. Solid state NMR analyses were carried out in a 500 MHz Bruker Avance III HD Spectrometer using the pulse program ZG. The samples were spun at a rate of 4 kHz and the $^{27}$Al NMR spectra were obtained with a relaxation delay of 5 s and 2048 scans.

# Chapter 5

# Diverse Physical States of Amorphous Precursors in Zeolite Syntheses

## 5.1 Motivation

The assembly and structural evolution of amorphous precursors during zeolite crystallization is an important area of interest owing to their putative roles in the nucleation and growth of aluminosilicate microporous materials. Precursors range in complexity from oligomeric molecules and colloidal particles to gels comprised of heterogeneous silica and alumina domains. The physical state of precursors in most zeolite syntheses is generally not well understood; however, it is evident that the physicochemical properties of precursors depend on a wide range of conditions that include (but are not limited to) the selection of reagents, the composition of growth mixtures, the methods of preparation, and the use of inorganic and/or organic structure-directing agents. The fact that precursors evolve in size, shape, and/or microstructure during the course of nucleation and potentially throughout crystallization leads to questions pertaining to their mode of action in the formation of zeolites. This also highlights the diversity of species that are present in growth media, thus rendering the topic of zeolite synthesis essentially a black box to those attempting to better understand the fundamental role(s) of precursors. In this chapter, we discuss the wide variety of precursors encountered in the synthesis of various framework types, emphasizing their complex physical states and the thermodynamic and kinetic factors that govern their heterogeneity.

Elucidating the mechanisms of zeolite crystallization is complex owing in large part to the vast number of species present in synthesis mixtures.[53,353] This is a contributing factor to the challenges associated with zeolite crystal engineering where it is difficult to design materials with predetermined physicochemical properties without sufficient knowledge of how synthesis variables can be tailored to mediate crystal growth.[372] The ubiquitous presence of amorphous precursors

throughout nucleation and growth make zeolites quintessential examples of materials that grow via *nonclassical* pathways, which include crystallization by particle attachment (or CPA).[78,231,360,373] This rapidly emerging area is garnering considerable attention owing to the expanding list of materials that show evidence of growth via multifaceted pathways.[228,374-378] Knowledge of nonclassical mechanisms, however, is rather limited due to inadequate analytical techniques available to observe dynamic processes of grow *in situ* with sufficient spatiotemporal resolution.

In this chapter, we highlight the various routes leading to the assembly and evolution of amorphous precursors in zeolite synthesis wherein it is recognized that changes in conditions – most notably the selection of silica/alumina sources and room temperature aging protocols – can significantly influence polymorphism, crystallization kinetics, and the properties of zeolites, among other factors. Here, we address the physical state of precursors with an emphasis on the appropriate use of the word "gel" to properly convey the heterogeneity of these species. In most zeolite syntheses, precursors undergo structural and/or compositional changes during the induction period. The exact microstructure of the evolved precursors is not well understood, nor are the detailed processes leading to their aggregation and densification. The direct role of precursors in the mechanism of crystal growth has been suggested for several framework types, such as LTA (zeolite A)[200], FAU (zeolite X/Y)[379,380], MFI (ZSM-5)[195,381], ANA (analcime)[382], SOD (sodalite)[202], CHA (SSZ-13),[78] and EMT[201]. Characterizing the role of precursors in zeolite crystallization is an active area of research, but there is still a significant knowledge gap in the understanding of molecular-level processes governing disorder-to-order transformations in zeolite synthesis. The presence of an amorphous phase can significantly modify zeolite crystallization, for example, by lowering the energetic barrier for heterogeneous nucleation by creating regions of high supersaturation, analogous to the two-step nucleation mechanism postulated for other materials such as proteins, polymers, colloids, and biominerals.[354,377,383,384] In this chapter, we do not attempt to reconcile this

gap, but merely seek to highlight the heterogeneous physical state that constitutes the majority of amorphous precursors observed during the preparation of (alumino)silicate zeolites.

## 5.2 Results and Discussion

**Figure 5.1** depicts various processes associated with precursor formation and evolution. **Figure 5.1A** is adapted from the review of Cundy and Cox[193] showing that the initial mixing of silica and alumina in alkaline media lead to the formation of nonhomogeneous amorphous precursors comprised of undissolved sources and species exchanged between solids and solution. The dashed boxes indicate aluminosilicate speciation in the solution state where prolonged time and/or higher temperature lead to precursor evolution in size, shape, and oftentimes microstructure. The terms primary and secondary have been used to differentiate the initial self-assembled precursors from those that have evolved through either room temperature aging or hydrothermal treatment. In literature, discussions of precursor assembly and evolution often invoke simplified schematics in a manner where precursors can be misconstrued as being homogeneous. The steady state distribution of species between solid and solution is established by the degree of silica dissolution. When silica sources such as colloidal silica, fumed silica, and alkali silicate are introduced into a high pH medium in either the presence or absence of an aluminum source, they are particulates. An example of precursor evolution is illustrated in **Figure 5.1B** for zeolite L prepared with colloidal silica. The sequence of steps during hydrothermal treatment begins with the aggregation and densification of silica particles. This is followed by the "fusing" of spherical aggregates into worm-like particles (WLPs) where undissolved silica is infused within a matrix of (alumino)silicate species.[206] The exact microstructure of these evolved (or secondary) precursors is unknown; however, it has been observed by multiple groups that secondary precursors can contain localized order that differs from the primary amorphous precursors, yet the evolved particles lack long-range (periodic) order that renders them amorphous by X-ray diffraction.[385,386] It is suggested in literature that silicon sources dissolve at high pH to produce a suspension of soluble monomer

or oligomeric species. Once dissolved, it is posited that these species can form gels that are often initiated by first preparing separate silica and alumina mixtures at high pH and then combining them after a fixed period of aging or hydrothermal treatment.

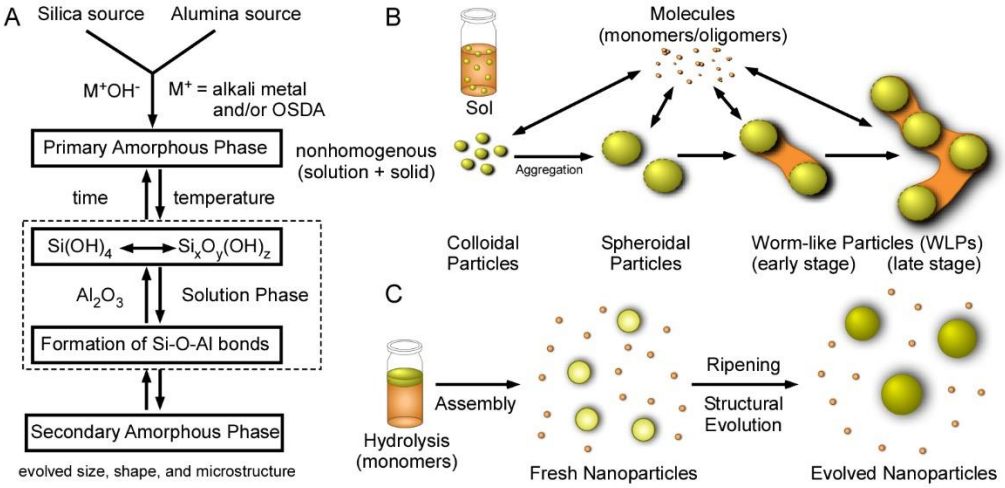


**Figure 5.1 (A)** General pathways leading to the formation of primary and secondary amorphous phases in zeolite synthesis.[193] **(B)** Schematic showing the formation of amorphous precursors in zeolite L synthesis beginning from a colloidal silica sol.[206]. **(C)** Illustration of silicalite-1 precursor assembly and evolution.

Herein, we argue that a majority of zeolite synthesis mixtures are prepared in such a manner that will never lead to the formation of gels owing to the inability to completely dissolve the silicon source. The sol gel process used to prepare zeolites involves different physical states in the synthesis medium (as depicted in **Figure 5.2**).[387-389] The mixing of reagents in zeolite synthesis can result in the formation of a *sol*, which is comprised of a suspension of colloidal particles in a continuous liquid medium. The viscosity of the suspension can vary with respect to particle volume fraction, but ultimately the rheological properties of sols are similar to a liquid. The second state is a *colloidal (or wet) gel*, which is a dilute cross-linked network of interacting colloidal particles that are generated from a suspension (sol) of colloidal particles. The nature of this gel may also derive from polymeric chains of aluminosilicates that form a dilute cross-linked network that is predominantly comprised of liquid. The rheological properties of these gels are more similar to a solid. A fourth state would be a hybrid of polymeric and colloidal gels. The idealized drawings in **Figure 5.2** illustrate the potential physical states of zeolite sol gel synthesis mixtures, beginning

with the introduction of the silicon source that leads to a sol **(Figure 5.2A)**. The latter can either form a colloidal (or wet) gel **(Figure 5.2B)** or the silicate particles can fully dissolve to generate a solution **(Figure 5.2C)** of dispersed monomers and/or oligomers.

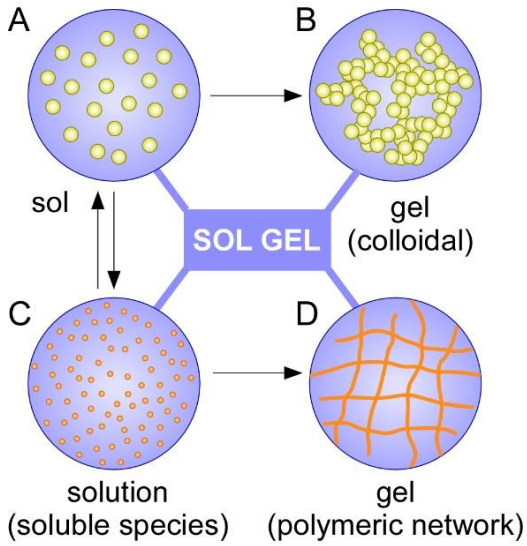


**Figure 5.2** Schematic illustrating the physical states of dispersed phases of colloidal particles (yellow) and soluble species (orange) in a dispersion medium of water (blue). The four corresponding states are **(A)** sol, **(B)** colloidal (or wet) gel, **(C)** solution, and **(D)** gel comprised of a polymeric network of aluminosilicates.

While it is less common to encounter the terms "colloidal" or "wet" gels in zeolite literature, these expressions are frequently used in sol gel literature to describe the gelation of sols.[387,390,391] Here, we distinguish this phase from the view of gels in the polymer and soft matter communities where the gel state is a network of polymeric chains formed by either physical aggregation or covalent bonds[392,393](represented as interconnected orange lines in **Figure 5.2D**). In the context of zeolite growth mixtures, these are tetrahedral $TO_4$ networks (T = Si or Al) derived from the condensation of soluble species. One uncertainty associated with (alumino)silicate gels is the nature of the cross-linked network. For instance, it is uncertain if the gel is comprised of covalently linked "polymer-like" chains of silicates (i.e., a chemical gel), or whether it is a network of interacting silicate species (i.e., a physical gel). We posit that the vast majority of zeolite precursor gels reported in literature are some combination of **Figure 5.2B and 5.2D** where

undissolved sols are contained within a network of condensed soluble species. This is analogous to the idealized depiction of WLPs in **Figure 5.1B** where the fusing of spheroidal aggregates occurs by an exchange with soluble species, leading to interstitial regions of unknown microstructure that may be similar to a gel-like network.

The use of tetraethylorthosilicate (TEOS) as a silica source can lead to unique pathways in the formation of amorphous precursors. While TEOS is not used in the commercial production of zeolites, it is heavily utilized in academic studies to assess the mechanisms of zeolite nucleation and crystal growth.[188,210,212,394-398] As illustrated in **Figure 5.1C**, TEOS forms an immiscible layer above water that leads to the progressive release of soluble silicates. For detailed speciation models of TEOS hydrolysis and silica condensation, we refer readers to several prior studies.[388,389,399-401] In alkaline solvent, silicates dissociate via a series of reactions.[402] Monomers can form oligomers, and at sufficiently high TEOS concentration these soluble silicates can further condense into nanoparticles **(Figure 5.3A)**. The rate of silica condensation is governed by the concentration of fully protonated silicates.[403] When the nanoparticles are formed, silanol groups on their exterior surfaces as well as undercoordinated (i.e., $Q^2$ or $Q^3$) sites within the interior of the nanoparticles can undergo protonation/deprotonation depending on the pH. The acid/base reactions associated with sol gel syntheses can lead to changes in pH and ionic conductivity, which can provide some indication of the chemistry associated with precursor assembly and evolution. The putative structure of silica nanoparticles shown in **Figure 5.3B** was derived from Monte Carlo simulations guided by $^{29}$Si NMR measurements of Si-O-Si connectivity.[404] The organic structure-directing agent (OSDA) tetrapropylammonium ($TPA^+$) forms a shell surrounding a core of hydrated amorphous silica.[212,405] The exact microstructure of silicalite-1 precursors is not well understood, although it is known that they evolve during the induction period. Notably, the particles grow in size by Ostwald ripening **(Figure 5. 1C)**[188,403,406] and also undergo a change in structure. Analogous

to secondary precursors, the microstructure of evolved nanoparticles differs from their primary state, yet they are not crystalline.[407]

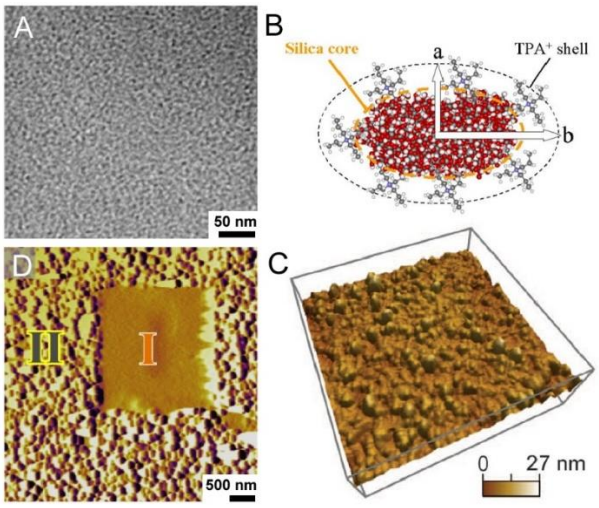


**Figure 5.3 (A)** Cryo-TEM image of nanoparticle precursors in silicalite-1.[210] **(B)** Idealized coreshell structure of nanoparticles from Monte Carlo simulations.[404] **(C)** AFM image of a silicalite-1 surface imaged during growth.[53] **(D)** AFM image of a LTA surface after continuous imaging where region I is the original area and region II is a freshly imaged area[218]

Nanoparticle growth ceases prior to the end of the induction period, after which the precursors remain in solution throughout crystallization and there is a temporal decrease in their population as silicalite-1 crystals grow in size. *In situ* atomic force microscopy (AFM) measurements of silicalite-1 (010) surface growth revealed that evolved particles attach to the crystal surface and undergo a disorder-to-order transition.[53] Amorphous precursors generated from TEOS occur by the assembly of monomer/oligomers, whereas alternative silica sources introduced into the synthesis mixture as sols **(Figure 5.1B)** evolve into larger amorphous spheroidal particles or branched WLPs through a sequence of events. Recent studies in our group focusing on the supernatant of sols revealed that gel-like features appear on zeolite surfaces at elevated temperature. For example, **Figure 5.3D** shows the result of an *in situ* AFM measurement of zeolite A (LTA) growth from its supernatant containing soluble aluminosilicate species where continuous imaging (region I) is smooth compared to the surrounding rough areas (region II).

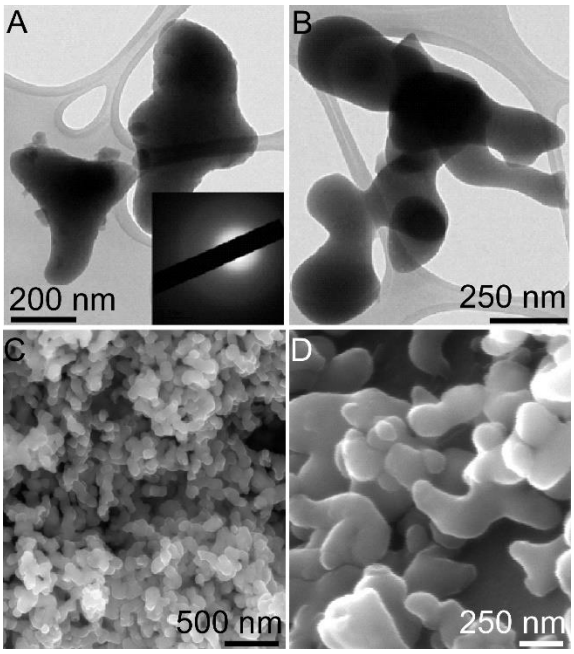


**Figure 5.4** Transmission (top) and scanning (bottom) electron micrographs of amorphous precursors in zeolite growth mixtures for zeolite L **(A and B)** and ZSM-5 **(C and D).**

Time-resolved images of rough surface features reveal a progressive reduction in height that suggests the roughness is due to gel-like islands that form on crystal surfaces.[218] This conclusion was drawn not only from the observation that the movement of the AFM tip progressively removes material from the surface during continuous imaging, but was corroborated by chemical force microscopy measurements on the roughened gel-like regions that yielded approach–retraction profiles characteristic of elastic lipid materials (e.g.,, lipid layers). Silicon sources other than TEOS can lead to the formation of amorphous colloidal precursors that are much larger than those formed in silicalite-1 synthesis. Examples are provided in **Figure 5.4** for two different zeolite types prepared with separate silicon sources (colloidal silica and fumed silica). Images of the precursors formed in growth mixtures of zeolite L **(Figure 5.4A and B)** are similar to those formed in the early stages of ZSM-5 growth **(Figure 5. 4C and D)**. The ubiquitous presence of bulk amorphous particles in zeolite growth mixtures has been widely reported for a range of frameworks including GIS, TON, MFI, CHA, and LTL. Despite the ubiquity, the role of amorphous precursors in zeolite crystallization is not fully understood. Two divergent hypotheses

exist in the literature regarding the role of WLPs in zeolite nucleation (refer to **Figure 5.9**): WLPs can either dissolve to generate molecular species that serve as growth units for crystallization or they can directly contribute to zeolite growth via pathways involving crystallization by particle attachment (CPA).[77,194]

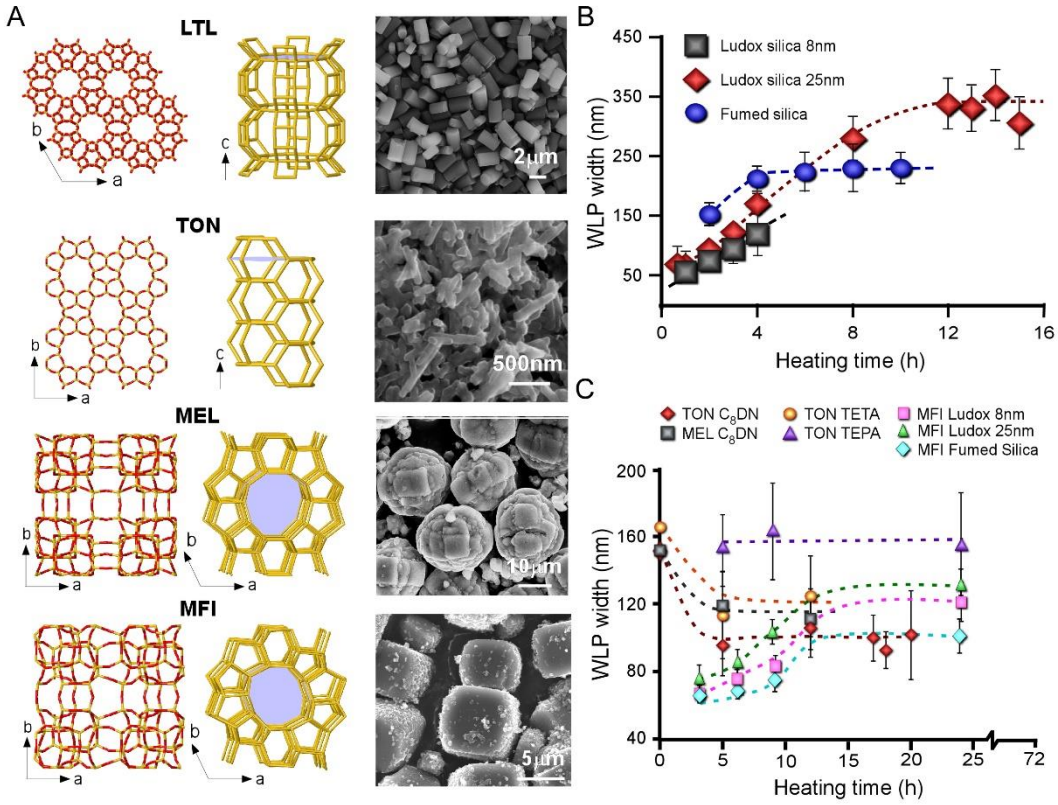


**Figure 5.5 (A)** Physicochemical properties of four zeolite different frameworks with distinct crystal size and morphology. **(B)** Temporal evolution of WLPs in K-LTL growth mixtures (OSDA-free). **(C)** Temporal evolution of WLPs in MFI, MEL, and TON growth mixtures using various OSDAs.

WLPs tend to have much higher silicon content compared to the crystalline product[195,206], which suggests a solution-mediated process must occur during zeolite crystallization that involves the exchange of alumina from solution and significant bond breakage of Si-O-Si bonds within the WLP. The nonhomogeneous segments containing pure silica calls into question putative solid-state rearrangement of precursors to crystals. It is also uncertain to what degree precursors become locally ordered during their evolution from primary to secondary species. Analogous to schemes

for zeolite L and silicate-1 **(Figure 5.1B and 5.1C**, respectively), the temporal evolution of WLPs has been observed in numerous other systems.[78,195,206,408] To illustrate the variety of pathways leading to WLP formation and evolution, we selected four different zeolite framework types and performed time-resolved analysis of precursor assembly. The structure of each zeolite selected for this study is shown in **Figure 5.5A** along with a scanning electron microscopy (SEM) image of the crystalline product. The framework types differ with respect to their composition (Si/Al ratio), the pore dimensions, and pore sizes, which are denoted by the n-membered rings (MRs) constituting the pore aperture: zeolite L (LTL, Si/Al = 3, 12-MR 1D pores), ZSM-22 (TON, Si/Al = 35, 10-MR 1D pores), ZSM-11 (MEL, Si/Al = 36, 10-MR, 3D pores), and ZSM-5 (MFI, Si/Al = 40, 10-MR, 3D pores).

**Figure 5.5B** plots the temporal change in precursor dimension with heating time during the synthesis of zeolite L using three different silicon sources (8 nm colloidal silica, 25 nm colloidal silica, and fumed silica). The general profile of each synthesis is a monotonic increase in precursor size (presumably through the incorporation of soluble species), followed by a plateau that coincides with the completion of the induction period. The precursor size remains constant throughout zeolite L crystallization, while the population of WLPs decreases at the expense of growing crystals. For zeolite L, the silicon source has a significant impact on the induction time[206], but does not appreciably influence the rate of WLP growth. Moreover, we observe for the smallest colloidal silica (ca. 8 nm) that once nucleation occurs, the crystallization timeframe is too fast to detect WLPs (i.e., they are rapidly consumed beyond 4 h). Similar studies of other zeolites are shown in **Figure 5.5C** where we observe different trends depending on the synthesis conditions. Samples were prepared from multiple silicon sources in the presence of different OSDAs. Profiles exhibit either increasing or decreasing size with heating time, while some show relatively no change over the time period analyzed. For studies of TON, the OSDA selection effects precursor evolution. For instance, precursor size decreases in mixtures prepared with 1,8-diaminooctane ($C_8$DN) and

triethylenetetramine (TETA), whereas the same composition prepared with tetraethylenepentamine (TEPA) resulted in relatively little change in precursor size. Comparisons of ZSM-5 (MFI) precursors prepared with TPA using three different silicon sources revealed analogous trends to zeolite L samples with less noticeable differences in precursor evolution. One potential cause of the disparity among samples is that the presence of OSDAs can assist in producing soluble silicates. For instance, prior studies have shown that an increased concentration of OSDA leads to an increase in pH, which impacts silica dissolution.[409,410] Given that many OSDAs exhibit positive charge (e.g., quaternary amines), it was suggested by Lowe and coworkers[410] that cationic OSDAs balance the negative charge(s) of silicate anions, thereby shifting the equilibrium of silicate speciation. Iler and others have posited similar effects by showing that organic molecules such as amines and catechol can form soluble complexes with silicates, which can further accelerate silica dissolution[388,409]. Conversely, Caratzoulas and coworkers have postulated an opposite role of OSDAs to stabilize silicates by shielding siloxanes from water, thereby reducing the rate of hydrolysis (i.e., as reported for tetramethylammonium stabilization of silica cubic octamers).[411]

During the transition from primary to secondary precursors **(Figure 5.1A)**, hydrothermal treatment leads to the opening of Si–O–Si bonds, whereas the presence of Si–O–Al bonds can significantly slow bond breakage at high pH. Evidence gathered from the elemental analysis of precursors in ZSM-5 and zeolite L synthesis[195,206] indicate that the silicon content can be much higher in secondary precursors than the crystalline product, which seems to indicate that the initial silicon source remains partially undissolved during the early stages of zeolite crystallization. Introduction of alumina into the growth medium can promote the aggregation of silica sols (i.e., destabilize colloidal suspensions), leading to the formation of spherical particulates that seemingly assemble via a combination of aggregation, densification (ripening), and growth processes. This general picture of precursor formation is highly suggestive that their composition is likely a hybrid of the colloidal and polymeric gels depicted in **Figure 5.2B and 5.2D** wherein the network is

comprised of undissolved silica particles linked through species from solution that "bridge" opposing particles; however, it is difficult to determine individual colloidal domains in transmission electron micrographs of precursors.

One of the critical questions regarding WLP assembly pertains to the microstructure of the amorphous particles as they evolve. This alludes to more ubiquitous uncertainties regarding how we define amorphous materials. Is it sufficient to simply label systems as being either crystalline or amorphous without considering the degree of local order that has been reported in many examples of secondary (evolved) precursors? Here, we do not attempt to answer this question, but merely point out that the starting materials used in the preparation of zeolite precursors can be quite different and that the evolution from amorphous to crystalline is not abrupt but progressive, and moreover, that the amorphous and crystalline phases can co-exist at given time. Indeed, it is common knowledge that subtle changes in zeolite compositions[67], such as the selection of silicon source, can have a pronounced impact on the final product. In some instances, zeolite syntheses will only work with a particular source, whereas other syntheses are much more robust to changes in synthesis protocol. To ascertain the differences in Si-O-Si connectivity among three common silicon sources, we conducted pair distribution function (PDF) analysis of as received colloidal silica, fumed silica, and potassium silicate sources **(Figure 5.6)**. The PDFs provide a histogram of all atom-atom distances within the silicate source, weighed by relative abundance and the scattering factor of the atoms. The first three peaks on all PDFs at 1.61 Å, ~2.6 Å and ~3.1 Å correspond to the closest Si-O, O…O, and Si…Si distances, respectively, that define corner-shared $SiO_4$ tetrahedra. The potassium silicate PDF includes additional features associated with interactions (e.g., at ~2.8 and 3.6 Å) with the $K^+$ ion. As is consistent with the non-crystalline nature of the silica sources, well defined peaks in the PDF are not observed in the PDFs at long distances, beyond ~20 Å.

While the local tetrahedral $SiO_4$ structure and absence of long range order is common to all silica sources in **Figure 5.6**, there are striking differences in the intermediate scale ordering from 3.5 - 12 Å. Most notably, in the case of the fumed silica, well defined peaks are evident in the PDF to ~12 Å, reflecting a well ordered intermediate-scale structure. Attempts to model these data showed that the structure did not correspond to the structural motifs of common dense $SiO_2$ polymorphs. While both the colloidal and potassium silicate source PDFs contain only broad/diffuse features beyond 4.5 Å, these diffuse features do not overlap, suggesting that different connectivity exists in these amorphous phases (although the correlations associated with K in the potassium silicate source will also contribute owing to differences in the structure). The broad diffuse features in the colloidal silica source shows similarities to the peaks observed for fumed silica. The difference in intermediate scale atomic-structure and ordering observed for the silicon sources may account for the different solubilities/rates of reaction. If we presume that less well-ordered structures will be less thermodynamically stable, then we would expect the solubility and rates of reactions to decrease in the order potassium silicate, colloidal silica, and fumed silica.

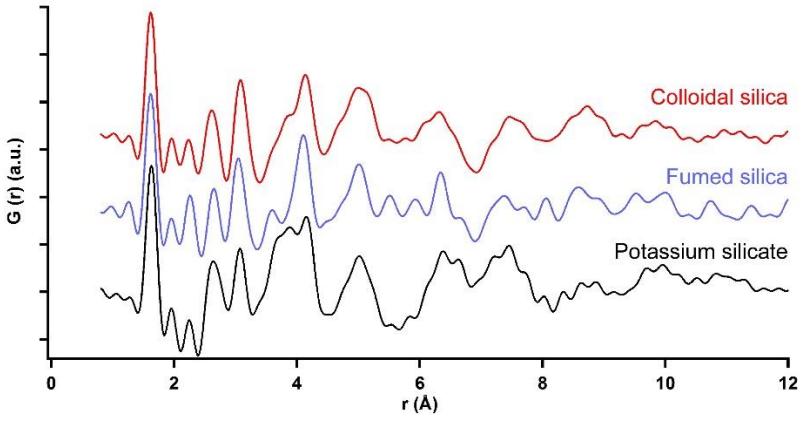


**Figure 5.6** Pair distribution function (PDF) data of three common silicon sources: LUDOX AS-40 colloidal silica (red line), CAB-O-SIL fumed silica (blue line), and potassium silicate (black line).

**Figure 5.7A – C** shows images of solids that have been extracted at periodic times during the synthesis of ZSM-5 where precursors are observed throughout crystallization. This is consistent

with many zeolite syntheses where the sequence of events is similar: the precursors first assemble and evolve during the induction period, they then cease growing at a time that approximately corresponds to the onset of nucleation, and over the course of zeolite crystallization the precursor content decreases. It is interesting that precursor assembly is rapid and that these particles exhibit a propensity to grow rather than to dissolve in highly alkaline media (i.e., pH 11 – 14). This prompts questions as to what degree silicon sources dissolve during room temperature aging and the early stages of hydrothermal treatment. For growth mixtures, such as those depicted in **Figure 5.7A** consisting of a high-volume fraction of colloidal precursors, the samples are opaque sols or wet gels. For growth mixtures shown in **Figure 5.3A**, which consist of much smaller precursors, the samples are referred to as "clear solutions," but a more accurate description is translucent sol. It is important to note that transparent liquids do not imply the absence of colloidal particles. Indeed, the degree of opacity is dependent upon both the size and concentration of colloidal particles in the suspension. This is an important point to raise since it is often assumed that placing silica in a high pH solution will lead to complete (or nearly complete) dissolution. As we discuss herein, this does not occur for the vast majority of zeolite syntheses.

To demonstrate that silica in zeolite syntheses remain largely undissolved, we refer to a recent study[141] using dynamic light scattering (DLS) to track the temporal change in hydrodynamic diameter of colloidal silica particles in alkali hydroxide solutions (in the absence of alumina). Using a typical silica content, measurements were performed in KOH (pH 12) over a range of temperatures (25 – 45 °C). As shown in **Figure 5.8A**, the rate of silica dissolution increases with increased temperature, as expected. For data collected at 45 °C, we observe a plateau (dashed line in **Figure 5.8A)** once the diameter decreases by 9 % of its original size. This indicates that the solution has reached thermodynamic equilibrium where an estimated 266 mM of dissolved silica corresponds to its solubility at that particular pH and temperature. During the preparation of zeolite synthesis mixtures, the addition of aluminum to these colloidal suspensions leads to its deposition

on the surfaces of silica particles, which dramatically reduces the rate of silica dissolution. This can extend the timeframe for reaching thermodynamic equilibrium or create a metastable state whereby the solution never reaches equilibrium prior to the onset of zeolite nucleation. The latter scenario was observed in a recent study where we examined silica concentrations in the supernatant of a zeolite A synthesis mixture (pH 13.7) as a function of heating time at 65 °C. In this system, silica concentrations ranged from 10 to 30 mM, which is well below the solubility of the colloidal silica used as a starting reagent.

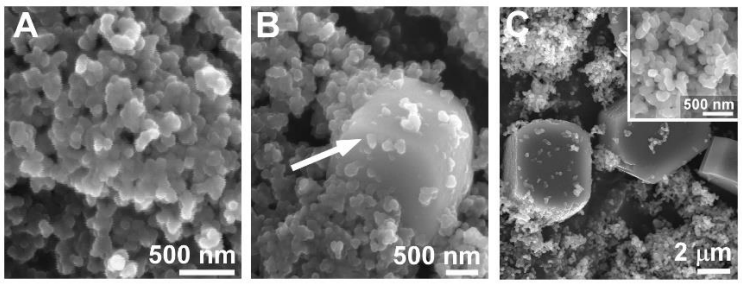


**Figure 5.7** Time-resolved electron scanning micrographs of solids extracted during periodic stages of ZSM-5 synthesis after **(A)** 3 h of heating, **(B)** 6 h of heating, and **(C)** 24 h of heating.

Iler and others[412-416] have previously reported silica solubility as a function of both temperature and pH. In Table 1, we compare the solubility of amorphous silica for a limited set of conditions where it is evident that solubility increases with increasing temperature and pH. For instance, another *ex situ* DLS study at higher alkalinity using NaOH (pH 13.6) and similar silica concentration revealed that equilibrium is reached after the diameter of colloidal silica particles is reduced by ca. 28 % **(Figure 5.8B)**[191]. The estimated silica solubility of 725 mM at 45°C is higher than the value in **Figure 5.8A** owing to the higher pH of the solution. Studies such as these to quantify silica solubility are limited to temperatures that are much lower than those of typical zeolites syntheses. This leads to questions regarding the actual composition of solutions during the early stages of hydrothermal treatment. It has been posited that silica solubility in highly alkaline solutions (pH > 12) and at high temperature (T > 100 °C) can reach values in the molar range.[413,417]

Experimental validation of these predictions is challenging owing to the difficulty of *in situ* analysis.

There is evidence in the literature, however, that predicted solubility may be overestimated in some instances. One example is the presence of amorphous silica nanoparticles in dilute silicalite-1 growth mixtures where *in situ* AFM measurements[53,222]of crystal surfaces (e.g., **Figure 5.3C**) reveal the presence of attached precursors at conditions that are predicted to be undersaturated. This may be due to the presence of OSDAs, which as previously mentioned, can potentially stabilize silicate species. In the context of dissolution kinetics, primary or secondary amorphous precursors may never reach thermodynamic equilibrium with soluble silicates.

**Table 5.1** Silica solubility for amorphous sources and select zeolites.

| Material | pH | $[SiO_2]_{eq}$ (mM) | $[SiO_2]_{eq}$ (g/L) | References |
|---|---|---|---|---|
| Amorphous silica (25°C) | 12 | 318 – 388 | 19 – 23 | [412,413] |
| LUDOX AS-40 (45°C) | 12 | 266 | 16 | [141] |
| | 13.6 | 725 | 43.5 | [191] |
| Zeolite LTA (25°C) | 13.6 | 5 – 10 | 0.3 – 0.6 | [218,418,419] |
| Zeolite MFI (25°C) | 11.3 | 0.18 | 0.010 | This work |
| Zeolite MEL (25°C) | 11.3 | 0.21 | 0.012 | This work |
| Zeolite TON (25°C) | 11.3 | 0.21 | 0.012 | This work |

Moreover, measurements of silica solubility, such as that presented in **Figure 5.8**, are typically conducted in purely siliceous solutions, whereas the solubility can be quite different in actual synthesis mixtures due to the presence of alumina, metals, and organics. For example, Iler has shown that the presence of aluminum can lower silica solubility by orders of magnitude at high pH[420]. To this end, a basic understanding of the thermodynamic factors governing solution chemistry during room temperature aging and early hydrothermal treatment of zeolite synthesis mixtures is generally lacking. This presents opportunities for future studies to better understand the complex reactions of precursor assembly and evolution as well as the growth units involved in zeolite crystallization. We measured the silica solubility for several zeolite framework types after allowing sufficient time for complete crystallization (e.g., 72 h). The corresponding solubilities

listed in **Table 5.1** were measured at 25 °C by extracting the supernatant and analyzing its Si content using inductively-coupled plasma (ICP). In **Table 5.1** we also list reported solubilities of other zeolites, such as LTA, to illustrate an upper range of silica solubility at higher pH. It is interesting to compare these values to those in **Table 5.2** listing the silica contents used in synthesis mixtures of commonly studied zeolite framework types.

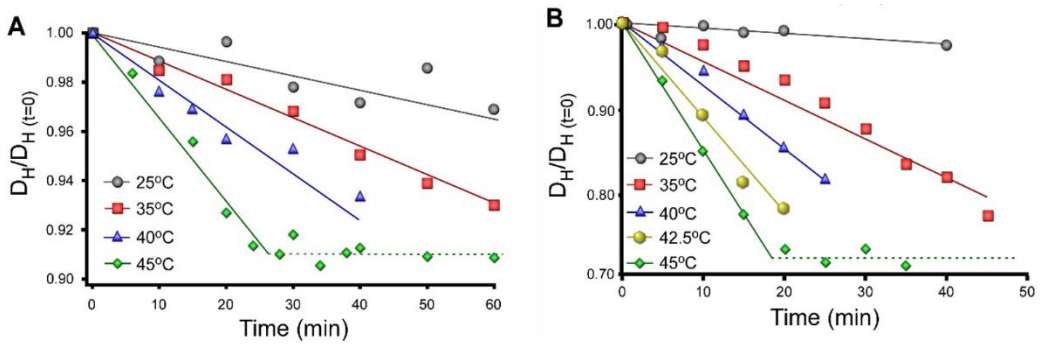


**Figure 5.8 (A)** Dissolution of LUDOX AS-40 colloidal silica particles in a KOH solution (pH = 12) at various temperatures.[141] **(B)** Identical experiments in a NaOH solution (pH 13.6) prepared with 1156 mM $SiO_2$.[191]

The range of values listed in **Table 5.2** are based on a limited survey of literature, and therefore do not represent the absolute lower and upper bounds. Nevertheless, they provide an approximate range of values where it is clearly evident that the vast majority of syntheses utilize silica content well in excess of the amorphous silica solubility. Under such conditions, it is impossible to fully dissolve silica. Only under rare cases where concentrations fall below 300 mM, such as purely siliceous MFI (silicalite-1) and MEL (silicalite-2), is it feasible to achieve growth solutions of dissolved silicate species. Several aluminosilicate zeolites are also prepared with low silica content (e.g., FAU, GIS, LTA, MFI); however, silica content in zeolite syntheses typically exceed 1000 mM. It should be noted that it is difficult to calculate and report the supersaturation with respect to silica due to the complexity of the medium given the presence of numerous species (i.e., monomers, a wide range of soluble aluminosilicate oligomers, and silica that is retained within metastable colloidal precursors). It is evident from the high silica content used in the starting mixtures of zeolite synthesis that aging silica sources in alkaline media will not result in the

complete dissolution of silica particles prior to zeolite nucleation. A more realistic scenario is that the equilibrium between silica and silicate species (monomers and small oligomers) at a given pH is shifted towards the dissolution of silica as they are consumed during zeolite crystallization.

**Table 5.2** Range of silica content in zeolite synthesis mixtures.[a]

| Zeolite | [$SiO_2$] (g/L) | Zeolite | [$SiO_2$](g/L) |
|---|---|---|---|
| AEI | 84 – 1020 | MER | 24 – 240 |
| BEA* | 111 – 477 | MFI | 2 – 90 |
| CHA | 72 – 600 | MOR | 74 – 420 |
| FAU | 11 – 167 | MTT | 56 – 256 |
| FER | 24 – 660 | MTW | 56 – 256 |
| GIS | 9 – 270 | MWW | 74 – 248 |
| HEU | 480 – 3120 | RHO | 180 – 540 |
| LTA | 14 – 96 | TON | 61 – 222 |
| LTL | 48 – 330 | UFI | 111 |
| MEL | 54 – 360 | | |

(a) Literature references for each framework type are provided in **Table D2** of the Appendix D

The kinetics of silica dissolution and the evolution of its properties (e.g., porosity, microstructure, etc.) during zeolite growth are frequently overlooked; and in some cases, to the point that it is assumed silica completely dissolves during aging, which is inconsistent with the low solubility of silica relative to the high silica content of many zeolite syntheses. This is particularly relevant for synthesis protocols that separately age (or pre-treat) silicon and aluminum sources prior to their mixing [421] relative to those that combine sources before aging.[191] In the former case, gelation is often observed when separately aged sources are combined; however, it should be noted that these sol gels contain undissolved silica particles. The densification process leading to what appears in electron microscopy images as a uniform spheroidal particle suggests that silica particles are interconnected through a network of condensed soluble species, which promote aggregation. The exact microstructure of amorphous precursors still remains a mystery, though it is evident that primary and secondary precursors exhibit a large degree of heterogeneity with respect to the spatial distribution of Si and Al owing, in part, to the incomplete dissolution of silicon sources. Differences in the viscosity of sol and gel mixtures can presumably influence zeolite crystallization by altering

mass transport between solution and solid phases. It remains to be determined if gelation persists at higher temperature, and to what degree the distribution of (alumino)silicate species between the solution and solid states varies as a function of the aging process. Based on the preponderance of evidence in literature that aging can significantly alter zeolite syntheses, it would come as no surprise that the selection of silicon and aluminum sources, the order of mixing these sources, and procedures for room temperature or hydrothermal treatment can impact zeolite growth and the physicochemical properties of the crystalline product.

References to amorphous precursors as *gels* coupled with the use of oversimplified schematics that depict these species as homogenous entities can lead to misconceptions regarding their composition and structure. Cundy and Cox[193] addressed this point by stating that "the primary amorphous phase represents the initial and immediate product from the reactants and is a non-equilibrium and probably heterogeneous product containing (for example) (a) precipitated amorphous aluminosilicates, (b) coagulated silica and alumina precipitated from starting materials destabilized by the change in pH and increase in salt content and (c) unchanged reactants." In cases where synthesis protocols are designed to first dissolve silica by aging sols at high pH, this can only be accomplished at silica content below 250 mM at room temperature or around 1000 mM for mixtures at higher temperature and pH. The presence of aluminum, however, makes it difficult to reach saturation owing to a reduced rate of silica dissolution. It is also possible that zeolite nucleation occurs prior to reaching equilibrium between the solution and amorphous precursors ($K_2$ in **Figure 5.9**), in which case the driving force for (alumino)silicate speciation in is governed by the equilibrium between the solution and crystalline phase ($K_1$ in **Figure 5.9**). This leads to a monotonic decrease in soluble species during crystal growth until the silicates concentration is on the order 0.1 – 10 mM. The exact role(s) of amorphous precursors in zeolite crystallization is a subject of ongoing investigation. **Figure 5.9** depicts several pathways of zeolite growth that can be categorized as either classical (involving monomer addition) or nonclassical (involving the addition

of species more complex than monomers). The mere presence of precursors implies their role in the latter pathway, although evidence shows that both classical and nonclassical pathways are involved with the former becoming more prevalent at later stages of growth when the population of precursors is small and the supersaturation of soluble silicate species is low. It is feasible that precursors serve as a reservoir of nutrient that is released by dissolution (path 2d in **Figure 5.9**), although the fact that precursor size remains constant during crystallization suggests that not all precursors dissolve, which implies that such processes are rapid and likely occur in the proximity of zeolite crystal surfaces.

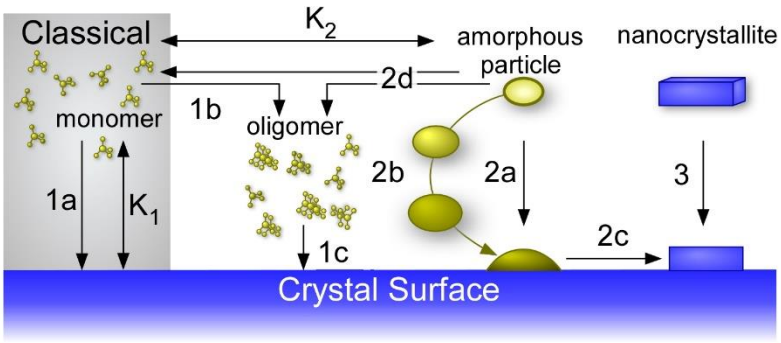


**Figure 5.9** Putative pathways of zeolite crystal growth from a diverse selection of precursors[77]

If precursors directly attach to crystal surfaces (Eq. 3; paths 2a and 2b in **Figure 5.9**), this process requires a disorder-to-order transition (path 2c in **Figure 5.9**). Indeed, there is still much that we do not know regarding the microstructure of precursors, and to what degree this structure changes during primary-to-secondary phase evolution. The lack of long-range order coupled with the presence of purely siliceous regions within these phases indicates that a significant amount of bond breaking and reforming is required to transition from nonhomogeneous precursors to a final zeolite where the Si and Al are more uniformly distributed.

## 5.3 Conclusions

In this study, we reemphasize the heterogeneity of gels encountered in zeolite synthesis mixtures. In general, gels encompass a broad spectrum of physical states. Classical polymer

literature defines gels as having four possible configurations: (1) well-ordered lamellar structures; (2) covalent polymeric networks, completely disordered; (3) polymer networks formed through physical aggregation, predominantly disordered; and (4) particular disordered structures[387,422]. In Brinker and Scherer's book on sol gel science[389], a signature property of the gel is defined by the combination of continuous solid and fluid phases wherein "one could travel through the solid phase from one side of the sample to the other without having to enter the liquid." These definitions allow significant latitude for the classification of gels in zeolite synthesis. Our intent is to highlight that many of the gels formed in zeolite growth mixtures are comprised of colloidal particles. To this end, any mechanism of zeolite growth involving precursors must take into account the fraction of undissolved silicon source that requires substantial bond breakage and reordering. Questions pertaining to how the physical state of the synthesis mixture (i.e., sol vs. gel) impacts crystallization pathways and/or kinetics, as well as the preservation of the physical state at high temperatures relevant to the majority of zeolite syntheses, remain elusive. It is also important to better characterize, clarify and describe the wide and diverse family of materials that are broadly referred as "amorphous precursors", as it is evident that a simple demarcation of crystalline versus noncrystalline is an insufficient description to explain the complex effects that source selection and aging have on zeolite synthesis.

## 5.4 Material and Methods

### 5.4.1 Materials

The following chemicals were purchased from Sigma-Aldrich (St. Louis, MO): LUDOX AS-30 (30 wt % suspension in water), LUDOX AS-40 (40 wt % suspension in water), Ludox SM-30 (30 wt % suspension in water), potassium hydroxide (85% pellets), aluminum sulfate hydrate (98%, 14-18 $H_2O$, calculated as 18 $H_2O$), tetrapropylammonium bromide (TPABr, 98%), and 1,8 diaminooctane (98%). Fumed silica was purchased from Spectrum (Cab-O-Sil M-5 Scintillation Grade). Deionized (DI) water used in all experiments was purified with an Aqua Solutions RODI-

C-12A purification system (18.2 MΩ). All reagents were used as received without further purification.

### 5.4.2 Crystallization of Zeolites

**ZSM-5**: ZSM-5 crystals were synthesized from a growth mixture with a molar composition of 2 TPABr: 11.9 $K_2O$: 1 $Al_2O_3$: 90 $SiO_2$: 3588 $H_2O$.[141] Aqueous solutions of potassium hydroxide (0.33 g in 1.44 g of DI water) and aluminum sulfate (0.14 g in 1.44 g of DI water) were mixed with 5.76 g of water, and LUDOX AS-30 solution (3.76 g in 2.13 g of DI water) was added under vigorous stirring. The resulting mixture was stirred for ca. 21 h at room temperature (referred to as aging). After aging, the OSDA (0.1515 g TPABr) was added and the solution was left to stir for another 2 h at room temperature. The growth mixture (ca. 10 g) was then placed in a Teflon lined stainless steel acid digestion bomb (Parr Instruments) and was heated under rotation (30 rpm) and autogenous pressure in a Thermo Fisher Precision Premium 3050 Series gravity oven. The nominal time and temperature for ZSM-5 synthesis was 3 days at 160 °C.

**ZSM-11 and ZSM-22**: ZSM-11 crystals were synthesized using 1,8 diaminooctane (DAO) as the OSDA. Aqueous solutions of aluminum sulfate (solution A) and DAO (solution B) were prepared separately in 20 mL beakers. Solution A was prepared by dissolving 0.099 g of aluminum sulfate hydrate in 1.00 g of DI water while stirring. Solution B was prepared by dissolving 0.59 g of DAO in 3.06 g of DI water while stirring. The synthesis mixture was then prepared by first placing 1m KOH (3.63 g) in a polypropylene bottle, followed by a slow addition of solution A, and then solution B, with continuous stirring. To the resulting mixture, 2.62 g of LUDOX AS-30 was added dropwise under continuous stirring to produce a final synthesis mixture with a molar composition of 27.3 DAO: 11.9 $K_2O$: 90 $SiO_2$: 1 $Al_2O_3$: 3588 $H_2O$. The mixture was aged at room temperature for 21 h with stirring and was transferred to a 23mL Teflon lined metal autoclave (Parr

Instruments). The sealed autoclave was heated in a Thermo Scientific Precision oven under static conditions for 3 days at 160 °C. The synthesis procedure of ZSM-22 was almost the same as that of ZSM-11 except for the use of rotation oven (30 rpm) during heating.[423]

**Zeolite L:** Zeolite L crystals were synthesized in the absence of an organic using $K^+$ as an inorganic structure-directing agent. Growth solutions were prepared with a molar ratio of 0.5 $Al_2O_3$: 20 $SiO_2$: 10.2 $K_2O$: 1030 $H_2O$.[206] Potassium hydroxide (0.64g, 9.66 x$10^{-3}$ mol) was first dissolved in water (7.78g), followed by the addition of aluminum sulfate (0.17g, 4.73 x$10^{-4}$ mol). This solution was stirred until clear (ca. 5 min). The silica source was added, and the resulting solution was left to stir overnight (ca. 21 h) at room temperature. The growth solution was prepared with Ludox AS-40 (1.42g, 9.47 x$10^{-3}$ mol). The colloidal silica source was added to the growth solution dropwise while stirring. After aging was complete, the growth solution (ca. 10g) was placed in a Teflon lined stainless steel acid digestion bomb (Parr Instruments) and was heated under static conditions (i.e., without mixing) in a Thermo- Fisher Precision Premium 3050 Series gravity oven at 180 °C and autogenous pressure.

The pH of the growth solutions was measured with a Thermo Scientific Orion 3 Star meter. For X-ray and microscopy analyses, the particulates in the growth mixture (amorphous and/or crystalline) were isolated as a white powder by centrifugation (Beckman Coulter Avanti® J-E series high-speed centrifuge) at 13,000 rpm for 45 min. The solid was washed with DI water to remove the supernatant and the centrifuge/washing step was repeated a second time. The resulting solid was dried at ambient conditions. During the preparation of microscopy samples, the solid was dispersed in DI water and an aliquot of the suspension was placed on a glass slide and dried overnight. Crystals on the glass slide were transferred to SEM sample holders (Ted Pella) by gently pressing the glass slide on the carbon tape.

### 5.4.3 Materials Characterization

Powder X-ray diffraction (XRD) patterns of as made samples were collected on a Siemens D5000 X-ray diffractometer using a Cu Kα source (40 kV, 30 mA). Scanning electron microscopy (SEM) images were obtained with a LEO 1525 FEG system operated at 15 kV and a 5 mm working distance. All SEM samples were coated with a thin carbon layer (ca. 30 nm) prior to imaging. Dynamic light scattering (DLS) measurements were performed on a Brookhaven Instruments BI-200SM machine equipped with a TurboCorr Digital Correlator, a red HeNe laser diode (30mW, 637 nm), and a decalin bath that was filtered to remove dust. The liquid sample cell was regulated at 25°C with a Polyscience digital temperature controller. Samples were prepared by diluting zeolite growth mixtures in pre-filtered DI water (0.45-µm nylon syringe filter, Pall Life Sciences) to achieve reasonable scattering counts (>20,000 count-sec-1). At least three measurements were performed per sample. Autocorrelation functions were collected over a 2 min timeframe and the hydrodynamic diameter DH was analyzed by the method of cumulants to assess particle size distribution. Silica dissolution experiments were performed by adding colloidal silica to metal hydroxide solutions (pH = 12) in the absence of aluminum. Solutions were separated into different vials and heated at specified temperatures in a Julabo ED-5M/B water bath. Vials were removed at periodic times and immersed in ice to cool down to room temperature before performing DLS analysis.

The morphology of amorphous precursors was studied by transmission electron microscopy using a JEOL instrument, a JEM-1400 Plus (120 kV, 0.38 nm resolution). Zeolites were grounded, suspended in ethanol and sonicated for 15 min. A few drops of this suspension were placed on a Lacey Formvar/Carbon copper grid. The ethanol was evaporated at room temperature. The digital analysis of the TEM micrographs was done using DigitalMicrographTM 3.6.1. by Gatan.

Total scattering data suitable for pair distribution function analysis were collected using the high energy X-rays ($\lambda$=0.2113 Å) available at the beamline 11-ID-B at the Advanced Photon Source at Argonne National Laboratory for samples contained within ~1.1mm diameter polyimide tubes. X-ray scattering images were collected to high values of momentum transfer (Q) using an amorphous silicon-based area detector from Perkin-Elmer and reduced to 1-dimensional scattering patterns within gsas-II.[424] The data were corrected for background, oblique incidence and Compton scattering within pdfgetX2[425] and Fourier transformed to Qmax =23 Å-1 to obtain the PDF, G(r).

# Chapter 6

# Tracking Zeolite Crystallization by Elemental Mapping

## 6.1 Motivation

Zeolites are an exemplary class of materials that grow via both classical and nonclassical pathways due to the wide variety of precursors present in the growth solutions consisting of (alumino)silicate oligomers, nanoparticles, and amorphous bulk phases.[53,77,224,231,360,426] One of the prominent examples is silicalite-1 (MFI framework), which grows through a dynamic sequence of events involving the addition of nanoparticles on the crystal surface and their subsequent rearrangement to undergo disorder-to-order transitions.[53,427] In recent studies of zeolite A (LTA) crystallization,[317] we demonstrated that surface growth involves multifaceted pathways wherein growth units can range from monomers/oligomers to gel-like islands. More broadly, the direct role of amorphous precursors in zeolite growth has been either confirmed or postulated for a range of frameworks including BEA, CHA, LTL, ANA, SOD, and EMT, among others.[203,206,379,428-432] An understanding of nucleation and growth mechanisms is essential to the development of synthetic protocols to optimize the physicochemical properties of zeolites for desired applications; however, one of the obstacles to elucidating fundamental aspects of zeolite crystallization is the lack of techniques capable of characterizing amorphous-to-crystal transformations, such as capturing the dynamics and/or time-resolved images with sufficient spatiotemporal resolution to identify the exact role(s) of amorphous precursors.[190]

Beyond studies of zeolites, there is mounting evidence that a large number of materials including (but not limited to) inorganic[229,433], biological (e.g., protein)[434], and organic crystals[435] nucleate and grow through nonclassical mechanisms. Among the most common precursors in these processes are amorphous particles that can serve as growth units via pathways which are referred to as crystallization by particle attachment (CPA).[77,190,436,437] Processes governed by CPA are

distinctly different from classical growth where two-dimensional layer generation and spreading on crystal surfaces occurs by the addition of monomers. There is a growing list of materials that have been identified to grow via CPA pathways, including metals[227], metal oxides[438,439], chalcogenides[440], and zeolites[230,353,361,441].

In recent years, advances in microscopy and spectroscopy techniques have shed light on these complex crystallization processes.[442,443] These techniques include transmission electron microscopy (TEM)[70,189,428,432,442], atomic force microscopy (AFM)[53,220,221,317,444], nuclear magnetic resonance (NMR) spectroscopy [219,406,445-447], infrared (IR) and Raman spectroscopy.[361,448,449] TEM is one of the most common imaging techniques used to obtain spatial information of individual particles at atomic scale; however, the large size of the precursors and the sensitivity of zeolites to electron beam damage presents challenges for their analysis by TEM.[442] Conversely, powder X-ray diffraction (XRD) is a bulk technique that provides information about average long-range order, but fails to provide any spatially-resolved insight on product speciation that may be useful for the identification of precursors and analyses of their evolution. Moreover, XRD is not a suitable technique to monitor the onset of nucleation since Bragg peaks are only detected once approximately 3 wt% of the sample is crystalline, as recently demonstrated by Valtchev and coworkers.[379] NMR can be a useful technique to capture molecular level processes that underlie crystallization wherein amorphous-to-crystal transformations can be tracked using a combination of solid state $^{27}$Al and $^{29}$Si MAS NMR. Lercher and coworkers[421] recently employed *in situ* NMR to elucidate the mechanistic details of zeolite Y (FAU) crystallization from amorphous gels. Kirschhock and coworkers[450] used $^{29}$Si MAS NMR to investigate the microstructure of precursors in silicalite-1 crystallization; however, recent studies by Chmelka and coworkers[451] have shown that it is often challenging to determine the structure of precursors using NMR data. For instance, the interpretation of data could lead to controversial results owing to the distributions in sizes and structures of particles. Furthermore, NMR suffers from poor time resolution (on the order of hours).

To this end, a characterization technique that is capable of providing local information regarding changes in both chemical composition and morphological evolution with relevant spatiotemporal resolution is desired.

In this study, we use scanning electron microscopy in combination with energy dispersive X-ray spectroscopy as a tool to create elemental maps of zeolite samples over the course of crystallization, thus providing a method of tracking the morphology and elemental composition of precursors involved in the crystallization of various zeolite frameworks. One of the distinguishing aspects of zeolites is the incorporation of extra-framework ions (e.g., alkali metals) that balance negatively-charged Al sites, and often serve as inorganic structure-directing agents. The number of Al sites in zeolites is limited to a minimum Si/Al = 1, in accordance with Löwenstein's rule that states the generation of proximal Al sites (i.e., –Al–O–Al– bond formation) is forbidden.[452] Zeolite synthesis is usually performed in highly alkaline conditions which leads to a high concentration of cations in the amorphous precursors owing to their introduction as metal hydroxides (mineralizing agents) necessary for (alumino)silicate condensation.[11] During the course of crystallization, cations are expelled from the solid phase with the maximum number of counterions is approximately determined by the aluminum content in the framework (assuming defect-free materials). Based on the differences in the distribution and concentration of inorganic cations in precursors and crystals, we show that it is possible to visualize the disorder-to-order transitions that occur during zeolite synthesis. A clear disparity in alkali metal concentration between precursors and crystalline products allows for spatially resolving ordered and disordered domains, thereby enabling the temporal tracking of microstructure evolution. To test the limitations of elemental mapping, we investigated the temporal evolution of precursors and crystals for two extreme cases where the crystal size is either too small or chemical composition is relatively constant throughout crystallization. Collectively, our findings reveal that elemental mapping is a facile and highly

versatile approach to characterize the onset of nucleation, the presence of residual amorphous species, and the putative role of precursors in the growth of zeolite crystals.

## 6.2 Results and Discussion

The presence of bulk amorphous worm-like particles (WLPs) as precursors in zeolite synthesis mixtures has been investigated[206,224,453,454] for a range of frameworks including GIS, TON, MFI, CHA, and LTL; however, the role(s) of amorphous precursors in zeolite crystallization is still not fully resolved. There are two distinct hypotheses in literature regarding the role of WLPs in zeolite nucleation: (i) WLPs can dissolve to generate monomers or oligomers that serve as growth units for crystallization; and/or (ii) WLPs directly contribute to zeolite growth via pathways involving crystallization by particle attachment (or CPA).[190,231,360] Recent studies by Rimer[77,190,206] and others[431,453] have demonstrated that WLPs evolve during the induction period through a complex sequence of events involving aggregation, densification, and ripening. In this study, we employ FE-SEM-EDX elemental mapping to systematically examine the compositional evolution of precursors and crystals involved during the crystallization of five different zeolite framework types **(Figure 6.1)**. MER crystals have a broccoli-like morphology **(Figure 6.1A)** with an average diameter of 5 μm, while MFI crystals **(Figure 6.1B)** have a typical coffin-like morphology (ca. 6 μm).[356] MOR crystals **(Figure 6.1C)** have a large variance in both size and shape. TON crystals have a rod-like morphology **(Figure 6.1D)** with a distribution of sizes and average dimension (length) of 600 nm. LTL crystals exhibit a cylindrical morphology **(Figure 6.1E)** with relatively monodisperse sizes of *ca.* 3 μm in length. Aside from differences in crystal habit, the framework types also differ with respect to their composition (Si/Al ratio) and crystal structure (i.e. pore dimensions and pore sizes, which are denoted by the n-membered rings (MRs) constituting the pore aperture). The physicochemical properties of zeolites used in this study are: zeolite W (Si/Al = 2, 8-MR, 3D pores), ZSM-5 (Si/Al = 40, 10-MR, 3D pores), mordenite (Si/Al=10, 12-MR 1D pores), ZSM-22 (Si/Al = 35, 10-MR 1D pores), and zeolite L (Si/Al = 3, 12-MR 1D pores).

We monitored the compositional and structural evolution of precursors using a combination of FE-SEM-EDX and powder X-ray diffraction (XRD), respectively. For zeolite W (MER) crystallization, powder XRD patterns **(Figure E1)** indicate that induction period lasts approximately 4 h, while the formation of fully crystalline zeolite W was evident after 8 h of heating. SEM images of extracted solids during the first 8 h of heating reveal two distinct populations: amorphous WLPs and crystals **(Figure E2)**. Zeolite W crystals exhibit a broccoli-like morphology **(Figure E2)**, analogous to other crystals such as zeolite offretite (OFF), ZnO, and $Al_2O_3$, among other materials.[457-461]

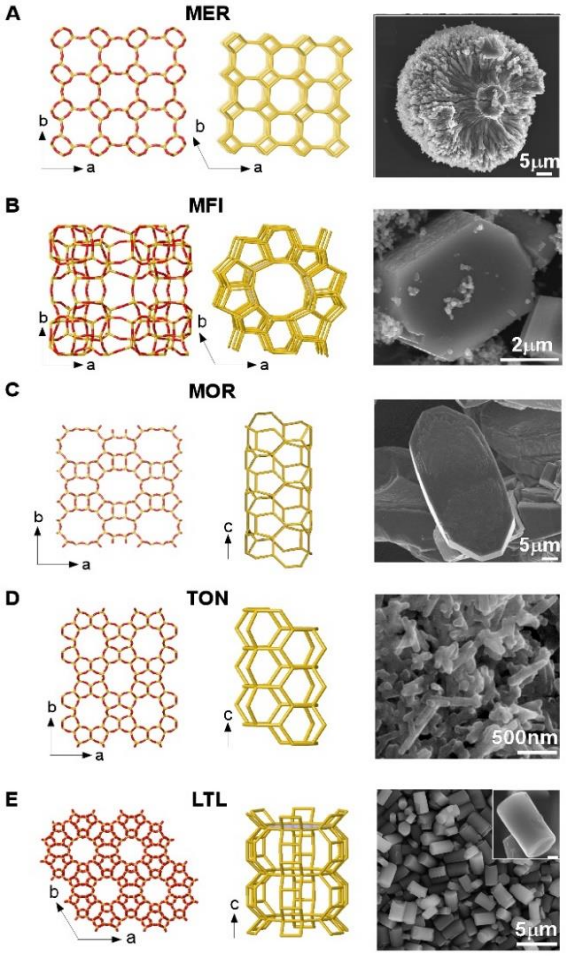


**Figure 6.1** Zeolite crystal structures (left) and representative scanning electron micrographs (right) of five different frameworks: **(A)** MER (zeolite W); **(B)** MFI (ZSM-5); **(C)** MOR (mordenite); **(D)** TON (ZSM-22); and **(E)** LTL (zeolite L). Inset of E: scale bar = 500 nm.

The evolution of composition (Si, Al, alkali) for amorphous WLPs and crystals was examined over a 12 h of heating period by *ex situ* FE-SEM-EDX **(Figure 6.2A-F)** spanning several stages of growth, including the induction period, intermediate times during zeolite W crystal formation (i.e., partially crystalline samples), and crystals at times when powder XRD patterns reveal a fully crystalline product. Interestingly, during the initial stages of crystallization the concentration of potassium in the amorphous precursors was significantly higher than the fully crystalline product (i.e., comparisons of **Figure 6.2D** and **2F**, respectively).

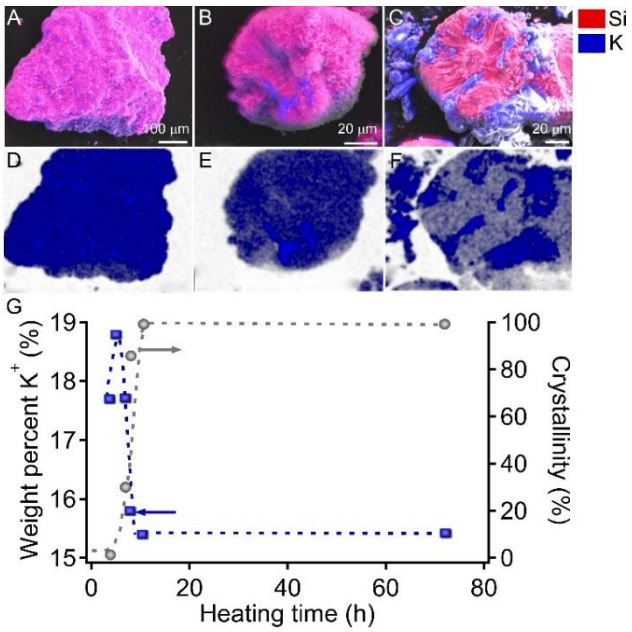


**Figure 6.2** FE-SEM-EDX images of solids extracted from the zeolite W synthesis after **(A)** 5, **(B)** 7, and **(C)** 12 h of heating. **(D-F)** Corresponding potassium mappings of each image. **(G)** Concentration of potassium in the extracted solid phase (squares, left y-axis) and its corresponding percent crystallinity (circles, right y-axis) as a function of heating.

Moreover, the potassium distribution is mostly homogeneous throughout the particles; however, when crystalline domains become evident in SEM images, elemental mapping clearly distinguishes these regions from the amorphous domains by virtue of differences in their potassium content (indicated as blue). This is apparent in samples after 7 h of heating **(Figure 6.2B and 2E)**, which shows a partially crystallized broccoli shaped particle in which the center has a higher potassium concentration, indicative of residual amorphous material. Conversely, crystals at the later

stages of crystallization **(Figure 6.2C and 2F)** where powder XRD seemingly indicates a fully crystalline sample **(Figure 6.2G)**, the excess potassium content is expelled from the crystalline structure and residual amorphous features surrounding the crystal (composed of higher potassium content) are observed. These findings can be attributed to the high concentrations of alkali metals typically employed in zeolite synthesis mixtures (commonly in the form of hydroxides), while the final product can only accommodate a limited amount of alkali metal ions depending on the ion exchange capacity of zeolite crystals (i.e., their total framework Al, which act as anionic sites for ion exchange). Thus, excess alkali ions are released from the solid phase into the liquid supernatant during zeolite crystallization. This was confirmed by elemental analysis of solids extracted from the synthesis mixture at various times **(Figure 6.2G)**, revealing an inverse relationship between the cation content in the solid with the crystallinity of the sample. Similar findings have been reported by other groups for zeolite A (LTA), faujasite (FAU), and UZM-9 (LTA).[204,205,219,421] For instance, Valtchev and coworkers showed that during zeolite A crystallization, excess sodium is expelled from the gel to the solution.[204,205] Lercher and coworkers reported a similar phenomenon using *in situ* $^{23}$Na NMR to verify that the concentration of $Na^+$ in the aqueous phase increases during faujasite crystallization.[421]

The applicability of elemental mapping as a technique for tracking amorphous-to-crystalline phases was further verified in the crystallization of ZSM-5 (MFI), which required the use of two structure-directing agents: tetrapropylammonium ($TPA^+$) and $K^+$. Elemental mapping images **(Figure 6.3A-F)** of solids extracted from ZSM-5 growth mixtures at periodic heating times reveal a distinct difference in the potassium content between amorphous and crystalline regions of the sample. Notably, samples extracted at intermediate times (i.e., partially crystalline samples in **Figure 6.3A,B**) exhibit two populations of particles: amorphous WLPs, which have substantially higher potassium content, and coffin-shaped crystals with fewer potassium ions. This is exemplified in **Figure 6.3B,E** where faceted crystals (potassium poor) are forming around an

amorphous (potassium-rich) center of ill-defined morphology. As such, the elemental mapping technique allows for the stages of crystallization to be tracked, and the phase purity of crystalline products to be assessed at later stages of syntheses. It also provides important morphological information and corresponding solid phases based on the emergence of different elemental compositions.

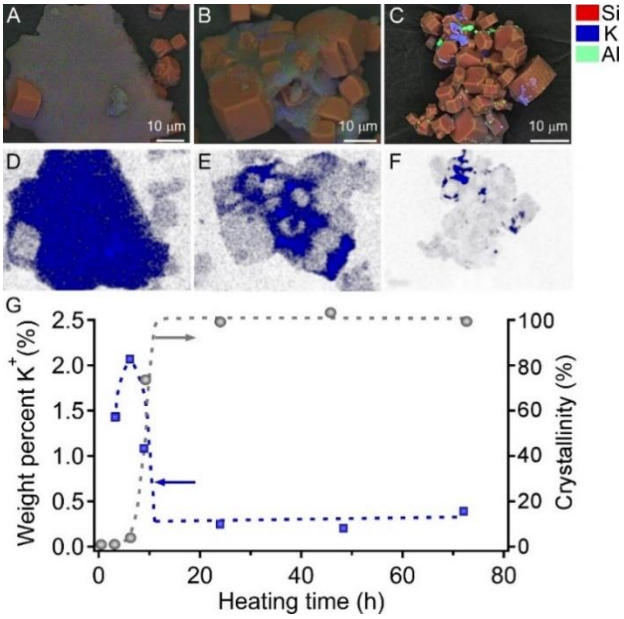


**Figure 6.3** Elemental mapping of solids extracted from a ZSM-5 synthesis after **(A)** 9, **(B)** 24, and **(C)** 48 h of heating. **(D – F)** Corresponding potassium mappings of each image. **(G)** Concentration of potassium (squares, left y-axis) in the extracted solid phase and percent crystallinity (circles, right y-axis).

In order to confirm that the compositional evolution of ZSM-5 precursors was representative of the entire sample, we performed ICP-OES analysis **(Figure 6.3G)** of solids extracted from growth mixtures at periodic heating times of ZSM-5 synthesis. We observed a slight increase in the content of potassium in crystals during the induction period (analogous to zeolite W, **Figure 6.2G**), whereas there is a significant decrease in the percentage of potassium in solids during ZSM-5 crystallization (consistent with elemental mapping images in **Figure 6.3A-F**). The high sensitivity of this technique allows for the onset of nucleation to be detected prior to the observation of Bragg peaks in powder XRD patterns. Likewise, elemental mapping identifies

residual amorphous material on zeolite products at stages where powder XRD patterns seemingly indicate a fully crystalline material **(Figure E3)**. Indeed, the presence of amorphous material less than ca. 5 wt% of the sample is generally undetectable by XRD. Therefore, the elemental mapping approach presented here is a unique and versatile tool to identify the crystallinity and phase purity of different zeolite structures.

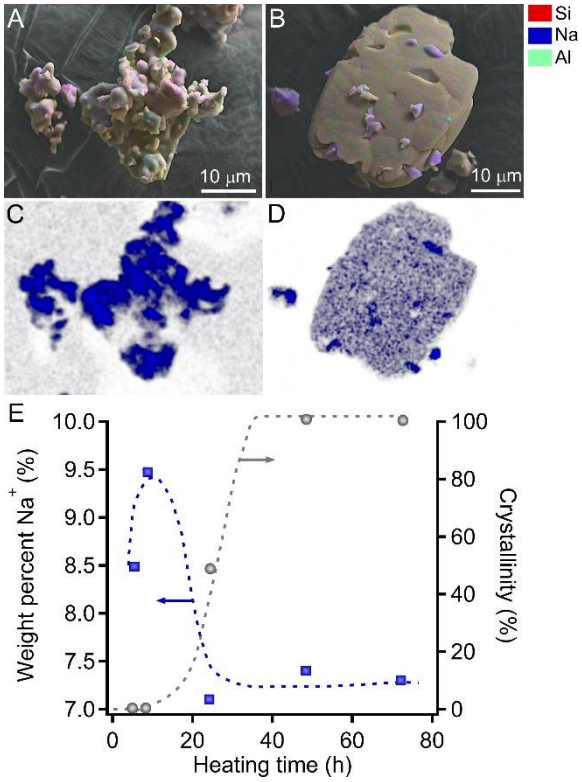


**Figure 6.4** Elemental mapping of solids extracted from a mordenite synthesis after **(A)** 8 and **(B)** 24 h of heating. **(C-D)** Corresponding sodium mappings of each image. **(E)** The sodium concentration in extracted solids (squares, left y-axis) and percent crystallinity (circles, right y-axis) as a function of heating.

To further exemplify the utility of elemental mapping, we examined a zeolite prepared with an alternative alkali metal as an inorganic structure-directing agent. To this end, we selected mordenite (MOR), which is conventionally synthesized by OSDA-free protocols, and performed a time-resolved study of solids extracted from the growth mixture during various stages of crystallization. FE-SEM-EDX elemental mapping of samples **(Figure 6.4A-D)** revealed a similar finding as zeolites W and ZSM-5. Solids extracted after 8 h of heating **(Figure 6.4A)** reveal

amorphous precursors resembling WLPs that are rich in sodium content **(Figure 6.4C)**. Samples extracted between 8 and 48 h are partially crystalline **(Figure E4)**, which is consistent with SEM and corresponding elemental mapping images showing that WLPs are progressively consumed as mordenite crystallizes. At intermediate times during mordenite growth (e.g., 24 h, **Figure 6.4B,D**), the disparate composition of sodium ions in amorphous precursors and crystals are clearly visible. In these elemental mapping images, the sodium-rich precursors are seemingly fused to the crystal, suggesting direct attachment of amorphous precursors as a viable pathway of mordenite crystallization. While tracking zeolite formation by elemental mapping cannot provide definitive evidence of growth pathways, an observation of crystallization by particle attachment would be consistent with our recent findings for SSZ-13[224] and zeolite L[206], which both grow via this nonclassical pathway.

The main experimental challenges associated with the use of FE-SEM-EDX elemental mapping are twofold: (i) the resolution does not allow amorphous and crystalline domains to be distinguished when particle sizes are smaller than 1 μm[455], and (ii) elemental mapping cannot provide the sufficient spatial resolution required to elucidate details of the crystallization mechanism when the alkali compositions of amorphous precursors and zeolite crystals are similar. To test the former scenario, we selected the synthesis of zeolite ZSM-22 (TON), which typically yields crystals smaller than 1 μm (see **Figure 6.1D**). Syntheses of ZSM-22 employ two different structure-directing agents: 1,8-diaminooctane (DAO) and K+. FE-SEM-EDX elemental mapping images of solids extracted at periodic times during ZSM-22 synthesis **(Figure 6.5A-F)** clearly show a change in color with prolonged hydrothermal treatment, indicating a shift from potassium-rich particles (associated with the amorphous phase) to crystals with less potassium content. The changes in potassium content were confirmed by ICP-OES analyses of extracted solids **(Figure 6.5G)**, revealing a profile that is identical to the previous three cases (i.e., there is a marked difference in the potassium content of precursors and crystals and an inverse relationship between

$K^+$ content and zeolite crystallinity). Despite the observed changes in elemental composition from time-resolved elemental mapping images, the small size of crystals makes it difficult to ascertain when nucleation begins as well as residual amorphous material in the final product.

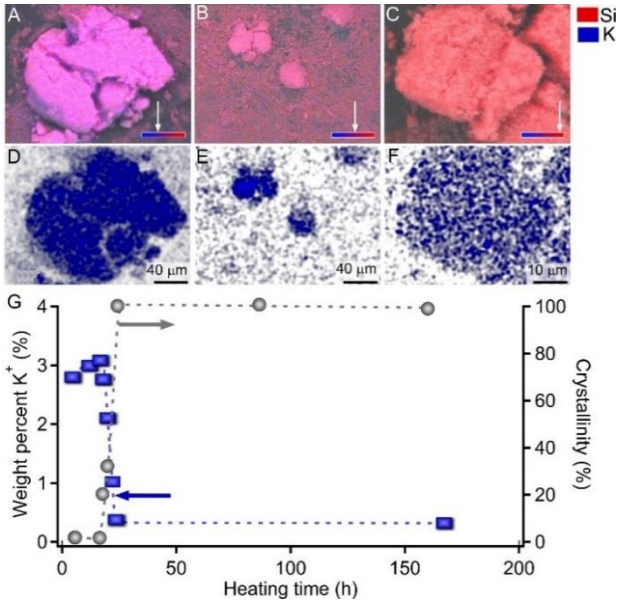


**Figure 6.5** Elemental mapping of solids extracted from a ZSM-22 synthesis after **(A)** 12, **(B)** 20, and **(C)** 168 h of heating. **(D – F)** Corresponding potassium mappings of each image. **(G)** Concentration of potassium in the extracted solid phase (squares, left y-axis) and percent crystallinity (circles, right y-axis as a function of synthesis time.

To test the second limitation of this technique, we obtained time-resolved FE-SEM-EDX elemental mapping images **(Figure 6.6A-D)** of solids extracted from a zeolite L synthesis mixture at periodic heating times. From SEM images, the presence of WLPs **(Figure 6.6A)** can be clearly differentiated from zeolite L crystals **(Figure 6.6B)** on the basis of their distinct morphologies, i.e., branched spheroidal structures versus faceted cylindrical particles, respectively. ICP-OES analysis of extracted solids **(Figure 6.6E)** reveal relatively little change in potassium content throughout various stages of crystallization. This profile is distinctly different than those of the other zeolites in this study, indicating an approximately constant level of $K^+$ concentration in both amorphous and crystalline phases of zeolite L. As such, elemental mapping cannot discern the induction period from any stage of crystallization, despite the fact that the crystal size (ca. 4 μm) is well above the

resolution limit of the technique. Thus, the amorphous precursors and crystals are indistinguishable in terms of alkali composition. One possible explanation for this unique observation is the low Si/Al ratio of zeolite L crystals (Si/Al = 3) relative to the other zeolites: ZSM-5 (Si/Al = 40), mordenite (Si/Al = 10), and ZSM-22 (Si/Al = 35). This indicates that the quantity of alkali metal ions ($Na^+$ or $K^+$) needed to compensate the negative charge of framework Al sites is much higher in zeolite L.

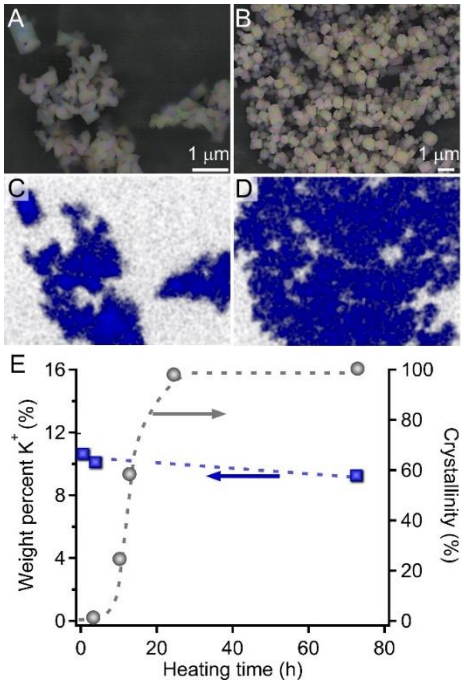


**Figure 6.6** Elemental mapping of solids extracted from a zeolite L synthesis after **(A,C)** 12 and **(B,D)** 72 h of hydrothermal treatment. **(E)** Concentration of potassium in the extracted solid phase (squares, left axis) and percent crystallinity (circles, right y-axis) as a function of heating.

Consequently, the charge density change in the solids as zeolite L transitions from amorphous WLPs to the crystalline product is less significant – a finding that is qualitatively consistent with Hong and coworkers[456] who reported for zeolites UZM-5 and UZM-9 crystallization that the Si/Al ratio of final product has a substantial impact on the observed charge density variations among extracted solids.

The three general scenarios exemplified in this study are illustrated in **Figure 6.7** to show conditions where elemental mapping is effective **(Figure 6.7A)** and those where resolution

challenges limits its applicability **(Figure 6.7B,C)**. In many cases, elemental mapping provides a unique tool to understand the mechanism(s) of zeolite crystallization using alkali metal segregation as a tracker to distinguish amorphous precursors and zeolite crystals, combined with the observation of local morphological changes. This is true when zeolite syntheses yield large crystal size (>1 μm) and there is a significant difference in alkali metal content between amorphous precursors and crystals **(Figure 6.7A)**.

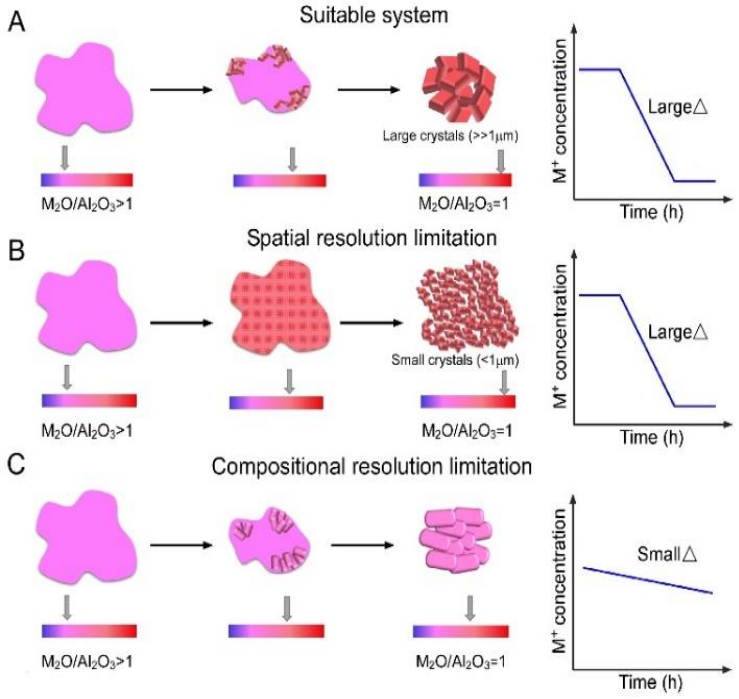


**Figure 6.7** Idealized schematic of alkali metal segregation pathways during the crystallization of different zeolite frameworks investigated in this study: **(A)** Suitable system (e.g., MFI, MOR, and MER); **(B)** Spatial resolution limitation (e.g., TON); and **(C)** Composition resolution limitation (e.g., LTL).

Examples were provided for three framework types (MER, MFI, and MOR) that meet these criteria, wherein it was demonstrated that elemental mapping is an ideal tool to elucidate stages of zeolite crystallization, the putative role of amorphous precursors, and the presence of residual amorphous material **(Figure 6.7A)**. For cases where zeolite syntheses yield small crystal sizes (e.g., TON), an appreciable difference in the alkali metal content of amorphous precursor and crystals allows for overall changes in percent crystallinity to be tracked **(Figure 6.7B)**; however, individual

crystals cannot be differentiated from precursors due to resolution limitations, which renders elemental mapping a complementary technique to XRD for tracking the progression of zeolite synthesis. The final scenario presented in this study is the case where minor differences in the alkali metal ion content in the amorphous precursors and crystalline product **(Figure 6.7C)** make it impossible to extract detailed information about the crystallization mechanism (e.g., LTL) by elemental mapping. FE-SEM-EDX provides at the same time information about the changes in the morphology and the elemental composition of the sample. Therefore, the system under study must fulfil these two criteria: changes in morphology that can be detected/observed by FE-SEM and large changes in composition to be followed by EDX.

## 6.3 Conclusions

In summary, we have demonstrated that elemental mapping can be a powerful technique to characterize the morphological and compositional transformations in zeolite synthesis, provided the crystalline product is of sufficient size and there are relatively large gradients in elemental composition of solids during the course of crystallization. In general, the use of ex situ techniques, such as electron microscopy, for resolving stages of crystallization is non-trivial for materials that grow via nonclassical pathways owing to the dual presence of amorphous and crystalline phases. These disparate phases can sometimes be distinguished on the basis of morphology, but such differences become convoluted when the crystals are not distinctly faceted, the product size distribution is polydisperse, and/or the unreacted amorphous material is broadly distributed on crystal surfaces. Likewise, techniques such as bulk powder XRD lack the sensitivity to detect the onset of crystallization, as well as the presence of small quantities of residual amorphous material and/or impurities in the product. To this end, the FE-SEM-EDX technique presented in this study is an effective alternative for tracking time-resolved evolution of zeolite syntheses and provides local information.

The zeolites selected for this study span the breadth of physicochemical properties that demonstrate the limits of the technique. For zeolites with sufficiently large crystal sizes (> 1 μm) and large differences in alkali metal content between amorphous and crystalline states, this technique has proven useful in its ability to characterize the compositional and morphological transitions related to the crystallization of zeolites. The majority of materials analyzed in this study that satisfy these criteria (e.g., MFI, MER, and MOR) were prepared with growth conditions spanning a range of Si/Al ratios, which are representative of numerous framework types. When crystal sizes are too small and/or alkali metal content is approximately constant throughout the course of crystallization, the technique is unable to resolve various stages of crystal growth. The fact that zeolites tend to exhibit large crystal sizes indicates that the limiting criterion for elemental mapping is predominantly governed by the alkali content of the initial amorphous precursors. Given that zeolites and numerous other crystalline materials grow by nonclassical pathways, the facile and effective method of generating elemental maps is potentially applicable to other frameworks types as a platform to understand the intricate mechanism(s) of complex crystallization pathways.

## 6.4 Material and Methods

### 6.4.1 Materials

The following chemicals were purchased from Sigma-Aldrich (St. Louis, MO): LUDOX AS-30 (30 wt % suspension in water), LUDOX AS-40 (40 wt % suspension in water), Ludox SM-30 (30 wt % suspension in water), silica gel (91%), sodium hydroxide (98% pellets), potassium hydroxide (85% pellets), aluminum sulfate hydrate (98%, 14-18 $H_2O$, calculated as 18 $H_2O$), tetrapropylammonium bromide (TPABr, 98%), and 1,8 diaminooctane (98%). Fumed silica was purchased from Spectrum (Cab-O-Sil M-5 Scintillation Grade). Deionized (DI) water used in all experiments was purified with an Aqua Solutions RODI-C-12A purification system (18.2 MΩ). All reagents were used as received without further purification.

### 6.4.2 Crystallization of Zeolites

**ZSM-5**: ZSM-5 crystals were synthesized from a growth mixture with a molar composition of 2 TPABr: 11.9 $K_2O$: 1 $Al_2O_3$: 90 $SiO_2$: 3588 $H_2O$.[141] Aqueous solutions of potassium hydroxide (0.33 g in 1.44 g of DI water) and aluminum sulfate (0.14 g in 1.44 g of DI water) were mixed with 5.76 g of water, and LUDOX AS-30 solution (3.76 g in 2.13 g of DI water) was added under vigorous stirring. The resulting mixture was stirred for ca. 21 h at room temperature (referred to as aging). After aging, the OSDA (0.1515 g TPABr) was added and the solution was left to stir for another 2 h at room temperature. The growth mixture (ca. 10 g) was then placed in a Teflon lined stainless steel acid digestion bomb (Parr Instruments) and was heated under rotation (30 rpm) and autogenous pressure in a Thermo Fisher Precision Premium 3050 Series gravity oven. The nominal time and temperature for ZSM-5 synthesis was 3 days at 160 °C.

**Zeolite W:** Zeolite W (MER) crystals were synthesized in the absence of an OSDA using $K^+$ as an inorganic structure-directing agent. Growth solutions were prepared with a molar composition of 20.4 $K_2O$: 1 $Al_2O_3$: 10 $SiO_2$: 2060 $H_2O$. Potassium hydroxide (0.67 g, 10 $x10^{-3}$ mol) was first dissolved in water (8.79 g), followed by the addition of aluminum sulfate (0.17 g, 4.73 $x10^{-4}$ mol). This solution was stirred until clear (ca. 5 min). The silica source LUDOX AS-40 (0.37 g, 2.47 $x10^{-3}$ mol) was added dropwise while stirring, and the resulting mixture was left to stir overnight (ca. 21 h) at room temperature. After aging was complete, the growth solution (ca. 10 g) was placed in a Teflon-lined stainless steel acid digestion bomb and was heated under static conditions (i.e., without rotation) in an oven at 180 °C.

**Zeolite L:** Zeolite L crystals were synthesized in the absence of an organic using $K^+$ as an inorganic structure-directing agent. Growth solutions were prepared with a molar ratio of 0.5 $Al_2O_3$: 20 $SiO_2$: 10.2 $K_2O$: 1030 $H_2O$.[206] Potassium hydroxide (0.64g, 9.66 $x10^{-3}$ mol) was first dissolved in water (7.78g), followed by the addition of aluminum sulfate (0.17g, 4.73 $x10^{-4}$ mol). This solution was stirred until clear (ca. 5 min). The silica source was added, and the resulting solution

was left to stir overnight (ca. 21 h) at room temperature. The growth solution was prepared with Ludox AS-40 (1.42g, 9.47 x$10^{-3}$ mol). The colloidal silica source was added to the growth solution dropwise while stirring. After aging was complete, the growth solution (ca. 10g) was placed in a Teflon lined stainless steel acid digestion bomb (Parr Instruments) and was heated under static conditions (i.e., without mixing) in a Thermo- Fisher Precision Premium 3050 Series gravity oven at 180 °C and autogenous pressure.

**Mordenite:** Mordenite (MOR) was synthesized using a growth solution with a molar composition of 5 $Na_2O$ : 1 $Al_2O_3$ : 30 $SiO_2$ : 780 $H_2O$.[357] Sodium hydroxide (0.25 g, 6.1 x $10^{-3}$ mol) was first dissolved in DI water (8.44 g, 0.47 mol), followed by the addition of sodium aluminate (0.10 g, 6.1 x $10^{-4}$ mol). The solution was stirred until it was clear (ca. 15 min), followed by the addition of silica gel (1.21 g, 0.018 mol), and the resulting mixture was stirred at room temperature for 24 h. Approximately 10 g of the growth mixture was placed in a Teflon-lined stainless steel acid digestion bomb and was heated under static conditions at a nominal temperature of 170 °C.

**ZSM-22:** ZSM-22 (TON) crystals were synthesized using 1,8-diaminooctane (DAO) as an OSDA. Aqueous solutions of aluminum sulfate (solution A) and DAO (solution B) were prepared separately in 20 mL beakers. Solution A was prepared by dissolving 0.099 g of aluminum sulfate hydrate in 1.00 g of DI water while stirring. Solution B was prepared by dissolving 0.59 g of DAO in 3.06 g of DI water while stirring. The synthesis mixture was then prepared by first placing KOH (3.63 g) in a polypropylene bottle, followed by a slow addition of solution A, and then solution B, with continuous stirring. To the resulting mixture, LUDOX AS-30 (2.62 g) was added dropwise under continuous stirring to produce a final synthesis mixture with a molar composition of 27.3 DAO: 11.9 $K_2O$: 1 $Al_2O_3$: 90 $SiO_2$: 3588 $H_2O$.[369] The mixture was aged at room temperature for 21 h with stirring, and was transferred to a 23 mL Teflon-lined stainless steel acid digestion bomb. The sealed autoclave was heated in an oven under rotation (30 rpm) at 160 °C.

The pH of the growth solutions was measured with a Thermo Scientific Orion 3 Star meter. For X-ray and microscopy analyses, the particulates in the growth mixture (amorphous and/or crystalline) were isolated as a white powder by centrifugation (Beckman Coulter Avanti® J-E series high-speed centrifuge) at 13,000 rpm for 45 min. The solid was washed with DI water to remove the supernatant and the centrifuge/washing step was repeated a second time. The resulting solid was dried at ambient conditions. During the preparation of microscopy samples, the solid was dispersed in DI water and an aliquot of the suspension was placed on a glass slide and dried overnight. Crystals on the glass slide were transferred to SEM sample holders (Ted Pella) by gently pressing the glass slide on the carbon tape.

### 6.4.3 Materials Characterization

Scanning electron microscopy (SEM) was performed with a FEI 235 Dual-Beam (Focused Ion-beam) system operated at 15 kV and a 5-mm working distance. All SEM samples were coated with a thin layer of carbon (ca. 30 nm) prior to imaging to minimize charging. Basic elemental analysis was done with Scanning Electron Microscopy – Energy Dispersive X-ray Spectroscopy (SEM-EDX) analysis using a JEOL SM-31010/METEK EDAX system at 15 kV and 15 mm working distance. Detailed elemental mapping experiments of sources and precursors were carried out in a field emission scanning electron microscope (FE-SEM) Merlin VP Compact from Zeiss, equipped with an EDX microanalysis system Quantax 400 from Bruker, at 10 kV and 7.4 mm working distance. The powder samples were placed on a SEM stub mount and coated with a thin layer of carbon before analysis. For every sample, 5 cycles of acquisition per image were taken using and acquisition time of 128 or 64 μs/line. Once obtaining the individual elemental mapping images of the different elements present on the synthetic gel, comprised of Si, Al and $M^+$ ($K^+$ or $Na^+$), they were combined proportionally to their content in the mixture (obtained by EDX at the same time). The combination of the individual images was carried out using the Esprit 1.9 software

from Bruker (in advanced mode). Finally, in order to better visualize the elemental mapping of the cations, the black background of the images was removed by Adobe Photoshop; and when necessary, the threshold was also adjusted for minimizing background noise.

# Chapter 7

## Summary and Future Outlook

There have been significant advancements in the design and implementation of zeolite catalysts over the past decades. The advantages of zeolites are due to their unique properties such as high (hydro)thermal stability, exceptional pore architecture, diverse active sites, and tunable acid strength which have led to their application in numerous industrial processes as catalysts for a wide variety of reactions. Despite these breakthroughs, only a limited fraction of zeolites is currently employed for commercial applications amongst the 248 synthetically realized zeolites. The challenges associated with the industrial implementation of zeolites are twofold: identifying facile and inexpensive methods to tailor the physicochemical properties of zeolite catalysts for desired applications and lack of fundamental understanding regarding the growth mechanism(s) of zeolites which is critical for the development of streamlined routes to optimize the properties of zeolites. This dissertation focusses on practical approaches to tune the physicochemical properties of zeolites such as size, morphology, aluminum distribution, and pore architecture of two commercial zeolites (MFI and FAU), through the use of inexpensive and versatile methods that include surfactants and seeds. Aside from tailoring the physicochemical properties, we present novel techniques such as AFM and FE-SEM-EDX elemental mapping as a platform to broaden our knowledge of the mechanism(s) involved in the generation of intracrystalline mesoporosity and crystallization in general.

In Chapter 2, we examined the effects of dual structure-directing agents using CTA and TPA as organic SDAs in combination with a variety of alkali metals as inorganic SDAs to tailor the physicochemical properties of ZSM-5 crystals. ZSM-5 is used as a catalyst and sorbent in a wide range of industrial applications. One of the challenges with ZSM-5 synthesis is to identify new and inexpensive organic SDAs that can tailor the physicochemical properties of the final

product. The most frequently used SDA in ZSM-5 synthesis is TPA; however, recent studies have shown that the surfactant CTA can be used as an alternative SDA. Our findings reveal that the selection of SDA combinations has a significant impact on the kinetics of ZSM-5 crystallization, as well as the properties of the resulting crystals. Notably, we show that TPA/Na and CTA/K are optimal combinations of SDAs that can markedly alter the size, morphology, and aluminum distribution in ZSM-5. Using a combination of experiments and molecular modeling, we explore the use of CTA as an alternative organic SDA for zeolite MFI and show that we can achieve smaller crystals (ca. 600 nm) in similar time (<24 h) as syntheses employing TPA. Given the relatively low cost of CTA and its high market availability compared to other organic SDAs, these findings have the potential to impact commercial production of ZSM-5 for a variety of applications.

In Chapter 3, we extended our studies to another commercial zeolite USY (FAU type) to show that post synthesis treatment of zeolites with surfactants is an effective and versatile technique to impart intracrystalline well-defined mesoporosity in these materials. We monitored the dynamics of surface reconstruction that occurs during the treatment of USY zeolite by surfactant-templating using in situ AFM. The development of surfactant-templated mesoporosity and the concurrent healing of defects that are characteristic of steamed zeolites occur in less than 1 h at room temperature, which emphasizes the low energy barriers needed to reorganize the crystalline structure of this zeolite. This transformation was also followed by X-ray diffraction, $N_2$ adsorption, and transmission electron microscopy analysis of ultramicrotomed samples to confirm that the rapid formation of surfactant-templated mesoporosity and the reconstruction of the zeolite crystals occur not only on the surface of the zeolite but also homogeneously throughout the whole zeolite. This process involves a significant and rapid breaking and re-formation of bonds; however, the zeolite does not dissolve during this process as solid recovery at any given time of the treatment is approximately 100% and the concentration of soluble Si or Al species in the liquid is negligible. Future initiatives in this area will likely employ natural surfactants and/or biopolymers owing to

their low cost and facile recovery as one of the potential candidates to impart tailored mesoporosity in zeolites.

Although surfactants offer significant advantages to tailor the properties of zeolites for a wide variety of applications, the commercialization of this approach is still in an early stage since they are irrecoverable due to postsynthesis calcination. An alternative method is seed-assisted zeolite growth, which is a facile route to reduce (or eliminate) organics in zeolite synthesis. Seeding also reduces the crystallization time and can alter the physicochemical properties of the final product; however, the exact mechanism of seed-assisted zeolite crystallization remains elusive. In Chapter 4, we present a unique approach to synthesize hierarchical ZSM-5 with intergrown nanosheets using a seed-assisted route in organic-free media. To the best of our knowledge, this is the first example of such a complex morphology for a MFI-type zeolite synthesized in the absence of mesoporogens and OSDAs. Our findings reveal nonclassical pathways of crystallization involving the nucleation of crystals at the exterior surface of amorphous precursor particles. Interestingly, the preparation of hierarchical ZSM-5 crystals is seemingly connected with the ability of MEL fragments (employed as seeds) to effectively bridge MFI nanosheets, thereby directing the organization of intergrown nanosheets with complex hierarchical architecture. Thus, it is possible that controlling these intergrowths can lead to new pathways for synthesizing these hierarchical structures without using organics.

To this end, machine learning will prove to be an essential tool to predict the possible intergrowth pairs and guide the selection of seeds to generate hierarchical structures. Future studies could draw upon the existing database of most commonly observed intergrowths reported by Gomez-Bombarelli and coworkers that include: MEL/MFI, FAU/EMT, AFX/CHA, and GME/CHA, among others. The organic-free synthesis of hierarchical zeolites opens exciting prospects for both fundamental studies and large-scale applications. We expect seed assisted synthesis may prove to be broadly applicable to other zeolite frameworks and related crystalline

porous materials. This new approach has the potential to be a paradigm shift in the design and possible commercial development of hierarchical zeolites.

One of the challenges in zeolite synthesis is the ability to predict and control crystal properties such as size, morphology, structure, and chemical composition. The control of any single property, let alone multiple simultaneously, can be a daunting task without sufficient knowledge of the pathways leading to materials formation and how these processes can be selectively manipulated to achieve a desired product. In this regard, the assembly and structural evolution of amorphous precursors during zeolite crystallization is an important area of interest owing to their putative roles in the nucleation and growth of aluminosilicate microporous materials. Precursors range in complexity from oligomeric molecules and colloidal particles to gels comprised of heterogeneous silica and alumina domains. The physical state of precursors in most zeolite syntheses is generally not well understood. In Chapter 5, we discussed the wide variety of precursors encountered in the synthesis of various framework types, emphasizing their complex physical states and the thermodynamic and kinetic factors that govern their heterogeneity. Our findings reveal that the majority of the zeolite synthesis mixtures are prepared in such a manner that does not lead to the formation of gels owing to the incomplete dissolution of silicon source. Notably, our findings also offer insights into the assembly of amorphous precursors, wherein we show that there is a monotonic increase in precursor size, followed by a plateau that coincides with the completion of the induction period.

Elucidating the assembly, microstructure, and mechanism(s) by which precursors are involved in processes of nucleation and growth is often non-trivial owing to the lack of available techniques that are capable of monitoring amorphous-to-crystal transformations with sufficient spatiotemporal resolution. In Chapter 6, we proposed an elemental mapping method employing FE-SEM-EDX as a versatile tool to characterize morphological and compositional properties of precursors during the crystallization of five zeolites (MER, MFI, MOR, TON, and LTL) that are

used in commercial applications that include (but are not limited to) catalysis, ion-exchange, separations, drug delivery, and adsorption. Time-resolved ex situ elemental mapping images of extracted solids during several stages of zeolite crystallization reveal that a sufficient disparity in the chemical composition (e.g., alkali metal content) between amorphous precursors and crystals can be exploited for: (i) tracking the early stages of zeolite crystallization, (ii) locating where it happens and (iii) resolving residual amorphous material among crystalline domains. Our findings reveal that FE-SEM-EDX elemental mapping is a highly sensitive technique to detect the onset of nucleation, the completion of crystallization, and the existence of impurities. Given the ubiquitous presence of amorphous precursors during nonclassical crystallization, we expect that elemental mapping may prove valuable for understanding and tracking the growth of other zeolites and minerals. Although we demonstrated that FE-SEM-EDX elemental mapping is a powerful technique to characterize the morphological and compositional transformations in zeolite synthesis; however, there are two major experimental challenges associated with the use of FE-SEM-EDX elemental mapping: (i) the resolution does not allow amorphous and crystalline domains to be distinguished when particle sizes are smaller than 1 μm, and (ii) ex situ nature of the technique limits mechanistic insights regarding the role of amorphous precursors in zeolite crystallization. Thus, future studies will likely expand the elemental mapping technique to include TEM that will enable the analysis of much smaller crystals (< 100 nm). This will allow the technique to be broadened to include many more framework types synthesized by a variety of alkali metals. In addition, the advent of in situ SEM and TEM techniques may allow for in situ elemental analysis in the near future.

# References


1 Davis, M. E. & Lobo, R. F. Zeolite and molecular sieve synthesis. *Chemistry of Materials* **4**, 756-768, doi:10.1021/cm00022a005 (1992).

2 Weckhuysen, B. M. & Yu, J. Recent advances in zeolite chemistry and catalysis. *Chemical Society Reviews* **44**, 7022-7024 (2015).

3 Flanigen, E. M. in *Studies in surface science and catalysis* Vol. 58 13-34 (Elsevier, 1991).

4 Barrer, R. M. 435. Syntheses and reactions of mordenite. *Journal of the Chemical Society (Resumed)*, 2158-2163, doi:10.1039/jr9480002158 (1948).

5 Jacobs, P., Flanigen, E. M., Jansen, J. & van Bekkum, H. *Introduction to zeolite science and practice*. (Elsevier, 2001).

6 Rabo, J. A. & Schoonover, M. W. Early discoveries in zeolite chemistry and catalysis at Union Carbide, and follow-up in industrial catalysis. *Applied Catalysis A: General* **222**, 261-275 (2001).

7 Snyder, M. A. & Tsapatsis, M. Hierarchical nanomanufacturing: from shaped zeolite nanoparticles to high-performance separation membranes. *Angewandte Chemie International Edition* **46**, 7560-7573 (2007).

8 Showell, M. S. in *Powdered detergents* 1-19 (Routledge, 2017).

9 Degnan, T. F. Applications of zeolites in petroleum refining. *Topics in Catalysis* **13**, 349-356 (2000).

10 Primo, A. & Garcia, H. Zeolites as catalysts in oil refining. *Chemical Society Reviews* **43**, 7548-7561, doi:10.1039/c3cs60394f (2014).

11 Auerbach, S. M., Carrado, K. A. & Dutta, P. K. *Handbook of zeolite science and technology*. (CRC press, 2003).

12 Jiang, J., Yun, Y., Zou, X., Jorda, J. L. & Corma, A. ITQ-54: a multi-dimensional extra-large pore zeolite with 20× 14× 12-ring channels. *Chemical Science* **6**, 480-485 (2015).

13 Schwalbe-Koda, D., Jensen, Z., Olivetti, E. & Gómez-Bombarelli, R. Graph similarity drives zeolite diffusionless transformations and intergrowth. *Nature Materials* **18**, 1177-1181 (2019).

14 Itabashi, K., Kamimura, Y., Iyoki, K., Shimojima, A. & Okubo, T. A working hypothesis for broadening framework types of zeolites in seed-assisted synthesis without organic structure-directing agent. *Journal of the American Chemical Society* **134**, 11542-11549, doi:10.1021/ja3022335 (2012).

15 Millini, R., Zou, X., Strohmaier, K., Schwieger, W., Eliasova, P., Morris, R. E., Weckhuysen, B., Zhou, W., Abdo, S. & Martinez, A. *Zeolites in catalysis: properties and applications*. (Royal Society of Chemistry, 2017).

16 Mishra, M. & Jain, S. K. Properties and applications of zeolites: A Review. *Proceedings of the National Academy of Sciences India Section B-Biological Sciences* **81**, 250-259 (2011).

17 Jiang, J., Yu, J. & Corma, A. Extra-Large-Pore Zeolites: Bridging the Gap between Micro and Mesoporous Structures. *Angewandte Chemie International Edition* **49**, 3120-3145, doi:10.1002/anie.200904016 (2010).

18 Chen, N. & Garwood, W. Some catalytic properties of ZSM-5, a new shape-selective zeolite. *J. Catal.;(United States)* **52** (1978).

19 Kaeding, W., Chu, C., Young, L., Weinstein, B. & Butter, S. Selective alkylation of toluene with methanol to produce para-xylene. *Journal of Catalysis* **67**, 159-174 (1981).

20 Tsai, T.-C., Liu, S.-B. & Wang, I. Disproportionation and transalkylation of alkylbenzenes over zeolite catalysts. *Applied Catalysis A: General* **181**, 355-398 (1999).

21 Di Iorio, J. R. & Gounder, R. Controlling the Isolation and Pairing of Aluminum in Chabazite Zeolites Using Mixtures of Organic and Inorganic Structure-Directing Agents. *Chemistry of Materials* **28**, 2236-2247, doi:10.1021/acs.chemmater.6b00181 (2016).

22 Knott, B. C., Nimlos, C. T., Robichaud, D. J., Nimlos, M. R., Kim, S. & Gounder, R. Consideration of the Aluminum Distribution in Zeolites in Theoretical and Experimental Catalysis Research. *ACS Catalysis* **8**, 770-784, doi:10.1021/acscatal.7b03676 (2018).

23 Li, S., Gounder, R., Debellis, A., Müller, I. B., Prasad, S., Moini, A. & Schneider, W. F. Influence of the N, N, N-Trimethyl-1-adamantyl Ammonium Structure-Directing Agent on Al Substitution in SSZ-13 Zeolite. *Journal of Physical Chemistry C* **123**, 17454-17458, doi:10.1021/acs.jpcc.9b05334 (2019).

24 Parrillo, D., Lee, C., Gorte, R., White, D. & Farneth, W. Comparison of the acidic properties of H-[Al] ZSM-5, H-[Fe] ZSM-5, and H-[Ga] ZSM-5 using microcalorimetry, hexane cracking, and propene oligomerization. *The Journal of Physical Chemistry* **99**, 8745-8749 (1995).

25 Vargas, N. G., Stevenson, S. & Shantz, D. F. Simultaneous isomorphous incorporation of boron and germanium in MFI zeolites. *Microporous and Mesoporous Materials* **170**, 131-140 (2013).

26 Mole, T., Anderson, J. & Creer, G. The reaction of propane over ZSM-5-H and ZSM-5-Zn zeolite catalysts. *Applied Catalysis* **17**, 141-154 (1985).

27 Hsieh, M. F., Zhou, Y., Thirumalai, H., Grabow, L. C. & Rimer, J. D. Silver-Promoted Dehydroaromatization of Ethylene over ZSM-5 Catalysts. *ChemCatChem* **9**, 1675-1682 (2017).

28 Paolucci, C., Parekh, A. A., Khurana, I., Di Iorio, J. R., Li, H., Albarracin Caballero, J. D., Shih, A. J., Anggara, T., Delgass, W. N., Miller, J. T., Ribeiro, F. H., Gounder, R. & Schneider, W. F. Catalysis in a Cage: Condition-Dependent Speciation and Dynamics of Exchanged Cu Cations in SSZ-13 Zeolites. *Journal of the American Chemical Society* **138**, 6028-6048, doi:10.1021/jacs.6b02651 (2016).

29 Bailleul, S., Yarulina, I., Hoffman, A. E., Dokania, A., Abou-Hamad, E., Chowdhury, A. D., Pieters, G., Hajek, J., De Wispelaere, K. & Waroquier, M. A supramolecular view on

the cooperative role of Brønsted and Lewis acid sites in zeolites for methanol conversion. *Journal of the American Chemical Society* **141**, 14823-14842 (2019).

30 Vermeiren, W. & Gilson, J.-P. Impact of zeolites on the petroleum and petrochemical industry. *Topics in Catalysis* **52**, 1131-1161 (2009).

31 Vogt, E. & Weckhuysen, B. Fluid catalytic cracking: recent developments on the grand old lady of zeolite catalysis. *Chemical Society Reviews* **44**, 7342-7370 (2015).

32 Degnan, T., Chitnis, G. & Schipper, P. H. History of ZSM-5 fluid catalytic cracking additive development at Mobil. *Microporous and Mesoporous Materials* **35**, 245-252 (2000).

33 de Jong, K. P., Zečević, J., Friedrich, H., de Jongh, P. E., Bulut, M., Van Donk, S., Kenmogne, R., Finiels, A., Hulea, V. & Fajula, F. Zeolite Y crystals with trimodal porosity as ideal hydrocracking catalysts. *Angewandte Chemie International Edition* **49**, 10074-10078 (2010).

34 Maxwell, I. Zeolite catalysis in hydroprocessing technology. *Catalysis Today* **1**, 385-413 (1987).

35 Li, Y., Li, L. & Yu, J. Applications of zeolites in sustainable chemistry. *Chem* **3**, 928-949 (2017).

36 Kubička, D. & Kikhtyanin, O. Opportunities for zeolites in biomass upgrading—Lessons from the refining and petrochemical industry. *Catalysis Today* **243**, 10-22 (2015).

37 Luo, H. Y., Lewis, J. D. & Román-Leshkov, Y. Lewis acid zeolites for biomass conversion: Perspectives and challenges on reactivity, synthesis, and stability. *Annual Review of Chemical and Biomolecular Engineering* **7**, 663-692 (2016).

38 Perego, C., Bosetti, A., Ricci, M. & Millini, R. Zeolite materials for biomass conversion to biofuel. *Energy & Fuels* **31**, 7721-7733 (2017).

39 Beale, A. M., Gao, F., Lezcano-Gonzalez, I., Peden, C. H. & Szanyi, J. Recent advances in automotive catalysis for NO x emission control by small-pore microporous materials. *Chemical Society Reviews* **44**, 7371-7405 (2015).

40 Zones, S. I. (Google Patents, 1985).

41 Taarning, E., Osmundsen, C. M., Yang, X., Voss, B., Andersen, S. I., Christensen, C. H. J. E. & Science, E. Zeolite-catalyzed biomass conversion to fuels and chemicals. **4**, 793-804 (2011).

42 Bjorgen, M., Svelle, S., Joensen, F., Nerlov, J., Kolboe, S., Bonino, F., Palumbo, L., Bordiga, S. & Olsbye, U. Conversion of methanol to hydrocarbons over zeolite H-ZSM-5: On the origin of the olefinic species. *Journal of Catalysis* **249**, 195-207, doi:10.1016/j.jcat.2007.04.006 (2007).

43 Teketel, S., Skistad, W., Benard, S., Olsbye, U., Lillerud, K. P., Beato, P. & Svelle, S. Shape selectivity in the conversion of methanol to hydrocarbons: the catalytic performance of one-dimensional 10-ring zeolites: ZSM-22, ZSM-23, ZSM-48, and EU-1. *ACS Catalysis* **2**, 26-37 (2012).

44 Olsbye, U., Svelle, S., Bjørgen, M., Beato, P., Janssens, T. V., Joensen, F., Bordiga, S. & Lillerud, K. P. Conversion of methanol to hydrocarbons: how zeolite cavity and pore size controls product selectivity. *Angewandte Chemie International Edition* **51**, 5810-5831 (2012).

45 Yarulina, I., Chowdhury, A. D., Meirer, F., Weckhuysen, B. M. & Gascon, J. Recent trends and fundamental insights in the methanol-to-hydrocarbons process. *Nature Catalysis* **1**, 398-411 (2018).

46 Lin, S., Shi, L. & Yu, T. Comparative Study of Acidic Properties of UZM-5 Nanosheets by Stepwise Adsorption Assisted by a Selective External Poisoning Approach. *The Journal of Physical Chemistry C* **119**, 1008-1015 (2015).

47 Rimer, J. D., Chawla, A. & Le, T. T. Crystal Engineering for Catalysis. *Annual Review of Chemical and Biomolecular Engineering* **9**, 283-309, doi:10.1146/annurev-chembioeng-060817-083953 (2018).

48 Caro, J. & Noack, M. Zeolite membranes–recent developments and progress. *Microporous and Mesoporous Materials* **115**, 215-233 (2008).

49 Rangnekar, N., Mittal, N., Elyassi, B., Caro, J. & Tsapatsis, M. Zeolite membranes–a review and comparison with MOFs. *Chemical Society Reviews* **44**, 7128-7154 (2015).

50 Li, Y. & Yang, W. Molecular sieve membranes: From 3D zeolites to 2D MOFs. *Chinese Journal of Catalysis* **36**, 692-697, doi:https://doi.org/10.1016/S1872-2067(15)60838-5 (2015).

51 Morigami, Y., Kondo, M., Abe, J., Kita, H. & Okamoto, K. The first large-scale pervaporation plant using tubular-type module with zeolite NaA membrane. *Separation and Purification Technology* **25**, 251-260 (2001).

52 Wee, S.-L., Tye, C.-T. & Bhatia, S. Membrane separation process—Pervaporation through zeolite membrane. *Separation and Purification Technology* **63**, 500-516 (2008).

53 Lupulescu, A. I. & Rimer, J. D. In Situ Imaging of Silicalite-1 Surface Growth Reveals the Mechanism of Crystallization. *Science* **344**, 729-732, doi:10.1126/science.1250984 (2014).

54 Lupulescu, A. I., Kumar, M. & Rimer, J. D. A Facile Strategy To Design Zeolite L Crystals with Tunable Morphology and Surface Architecture. *Journal of the American Chemical Society* **135**, 6608-6617, doi:10.1021/ja4015277 (2013).

55 Lupulescu, A. I., Qin, W. & Rimer, J. D. Tuning Zeolite Precursor Interactions by Switching the Valence of Polyamine Modifiers. *Langmuir* **32**, 11888-11898, doi:10.1021/acs.langmuir.6b03212 (2016).

56 Lupulescu, A. I. & Rimer, J. D. Tailoring Silicalite-1 Crystal Morphology with Molecular Modifiers. *Angewandte Chemie International Edition* **51**, 3345-3349, doi:10.1002/anie.201107725 (2012).

57 Rimer, J. D., Kumar, M., Li, R., Lupulescu, A. I. & Oleksiak, M. D. Tailoring the physicochemical properties of zeolite catalysts. *Catalysis Science & Technology* **4**, 3762-3771, doi:10.1039/C4CY00858H (2014).

58 Jeon, M. Y., Kim, D., Kumar, P., Lee, P. S., Rangnekar, N., Bai, P., Shete, M., Elyassi, B., Lee, H. S., Narasimharao, K., Basahel, S. N., Al-Thabaiti, S., Xu, W., Cho, H. J., Fetisov, E. O., Thyagarajan, R., DeJaco, R. F., Fan, W., Mkhoyan, K. A., Siepmann, J. I. & Tsapatsis, M. Ultra-selective high-flux membranes from directly synthesized zeolite nanosheets. *Nature* **543**, 690-694, doi:10.1038/nature21421 (2017).

59 Varoon, K., Zhang, X., Elyassi, B., Brewer, D. D., Gettel, M., Kumar, S., Lee, J. A., Maheshwari, S., Mittal, A., Sung, C.-Y., Cococcioni, M., Francis, L. F., McCormick, A. V., Mkhoyan, K. A. & Tsapatsis, M. Dispersible Exfoliated Zeolite Nanosheets and Their Application as a Selective Membrane. *Science* **334**, 72-75, doi:10.1126/science.1208891 (2011).

60 Erdem, E., Karapinar, N. & Donat, R. The removal of heavy metal cations by natural zeolites. *Journal of Colloid and Interface Science* **280**, 309-314 (2004).

61 Ouki, S. & Kavannagh, M. Treatment of metals-contaminated wastewaters by use of natural zeolites. *Water Science and Technology* **39**, 115-122 (1999).

62 Dyer, A., Chimedtsogzol, A., Campbell, L. & Williams, C. Uptake of caesium and strontium radioisotopes by natural zeolites from Mongolia. *Microporous and Mesoporous Materials* **95**, 172-175 (2006).

63 Wang, S. & Peng, Y. Natural zeolites as effective adsorbents in water and wastewater treatment. *Chemical Engineering Journal* **156**, 11-24 (2010).

64 Krishnani, K., Zhang, Y., Xiong, L., Yan, Y., Boopathy, R. & Mulchandani, A. Bactericidal and ammonia removal activity of silver ion-exchanged zeolite. *Bioresource technology* **117**, 86-91 (2012).

65 Demirci, S., Ustaoğlu, Z., Yılmazer, G. A., Sahin, F. & Baç, N. Antimicrobial properties of zeolite-X and zeolite-A ion-exchanged with silver, copper, and zinc against a broad range of microorganisms. *Applied biochemistry and biotechnology* **172**, 1652-1662 (2014).

66 Zhang, X., Liu, D., Xu, D., Asahina, S., Cychosz, K. A., Agrawal, K. V., Al Wahedi, Y., Bhan, A., Al Hashimi, S., Terasaki, O., Thommes, M. & Tsapatsis, M. Synthesis of Self-Pillared Zeolite Nanosheets by Repetitive Branching. *Science* **336**, 1684-1687, doi:10.1126/science.1221111 (2012).

67 Oleksiak Matthew, D. & Rimer Jeffrey, D. in *Reviews in Chemical Engineering* Vol. 30 1 (2014).

68 Mintova, S., Grand, J. & Valtchev, V. Nanosized zeolites: Quo Vadis? *Comptes Rendus Chimie* **19**, 183-191, doi:http://dx.doi.org/10.1016/j.crci.2015.11.005 (2016).

69 Tosheva, L. & Valtchev, V. P. Nanozeolites: Synthesis, Crystallization Mechanism, and Applications. *Chemistry of Materials* **17**, 2494-2513, doi:10.1021/cm047908z (2005).

70 Ng, E.-P., Chateigner, D., Bein, T., Valtchev, V. & Mintova, S. Capturing Ultrasmall EMT Zeolite from Template-Free Systems. *Science* **335**, 70-73, doi:10.1126/science.1214798 (2012).

71 Awala, H., Gilson, J.-P., Retoux, R., Boullay, P., Goupil, J.-M., Valtchev, V. & Mintova, S. Template-free nanosized faujasite-type zeolites. *Nat Mater* **14**, 447-451, doi:10.1038/nmat4173 (2015).

72 Petkovich, N. D. & Stein, A. Controlling macro- and mesostructures with hierarchical porosity through combined hard and soft templating. *Chemical Society Reviews* **42**, 3721-3739, doi:10.1039/c2cs35308c (2013).

73 Fan, W., Snyder, M. A., Kumar, S., Lee, P.-S., Yoo, W. C., McCormick, A. V., Lee Penn, R., Stein, A. & Tsapatsis, M. Hierarchical nanofabrication of microporous crystals with ordered mesoporosity. *Nat Mater* **7**, 984-991, doi:http://www.nature.com/nmat/journal/v7/n12/suppinfo/nmat2302_S1.html (2008).

74 Fan, W., Snyder, M. A., Kumar, S., Lee, P. S., Yoo, W. C., McCormick, A. V., Penn, R. L., Stein, A. & Tsapatsis, M. Hierarchical nanofabrication of microporous crystals with ordered mesoporosity. *Nature Materials* **7**, 984-991, doi:10.1038/nmat2302 (2008).

75 Liu, D., Bhan, A., Tsapatsis, M. & Al Hashimi, S. Catalytic Behavior of Brønsted Acid Sites in MWW and MFI Zeolites with Dual Meso- and Microporosity. *ACS Catalysis* **1**, 7-17, doi:10.1021/cs100042r (2011).

76 Ng, E. P., Chateigner, D., Bein, T., Valtchev, V. & Mintova, S. Capturing ultrasmall EMT zeolite from template-free systems. *Science* **335**, 70-73, doi:10.1126/science.1214798 (2012).

77 Olafson, K. N., Li, R., Alamani, B. G. & Rimer, J. D. Engineering crystal modifiers: Bridging classical and nonclassical crystallization. *Chemistry of Materials* **28**, 8453-8465 (2016).

78 Kumar, M., Luo, H., Román-Leshkov, Y. & Rimer, J. D. SSZ-13 Crystallization by Particle Attachment and Deterministic Pathways to Crystal Size Control. *Journal of the American Chemical Society* **137**, 13007-13017, doi:10.1021/jacs.5b07477 (2015).

79 Jegatheeswaran, S., Cheng, C.-M. & Cheng, C.-H. Effects of adding alcohols on ZSM-12 synthesis. *Microporous and Mesoporous Materials* **201**, 24-34, doi:http://dx.doi.org/10.1016/j.micromeso.2014.09.008 (2015).

80 Jamil, A. K., Muraza, O. & Al-Amer, A. M. The role of alcohols and diols as co-solvents in fabrication of TON zeolite. *Journal of Industrial and Engineering Chemistry* **29**, 112-119, doi:http://dx.doi.org/10.1016/j.jiec.2015.03.023 (2015).

81 Sanhoob, M. A., Muraza, O., Al-Mutairi, E. M. & Ullah, N. Role of crystal growth modifiers in the synthesis of ZSM-12 zeolite. *Advanced Powder Technology* **26**, 188-192, doi:http://dx.doi.org/10.1016/j.apt.2014.09.007 (2015).

82 Das, R., Ghosh, S. & Kanti Naskar, M. Effect of secondary and tertiary alkylamines for the synthesis of Zeolite L. *Materials Letters* **143**, 94-97, doi:http://dx.doi.org/10.1016/j.matlet.2014.12.076 (2015).

83 Chawla, A., Li, R., Jain, R., Clark, R. J., Sutjianto, J. G., Palmer, J. & Rimer, J. D. Cooperative Effects of Inorganic and Organic Structure-Directing Agents in ZSM-5 Crystallization. *Molecular Systems Design & Engineering*, doi:10.1039/C7ME00097A (2017).

84 Shen, Y., Le, T. T., Li, R. & Rimer, J. D. Optimized Synthesis of ZSM-11 Catalysts using 1,8-Diaminooctane as a Structure-Directing Agent. *ChemPhysChem*, n/a-n/a, doi:10.1002/cphc.201700968.

85 Na, K., Choi, M. & Ryoo, R. Cyclic diquaternary ammoniums for nanocrystalline BEA, MTW and MFI zeolites with intercrystalline mesoporosity. *Journal of Materials Chemistry* **19**, 6713-6719, doi:10.1039/b909792a (2009).

86 Na, K., Jo, C., Kim, J., Cho, K., Jung, J., Seo, Y., Messinger, R. J., Chmelka, B. F. & Ryoo, R. Directing Zeolite Structures into Hierarchically Nanoporous Architectures. *Science* **333**, 328-332, doi:10.1126/science.1204452 (2011).

87 Luo, H. Y., Michaelis, V. K., Hodges, S., Griffin, R. G. & Roman-Leshkov, Y. One-pot synthesis of MWW zeolite nanosheets using a rationally designed organic structure-directing agent. *Chemical Science* **6**, 6320-6324, doi:10.1039/C5SC01912E (2015).

88 Choi, M., Na, K., Kim, J., Sakamoto, Y., Terasaki, O. & Ryoo, R. Stable single-unit-cell nanosheets of zeolite MFI as active and long-lived catalysts. *Nature* **461**, 246-249, doi:http://www.nature.com/nature/journal/v461/n7261/suppinfo/nature08288_S1.html (2009).

89 Chaikittisilp, W., Suzuki, Y., Mukti, R. R., Suzuki, T., Sugita, K., Itabashi, K., Shimojima, A. & Okubo, T. Formation of hierarchically organized zeolites by sequential intergrowth. *Angewandte Chemie International Edition* **52**, 3355-3359 (2013).

90 Bonilla, G., Díaz, I., Tsapatsis, M., Jeong, H.-K., Lee, Y. & Vlachos, D. G. Zeolite (MFI) Crystal Morphology Control Using Organic Structure-Directing Agents. *Chemistry of Materials* **16**, 5697-5705, doi:10.1021/cm048854w (2004).

91 Corma, A., Fornes, V., Pergher, S. B., Maesen, T. L. M. & Buglass, J. G. Delaminated zeolite precursors as selective acidic catalysts. *Nature* **396**, 353-356, doi:http://www.nature.com/nature/journal/v396/n6709/suppinfo/396353a0_S1.html (1998).

92 Ogino, I., Nigra, M. M., Hwang, S.-J., Ha, J.-M., Rea, T., Zones, S. I. & Katz, A. Delamination of Layered Zeolite Precursors under Mild Conditions: Synthesis of UCB-1 via Fluoride/Chloride Anion-Promoted Exfoliation. *Journal of the American Chemical Society* **133**, 3288-3291, doi:10.1021/ja111147z (2011).

93 Corma, A., Fornés, V., Martínez-Triguero, J. & Pergher, S. B. Delaminated Zeolites: Combining the Benefits of Zeolites and Mesoporous Materials for Catalytic Uses. *Journal of Catalysis* **186**, 57-63, doi:https://doi.org/10.1006/jcat.1999.2503 (1999).

94 Chaikittisilp, W., Suzuki, Y., Mukti, R. R., Suzuki, T., Sugita, K., Itabashi, K., Shimojima, A. & Okubo, T. Formation of hierarchically organized zeolites by sequential intergrowth. *Angewandte Chemie - International Edition* **52**, 3355-3359, doi:10.1002/anie.201209638 (2013).

95 Pophale, R., Daeyaert, F. & Deem, M. W. Computational prediction of chemically synthesizable organic structure directing agents for zeolites. *J Mater Chem A* **1**, 6750-6760, doi:10.1039/c3ta10626h (2013).

96 Davis, T. M., Liu, A. T., Lew, C. M., Xie, D., Benin, A. I., Elomari, S., Zones, S. I. & Deem, M. W. Computationally Guided Synthesis of SSZ-52: A Zeolite for Engine Exhaust Clean-up. *Chem. Mat.* **28**, 708-711, doi:10.1021/acs.chemmater.5b04578 (2016).

97 Tong, M., Zhang, D., Fan, W., Xu, J., Zhu, L., Guo, W., Yan, W., Yu, J., Qiu, S., Wang, J., Deng, F. & Xu, R. Synthesis of chiral polymorph A-enriched zeolite Beta with an extremely concentrated fluoride route. **5**, 11521, doi:10.1038/srep11521 https://www.nature.com/articles/srep11521#supplementary-information (2015).

98 Brand, S. K., Schmidt, J. E., Deem, M. W., Daeyaert, F., Ma, Y., Terasaki, O., Orazov, M. & Davis, M. E. Enantiomerically enriched, polycrystalline molecular sieves. *Proceedings of the National Academy of Sciences* **114**, 5101-5106 (2017).

99 Roth, W. J., Nachtigall, P., Morris, R. E. & Cejka, J. Two-dimensional zeolites: current status and perspectives. *Chemical reviews* **114**, 4807-4837 (2014).

100 Mazur, M., Wheatley, P. S., Navarro, M., Roth, W. J., Položij, M., Mayoral, A., Eliášová, P., Nachtigall, P., Čejka, J. & Morris, R. E. Synthesis of 'unfeasible' zeolites. **8**, 58, doi:10.1038/nchem.2374 https://www.nature.com/articles/nchem.2374#supplementary-information (2015).

101 Roth, W. J., Nachtigall, P., Morris, R. E., Wheatley, P. S., Seymour, V. R., Ashbrook, S. E., Chlubná, P., Grajciar, L., Položij, M., Zukal, A., Shvets, O. & Čejka, J. A family of zeolites with controlled pore size prepared using a top-down method. **5**, 628, doi:10.1038/nchem.1662 https://www.nature.com/articles/nchem.1662#supplementary-information (2013).

102 Verheyen, E., Joos, L., Van Havenbergh, K., Breynaert, E., Kasian, N., Gobechiya, E., Houthoofd, K., Martineau, C., Hinterstein, M., Taulelle, F., Van Speybroeck, V., Waroquier, M., Bals, S., Van Tendeloo, G., Kirschhock, C. E. A. & Martens, J. A. Design

of zeolite by inverse sigma transformation. **11**, 1059, doi:10.1038/nmat3455 https://www.nature.com/articles/nmat3455#supplementary-information (2012).

103 Gallego, E. M., Portilla, M. T., Paris, C., León-Escamilla, A., Boronat, M., Moliner, M. & Corma, A. "Ab initio" synthesis of zeolites for preestablished catalytic reactions. *Science* **355**, 1051 (2017).

104 Jones, A. J., Zones, S. I. & Iglesia, E. Implications of Transition State Confinement within Small Voids for Acid Catalysis. *The Journal of Physical Chemistry C* **118**, 17787-17800, doi:10.1021/jp5050095 (2014).

105 Parlett, C. M. A., Wilson, K. & Lee, A. F. Hierarchical porous materials: catalytic applications. *Chemical Society Reviews* **42**, 3876-3893, doi:10.1039/c2cs35378d (2013).

106 Valtchev, V., Majano, G., Mintova, S. & Perez-Ramirez, J. Tailored crystalline microporous materials by post-synthesis modification. *Chemical Society Reviews* **42**, 263-290, doi:10.1039/c2cs35196j (2013).

107 Perez-Ramirez, J., Christensen, C. H., Egeblad, K., Christensen, C. H. & Groen, J. C. Hierarchical zeolites: enhanced utilisation of microporous crystals in catalysis by advances in materials design. *Chemical Society Reviews* **37**, 2530-2542, doi:10.1039/b809030k (2008).

108 Holm, M. S., Taarning, E., Egeblad, K. & Christensen, C. H. Catalysis with hierarchical zeolites. *Catalysis Today* **168**, 3-16, doi:https://doi.org/10.1016/j.cattod.2011.01.007 (2011).

109 Xie, S., Choi, S.-I., Lu, N., Roling, L. T., Herron, J. A., Zhang, L., Park, J., Wang, J., Kim, M. J., Xie, Z., Mavrikakis, M. & Xia, Y. Atomic Layer-by-Layer Deposition of Pt on Pd Nanocubes for Catalysts with Enhanced Activity and Durability toward Oxygen Reduction. *Nano Letters* **14**, 3570-3576, doi:10.1021/nl501205j (2014).

110 Chal, R., Gérardin, C., Bulut, M. & van Donk, S. Overview and Industrial Assessment of Synthesis Strategies towards Zeolites with Mesopores. *ChemCatChem* **3**, 67-81, doi:10.1002/cctc.201000158 (2011).

111 Janssen, A. H., Koster, A. J. & de Jong, K. P. Three-dimensional transmission electron microscopic observations of mesopores in dealuminated zeolite Y. *Angewandte Chemie-International Edition* **40**, 1102-+, doi:10.1002/1521-3773(20010316)40:6<1102::aid-anie11020>3.0.co;2-6 (2001).

112 Verboekend, D. & Perez-Ramirez, J. Design of hierarchical zeolite catalysts by desilication. *Catalysis Science & Technology* **1**, 879-890, doi:10.1039/c1cy00150g (2011).

113 Groen, J. C., Jansen, J. C., Moulijn, J. A. & Pérez-Ramírez, J. Optimal Aluminum-Assisted Mesoporosity Development in MFI Zeolites by Desilication. *The Journal of Physical Chemistry B* **108**, 13062-13065, doi:10.1021/jp047194f (2004).

114 Serrano, D. P., Escola, J. M. & Pizarro, P. Synthesis strategies in the search for hierarchical zeolites. *Chemical Society Reviews* **42**, 4004-4035, doi:10.1039/c2cs35330j (2013).

115 Sachse, A., Grau-Atienza, A., Jardim, E. O., Linares, N., Thommes, M. & García-Martínez, J. Development of Intracrystalline Mesoporosity in Zeolites through Surfactant-Templating. *Crystal Growth & Design* **17**, 4289-4305, doi:10.1021/acs.cgd.7b00619 (2017).

116 Sachse, A. & García-Martínez, J. Surfactant-Templating of Zeolites: From Design to Application. *Chemistry of Materials* **29**, 3827-3853, doi:10.1021/acs.chemmater.7b00599 (2017).

117 Li, K., Valla, J. & Garcia-Martinez, J. Realizing the commercial potential of hierarchical zeolites: new opportunities in catalytic cracking. *ChemCatChem* **6**, 46-66 (2014).

118 Garcia-Martinez, J., Xiao, C., Cychosz, K. A., Li, K., Wan, W., Zou, X. & Thommes, M. Evidence of intracrystalline mesostructured porosity in zeolites by advanced gas sorption,

electron tomography and rotation electron diffraction. *ChemCatChem* **6**, 3110-3115 (2014).

119 Jo, D., Ryu, T., Park, G. T., Kim, P. S., Kim, C. H., Nam, I.-S. & Hong, S. B. Synthesis of High-Silica LTA and UFI Zeolites and NH3–SCR Performance of Their Copper-Exchanged Form. *ACS Catalysis* **6**, 2443-2447, doi:10.1021/acscatal.6b00489 (2016).

120 Guisnet, M. & Ribeiro, F. R. *Deactivation and Regeneration of Zeolite Catalysts*. Vol. 9 293 (Imperial College Press, 2011).

121 Kistler, J. D., Chotigkrai, N., Xu, P., Enderle, B., Praserthdam, P., Chen, C.-Y., Browning, N. D. & Gates, B. C. A Single-Site Platinum CO Oxidation Catalyst in Zeolite KLTL: Microscopic and Spectroscopic Determination of the Locations of the Platinum Atoms. *Angewandte Chemie International Edition* **53**, 8904-8907, doi:10.1002/anie.201403353 (2014).

122 Kletnieks, P. W., Liang, A. J., Craciun, R., Ehresmann, J. O., Marcus, D. M., Bhirud, V. A., Klaric, M. M., Hayman, M. J., Guenther, D. R., Bagatchenko, O. P., Dixon, D. A., Gates, B. C. & Haw, J. F. Molecular Heterogeneous Catalysis: A Single-Site Zeolite-Supported Rhodium Complex for Acetylene Cyclotrimerization. *Chemistry – A European Journal* **13**, 7294-7304, doi:10.1002/chem.200700721 (2007).

123 Hoffman, A. S., Fang, C.-Y. & Gates, B. C. Homogeneity of Surface Sites in Supported Single-Site Metal Catalysts: Assessment with Band Widths of Metal Carbonyl Infrared Spectra. *The Journal of Physical Chemistry Letters* **7**, 3854-3860, doi:10.1021/acs.jpclett.6b01825 (2016).

124 Ehresmann, J. O., Kletnieks, P. W., Liang, A., Bhirud, V. A., Bagatchenko, O. P., Lee, E. J., Klaric, M., Gates, B. C. & Haw, J. F. Evidence from NMR and EXAFS Studies of a Dynamically Uniform Mononuclear Single-Site Zeolite-Supported Rhodium Catalyst. *Angewandte Chemie International Edition* **45**, 574-576, doi:10.1002/anie.200502864 (2006).

125 Gates, B. C., Flytzani-Stephanopoulos, M., Dixon, D. A. & Katz, A. Atomically dispersed supported metal catalysts: perspectives and suggestions for future research. *Catalysis Science & Technology* **7**, 4259-4275, doi:10.1039/C7CY00881C (2017).

126 Choi, M., Wu, Z. & Iglesia, E. Mercaptosilane-Assisted Synthesis of Metal Clusters within Zeolites and Catalytic Consequences of Encapsulation. *Journal of the American Chemical Society* **132**, 9129-9137, doi:10.1021/ja102778e (2010).

127 Goel, S., Wu, Z., Zones, S. I. & Iglesia, E. Synthesis and Catalytic Properties of Metal Clusters Encapsulated within Small-Pore (SOD, GIS, ANA) Zeolites. *Journal of the American Chemical Society* **134**, 17688-17695, doi:10.1021/ja307370z (2012).

128 Wu, Z., Goel, S., Choi, M. & Iglesia, E. Hydrothermal synthesis of LTA-encapsulated metal clusters and consequences for catalyst stability, reactivity, and selectivity. *Journal of Catalysis* **311**, 458-468, doi:https://doi.org/10.1016/j.jcat.2013.12.021 (2014).

129 Goel, S., Zones, S. I. & Iglesia, E. Encapsulation of Metal Clusters within MFI via Interzeolite Transformations and Direct Hydrothermal Syntheses and Catalytic Consequences of Their Confinement. *Journal of the American Chemical Society* **136**, 15280-15290, doi:10.1021/ja507956m (2014).

130 Liu, L., Diaz, U., Arenal, R., Agostini, G., Concepcion, P. & Corma, A. Generation of subnanometric platinum with high stability during transformation of a 2D zeolite into 3D. *Nat Mater* **16**, 132-138, doi:10.1038/nmat4757 http://www.nature.com/nmat/journal/v16/n1/abs/nmat4757.html#supplementary-information (2017).

131 Dědeček, J., Sobalík, Z. & Wichterlová, B. Siting and Distribution of Framework Aluminium Atoms in Silicon-Rich Zeolites and Impact on Catalysis. *Catalysis Reviews - Science and Engineering* **54**, 135-223, doi:10.1080/01614940.2012.632662 (2012).

132 Dědeček, J., Tabor, E. & Sklenak, S. Tuning the Aluminum Distribution in Zeolites to Increase their Performance in Acid-Catalyzed Reactions. *ChemSusChem* **12**, 556-576, doi:10.1002/cssc.201801959 (2019).

133 Ghorbanpour, A., Rimer, J. D. & Grabow, L. C. Computational Assessment of the Dominant Factors Governing the Mechanism of Methanol Dehydration over H-ZSM-5 with Heterogeneous Aluminum Distribution. *ACS Catalysis* **6**, 2287-2298, doi:10.1021/acscatal.5b02367 (2016).

134 Ghorbanpour, A., Rimer, J. D. & Grabow, L. C. Periodic, vdW-corrected density functional theory investigation of the effect of Al siting in H-ZSM-5 on chemisorption properties and site-specific acidity. *Catalysis Communications* **52**, 98-102, doi:https://doi.org/10.1016/j.catcom.2014.04.005 (2014).

135 Brändle, M. & Sauer, J. Acidity differences between inorganic solids induced by their framework structure. A combined quantum mechanics/molecular mechanics ab initio study on zeolites. *Journal of the American Chemical Society* **120**, 1556-1570, doi:10.1021/ja9729037 (1998).

136 Kester, P. M., Miller, J. T. & Gounder, R. Ammonia Titration Methods to Quantify Brønsted Acid Sites in Zeolites Substituted with Aluminum and Boron Heteroatoms. *Industrial and Engineering Chemistry Research* **57**, 6673-6683, doi:10.1021/acs.iecr.8b00933 (2018).

137 Haag, W., Lago, R. & Weisz, P. The active site of acidic aluminosilicate catalysts. *Nature* **309**, 589-591 (1984).

138 Carr, R. T., Neurock, M. & Iglesia, E. Catalytic consequences of acid strength in the conversion of methanol to dimethyl ether. *Journal of Catalysis* **278**, 78-93, doi:10.1016/j.jcat.2010.11.017 (2011).

139 Jones, A. J., Carr, R. T., Zones, S. I. & Iglesia, E. Acid strength and solvation in catalysis by MFI zeolites and effects of the identity, concentration and location of framework heteroatoms. *Journal of Catalysis* **312**, 58-68, doi:10.1016/j.jcat.2014.01.007 (2014).

140 Jones, A. J. & Iglesia, E. The Strength of Brønsted Acid Sites in Microporous Aluminosilicates. *ACS Catalysis* **5**, 5741-5755, doi:10.1021/acscatal.5b01133 (2015).

141 Chawla, A., Li, R., Jain, R., Clark, R. J., Sutjianto, J. G., Palmer, J. C. & Rimer, J. D. Cooperative effects of inorganic and organic structure-directing agents in ZSM-5 crystallization. *Molecular Systems Design & Engineering* **3**, 159-170, doi:10.1039/c7me00097a (2018).

142 Dedecek, J., Balgová, V., Pashkova, V., Klein, P. & Wichterlová, B. Synthesis of ZSM-5 zeolites with defined distribution of Al atoms in the framework and multinuclear MAS NMR analysis of the control of Al distribution. *Chemistry of Materials* **24**, 3231-3239, doi:10.1021/cm301629a (2012).

143 Biligetu, T., Wang, Y., Nishitoba, T., Otomo, R., Park, S., Mochizuki, H., Kondo, J. N., Tatsumi, T. & Yokoi, T. Al distribution and catalytic performance of ZSM-5 zeolites synthesized with various alcohols. *Journal of Catalysis* **353**, 1-10, doi:10.1016/j.jcat.2017.06.026 (2017).

144 Pinar, A. B., Gómez-Hortigüela, L., McCusker, L. B. & Pérez-Pariente, J. Controlling the aluminum distribution in the zeolite ferrierite via the organic structure directing agent. *Chemistry of Materials* **25**, 3654-3661, doi:10.1021/cm4018024 (2013).

145 Pinar, A. B., Gomez-Hortiguela, L. & Perez-Pariente, J. Cooperative structure directing role of the cage-forming tetramethylammonium cation and the bulkier benzylmethylpyrrolidinium in the synthesis of zeolite ferrierite. *Chemistry of Materials* **19**, 5617-5626, doi:10.1021/cm071753o (2007).

146 Wang, S., Zhang, L., Li, S., Qin, Z., Shi, D., He, S., Yuan, K., Wang, P., Zhao, T.-S., Fan, S., Dong, M., Li, J., Fan, W. & Wang, J. Tuning the siting of aluminum in ZSM-11 zeolite

and regulating its catalytic performance in the conversion of methanol to olefins. *Journal of Catalysis* **377**, 81-97, doi:10.1016/j.jcat.2019.07.028 (2019).

147 Yokoi, T., Mochizuki, H., Biligetu, T., Wang, Y. & Tatsumi, T. Unique Al Distribution in the MFI Framework and Its Impact on Catalytic Properties. *Chem. Lett.* **46**, 798-800, doi:10.1246/cl.170156 (2017).

148 Muraoka, K., Chaikittisilp, W., Yanaba, Y., Yoshikawa, T. & Okubo, T. Directing Aluminum Atoms into Energetically Favorable Tetrahedral Sites in a Zeolite Framework by Using Organic Structure-Directing Agents. *Angewandte Chemie* **130**, 3804-3808, doi:10.1002/ange.201713308 (2018).

149 Gábová, V., Dědeček, J. & čejka, J. Control of Al distribution in ZSM-5 by conditions of zeolite synthesis. *Chemical Communications* **3**, 1196-1197, doi:10.1039/b301634j (2003).

150 Li, C., Vidal-Moya, A., Miguel, P. J., Dedecek, J., Boronat, M. & Corma, A. Selective Introduction of Acid Sites in Different Confined Positions in ZSM-5 and Its Catalytic Implications. *ACS Catalysis* **8**, 7688-7697, doi:10.1021/acscatal.8b02112 (2018).

151 Nishitoba, T., Yoshida, N., Kondo, J. N. & Yokoi, T. Control of Al Distribution in the CHA-Type Aluminosilicate Zeolites and Its Impact on the Hydrothermal Stability and Catalytic Properties. *Industrial and Engineering Chemistry Research* **57**, 3914-3922, doi:10.1021/acs.iecr.7b04985 (2018).

152 Devos, J., Bols, M. L., Plessers, D., Van Goethem, C., eacute, dric, Seo, J. W., Hwang, S.-J., Sels, B. F. & Dusselier, M. Synthesis-structure-activity relations in Fe-CHA for C-H activation: control of Al-distribution by interzeolite conversion. *Chemistry of Materials* **32**, acs.chemmater.9b03738-acs.chemmater.03739b03738, doi:10.1021/acs.chemmater.9b03738 (2019).

153 Gallego, E. M., Li, C., Paris, C., Martín, N., Martínez-Triguero, J., Boronat, M., Moliner, M. & Corma, A. Making Nanosized CHA Zeolites with Controlled Al Distribution for

Optimizing Methanol-to-Olefin Performance. *Chemistry - A European Journal* **24**, 14631-14635, doi:10.1002/chem.201803637 (2018).

154 Muraoka, K., Sada, Y., Shimojima, A., Chaikittisilp, W. & Okubo, T. Tracking the rearrangement of atomic configurations during the conversion of FAU zeolite to CHA zeolite. *Chemical Science* **10**, 8533-8540, doi:10.1039/c9sc02773d (2019).

155 Kim, S., Park, G., Woo, M. H., Kwak, G. & Kim, S. K. Control of Hierarchical Structure and Framework-Al Distribution of ZSM-5 via Adjusting Crystallization Temperature and Their Effects on Methanol Conversion. *ACS Catalysis* **9**, 2880-2892, doi:10.1021/acscatal.8b04493 (2019).

156 Wang, S., Zhang, L., Li, S., Qin, Z., Shi, D., He, S., Yuan, K., Wang, P., Zhao, T. S., Fan, S., Dong, M., Li, J., Fan, W. & Wang, J. Tuning the siting of aluminum in ZSM-11 zeolite and regulating its catalytic performance in the conversion of methanol to olefins. *Journal of Catalysis* **377**, 81-97, doi:10.1016/j.jcat.2019.07.028 (2019).

157 Sazama, P., Dědeček, J., Gábová, V., Wichterlová, B., Spoto, G. & Bordiga, S. Effect of aluminium distribution in the framework of ZSM-5 on hydrocarbon transformation. Cracking of 1-butene. *Journal of Catalysis* **254**, 180-189, doi:10.1016/j.jcat.2007.12.005 (2008).

158 Chen, J., Liang, T., Li, J., Wang, S., Qin, Z., Wang, P., Huang, L., Fan, W. & Wang, J. Regulation of Framework Aluminum Siting and Acid Distribution in H-MCM-22 by Boron Incorporation and Its Effect on the Catalytic Performance in Methanol to Hydrocarbons. *ACS Catalysis* **6**, 2299-2313, doi:10.1021/acscatal.5b02862 (2016).

159 Wang, S., Li, S., Zhang, L., Qin, Z., Dong, M., Li, J., Wang, J. & Fan, W. Insight into the effect of incorporation of boron into ZSM-11 on its catalytic performance for conversion of methanol to olefins. *Catalysis Science & Technology* **7**, 4766-4779 (2017).

160 Oleksiak, M. D., Muraoka, K., Hsieh, M. F., Conato, M. T., Shimojima, A., Okubo, T., Chaikittisilp, W. & Rimer, J. D. Organic-Free Synthesis of a Highly Siliceous Faujasite

Zeolite with Spatially Biased Q4 (nAl) Si Speciation. *Angewandte Chemie* **129**, 13551-13556 (2017).

161 Di Iorio, J. R., Nimlos, C. T. & Gounder, R. Introducing catalytic diversity into single-site chabazite zeolites of fixed composition via synthetic control of active site proximity. *ACS Catalysis* **7**, 6663-6674, doi:10.1021/acscatal.7b01273 (2017).

162 Janda, A. & Bell, A. T. Effects of Si/Al ratio on the distribution of framework Al and on the rates of alkane monomolecular cracking and dehydrogenation in H-MFI. *Journal of the American Chemical Society* **135**, 19193-19207, doi:10.1021/ja4081937 (2013).

163 Song, C., Chu, Y., Wang, M., Shi, H., Zhao, L., Guo, X., Yang, W., Shen, J., Xue, N., Peng, L. & Ding, W. Cooperativity of adjacent BrØnsted acid sites in MFI zeolite channel leads to enhanced polarization and cracking of alkanes. *Journal of Catalysis* **349**, 163-174, doi:10.1016/j.jcat.2016.12.024 (2017).

164 Román-Leshkov, Y., Moliner, M. & Davis, M. E. Impact of controlling the site distribution of al atoms on catalytic properties in ferrierite-type zeolites. *Journal of Physical Chemistry C* **115**, 1096-1102, doi:10.1021/jp106247g (2011).

165 Liang, T., Chen, J., Qin, Z., Li, J., Wang, P., Wang, S., Wang, G., Dong, M., Fan, W. & Wang, J. Conversion of Methanol to Olefins over H-ZSM-5 Zeolite: Reaction Pathway Is Related to the Framework Aluminum Siting. *ACS Catalysis* **6**, 7311-7325, doi:10.1021/acscatal.6b01771 (2016).

166 Wang, S., He, Y., Jiao, W., Wang, J. & Fan, W. Recent experimental and theoretical studies on Al siting/acid site distribution in zeolite framework. *Current Opinion in Chemical Engineering* **23**, 146-154, doi:10.1016/j.coche.2019.04.002 (2019).

167 Wang, S., Wang, P., Qin, Z., Chen, Y., Dong, M., Li, J., Zhang, K., Liu, P., Wang, J. & Fan, W. Relation of catalytic performance to the aluminum siting of acidic zeolites in the conversion of methanol to olefins, viewed via a comparison between ZSM-5 and ZSM-11. *ACS Catalysis* **8**, 5485-5505, doi:10.1021/acscatal.8b01054 (2018).

168 Mlinar, A. N., Zimmerman, P. M., Celik, F. E., Head-Gordon, M. & Bell, A. T. Effects of Brønsted-acid site proximity on the oligomerization of propene in H-MFI. *Journal of Catalysis* **288**, 65-73, doi:10.1016/j.jcat.2012.01.002 (2012).

169 Kulkarni, A. R., Zhao, Z. J., Siahrostami, S., Nørskov, J. K. & Studt, F. Monocopper Active Site for Partial Methane Oxidation in Cu-Exchanged 8MR Zeolites. *ACS Catalysis* **6**, 6531-6536, doi:10.1021/acscatal.6b01895 (2016).

170 Dinh, K. T., Sullivan, M. M., Narsimhan, K., Serna, P., Meyer, R. J., Dincă, M. & Román-Leshkov, Y. Continuous Partial Oxidation of Methane to Methanol Catalyzed by Diffusion-Paired Copper Dimers in Copper-Exchanged Zeolites. *Journal of the American Chemical Society* **141**, 11641-11650, doi:10.1021/jacs.9b04906 (2019).

171 Ghorbanpour, A., Rimer, J. D. & Grabow, L. C. Periodic, vdW-corrected density functional theory investigation of the effect of Al siting in HZSM-5 on chemisorption properties and site-specific acidity. *Catalysis Communications* **52**, 98-102 (2014).

172 Cheung, P., Bhan, A., Sunley, G. J., Law, D. J. & Iglesia, E. Site requirements and elementary steps in dimethyl ether carbonylation catalyzed by acidic zeolites. *Journal of Catalysis* **245**, 110-123 (2007).

173 Bhan, A., Allian, A. D., Sunley, G. J., Law, D. J. & Iglesia, E. Specificity of sites within eight-membered ring zeolite channels for carbonylation of methyls to acetyls. *Journal of the American Chemical Society* **129**, 4919-4924 (2007).

174 Kosinov, N., Liu, C., Hensen, E. J. M. & Pidko, E. A. Engineering of Transition Metal Catalysts Confined in Zeolites. *Chemistry of Materials* **30**, 3177-3198, doi:10.1021/acs.chemmater.8b01311 (2018).

175 Sobalik, Z., Sazama, P., Dedecek, J. & Wichterlová, B. Critical evaluation of the role of the distribution of Al atoms in the framework for the activity of metallo-zeolites in redox N2O/NOx reactions. *Applied Catalysis A: General* **474**, 178-185, doi:10.1016/j.apcata.2013.07.033 (2014).

176 Paolucci, C., Parekh, A. A., Khurana, I., Di Iorio, J. R., Li, H., Albarracin Caballero, J. D., Shih, A. J., Anggara, T., Delgass, W. N. & Miller, J. T. Catalysis in a cage: condition-dependent speciation and dynamics of exchanged Cu cations in SSZ-13 zeolites. *Journal of the American Chemical Society* **138**, 6028-6048 (2016).

177 Lemishko, T., Jiménez-Ruiz, M., Rey, F., Valencia, S., Blasco, T., Vidal Moya, A. & Sastre, G. Inelastic Neutron Scattering Study of the Aluminum and Brønsted Site Location in Aluminosilicate LTA Zeolites. *Journal of Physical Chemistry C* **122**, 11450-11454, doi:10.1021/acs.jpcc.8b02882 (2018).

178 Han, O. H., Kim, C. S. & Hong, S. B. Direct evidence for the nonrandom nature of Al substitution in zeolite ZSM-5: An investigation by 27Al MAS and MQ MAS NMR. *Angewandte Chemie - International Edition* **41**, 469-472, doi:10.1002/1521-3773(20020201)41:3<469::aid-anie469>3.0.co;2-k (2002).

179 Dedecek, J., Lucero, M. J., Li, C., Gao, F., Klein, P., Urbanova, M., Tvaruzkova, Z., Sazama, P. & Sklenak, S. Complex analysis of the aluminum siting in the framework of silicon-rich zeolites. A case study on ferrierites. *Journal of Physical Chemistry C* **115**, 11056-11064, doi:10.1021/jp200310b (2011).

180 Yokoi, T., Mochizuki, H., Namba, S., Kondo, J. N. & Tatsumi, T. Control of the Al Distribution in the Framework of ZSM-5 Zeolite and Its Evaluation by Solid-State NMR Technique and Catalytic Properties. *J. Phys. Chem. C* **119**, 15303-15315, doi:10.1021/acs.jpcc.5b03289 (2015).

181 Vjunov, A., Fulton, J. L., Huthwelker, T., Pin, S., Mei, D., Schenter, G. K., Govind, N., Camaioni, D. M., Hu, J. Z. & Lercher, J. A. Quantitatively probing the al distribution in zeolites. *Journal of the American Chemical Society* **136**, 8296-8306, doi:10.1021/ja501361v (2014).

182 Bohinc, R., Hoszowska, J., Dousse, J. C., Błachucki, W., Zeeshan, F., Kayser, Y., Nachtegaal, M., Pinar, A. B. & Van Bokhoven, J. A. Distribution of aluminum over

different T-sites in ferrierite zeolites studied with aluminum valence to core X-ray emission spectroscopy. *Physical Chemistry Chemical Physics* **19**, 29271-29277, doi:10.1039/c7cp05001a (2017).

183 Van Bokhoven, J. A., Lee, T. L., Drakopoulos, M., Lamberti, C., Thie, S. & Zegenhagen, J. Determining the aluminium occupancy on the active T-sites in zeolites using X-ray standing waves. *Nature Materials* **7**, 551-555, doi:10.1038/nmat2220 (2008).

184 Kumar, M., Berkson, Z. J., Clark, R. J., Shen, Y., Prisco, N. A., Zheng, Q., Zeng, Z., Zheng, H., McCusker, L. B., Palmer, J. C., Chmelka, B. F. & Rimer, J. D. Crystallization of Mordenite Platelets using Cooperative Organic Structure-Directing Agents. *Journal of the American Chemical Society* **141**, 20155-20165, doi:10.1021/jacs.9b09697 (2019).

185 Perea, D. E., Arslan, I., Liu, J., Ristanović, Z., Kovarik, L., Arey, B. W., Lercher, J. A., Bare, S. R. & Weckhuysen, B. M. Determining the location and nearest neighbours of aluminium in zeolites with atom probe tomography. *Nature Communications* **6**, 1-8, doi:10.1038/ncomms8589 (2015).

186 Zones, S. I. & Harris, T. V. The Constraint Index test revisited: Anomalies based upon new zeolite structure types. *Microporous and Mesoporous Materials* **35-36**, 31-46, doi:10.1016/s1387-1811(99)00206-1 (2000).

187 Rimer, J. D. & Tsapatsis, M. Nucleation of open framework materials: Navigating the voids. *MRS Bulletin* **41**, 393-398, doi:10.1557/mrs.2016.89 (2016).

188 Davis, T. M., Drews, T. O., Ramanan, H., He, C., Dong, J., Schnablegger, H., Katsoulakis, M. A., Kokkoli, E., McCormick, A. V., Penn, R. L. & Tsapatsis, M. Mechanistic principles of nanoparticle evolution to zeolite crystals. *Nature Materials* **5**, 400, doi:10.1038/nmat1636https://www.nature.com/articles/nmat1636#supplementary-information (2006).

189 Kumar, S., Wang, Z., Penn, R. L. & Tsapatsis, M. A structural resolution cryo-TEM study of the early stages of MFI growth. *Journal of the American Chemical Society* **130**, 17284-17286 (2008).

190 Li, R., Chawla, A., Linares, N., Sutjianto, J. G., Chapman, K. W., Martínez, J. G. & Rimer, J. D. Diverse Physical States of Amorphous Precursors in Zeolite Synthesis. *Industrial & Engineering Chemistry Research* **57**, 8460-8471 (2018).

191 Oleksiak, M. D., Soltis, J. A., Conato, M. T., Penn, R. L. & Rimer, J. D. Nucleation of FAU and LTA Zeolites from Heterogeneous Aluminosilicate Precursors. *Chemistry of Materials* **28**, 4906-4916, doi:10.1021/acs.chemmater.6b01000 (2016).

192 Kashchiev, D. Thermodynamically consistent description of the work to form a nucleus of any size. *The Journal of chemical physics* **118**, 1837-1851 (2003).

193 Cundy, C. S. & Cox, P. A. The hydrothermal synthesis of zeolites: Precursors, intermediates and reaction mechanism. *Microporous and Mesoporous Materials* **82**, 1-78, doi:https://doi.org/10.1016/j.micromeso.2005.02.016 (2005).

194 Ren, N., Bosnar, S., Bronić, J., Dutour Sikirić, M., Mišić, T., Svetličić, V., Mao, J.-J., Antonić Jelić, T., Hadžija, M. & Subotić, B. Role of Subcolloidal (Nanosized) Precursor Species in the Early Stage of the Crystallization of Zeolites in Heterogeneous Systems. *Langmuir* **30**, 8570-8579, doi:10.1021/la5012296 (2014).

195 Ren, N., Subotić, B., Bronić, J., Tang, Y., Dutour Sikirić, M., Mišić, T., Svetličić, V., Bosnar, S. & Antonić Jelić, T. Unusual Pathway of Crystallization of Zeolite ZSM-5 in a Heterogeneous System: Phenomenology and Starting Considerations. *Chemistry of Materials* **24**, 1726-1737, doi:10.1021/cm203194v (2012).

196 Choudhary, M. K., Kumar, M. & Rimer, J. D. Regulating Nonclassical Pathways of Silicalite-1 Crystallization through Controlled Evolution of Amorphous Precursors. *Angewandte Chemie* **131**, 15859-15863 (2019).

197 Vekilov, P. G. Two-step mechanism for the nucleation of crystals from solution. *Journal of Crystal Growth* **275**, 65-76 (2005).

198 Wallace, A. F., Hedges, L. O., Fernandez-Martinez, A., Raiteri, P., Gale, J. D., Waychunas, G. A., Whitelam, S., Banfield, J. F. & De Yoreo, J. J. Microscopic evidence for liquid-liquid separation in supersaturated CaCO3 solutions. *Science* **341**, 885-889 (2013).

199 Kashchiev, D., Vekilov, P. G. & Kolomeisky, A. B. Kinetics of two-step nucleation of crystals. *The Journal of chemical physics* **122**, 244706 (2005).

200 Mintova, S., Olson, N. H., Valtchev, V. & Bein, T. Mechanism of Zeolite A Nanocrystal Growth from Colloids at Room Temperature. *Science* **283**, 958 (1999).

201 Melinte, G., Georgieva, V., Springuel-Huet, M. A., Nossov, A., Ersen, O., Guenneau, F., Gedeon, A., Palčić, A., Bozhilov Krassimir, N., Pham-Huu, C., Qiu, S., Mintova, S. & Valtchev, V. 3D Study of the Morphology and Dynamics of Zeolite Nucleation. *Chemistry – A European Journal* **21**, 18316-18327, doi:10.1002/chem.201501919 (2015).

202 Greer, H., Wheatley, P. S., Ashbrook, S. E., Morris, R. E. & Zhou, W. Early Stage Reversed Crystal Growth of Zeolite A and Its Phase Transformation to Sodalite. *Journal of the American Chemical Society* **131**, 17986-17992, doi:10.1021/ja907475z (2009).

203 Chen, X., Qiao, M., Xie, S., Fan, K., Zhou, W. & He, H. Self-construction of core− shell and hollow zeolite analcime icositetrahedra: A reversed crystal growth process via oriented aggregation of nanocrystallites and recrystallization from surface to core. *Journal of the American Chemical Society* **129**, 13305-13312 (2007).

204 Itani, L., Liu, Y., Zhang, W., Bozhilov, K. N., Delmotte, L. & Valtchev, V. Investigation of the physicochemical changes preceding zeolite nucleation in a sodium-rich aluminosilicate gel. *Journal of the American Chemical Society* **131**, 10127-10139 (2009).

205 Valtchev, V. P. & Bozhilov, K. N. Evidences for zeolite nucleation at the solid− liquid interface of gel cavities. *Journal of the American Chemical Society* **127**, 16171-16177 (2005).

206 Kumar, M., Li, R. & Rimer, J. D. Assembly and Evolution of Amorphous Precursors in Zeolite L Crystallization. *Chemistry of Materials* **28**, 1714-1727, doi:10.1021/acs.chemmater.5b04569 (2016).

207 Melero, J. A., van Grieken, R., Serrano, D. P. & Espada, J. J. Crystallization mechanism of Al-TS-1 synthesised from amorphous wetness-impregnated Al2O3–TiO2–SiO2 xerogels: role of aluminium species. *Journal of Materials Chemistry* **11**, 1519-1525 (2001).

208 Serrano, D. P., Uguina, M. A., Ovejero, G., van Grieken, R., Camacho, M. & Melero, J. A. Crystallization mechanism of Al–Ti-beta zeolite synthesized from amorphous wetness impregnated xerogels. *Journal of Materials Chemistry* **9**, 2899-2905 (1999).

209 Uguina, M., Serrano, D., Ovejero, G., Van Grieken, R. & Camacho, M. TS-2 synthesis from wetness-impregnated SiO2-TiO2 xerogels. *Zeolites* **18**, 368-378 (1997).

210 Kumar, S., Davis, T. M., Ramanan, H., Penn, R. L. & Tsapatsis, M. Aggregative Growth of Silicalite-1. *The Journal of Physical Chemistry B* **111**, 3398-3403, doi:10.1021/jp0677445 (2007).

211 Rimer, J. D., Vlachos, D. G. & Lobo, R. F. Evolution of self-assembled silica−tetrapropylammonium nanoparticles at elevated temperatures. *The Journal of Physical Chemistry B* **109**, 12762-12771 (2005).

212 Fedeyko, J. M., Rimer, J. D., Lobo, R. F. & Vlachos, D. G. Spontaneous Formation of Silica Nanoparticles in Basic Solutions of Small Tetraalkylammonium Cations. *The Journal of Physical Chemistry B* **108**, 12271-12275, doi:10.1021/jp047623+ (2004).

213 Rimer, J. D., Lobo, R. F. & Vlachos, D. G. Physical basis for the formation and stability of silica nanoparticles in basic solutions of monovalent cations. *Langmuir* **21**, 8960-8971 (2005).

214 Malani, A., Auerbach, S. M. & Monson, P. A. Monte Carlo simulations of silica polymerization and network formation. *The Journal of Physical Chemistry C* **115**, 15988-16000 (2011).

215 Verstraelen, T., Szyja, B. M., Lesthaeghe, D., Declerck, R., Van Speybroeck, V., Waroquier, M., Jansen, A. P., Aerts, A., Follens, L. R. & Martens, J. A. Multi-level Modeling of Silica–Template Interactions During Initial Stages of Zeolite Synthesis. *Topics in Catalysis* **52**, 1261-1271 (2009).

216 Markov, I. V. *Crystal growth for beginners: fundamentals of nucleation, crystal growth and epitaxy*. (World scientific, 2003).

217 Vekilov, P. G. What determines the rate of growth of crystals from solution? *Crystal Growth and Design* **7**, 2796-2810 (2007).

218 Kumar, M., Choudhary, M.K., Rimer, J.D. Transient Modes of Zeolite Surface Growth from 3D Gel-like Islands to 2D Single Layers. *Nature Communications* **In Press** (2018).

219 Park, M. B., Lee, Y., Zheng, A., Xiao, F.-S., Nicholas, C. P., Lewis, G. J. & Hong, S. B. Formation pathway for LTA zeolite crystals synthesized via a charge density mismatch approach. *Journal of the American Chemical Society* **135**, 2248-2255 (2012).

220 Anderson, M. W., Gebbie-Rayet, J. T., Hill, A. R., Farida, N., Attfield, M. P., Cubillas, P., Blatov, V. A., Proserpio, D. M., Akporiaye, D. & Arstad, B. Predicting crystal growth via a unified kinetic three-dimensional partition model. *Nature* **544**, 456 (2017).

221 Brent, R. & Anderson, M. W. Fundamental Crystal Growth Mechanism in Zeolite L Revealed by Atomic Force Microscopy. *Angewandte Chemie International Edition* **47**, 5327-5330, doi:10.1002/anie.200800977 (2008).

222 Shete, M., Kumar, M., Kim, D., Rangnekar, N., Xu, D., Topuz, B., Agrawal, K. V., Karapetrova, E., Stottrup, B., Al-Thabaiti, S., Basahel, S., Narasimharao, K., Rimer, J. D. & Tsapatsis, M. Nanoscale Control of Homoepitaxial Growth on a Two-Dimensional Zeolite. *Angewandte Chemie International Edition* **56**, 535-539, doi:doi:10.1002/anie.201607063 (2017).

223 Cubillas, P., Castro, M., Jelfs, K. E., Lobo, A. J. W., Slater, B., Lewis, D. W., Wright, P. A., Stevens, S. M. & Anderson, M. W. Spiral Growth on Nanoporous

Silicoaluminophosphate STA-7 as Observed by Atomic Force Microscopy. *Crystal Growth & Design* **9**, 4041-4050, doi:10.1021/cg900255u (2009).

224 Kumar, M., Luo, H., Román-Leshkov, Y. & Rimer, J. D. SSZ-13 crystallization by particle attachment and deterministic pathways to crystal size control. *Journal of the American Chemical Society* **137**, 13007-13017 (2015).

225 Houlleberghs, M., Breynaert, E., Asselman, K., Vaneeckhaute, E., Radhakrishnan, S., Anderson, M. W., Taulelle, F., Haouas, M., Martens, J. A. & Kirschhock, C. E. A. Evolution of the crystal growth mechanism of zeolite W (MER) with temperature. *Microporous and Mesoporous Materials* **274**, 379-384, doi:https://doi.org/10.1016/j.micromeso.2018.09.012 (2019).

226 Nenoff, T. M., Harrison, W. T., Gier, T. E. & Stucky, G. D. Room-temperature synthesis and characterization of new ZnPO and ZnAsO sodalite open frameworks. *Journal of the American Chemical Society* **113**, 378-379 (1991).

227 Liao, H.-G., Cui, L., Whitelam, S. & Zheng, H. Real-time imaging of Pt3Fe nanorod growth in solution. *Science* **336**, 1011-1014 (2012).

228 Zheng, H., Smith, R. K., Jun, Y.-w., Kisielowski, C., Dahmen, U. & Alivisatos, A. P. Observation of Single Colloidal Platinum Nanocrystal Growth Trajectories. *Science* **324**, 1309 (2009).

229 Patterson, S., Arora, P., Price, P., Dittmar, J. W., Das, V. K., Pink, M., Stein, B., Morgan, D. G., Losovyj, Y. & Koczkur, K. M. Oriented attachment is a major control mechanism to form nail-like mn-doped ZnO nanocrystals. *Langmuir* **33**, 14709-14717 (2017).

230 Zhao, Y., Ye, Z., Wang, L., Zhang, H., Xue, F., Xie, S., Cao, X.-M., Zhang, Y. & Tang, Y. Engineering Fractal MTW Zeolite Mesocrystal: Particle-Based Dendritic Growth via Twinning-Plane Induced Crystallization. *Crystal Growth & Design* **18**, 1101-1108 (2017).

231 Zhao, Y., Zhang, H., Wang, P., Xue, F., Ye, Z., Zhang, Y. & Tang, Y. Tailoring the Morphology of MTW Zeolite Mesocrystals: Intertwined Classical/Nonclassical

Crystallization. *Chemistry of Materials* **29**, 3387-3396, doi:10.1021/acs.chemmater.6b03813 (2017).

232 Kumar, M., Choudhary, M. K. & Rimer, J. D. Transient modes of zeolite surface growth from 3D gel-like islands to 2D single layers. *Nature Communications* **9**, 2129-2129, doi:10.1038/s41467-018-04296-4 (2018).

233 Shete, M., Kumar, M., Kim, D., Rangnekar, N., Xu, D., Topuz, B., Agrawal, K. V., Karapetrova, E., Stottrup, B., Al-Thabaiti, S., Basahel, S., Narasimharao, K., Rimer, J. D. & Tsapatsis, M. Nanoscale Control of Homoepitaxial Growth on a Two-Dimensional Zeolite. *Angewandte Chemie International Edition* **56**, 535-539, doi:10.1002/anie.201607063 (2017).

234 Wang, Q., Luo, J., Zhong, Z. & Borgna, A. CO2 capture by solid adsorbents and their applications: current status and new trends. *Energy & Environmental Science* **4**, 42-55, doi:10.1039/c0ee00064g (2011).

235 Martínez, C. & Corma, A. Inorganic molecular sieves: Preparation, modification and industrial application in catalytic processes. *Coordination Chemistry Reviews* **255**, 1558-1580, doi:http://dx.doi.org/10.1016/j.ccr.2011.03.014 (2011).

236 Snyder, M. A. & Tsapatsis, M. Hierarchical Nanomanufacturing: From Shaped Zeolite Nanoparticles to High-Performance Separation Membranes. *Angewandte Chemie International Edition* **46**, 7560-7573, doi:10.1002/anie.200604910 (2007).

237 Zhang, W. D., Liu, B. S., Zhu, C. & Tian, Y. Preparation of La2NiO4/ZSM-5 catalyst and catalytic performance in CO2/CH4 reforming to syngas. *Appl. Catal. A-Gen.* **292**, 138-143, doi:10.1016/j.apcata.2005.05.018 (2005).

238 Fernandez, C., Stan, I., Gilson, J. P., Thomas, K., Vicente, A., Bonilla, A. & Perez-Ramirez, J. Hierarchical ZSM-5 Zeolites in Shape-Selective Xylene Isomerization: Role of Mesoporosity and Acid Site Speciation. *Chem.-Eur. J.* **16**, 6224-6233, doi:10.1002/chem.200903426 (2010).

239 Corma, A., Mengual, J. & Miguel, P. J. Steam catalytic cracking of naphtha over ZSM-5 zeolite for production of propene and ethene: Micro and macroscopic implications of the presence of steam. *Appl. Catal. A-Gen.* **417**, 220-235, doi:10.1016/j.apcata.2011.12.044 (2012).

240 Jae, J., Tompsett, G. A., Foster, A. J., Hammond, K. D., Auerbach, S. M., Lobo, R. F. & Huber, G. W. Investigation into the shape selectivity of zeolite catalysts for biomass conversion. *Journal of Catalysis* **279**, 257-268, doi:http://dx.doi.org/10.1016/j.jcat.2011.01.019 (2011).

241 Moliner, M., Rey, F. & Corma, A. Towards the Rational Design of Efficient Organic Structure-Directing Agents for Zeolite Synthesis. *Angewandte Chemie International Edition* **52**, 13880-13889, doi:10.1002/anie.201304713 (2013).

242 Narita, E., Sato, K., Yatabe, N. & Okabe, T. Synthesis and crystal growth of zeolite SZM-5 from sodium aluminosilicate systems free of Hachinohe, Aomori. *Industrial & Engineering Chemistry Product Research and Development* **24**, 507-512, doi:10.1021/i300020a004 (1985).

243 Kim, S. D., Noh, S. H., Park, J. W. & Kim, W. J. Organic-free synthesis of ZSM-5 with narrow crystal size distribution using two-step temperature process. *Microporous and Mesoporous Materials* **92**, 181-188, doi:http://dx.doi.org/10.1016/j.micromeso.2006.01.009 (2006).

244 Chauhan, N. L., Das, J., Jasra, R. V., Parikh, P. A. & Murthy, Z. V. P. Synthesis of small-sized ZSM-5 zeolites employing mixed structure directing agents. *Materials Letters* **74**, 115-117, doi:http://dx.doi.org/10.1016/j.matlet.2012.01.094 (2012).

245 Keoh, S. H., Chaikittisilp, W., Muraoka, K., Mukti, R. R., Shimojima, A., Kumar, P., Tsapatsis, M. & Okubo, T. Factors Governing the Formation of Hierarchically and Sequentially Intergrown MFI Zeolites by Using Simple Diquaternary Ammonium

Structure-Directing Agents. *Chemistry of Materials* **28**, 8997-9007, doi:10.1021/acs.chemmater.6b03887 (2016).

246 Naskar, M. K., Kundu, D. & Chatterjee, M. Synthesis of ZSM-5 Zeolite Particles Using Triethanol Amine as Structure-Directing Agent. *Journal of the American Ceramic Society* **95**, 449-452, doi:10.1111/j.1551-2916.2011.05006.x (2012).

247 Falamaki, C., Edrissi, M. & Sohrabi, M. Studies on the Crystallization Kinetics of Zeolite ZSM-5 With 1,6-Hexanediol as a Structure-Directing Agent. *Zeolites* **19**, 2-5, doi:http://dx.doi.org/10.1016/S0144-2449(97)00025-0 (1997).

248 Aziz, A. & Kim, K. S. Investigation of tertiary butyl alcohol as template for the synthesis of ZSM-5 zeolite. *Journal of Porous Materials* **22**, 1401-1406, doi:10.1007/s10934-015-0019-5 (2015).

249 Moteki, T., Keoh, S. H. & Okubo, T. Synthesis of zeolites using highly amphiphilic cations as organic structure-directing agents by hydrothermal treatment of a dense silicate gel. *Chemical Communications* **50**, 1330-1333, doi:10.1039/c3cc48396g (2014).

250 Xu, D., Feng, J. & Che, S. An insight into the role of the surfactant CTAB in the formation of microporous molecular sieves. *Dalton Transactions* **43**, 3612-3617, doi:10.1039/c3dt53308e (2014).

251 Meng, L., Mezari, B., Goesten, M. G. & Hensen, E. J. M. One-Step Synthesis of Hierarchical ZSM-5 Using Cetyltrimethylammonium as Mesoporogen and Structure-Directing Agent. *Chemistry of Materials* **29**, 4091-4096, doi:10.1021/acs.chemmater.7b00913 (2017).

252 Jin, Y., Li, Y., Zhao, S., Lv, Z., Wang, Q., Liu, X. & Wang, L. Synthesis of mesoporous MOR materials by varying temperature crystallizations and combining ternary organic templates. *Microporous and Mesoporous Materials* **147**, 259-266, doi:https://doi.org/10.1016/j.micromeso.2011.06.023 (2012).

253 Maheshwari, S., Jordan, E., Kumar, S., Bates, F. S., Penn, R. L., Shantz, D. F. & Tsapatsis, M. Layer Structure Preservation during Swelling, Pillaring, and Exfoliation of a Zeolite Precursor. *Journal of the American Chemical Society* **130**, 1507-1516, doi:10.1021/ja077711i (2008).

254 Xu, L., Ji, X., Li, S., Zhou, Z., Du, X., Sun, J., Deng, F., Che, S. & Wu, P. Self-Assembly of Cetyltrimethylammonium Bromide and Lamellar Zeolite Precursor for the Preparation of Hierarchical MWW Zeolite. *Chemistry of Materials* **28**, 4512-4521, doi:10.1021/acs.chemmater.6b02155 (2016).

255 Sabnis, S., Tanna, V. A., Li, C., Zhu, J., Vattipalli, V., Nonnenmann, S. S., Sheng, G., Lai, Z., Winter, H. H. & Fan, W. Exfoliation of two-dimensional zeolites in liquid polybutadienes. *Chemical Communications* **53**, 7011-7014, doi:10.1039/c7cc03256k (2017).

256 Garcia-Martinez, J., Johnson, M., Valla, J., Li, K. & Ying, J. Y. Mesostructured zeolite Y-high hydrothermal stability and superior FCC catalytic performance. *Catalysis Science & Technology* **2**, 987-994, doi:10.1039/c2cy00309k (2012).

257 Ivanova, I. I. & Knyazeva, E. E. Micro-mesoporous materials obtained by zeolite recrystallization: synthesis, characterization and catalytic applications. *Chemical Society Reviews* **42**, 3671-3688, doi:10.1039/c2cs35341e (2013).

258 Garcia-Martinez, J., Xiao, C., Cychosz, K. A., Li, K., Wan, W., Zou, X. & Thommes, M. Evidence of Intracrystalline Mesostructured Porosity in Zeolites by Advanced Gas Sorption, Electron Tomography and Rotation Electron Diffraction. *ChemCatChem* **6**, 3110-3115, doi:10.1002/cctc.201402499 (2014).

259 Garcia-Martinez, J., Li, K. & Krishnaiah, G. A mesostructured Y zeolite as a superior FCC catalyst - from lab to refinery. *Chemical Communications* **48**, 11841-11843, doi:10.1039/c2cc35659g (2012).

260 Ahn, N. H., Seo, S. & Hong, S. B. Small-pore molecular sieves SAPO-57 and SAPO-59: synthesis, characterization, and catalytic properties in methanol-to-olefins conversion. *Catalysis Science & Technology* **6**, 2725-2734, doi:10.1039/c5cy02103k (2016).

261 Lee, J. K., Lee, J. H., Ahn, N. H., Cho, K. H. & Hong, S. B. Solid solution of a zeolite and a framework-bound OSDA-containing molecular sieve. *Chemical Science* **7**, 5805-5814, doi:10.1039/c6sc02092e (2016).

262 Park, M. B., Ahn, S. H., Nicholas, C. P., Lewis, G. J. & Hong, S. B. Charge density mismatch synthesis of zeolite beta in the presence of tetraethylammonium, tetramethylammonium, and sodium ions: Influence of tetraethylammonium decomposition. *Microporous and Mesoporous Materials* **240**, 159-168, doi:10.1016/j.micromeso.2016.11.013 (2017).

263 Jo, D., Ryu, T., Park, G. T., Kim, P. S., Kim, C. H., Nam, I. S. & Hong, S. B. Synthesis of High-Silica LTA and UFI Zeolites and NH3-SCR Performance of Their Copper-Exchanged Form. *Acs Catalysis* **6**, 2443-2447, doi:10.1021/acscatal.6b00489 (2016).

264 Bae, J., Cho, J., Lee, J. H., Seo, S. M. & Hong, S. B. EU-12: A Small-Pore, High-Silica Zeolite Containing Sinusoidal Eight-Ring Channels. *Angewandte Chemie-International Edition* **55**, 7369-7373, doi:10.1002/anie.201600146 (2016).

265 Blackwell, C. S., Broach, R. W., Gatter, M. G., Holmgren, J. S., Jan, D. Y., Lewis, G. J., Mezza, B. J., Mezza, T. M., Miller, M. A., Moscoso, J. G., Patton, R. L., Rohde, L. M., Schoonover, M. W., Sinkler, W., Wilson, B. A. & Wilson, S. T. Open-framework materials synthesized in the TMA(+)/TEA(+) mixed-template system: The new low Si/Al ratio zeolites UZM-4 and UZM-5. *Angewandte Chemie-International Edition* **42**, 1737-1740, doi:10.1002/anie.200250076 (2003).

266 Goepper, M., Li, H. X. & Davis, M. E. A POSSIBLE ROLE OF ALKALI-METAL IONS IN THE SYNTHESIS OF PURE-SILICA MOLECULAR-SIEVES. *Journal of the*

*Chemical Society-Chemical Communications*, 1665-1666, doi:10.1039/c39920001665 (1992).

267 Gabelica, Z., Blom, N. & Derouane, E. G. Synthesis and characterization of zsm-5 type zeolites. *Applied Catalysis* **5**, 227-248, doi:http://dx.doi.org/10.1016/0166-9834(83)80135-3 (1983).

268 Liu, C., Gu, W., Kong, D. & Guo, H. The significant effects of the alkali-metal cations on ZSM-5 zeolite synthesis: From mechanism to morphology. *Microporous and Mesoporous Materials* **183**, 30-36, doi:http://dx.doi.org/10.1016/j.micromeso.2013.08.037 (2014).

269 Seo, Y.-H., Prasetyanto, E. A., Jiang, N., Oh, S.-M. & Park, S.-E. Catalytic dehydration of methanol over synthetic zeolite W. *Microporous and Mesoporous Materials* **128**, 108-114, doi:http://dx.doi.org/10.1016/j.micromeso.2009.08.011 (2010).

270 Valtchev, V. P. & Bozhilov, K. N. Transmission electron microscopy study of the formation of FAU-type zeolite at room temperature. *J. Phys. Chem. B* **108**, 15587-15598, doi:10.1021/jp048341c (2004).

271 Burchart, E. D., vanKoningsveld, H. & vandeGraaf, B. Molecular mechanics studies of TBA and TPA in MEL and MFI. *Microporous Mater* **8**, 215-222 (1997).

272 Yokomori, Y. & Idaka, S. The structure of TPA-ZSM-5 with Si/Al=23. *Microporous and Mesoporous Materials* **28**, 405-413, doi:https://doi.org/10.1016/S1387-1811(98)00311-4 (1999).

273 van Koningsveld, H., van Bekkum, H. & Jansen, J. C. On the location and disorder of the tetrapropylammonium (TPA) ion in zeolite ZSM-5 with improved framework accuracy. *Acta Crystallographica Section B* **43**, 127-132, doi:doi:10.1107/S0108768187098173 (1987).

274 Lewis, D. W., Freeman, C. M. & Catlow, C. R. A. Predicting the Templating Ability of Organic Additives for the Synthesis of Microporous Materials. *The Journal of Physical Chemistry* **99**, 11194-11202, doi:10.1021/j100028a022 (1995).

275 Muraoka, K., Chaikittisilp, W. & Okubo, T. Energy Analysis of Aluminosilicate Zeolites with Comprehensive Ranges of Framework Topologies, Chemical Compositions, and Aluminum Distributions. *Journal of the American Chemical Society* **138**, 6184-6193, doi:10.1021/jacs.6b01341 (2016).

276 Hughes, A. E., Wilshier, K. G., Sexton, B. A. & Smart, P. Aluminum distribution in ZSM-5 as determined by X-Ray photoelectron spectroscopy. *Journal of Catalysis* **80**, 221-227, doi:http://dx.doi.org/10.1016/0021-9517(83)90246-4 (1983).

277 Althoff, R., Schulzdobrick, B., Schuth, F. & Unger, K. CONTROLLING THE SPATIAL-DISTRIBUTION OF ALUMINUM IN ZSM-5 CRYSTALS. *Microporous Mater* **1**, 207-218, doi:10.1016/0927-6513(93)80079-a (1993).

278 Padovan, M., Leofanti, G., Solari, M. & Moretti, E. Studies on the ZSM—5 zeolite formation. *Zeolites* **4**, 295-299, doi:https://doi.org/10.1016/0144-2449(84)90042-3 (1984).

279 Danilina, N., Krumeich, F., Castelanelli, S. A. & van Bokhoven, J. A. Where Are the Active Sites in Zeolites? Origin of Aluminum Zoning in ZSM-5. *The Journal of Physical Chemistry C* **114**, 6640-6645, doi:10.1021/jp1006044 (2010).

280 Wijnen, P. W. J. G., Beelen, T. P. M., de Haan, J. W., Rummens, C. P. J., van de Ven, L. J. M. & van Santen, R. A. Silica gel dissolution in aqueous alkali metal hydroxides studied by 29Si・NMR. *Journal of Non-Crystalline Solids* **109**, 85-94, doi:https://doi.org/10.1016/0022-3093(89)90446-8 (1989).

281 Iler, R. K. EFFECT OF ADSORBED ALUMINA ON SOLUBILITY OF AMORPHOUS SILICA IN WATER. *Journal of Colloid and Interface Science* **43**, 399-408, doi:10.1016/0021-9797(73)90386-x (1973).

282 Ren, N., Subotic, B., Bronic, J., Tang, Y., Sikiric, M. D., Misic, T., Svetlicic, V., Bosnar, S. & Jelic, T. A. Unusual Pathway of Crystallization of Zeolite ZSM-5 in a Heterogeneous

System: Phenomenology and Starting Considerations. *Chemistry of Materials* **24**, 1726-1737, doi:10.1021/cm203194v (2012).

283 De Yoreo, J. J., Gilbert, P., Sommerdijk, N., Penn, R. L., Whitelam, S., Joester, D., Zhang, H. Z., Rimer, J. D., Navrotsky, A., Banfield, J. F., Wallace, A. F., Michel, F. M., Meldrum, F. C., Colfen, H. & Dove, P. M. Crystallization by particle attachment in synthetic, biogenic, and geologic environments. *Science* **349**, doi:10.1126/science.aaa6760 (2015).

284 Li, R., Smolyakova, A., Maayan, G. & Rimer, J. D. Designed Peptoids as Tunable Modifiers of Zeolite Crystallization. *Chemistry of Materials*, doi:10.1021/acs.chemmater.7b03798 (2017).

285 Oleksiak, M. D. & Rimer, J. D. Synthesis of zeolites in the absence of organic structure-directing agents: factors governing crystal selection and polymorphism. *Reviews in Chemical Engineering* **30**, 1-49, doi:10.1515/revce-2013-0020 (2014).

286 Hogan, P. J., Whittam, T. V., Birtill, J. J. & Stewart, A. Synthesis properties and catalytic behaviour of zeolite Nu—10. *Zeolites* **4**, 275-279, doi:http://dx.doi.org/10.1016/0144-2449(84)90038-1 (1984).

287 Larsen, J. W. & Magid, L. J. Calorimetric and counterion binding studies of the interactions between micelles and ions. Observation of lyotropic series. *Journal of the American Chemical Society* **96**, 5774-5782, doi:10.1021/ja00825a013 (1974).

288 Modaressi, A., Sifaoui, H., Grzesiak, B., Solimando, R., Domanska, U. & Rogalski, M. CTAB aggregation in aqueous solutions of ammonium based ionic liquids; conductimetric studies. *Colloids and Surfaces A: Physicochemical and Engineering Aspects* **296**, 104-108, doi:http://dx.doi.org/10.1016/j.colsurfa.2006.09.031 (2007).

289 Linares, N., Sachse, A., Serrano, E., Grau-Atienza, A., De Oliveira Jardim, E., Silvestre-Albero, J., Cordeiro, M. A. L., Fauth, F., Beobide, G., Castillo, O. & García-Martínez, J. In Situ Time-Resolved Observation of the Development of Intracrystalline Mesoporosity

in USY Zeolite. *Chemistry of Materials* **28**, 8971-8979, doi:10.1021/acs.chemmater.6b03688 (2016).

290 Hess, B., Kutzner, C., van der Spoel, D. & Lindahl, E. GROMACS 4: Algorithms for highly efficient, load-balanced, and scalable molecular simulation. *J Chem Theory Comput* **4**, 435-447, doi:10.1021/ct700301q (2008).

291 Cygan, R. T., Liang, J. J. & Kalinichev, A. G. Molecular models of hydroxide, oxyhydroxide, and clay phases and the development of a general force field. *J. Phys. Chem. B* **108**, 1255-1266, doi:10.1021/jp0363287 (2004).

292 Wang, J. M., Wolf, R. M., Caldwell, J. W., Kollman, P. A. & Case, D. A. Development and testing of a general amber force field (vol 25, pg 1157, 2004). *J Comput Chem* **26**, 114-114, doi:10.1002/jcc.20145 (2005).

293 Frenkel, D. & Smit, B. *Understanding molecular simulation : from algorithms to applications*. 2nd edn, (Academic Press, 2002).

294 Bussi, G., Donadio, D. & Parrinello, M. Canonical sampling through velocity rescaling. *J Chem Phys* **126**, 014101, doi:Artn 014101 10.1063/1.2408420 (2007).

295 Parrinello, M. & Rahman, A. Polymorphic Transitions in Single-Crystals - a New Molecular-Dynamics Method. *J Appl Phys* **52**, 7182-7190, doi:Doi 10.1063/1.328693 (1981).

296 Shirts, M. R., Mobley, D. L. & Chodera, J. D. Alchemical free energy calculations: Ready for prime time? *Annual Reports in Computational Chemistry*, 41-59 (2007).

297 Kim, S. B., Palmer, J. C. & Debenedetti, P. G. A Computational Study of the Effect of Matrix Structural Order on Water Sorption by Trp-Cage Miniproteins. *J. Phys. Chem. B* **119**, 1847-1856, doi:10.1021/jp510172w (2015).

298 Kresge, C. T. & Roth, W. J. The discovery of mesoporous molecular sieves from the twenty year perspective. *Chemical Society Reviews* **42**, 3663-3670 (2013).

299 Kresge, C., Leonowicz, M., Roth, W. J., Vartuli, J. & Beck, J. Ordered mesoporous molecular sieves synthesized by a liquid-crystal template mechanism. *Nature* **359**, 710 (1992).

300 Perego, C. & Millini, R. Porous materials in catalysis: challenges for mesoporous materials. *Chemical Society Reviews* **42**, 3956-3976 (2013).

301 Linares, N., Silvestre-Albero, A. M., Serrano, E., Silvestre-Albero, J. & Garcia-Martinez, J. Mesoporous materials for clean energy technologies. *Chemical Society Reviews* **43**, 7681-7717 (2014).

302 Van Der Voort, P., Esquivel, D., De Canck, E., Goethals, F., Van Driessche, I. & Romero-Salguero, F. J. Periodic mesoporous organosilicas: from simple to complex bridges; a comprehensive overview of functions, morphologies and applications. *Chemical Society Reviews* **42**, 3913-3955 (2013).

303 Hatton, B., Landskron, K., Whitnall, W., Perovic, D. & Ozin, G. A. Past, present, and future of periodic mesoporous organosilicas the PMOs. *Accounts of chemical research* **38**, 305-312 (2005).

304 García-Martínez, J., Lancaster, T. M. & Ying, J. Y. Synthesis and Catalytic Applications of Self-Assembled Carbon Nanofoams. *Advanced Materials* **20**, 288-292 (2008).

305 Meng, Y., Gu, D., Zhang, F., Shi, Y., Yang, H., Li, Z., Yu, C., Tu, B. & Zhao, D. Ordered mesoporous polymers and homologous carbon frameworks: amphiphilic surfactant templating and direct transformation. *Angewandte Chemie International Edition* **44**, 7053-7059 (2005).

306 Sachse, A. & Garcia-Martinez, J. Surfactant-templating of zeolites: from design to application. *Chemistry of Materials* **29**, 3827-3853 (2017).

307 Prasomsri, T., Jiao, W., Weng, S. Z. & Martinez, J. G. Mesostructured zeolites: bridging the gap between zeolites and MCM-41. *Chemical Communications* **51**, 8900-8911 (2015).

308 Davis, M. E. *Mesoporous zeolites: preparation, characterization and applications*. (John Wiley & Sons, 2015).

309 Pérez-Ramírez, J., Christensen, C. H., Egeblad, K., Christensen, C. H. & Groen, J. C. Hierarchical zeolites: enhanced utilisation of microporous crystals in catalysis by advances in materials design. *Chemical Society Reviews* **37**, 2530-2542 (2008).

310 Serrano, D. & Pizarro, P. Synthesis strategies in the search for hierarchical zeolites. *Chemical Society Reviews* **42**, 4004-4035 (2013).

311 Ying, J. Y. & Martinez, J. G. (Google Patents, 2009).

312 García-Martínez, J., Johnson, M., Valla, J., Li, K. & Ying, J. Y. Mesostructured zeolite Y—high hydrothermal stability and superior FCC catalytic performance. *Catalysis Science & Technology* **2**, 987-994 (2012).

313 García-Martínez, J., Li, K. & Krishnaiah, G. A mesostructured Y zeolite as a superior FCC catalyst–from lab to refinery. *Chemical Communications* **48**, 11841-11843 (2012).

314 Thomas, J. M. & Leary, R. K. A Major Advance in Characterizing Nanoporous Solids Using a Complementary Triad of Existing Techniques. *Angewandte Chemie International Edition* **53**, 12020-12021 (2014).

315 Sachse, A., Grau-Atienza, A., Jardim, E. O., Linares, N., Thommes, M. & Garcia-Martinez, J. Development of intracrystalline mesoporosity in zeolites through surfactant-templating. *Crystal Growth & Design* **17**, 4289-4305 (2017).

316 Linares, N., Jardim, E. O., Sachse, A., Serrano, E. & García-Martínez, J. The Energetics of Surfactant-Templating of Zeolites. *Angewandte Chemie International Edition* **57**, 8724-8728 (2018).

317 Kumar, M., Choudhary, M. K. & Rimer, J. D. Transient modes of zeolite surface growth from 3D gel-like islands to 2D single layers. *Nature communications* **9**, 2129 (2018).

318 Mandemaker, L. D. B., Filez, M., Delen, G., Tan, H., Zhang, X., Lohse, D. & Weckhuysen, B. M. Time-Resolved In Situ Liquid-Phase Atomic Force Microscopy and Infrared

Nanospectroscopy during the Formation of Metal–Organic Framework Thin Films. *The Journal of Physical Chemistry Letters* **9**, 1838-1844, doi:10.1021/acs.jpclett.8b00203 (2018).

319 Kenvin, J., Mitchell, S., Sterling, M., Warringham, R., Keller, T. C., Crivelli, P., Jagiello, J. & Pérez-Ramírez, J. Quantifying the complex pore architecture of hierarchical faujasite zeolites and the impact on diffusion. *Advanced Functional Materials* **26**, 5621-5630 (2016).

320 Thommes, M., Kaneko, K., Neimark, A. V., Olivier, J. P., Rodriguez-Reinoso, F., Rouquerol, J. & Sing, K. S. Physisorption of gases, with special reference to the evaluation of surface area and pore size distribution (IUPAC Technical Report). *Pure and Applied Chemistry* **87**, 1051-1069 (2015).

321 Mehlhorn, D., Rodriguez, J., Cacciaguerra, T., Andrei, R.-D., Cammarano, C., Guenneau, F., Gedeon, A., Coasne, B., Thommes, M., Minoux, D., Aquino, C., Dath, J.-P., Fajula, F. & Galarneau, A. Revelation on the Complex Nature of Mesoporous Hierarchical FAU-Y Zeolites. *Langmuir* **34**, 11414-11423, doi:10.1021/acs.langmuir.8b03010 (2018).

322 Agudelo, J., Hensen, E., Giraldo, S. & Hoyos, L. Influence of steam-calcination and acid leaching treatment on the VGO hydrocracking performance of faujasite zeolite. *Fuel Processing Technology* **133**, 89-96 (2015).

323 Agudelo, J., Mezari, B., Hensen, E., Giraldo, S. & Hoyos, L. On the effect of EDTA treatment on the acidic properties of USY zeolite and its performance in vacuum gas oil hydrocracking. *Applied Catalysis A: General* **488**, 219-230 (2014).

324 Zhang, Z., Liu, X., Xu, Y. & Xu, R. Realumination of dealuminated zeolites Y. *Zeolites* **11**, 232-238 (1991).

325 Calsavara, V., Sousa-Aguiar, E. F. & Machado, N. R. F. Reactivity of USY extraframework alumina in alkaline medium. *Zeolites* **17**, 340-345 (1996).

326 Menezes, S., Camorim, V., Lam, Y., San Gil, R., Bailly, A. & Amoureux, J. Characterization of extra-framework species of steamed and acid washed faujasite by MQMAS NMR and IR measurements. *Applied Catalysis A: General* **207**, 367-377 (2001).

327 Katada, N., Nakata, S., Kato, S., Kanehashi, K., Saito, K. & Niwa, M. Detection of active sites for paraffin cracking on USY zeolite by 27Al MQMAS NMR operated at high magnetic field 16 T. *Journal of Molecular Catalysis A: Chemical* **236**, 239-245 (2005).

328 Malicki, N., Mali, G., Quoineaud, A.-A., Bourges, P., Simon, L. J., Thibault-Starzyk, F. & Fernandez, C. Aluminium triplets in dealuminated zeolites detected by 27Al NMR correlation spectroscopy. *Microporous and Mesoporous Materials* **129**, 100-105 (2010).

329 Cychosz, K. A., Guillet-Nicolas, R., Garcia-Martinez, J. & Thommes, M. Recent advances in the textural characterization of hierarchically structured nanoporous materials. *Chemical Society Reviews* **46**, 389-414 (2017).

330 Hartmann, M., Machoke, A. G. & Schwieger, W. Vol. 45 3313-3330 (2016).

331 Awala, H., Gilson, J. P., Retoux, R., Boullay, P., Goupil, J. M., Valtchev, V. & Mintova, S. Template-free nanosized faujasite-type zeolites. *Nature Materials* **14**, 447-451, doi:10.1038/nmat4173 (2015).

332 Choi, M., Na, K., Kim, J., Sakamoto, Y., Terasaki, O. & Ryoo, R. Stable single-unit-cell nanosheets of zeolite MFI as active and long-lived catalysts. *Nature* **461**, 828-828, doi:10.1038/nature08493 (2009).

333 Kärger, J., Crivelli, P., Pérez-Ramírez, J., Mitchell, S., Pinar, A. B. & Kenvin, J. Structural analysis of hierarchically organized zeolites. *Nature Communications* **6**, doi:10.1038/ncomms9633 (2015).

334 Ma, Y., Han, L., Singh, B., Shen, X., Terasaki, O., Xu, D., Cao, F., Oleynikov, P., Jing, Z., Che, S., Sun, H. & Feng, J. π–π interaction of aromatic groups in amphiphilic molecules directing for single-crystalline mesostructured zeolite nanosheets. *Nature Communications* **5**, doi:10.1038/ncomms5262 (2014).

335 Sachse, A. & García-Martínez, J. Vol. 29 3827-3853 (2017).

336 Zhang, Y. & Che, S. π-π Interactions of Aromatic Groups in Amphiphilic Molecules for Directing Hierarchical Porous Zeolites. *Angewandte Chemie International Edition*, doi:10.1002/anie.201903364 (2019).

337 Grand, J., Talapaneni, S. N., Vicente, A., Fernandez, C., Dib, E., Aleksandrov, H. A., Vayssilov, G. N., Retoux, R., Boullay, P., Gilson, J. P., Valtchev, V. & Mintova, S. One-pot synthesis of silanol-free nanosized MFI zeolite. *Nature Materials* **16**, 1010-1015, doi:10.1038/nmat4941 (2017).

338 Jacobsen, C. J., Madsen, C., Houzvicka, J., Schmidt, I. & Carlsson, A. Mesoporous zeolite single crystals. *Journal of the American Chemical Society* **122**, 7116-7117 (2000).

339 Holland, B. T., Abrams, L. & Stein, A. Dual templating of macroporous silicates with zeolitic microporous frameworks. *Journal of the American Chemical Society* **121**, 4308-4309 (1999).

340 Garcıa-Martınez, J., Johnson, M., Valla, J., Li, K. & Ying, J. Mesostructured zeolite Y–high hydrothermal stability and superior FCC performance. *Catal. Sci. Technol* **2**, 987-994 (2012).

341 Groen, J. C., Bach, T., Ziese, U., Paulaime-van Donk, A. M., De Jong, K. P., Moulijn, J. A. & Pérez-Ramírez, J. Creation of hollow zeolite architectures by controlled desilication of Al-zoned ZSM-5 crystals. *Journal of the American Chemical Society* **127**, 10792-10793 (2005).

342 Lee, E. F. & Rees, L. V. Dealumination of sodium Y zeolite with hydrochloric acid. *Journal of the Chemical Society, Faraday Transactions 1: Physical Chemistry in Condensed Phases* **83**, 1531-1537 (1987).

343 Zhang, X., Liu, D., Xu, D., Asahina, S., Cychosz, K. A., Agrawal, K. V., Al Wahedi, Y., Bhan, A., Al Hashimi, S. & Terasaki, O. Synthesis of self-pillared zeolite nanosheets by repetitive branching. *Science* **336**, 1684-1687 (2012).

344 Khaleel, M., Wagner, A. J., Mkhoyan, K. A. & Tsapatsis, M. On the rotational intergrowth of hierarchical FAU/EMT zeolites. *Angewandte Chemie International Edition* **53**, 9456-9461 (2014).

345 Roth, W. J., Nachtigall, P., Morris, R. E., Wheatley, P. S., Seymour, V. R., Ashbrook, S. E., Chlubná, P., Grajciar, L., Položij, M., Zukal, A., Shvets, O. & Čejka, J. A family of zeolites with controlled pore size prepared using a top-down method. *Nature Chemistry* **5**, 628-633, doi:10.1038/nchem.1662 (2013).

346 Mazur, M., Wheatley, P. S., Navarro, M., Roth, W. J., Položij, M., Mayoral, A., Eliášová, P., Nachtigall, P., Čejka, J. & Morris, R. E. J. N. c. Synthesis of 'unfeasible'zeolites. **8**, 58-62 (2016).

347 Kumar, P., Kim, D. W., Rangnekar, N., Xu, H., Fetisov, E. O., Ghosh, S., Zhang, H., Xiao, Q., Shete, M. & Siepmann, J. I. One-dimensional intergrowths in two-dimensional zeolite nanosheets and their effect on ultra-selective transport. *Nature Materials*, 1-7 (2020).

348 Inayat, A., Knoke, I., Spiecker, E. & Schwieger, W. Assemblies of mesoporous FAU-type zeolite nanosheets. *Angewandte Chemie International Edition* **51**, 1962-1965 (2012).

349 Khaleel, M., Wagner, A. J., Mkhoyan, K. A. & Tsapatsis, M. On the rotational intergrowth of hierarchical FAU/EMT zeolites. *Angewandte Chemie - International Edition* **53**, 9456-9461, doi:10.1002/anie.201402024 (2014).

350 Gaber, S., Gaber, D., Ismail, I., Alhassan, S. M. & Khaleel, M. Additive-free Synthesis of House-of-Card Faujasite Zeolite by Utilizing Aluminosilicate Gel Memory. *CrystEngComm*, doi:10.1039/c8ce01804a (2019).

351 Corma, A., Li, C. & Moliner, M. Building zeolites from pre-crystallized units: nanoscale architecture. *Angewandte Chemie International Edition*, doi:10.1002/anie.201711422 (2018).

352 Jain, R. & Rimer, J. D. Seed-Assisted Zeolite Synthesis: The Impact of Seeding Conditions and Interzeolite Transformations on Crystal Structure and Morphology. *Microporous and*

*Mesoporous Materials*, 110174, doi:https://doi.org/10.1016/j.micromeso.2020.110174 (2020).

353 Grand, J., Awala, H. & Mintova, S. Mechanism of zeolites crystal growth: new findings and open questions. *CrystEngComm* **18**, 650-664, doi:10.1039/c5ce02286j (2016).

354 Vorontsova, M. A., Maes, D. & Vekilov, P. G. Recent advances in the understanding of two-step nucleation of protein crystals. *Faraday Discussions* **179**, 27-40, doi:10.1039/c4fd00217b (2015).

355 De Yoreo, J. J., Gilbert, P. U. P. A., Sommerdijk, N. A. J. M., Penn, R. L., Whitelam, S., Joester, D., Zhang, H., Rimer, J. D., Navrotsky, A., Banfield, J. F., Wallace, A. F., Michel, F. M., Meldrum, F. C., Cölfen, H. & Dove, P. M. Vol. 349 (2015).

356 Qin, W., Jain, R., Robles Hernández, F. C. & Rimer, J. D. Organic-Free Interzeolite Transformation in the Absence of Common Building Units. *Chemistry – A European Journal* **25**, 5893-5898, doi:10.1002/chem.201901067 (2019).

357 Santos, B. P. S., Almeida, N. C., Santos, I. S., Maria de Fátima, V. M. & Fernandes, L. D. Synthesis and Characterization of Mesoporous Mordenite Zeolite Using Soft Templates. *Catalysis Letters* **148**, 1870-1878 (2018).

358 Maldonado, M., Oleksiak, M. D., Chinta, S. & Rimer, J. D. Controlling crystal polymorphism in organic-free synthesis of Na-zeolites. *Journal of the American Chemical Society* **135**, 2641-2652 (2013).

359 Petrovic, I., Navrotsky, A., Davis, M. E. & Zones, S. I. Thermochemical study of the stability of frameworks in high silica zeolites. *Chemistry of Materials* **5**, 1805-1813 (1993).

360 Zhang, H., Zhang, H., Zhao, Y., Shi, Z., Zhang, Y. & Tang, Y. Seeding Bundlelike MFI Zeolite Mesocrystals: A Dynamic, Nonclassical Crystallization via Epitaxially Anisotropic Growth. *Chemistry of Materials* **29**, 9247-9255, doi:10.1021/acs.chemmater.7b03121 (2017).

361 Zhang, H., Zhao, Y., Zhang, H., Wang, P., Shi, Z., Mao, J., Zhang, Y. & Tang, Y. Tailoring Zeolite ZSM-5 Crystal Morphology/Porosity through Flexible Utilization of Silicalite-1 Seeds as Templates: Unusual Crystallization Pathways in a Heterogeneous System. *Chemistry–A European Journal* **22**, 7141-7151 (2016).

362 Hedström, A. J. J. o. e. e. Ion exchange of ammonium in zeolites: a literature review. **127**, 673-681 (2001).

363 Serrano, D. P., Escola, J. M. & Pizarro, P. Synthesis strategies in the search for hierarchical zeolites. *Chem. Soc. Rev.* **42**, 4004-4035, doi:10.1039/c2cs35330j (2013).

364 Ilias, S., Khare, R., Malek, A. & Bhan, A. A descriptor for the relative propagation of the aromatic-and olefin-based cycles in methanol-to-hydrocarbons conversion on H-ZSM-5. *Journal of Catalysis* **303**, 135-140 (2013).

365 Khare, R., Millar, D. & Bhan, A. A mechanistic basis for the effects of crystallite size on light olefin selectivity in methanol-to-hydrocarbons conversion on MFI. *Journal of Catalysis* **321**, 23-31 (2015).

366 Khare, R., Liu, Z., Han, Y. & Bhan, A. A mechanistic basis for the effect of aluminum content on ethene selectivity in methanol-to-hydrocarbons conversion on HZSM-5. *Journal of Catalysis* **348**, 300-305 (2017).

367 Shen, Y., Le, T. T., Fu, D., Schmidt, J. E., Filez, M., Weckhuysen, B. M. & Rimer, J. D. Deconvoluting the Competing Effects of Zeolite Framework Topology and Diffusion Path Length on Methanol to Hydrocarbons Reaction. *ACS Catalysis* **8**, 11042-11053, doi:10.1021/acscatal.8b02274 (2018).

368 Piccione, P. M. & Davis, M. E. A new structure-directing agent for the synthesis of pure-phase ZSM-11. *Microporous and mesoporous materials* **49**, 163-169 (2001).

369 Shen, Y., Le, T. T., Li, R. & Rimer, J. D. Optimized Synthesis of ZSM-11 Catalysts using 1, 8-Diaminooctane as a Structure-Directing Agent. *ChemPhysChem* **19**, 529-537 (2018).

370 Čižmek, A., Subotić, B., Aiello, R., Crea, F., Nastro, A. & Tuoto, C. Dissolution of high-silica zeolites in alkaline solutions I. Dissolution of silicalite-1 and ZSM-5 with different aluminum content. *Microporous Mater* **4**, 159-168 (1995).

371 Keijsper, J. J. & Post, M. F. M. in *Zeolite Synthesis* Vol. 398 *ACS Symposium Series* Ch. 3, 28-48 (American Chemical Society, 1989).

372 Rimer, J. D., Chawla, A. & Le, T. T. Crystal Engineering for Catalysis. *Annual Review of Chemical and Biomolecular Engineering*, doi:10.1146/annurev-chembioeng-060817-083953 (2018).

373 De Yoreo, J. J., Gilbert, P. U. P. A., Sommerdijk, N. A. J. M., Penn, R. L., Whitelam, S., Joester, D., Zhang, H., Rimer, J. D., Navrotsky, A., Banfield, J. F., Wallace, A. F., Michel, F. M., Meldrum, F. C., Cölfen, H. & Dove, P. M. Crystallization by particle attachment in synthetic, biogenic, and geologic environments. *Science* **349** (2015).

374 Liao, H.-G., Cui, L., Whitelam, S. & Zheng, H. Real-Time Imaging of Pt<sub>3</sub>Fe Nanorod Growth in Solution. *Science* **336**, 1011 (2012).

375 Habraken, W., Tao, J. H., Brylka, L. J., Friedrich, H., Bertinetti, L., Schenk, A. S., Verch, A., Dmitrovic, V., Bomans, P. H. H., Frederik, P. M., Laven, J., van der Schoot, P., Aichmayer, B., de With, G., DeYoreo, J. J. & Sommerdijk, N. Ion-association complexes unite classical and non-classical theories for the biomimetic nucleation of calcium phosphate. *Nature Communications* **4**, doi:10.1038/ncomms2490 (2013).

376 Mukherjee, S., Kim, K. & Nair, S. Short, Highly Ordered, Single-Walled Mixed-Oxide Nanotubes Assemble from Amorphous Nanoparticles. *Journal of the American Chemical Society* **129**, 6820-6826, doi:10.1021/ja070124c (2007).

377 Nielsen, M. H., Aloni, S. & De Yoreo, J. J. In situ TEM imaging of CaCO<sub>3</sub> nucleation reveals coexistence of direct and indirect pathways. *Science* **345**, 1158 (2014).

378 Li, D., Nielsen, M. H., Lee, J. R. I., Frandsen, C., Banfield, J. F. & De Yoreo, J. J. Direction-Specific Interactions Control Crystal Growth by Oriented Attachment. *Science* **336**, 1014 (2012).

379 Valtchev, V. P. & Bozhilov, K. N. Transmission electron microscopy study of the formation of FAU-type zeolite at room temperature. *The Journal of Physical Chemistry B* **108**, 15587-15598 (2004).

380 Valtchev, V., Rigolet, S. & Bozhilov, K. N. Gel evolution in a FAU-type zeolite yielding system at 90°C. *Microporous and Mesoporous Materials* **101**, 73-82, doi:https://doi.org/10.1016/j.micromeso.2006.10.016 (2007).

381 Chang, C. D. & Bell, A. T. Studies on the mechanism of ZSM-5 formation. *Catalysis Letters* **8**, 305-316, doi:10.1007/bf00764192 (1991).

382 Chen, Qiao, Xie, Fan, Zhou & He. Self-Construction of Core−Shell and Hollow Zeolite Analcime Icositetrahedra: A Reversed Crystal Growth Process via Oriented Aggregation of Nanocrystallites and Recrystallization from Surface to Core. *Journal of the American Chemical Society* **129**, 13305-13312, doi:10.1021/ja074834u (2007).

383 Vekilov, P. G. Dense Liquid Precursor for the Nucleation of Ordered Solid Phases from Solution. *Crystal Growth & Design* **4**, 671-685, doi:10.1021/cg049977w (2004).

384 Vekilov, P. G. Two-step mechanism for the nucleation of crystals from solution. *Journal of Crystal Growth* **275**, 65-76, doi:https://doi.org/10.1016/j.jcrysgro.2004.10.068 (2005).

385 Walton, R. I., Millange, F., O'Hare, D., Davies, A. T., Sankar, G. & Catlow, C. R. A. An in Situ Energy-Dispersive X-ray Diffraction Study of the Hydrothermal Crystallization of Zeolite A. 1. Influence of Reaction Conditions and Transformation into Sodalite. *The Journal of Physical Chemistry B* **105**, 83-90, doi:10.1021/jp002711p (2001).

386 Burkett, S. L. & Davis, M. E. Mechanism of Structure Direction in the Synthesis of Si-ZSM-5: An Investigation by Intermolecular 1H-29Si CP MAS NMR. *The Journal of Physical Chemistry* **98**, 4647-4653, doi:10.1021/j100068a027 (1994).

387 Hench, L. L. & West, J. K. The sol-gel process. *Chemical Reviews* **90**, 33-72, doi:10.1021/cr00099a003 (1990).

388 Iler, R. K. The Chemistry of Silica: Solubility, Polymerization, Colloid and Surface Properties and Biochemistry of Silica. (1979).

389 Brinker, C. S., G. Sol-Gel Science: The Physics and Chemistry of Sol-Gel Processing. (1990).

390 Feinle, A., Elsaesser, M. S. & Husing, N. Sol-gel synthesis of monolithic materials with hierarchical porosity. *Chemical Society Reviews* **45**, 3377-3399, doi:10.1039/c5cs00710k (2016).

391 Tian, T., Zeng, Z., Vulpe, D., Casco, M. E., Divitini, G., Midgley, P. A., Silvestre-Albero, J., Tan, J.-C., Moghadam, P. Z. & Fairen-Jimenez, D. A sol–gel monolithic metal–organic framework with enhanced methane uptake. *Nature Materials* **17**, 174, doi:10.1038/nmat5050https://www.nature.com/articles/nmat5050#supplementary-information (2017).

392 Flory, P. J. Introductory lecture. *Faraday Discussions of the Chemical Society* **57**, 7-18, doi:10.1039/dc9745700007 (1974).

393 Estroff, L. A. & Hamilton, A. D. Water Gelation by Small Organic Molecules. *Chemical Reviews* **104**, 1201-1218, doi:10.1021/cr0302049 (2004).

394 Fan, W., Meneau, F., Bras, W., Ogura, M., Sankar, G. & Okubo, T. Effects of silicon sources on the formation of nanosized LTA: An in situ small angle X-ray scattering and wide angle X-ray scattering study. *Microporous and Mesoporous Materials* **101**, 134-141, doi:https://doi.org/10.1016/j.micromeso.2006.10.007 (2007).

395 Zhu, G., Qiu, S., Yu, J., Sakamoto, Y., Xiao, F., Xu, R. & Terasaki, O. Synthesis and Characterization of High-Quality Zeolite LTA and FAU Single Nanocrystals. *Chemistry of Materials* **10**, 1483-1486, doi:10.1021/cm980061k (1998).

396 Ravishankar, R., Kirschhock, C. E. A., Knops-Gerrits, P. P., Feijen, E. J. P., Grobet, P. J., Vanoppen, P., De Schryver, F. C., Miehe, G., Fuess, H., Schoeman, B. J., Jacobs, P. A. & Martens, J. A. Characterization of nanosized material extracted from clear suspensions for MFI zeolite synthesis. *J. Phys. Chem. B* **103**, 4960-4964, doi:10.1021/jp990296z (1999).

397 Kirschhock, C. E. A., Ravishankar, R., Jacobs, P. A. & Martens, J. A. Aggregation mechanism of nanoslabs with zeolite MFI-type structure. *J. Phys. Chem. B* **103**, 11021-11027, doi:10.1021/jp992272y (1999).

398 Houssin, C. J. Y., Mojet, B. L., Kirschhock, C. E. A., Buschmann, V., Jacobs, P. A., Martens, J. A. & van Santen, R. A. in *Studies in Surface Science and Catalysis* Vol. 135 (eds A. Galarneau, F. Fajula, F. Di Renzo, & J. Vedrine) 140 (Elsevier, 2001).

399 Brinker, C. J. Hydrolysis and condensation of silicates: Effects on structure. *Journal of Non-Crystalline Solids* **100**, 31-50, doi:https://doi.org/10.1016/0022-3093(88)90005-1 (1988).

400 Cihlář, J. Hydrolysis and polycondensation of ethyl silicates. 1. Effect of pH and catalyst on the hydrolysis and polycondensation of tetraethoxysilane (TEOS). *Colloids and Surfaces A: Physicochemical and Engineering Aspects* **70**, 239-251, doi:https://doi.org/10.1016/0927-7757(93)80298-S (1993).

401 Buckley, A. M. & Greenblatt, M. The Sol-Gel Preparation of Silica Gels. *Journal of Chemical Education* **71**, 599, doi:10.1021/ed071p599 (1994).

402 Sefcik, J. & McCormick, A. V. Thermochemistry of aqueous silicate solution precursors to ceramics. *Aiche Journal* **43**, 2773-2784, doi:10.1002/aic.690431324 (1997).

403 Rimer, J. D., Vlachos, D. G. & Lobo, R. F. Evolution of Self-Assembled Silica−Tetrapropylammonium Nanoparticles at Elevated Temperatures. *The Journal of Physical Chemistry B* **109**, 12762-12771, doi:10.1021/jp052045y (2005).

404 Fedeyko, J. *Silica Self-Assembly in Basic Aqueous Solutions* Ph. D thesis, University of Delaware, (2006).

405 Rimer, J. D., Trofymluk, O., Lobo, R. F., Navrotsky, A. & Vlachos, D. G. Thermodynamics of Silica Nanoparticle Self-Assembly in Basic Solutions of Monovalent Cations. *The Journal of Physical Chemistry C* **112**, 14754-14761, doi:10.1021/jp802902x (2008).

406 Rivas-Cardona, A. & Shantz, D. F. In Situ PFG NMR of Silicalite-1 Synthesis Mixtures. *The Journal of Physical Chemistry C* **115**, 13016-13026, doi:10.1021/jp203298m (2011).

407 Rimer, J. D., Trofymluk, O., Navrotsky, A., Lobo, R. F. & Vlachos, D. G. Kinetic and Thermodynamic Studies of Silica Nanoparticle Dissolution. *Chemistry of Materials* **19**, 4189-4197, doi:10.1021/cm070708d (2007).

408 Sharma, P., Yeo, J.-g., Han, M. H. & Cho, C. H. Knobby surfaced, mesoporous, single-phase GIS-NaP1 zeolite microsphere synthesis and characterization for H2 gas adsorption. *Journal of Materials Chemistry A* **1**, 2602-2612, doi:10.1039/c2ta01311h (2013).

409 Lok, B. M., Cannan, T. R. & Messina, C. A. The role of organic molecules in molecular sieve synthesis. *Zeolites* **3**, 282-291, doi:https://doi.org/10.1016/0144-2449(83)90169-0 (1983).

410 Lowe, B. M. An equilibrium model for the crystallization of high silica zeolites. *Zeolites* **3**, 300-305, doi:https://doi.org/10.1016/0144-2449(83)90173-2 (1983).

411 Caratzoulas, S., Vlachos, D. G. & Tsapatsis, M. Molecular Dynamics Studies on the Role of Tetramethylammonium Cations in the Stability of the Silica Octamers Si8 in Solution. *The Journal of Physical Chemistry B* **109**, 10429-10434, doi:10.1021/jp0500891 (2005).

412 Alexander, G. B., Heston, W. M. & Iler, R. K. The Solubility of Amorphous Silica in Water. *The Journal of Physical Chemistry* **58**, 453-455, doi:10.1021/j150516a002 (1954).

413 Fleming, B. A. & Crerar, D. A. Silicic acid ionization and calculation of silica solubility at elevated temperature and pH application to geothermal fluid processing and reinjection. *Geothermics* **11**, 15-29, doi:https://doi.org/10.1016/0375-6505(82)90004-9 (1982).

414 Chan, S. H. A review on solubility and polymerization of silica. *Geothermics* **18**, 49-56, doi:10.1016/0375-6505(89)90009-6 (1989).

415 Gunnarsson, I. & Arnórsson, S. Amorphous silica solubility and the thermodynamic properties of H4SiO4° in the range of 0°to 350°C at P(sat). *Geochimica et Cosmochimica Acta* **64**, 2295-2307, doi:10.1016/s0016-7037(99)00426-3 (2000).

416 Niibori, Y., Kunita, M., Tochiyama, O. & Chida, T. Dissolution Rates of Amorphous Silica in Highly Alkaline Solution. *Journal of Nuclear Science and Technology* **37**, 349-357, doi:10.1080/18811248.2000.9714905 (2000).

417 Busey, R. H. & Mesmer, R. E. IONIZATION EQUILIBRIA OF SILICIC-ACID AND POLYSILICATE FORMATION IN AQUEOUS SODIUM-CHLORIDE SOLUTIONS TO 300-DEGREES-C. *Inorg. Chem.* **16**, 2444-2450, doi:10.1021/ic50176a004 (1977).

418 Addai-Mensah, J., Li, J., Rosencrance, S. & Wilmarth, W. Solubility of Amorphous Sodium Aluminosilicate and Zeolite A Crystals in Caustic and Nitrate/Nitrite-Rich Caustic Aluminate Liquors. *Journal of Chemical & Engineering Data* **49**, 1682-1687, doi:10.1021/je049889f (2004).

419 Ejaz, T., Jones, A. G. & Graham, P. Solubility of Zeolite A and Its Amorphous Precursor under Synthesis Conditions. *Journal of Chemical & Engineering Data* **44**, 574-576, doi:10.1021/je980164j (1999).

420 Iler, R. K. Effect of adsorbed alumina on the solubility of amorphous silica in water. *Journal of Colloid and Interface Science* **43**, 399-408, doi:https://doi.org/10.1016/0021-9797(73)90386-X (1973).

421 Prodinger, S., Vjunov, A., Hu, J. Z., Fulton, J. L., Camaioni, D. M., Derewinski, M. A. & Lercher, J. A. Elementary steps of faujasite formation followed by in situ spectroscopy. *Chemistry of Materials* **30**, 888-897 (2018).

422 Flory, P. J. (Cornell University Press, Ithaca, NY, 1953).

423 Shen, Y., Le Thuy, T., Li, R. & Rimer Jeffrey, D. Optimized Synthesis of ZSM-11 Catalysts using 1,8-Diaminooctane as a Structure-Directing Agent. *ChemPhysChem* **19**, 529-537, doi:10.1002/cphc.201700968 (2017).

424 Toby, B. H. & Von Dreele, R. B. GSAS-II: the genesis of a modern open-source all purpose crystallography software package. *Journal of Applied Crystallography* **46**, 544-549, doi:doi:10.1107/S0021889813003531 (2013).

425 Qiu, X., Thompson, J. W. & Billinge, S. J. L. PDFgetX2: a GUI-driven program to obtain the pair distribution function from X-ray powder diffraction data. *Journal of Applied Crystallography* **37**, 678 (2004).

426 Rimer, J. D., Chawla, A. & Le, T. T. Crystal Engineering for Catalysis. *Annual review of chemical and biomolecular engineering* **9**, 283-309 (2018).

427 Davis, T. M., Drews, T. O., Ramanan, H., He, C., Dong, J., Schnablegger, H., Katsoulakis, M. A., Kokkoli, E., McCormick, A. V. & Penn, R. L. Mechanistic principles of nanoparticle evolution to zeolite crystals. *Nature materials* **5**, 400 (2006).

428 Mintova, S., Olson, N. H., Valtchev, V. & Bein, T. Mechanism of zeolite A nanocrystal growth from colloids at room temperature. *Science* **283**, 958-960 (1999).

429 Valtchev, V., Rigolet, S. & Bozhilov, K. N. Gel evolution in a FAU-type zeolite yielding system at 90 C. *Microporous and Mesoporous Materials* **101**, 73-82 (2007).

430 Chang, C. D. & Bell, A. T. Studies on the mechanism of ZSM-5 formation. *Catalysis Letters* **8**, 305-316 (1991).

431 Ren, N., Subotić, B., Bronić, J., Tang, Y., Dutour Sikirić, M., Mišić, T., Svetličić, V., Bosnar, S. & Antonić Jelić, T. Unusual pathway of crystallization of zeolite ZSM-5 in a heterogeneous system: phenomenology and starting considerations. *Chemistry of Materials* **24**, 1726-1737 (2012).

432 Melinte, G., Georgieva, V., Springuel-Huet, M. A., Nossov, A., Ersen, O., Guenneau, F., Gedeon, A., Palčić, A., Bozhilov, K. N. & Pham-Huu, C. 3D study of the morphology and dynamics of zeolite nucleation. *Chemistry–A European Journal* **21**, 18316-18327 (2015).

433 Zheng, H., Smith, R. K., Jun, Y.-w., Kisielowski, C., Dahmen, U. & Alivisatos, A. P. Observation of single colloidal platinum nanocrystal growth trajectories. *Science* **324**, 1309-1312 (2009).

434 Vorontsova, M. A., Maes, D. & Vekilov, P. G. Recent advances in the understanding of two-step nucleation of protein crystals. *Faraday discussions* **179**, 27-40 (2015).

435 Tsarfati, Y., Rosenne, S., Weissman, H., Shimon, L. J., Gur, D., Palmer, B. A. & Rybtchinski, B. Crystallization of Organic Molecules: Nonclassical Mechanism Revealed by Direct Imaging. *ACS central science* **4**, 1031-1036 (2018).

436 De Yoreo, J. J., Gilbert, P. U., Sommerdijk, N. A., Penn, R. L., Whitelam, S., Joester, D., Zhang, H., Rimer, J. D., Navrotsky, A. & Banfield, J. F. Crystallization by particle attachment in synthetic, biogenic, and geologic environments. *Science* **349**, aaa6760 (2015).

437 Jehannin, M., Rao, A. & Cölfen, H. New horizons of nonclassical crystallization. *Journal of the American Chemical Society* **141**, 10120-10136 (2019).

438 Li, D., Soberanis, F., Fu, J., Hou, W., Wu, J. & Kisailus, D. Growth mechanism of highly branched titanium dioxide nanowires via oriented attachment. *Crystal Growth & Design* **13**, 422-428 (2013).

439 Baumgartner, J., Dey, A., Bomans, P. H., Le Coadou, C., Fratzl, P., Sommerdijk, N. A. & Faivre, D. Nucleation and growth of magnetite from solution. *Nature materials* **12**, 310 (2013).

440 Zhou, Z., Bedwell, G. J., Li, R., Prevelige, P. E. & Gupta, A. Formation mechanism of chalcogenide nanocrystals confined inside genetically engineered virus-like particles. *Scientific reports* **4**, 3832 (2014).

441 Jin, D., Liu, Z., Zheng, J., Hua, W., Chen, J., Zhu, K. & Zhou, X. Nonclassical from-shell-to-core growth of hierarchically organized SAPO-11 with enhanced catalytic performance in hydroisomerization of n-heptane. *RSC Advances* **6**, 32523-32533 (2016).

442 Wan, W., Su, J., Zou, X. D. & Willhammar, T. Transmission electron microscopy as an important tool for characterization of zeolite structures. *Inorganic Chemistry Frontiers* **5**, 2836-2855 (2018).

443 Shen, B., Chen, X., Cai, D., Xiong, H., Liu, X., Meng, C., Han, Y. & Wei, F. Atomic Spatial and Temporal Imaging of Local Structures and Light Elements inside Zeolite Frameworks. *Advanced Materials* (2019).

444 Chawla, A., Linares, N., Rimer, J. D. & García-Martínez, J. Time-Resolved Dynamics of Intracrystalline Mesoporosity Generation in USY Zeolite. *Chemistry of Materials* (2019).

445 Yan, Z., Chen, B. & Huang, Y. A solid-state NMR study of the formation of molecular sieve SAPO-34. *Solid state nuclear magnetic resonance* **35**, 49-60 (2009).

446 Férey, G. r., Haouas, M., Loiseau, T. & Taulelle, F. Nanoporous solids: how do they form? An in situ approach. *Chemistry of Materials* **26**, 299-309 (2013).

447 Castro, M., Losch, P., Park, W., Haouas, M., Taulelle, F., Loerbroks, C., Brabants, G., Breynaert, E., Kirschhock, C. E. & Ryoo, R. Unraveling Direct Formation of Hierarchical Zeolite Beta by Dynamic Light Scattering, Small Angle X-ray Scattering, and Liquid and Solid-State NMR: Insights at the Supramolecular Level. *Chemistry of Materials* **30**, 2676-2686 (2018).

448 Xiao, Y., Sheng, N., Chu, Y., Wang, Y., Wu, Q., Liu, X., Deng, F., Meng, X. & Feng, Z. Mechanism on solvent-free crystallization of NaA zeolite. *Microporous and Mesoporous Materials* **237**, 201-209 (2017).

449 Öztürk, Z., Filez, M. & Weckhuysen, B. M. Decoding Nucleation and Growth of Zeolitic Imidazolate Framework Thin Films with Atomic Force Microscopy and Vibrational Spectroscopy. *Chemistry–A European Journal* **23**, 10915-10924 (2017).

450 Kirschhock, C. E. A., Buschmann, V., Kremer, S., Ravishankar, R., Houssin, C. J. Y., Mojet, B. L., van Santen, R. A., Grobet, P. J., Jacobs, P. A. & Martens, J. A. Zeosil Nanoslabs: Building Blocks in nPr4N+-Mediated Synthesis of MFI Zeolite. *Angewandte Chemie International Edition* **40**, 2637-2640, doi:10.1002/1521-3773(20010716)40:14<2637::aid-anie2637>3.0.co;2-7 (2001).

451 Epping, J. D. & Chmelka, B. F. Nucleation and growth of zeolites and inorganic mesoporous solids: Molecular insights from magnetic resonance spectroscopy. *Current opinion in colloid & interface science* **11**, 81-117 (2006).

452 Loewenstein, W. The distribution of aluminum in the tetrahedra of silicates and aluminates. *American Mineralogist: Journal of Earth and Planetary Materials* **39**, 92-96 (1954).

453 Ren, N., Bosnar, S., Bronić, J., Dutour Sikirić, M., Mišić, T., Svetličić, V., Mao, J.-J., Antonić Jelić, T., Hadžija, M. & Subotić, B. Role of subcolloidal (nanosized) precursor species in the early stage of the crystallization of zeolites in heterogeneous systems. *Langmuir* **30**, 8570-8579 (2014).

454 Sharma, P., Yeo, J.-g., Han, M. H. & Cho, C. H. Knobby surfaced, mesoporous, single-phase GIS-NaP1 zeolite microsphere synthesis and characterization for H 2 gas adsorption. *Journal of Materials Chemistry A* **1**, 2602-2612 (2013).

455 Kohl, H. & Berger, A. The resolution limit for elemental mapping in energy-filtering transmission electron microscopy. *Ultramicroscopy* **59**, 191-194 (1995).

456 Park, M. B., Jo, D., Jeon, H. C., Nicholas, C. P., Lewis, G. J. & Hong, S. B. Zeolite Synthesis from a Charge Density Perspective: The Charge Density Mismatch Synthesis of UZM-5 and UZM-9. *Chemistry of Materials* **26**, 6684-6694 (2014).

457 Brittain, H. G. *Polymorphism in pharmaceutical solids*. (CRC Press, 2016).

458 Cartwright, J. H., Checa, A. G., Gale, J. D., Gebauer, D. & Sainz-Díaz, C. I. J. A. C. I. E. Calcium carbonate polyamorphism and its role in biomineralization: how many amorphous calcium carbonates are there? **51**, 11960-11970 (2012).

459 Lee, A. Y., Erdemir, D. & Myerson, A. S. Crystal Polymorphism in Chemical Process Development. *Annual Review of Chemical and Biomolecular Engineering* **2**, 259-280, doi:10.1146/annurev-chembioeng-061010-114224 (2011).

460 Cocca, M., Di Lorenzo, M. L., Malinconico, M. & Frezza, V. J. E. P. J. Influence of crystal polymorphism on mechanical and barrier properties of poly (l-lactic acid). **47**, 1073-1080 (2011).

461 Aulakh, D., Varghese, J. R. & Wriedt, M. J. I. c. The Importance of Polymorphism in Metal–Organic Framework Studies. **54**, 8679-8684 (2015).

462 Oleksiak, M. D. & Rimer, J. D. J. R. i. C. E. Synthesis of zeolites in the absence of organic structure-directing agents: factors governing crystal selection and polymorphism. **30**, 1-49 (2014).

463 Talaczynska, A., Dzitko, J. & Cielecka-Piontek, J. J. C. p. d. Benefits and limitations of polymorphic and amorphous forms of active pharmaceutical ingredients. **22**, 4975-4980 (2016).

464 Oleksiak, M. & D. Rimer, J. *Synthesis of zeolites in the absence of organic structure-directing agents: Factors governing crystal selection and polymorphism*. Vol. 30 (2014).

465 Breck, D. W. *Zeolite molecular sieves: structure, chemistry and use*. (Krieger, 1984).

466 Navrotsky, A. J. P. o. t. N. A. o. S. Energetic clues to pathways to biomineralization: Precursors, clusters, and nanoparticles. **101**, 12096-12101 (2004).

467 Navrotsky, A., Trofymluk, O. & Levchenko, A. A. J. C. r. Thermochemistry of microporous and mesoporous materials. **109**, 3885-3902 (2009).

468 Navrotsky, A., Trofymluk, O. & Levchenko, A. A. Thermochemistry of Microporous and Mesoporous Materials. *Chemical Reviews* **109**, 3885-3902, doi:10.1021/cr800495t (2009).

469 Muraoka, K., Sada, Y., Miyazaki, D., Chaikittisilp, W. & Okubo, T. Linking synthesis and structure descriptors from a large collection of synthetic records of zeolite materials. *Nature Communications* **10**, 4459, doi:10.1038/s41467-019-12394-0 (2019).

470 Van Tendeloo, L., Wangermez, W., Vandekerkhove, A., Willhammar, T., Bals, S., Maes, A., Martens, J. A., Kirschhock, C. E. A. & Breynaert, E. Postsynthetic High-Alumina Zeolite Crystal Engineering in Organic-Free Hyper-Alkaline Media. *Chemistry of Materials* **29**, 629-638, doi:10.1021/acs.chemmater.6b04052 (2017).

471 Van Tendeloo, L., Gobechiya, E., Breynaert, E., Martens, J. A. & Kirschhock, C. E. A. Alkaline cations directing the transformation of FAU zeolites into five different framework types. *Chemical Communications* **49**, 11737-11739, doi:10.1039/C3CC47292B (2013).

472 Itani, L., Bozhilov, K. N., Clet, G., Delmotte, L. & Valtchev, V. Factors That Control Zeolite L Crystal Size. *Chemistry – A European Journal* **17**, 2199-2210, doi:10.1002/chem.201002622 (2011).

473 Tsapatsis, M., Lovallo, M. & Davis, M. E. High-resolution electron microscopy study on the growth of zeolite L nanoclusters. *Microporous Mater* **5**, 381-388, doi:https://doi.org/10.1016/0927-6513(95)00069-0 (1996).

474 Broach, R. W. & Kirchner, R. M. Structures of the K+ and NH4+ forms of Linde J. *Microporous and Mesoporous Materials* **143**, 398-400, doi:https://doi.org/10.1016/j.micromeso.2011.03.025 (2011).

475 Ng, E.-P., Lim, G. K., Khoo, G.-L., Tan, K.-H., Ooi, B. S., Adam, F., Ling, T. C. & Wong, K.-L. Synthesis of colloidal stable Linde Type J (LTJ) zeolite nanocrystals from rice husk silica and their catalytic performance in Knoevenagel reaction. *Materials Chemistry and Physics* **155**, 30-35, doi:https://doi.org/10.1016/j.matchemphys.2015.01.061 (2015).

476 Shi, J., Hong, H., Ding, Y., Yang, Y., Wang, F., Cai, W. & Wang, X. Evolution of zinc oxide nanostructures through kinetics control. *Journal of Materials Chemistry* **21**, 9000-9008, doi:10.1039/C1JM10918A (2011).

477 Kang, D., Tong, S., Yu, X. & Ge, M. Template-free synthesis of 3D hierarchical amorphous aluminum oxide microspheres with broccoli-like structure and their application in fluoride removal. *RSC Advances* **5**, 19159-19165, doi:10.1039/C4RA13688H (2015).

478 Busch, S., Schwarz, U. & Kniep, R. Morphogenesis and Structure of Human Teeth in Relation to Biomimetically Grown Fluorapatite−Gelatine Composites. *Chemistry of Materials* **13**, 3260-3271, doi:10.1021/cm0110728 (2001).

479 Burgener, M., Putzeys, T., Gashti, M. P., Busch, S., Aboulfadl, H., Wübbenhorst, M., Kniep, R. & Hulliger, J. Polar Nature of Biomimetic Fluorapatite/Gelatin Composites: A Comparison of Bipolar Objects and the Polar State of Natural Tissue. *Biomacromolecules* **16**, 2814-2819, doi:10.1021/acs.biomac.5b00770 (2015).

480 Li, R., Linares, N., Sutjianto, J. G., Chawla, A., Garcia-Martinez, J. & Rimer, J. D. Ultrasmall Zeolite L Crystals Prepared from Highly Interdispersed Alkali-Silicate Precursors. *Angewandte Chemie International Edition* **57**, 11283-11288, doi:10.1002/anie.201805877 (2018).

# Appendix A

## Chapter 2 Supplementary Information

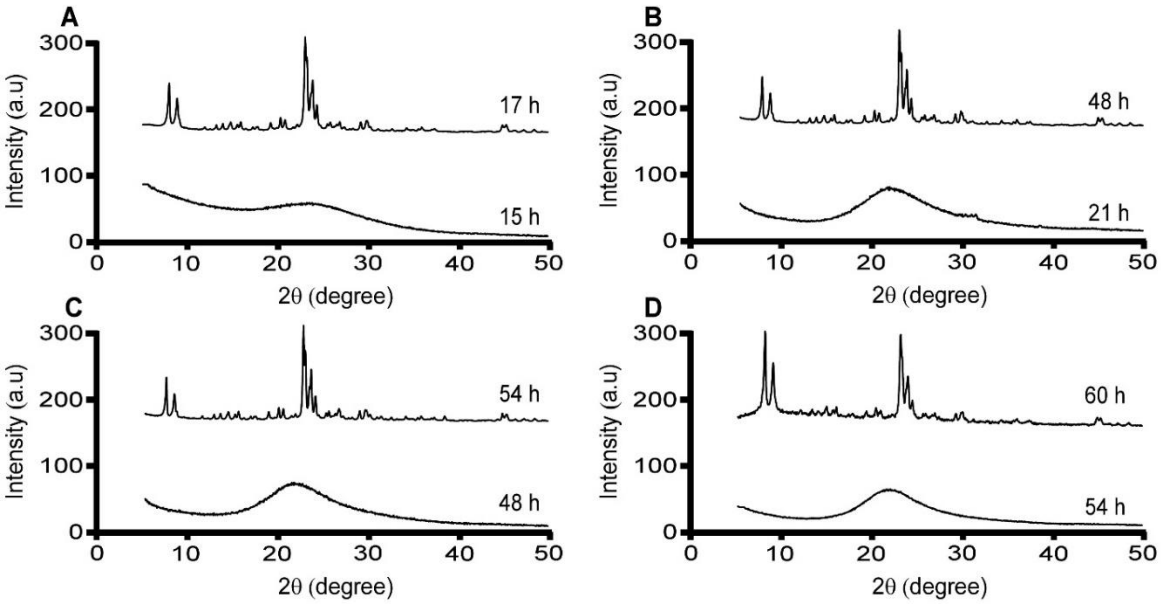


**Figure A1.** Time-elapsed powder XRD patterns of solids extracted from ZSM-5 growth solutions containing CTA as the organic SDA and the following ratios of inorganic SDAs (listed as molar fractions of K:Na): (A) 1:0, (B) 0.75:0.25, (C) 0.5:0.5, and (D) 0:1.

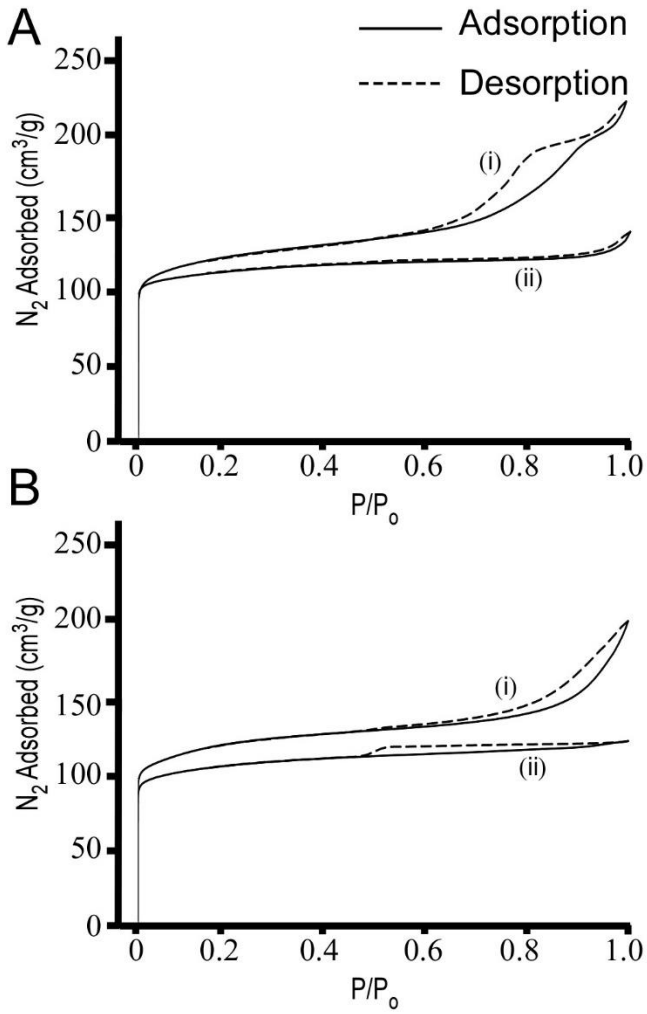


**Figure A2.** $N_2$ adsorption/desorption isotherms of ZSM-5 crystals synthesized in the presence of (A) potassium and (B) sodium. Isotherms of samples prepared with CTA (i) are type IV, which indicates the presence of mesopores. Isotherms of samples prepared with TPA (ii) are type I, which is characteristic of microporous materials.

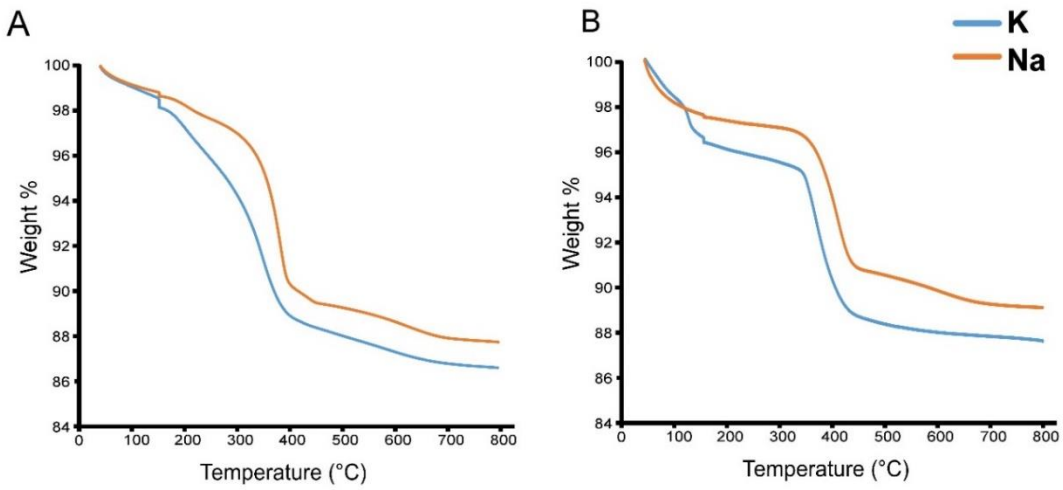


**Figure A3.** Thermogravimetric analysis (TGA) of ZSM-5 crystals prepared in the presence of (A) CTA and (B) TPA. Blue and orange lines denote samples prepared with potassium and sodium, respectively. TGA data were obtained using a 1 °C/min temperature ramp rate under the constant flow of N2 gas.

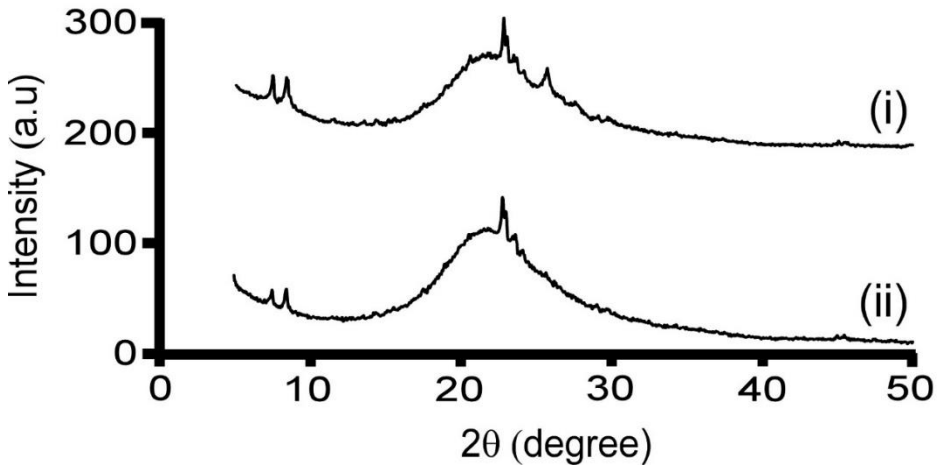


**Figure A4.** Powder X-ray diffraction patterns of solids extracted from growth mixtures after 72 h of hydrothermal treatment. The inorganic SDA in both samples is sodium. Here we compare a sample prepared with (i) tetramethylammonium (TMA) as the organic SDA to (ii) a sample prepared from an organic-free growth mixture.

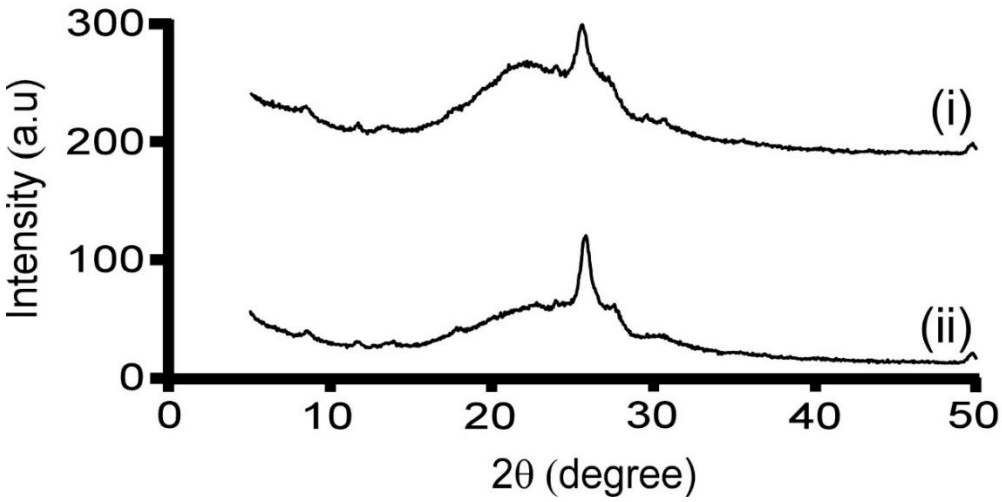


**Figure A5.** Powder X-ray diffraction patterns of solids extracted from growth solutions after 72 h of hydrothermal treatment. The inorganic SDA in both samples is potassium. Here we compare a sample prepared with (i) tetramethylammonium (TMA) as the organic SDA to (ii) a sample prepared from an organic-free growth mixture.

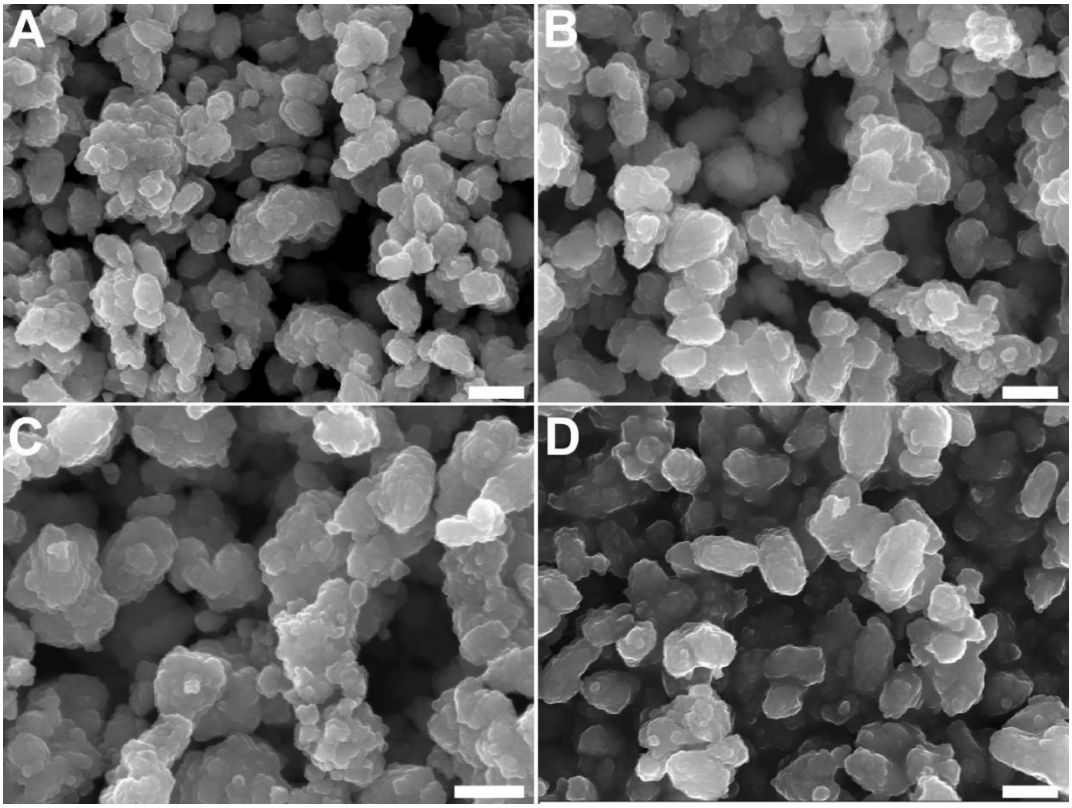


**Figure A6.** Scanning electron micrographs of ZSM-5 samples prepared with CTA as the organic SDA in the presence of the following molar percentages of potassium relative to the total alkali content (K + Na): (A) 0%, (B) 50%, (C) 75%, and (D) 100%. Scale bars equal 1 μm.

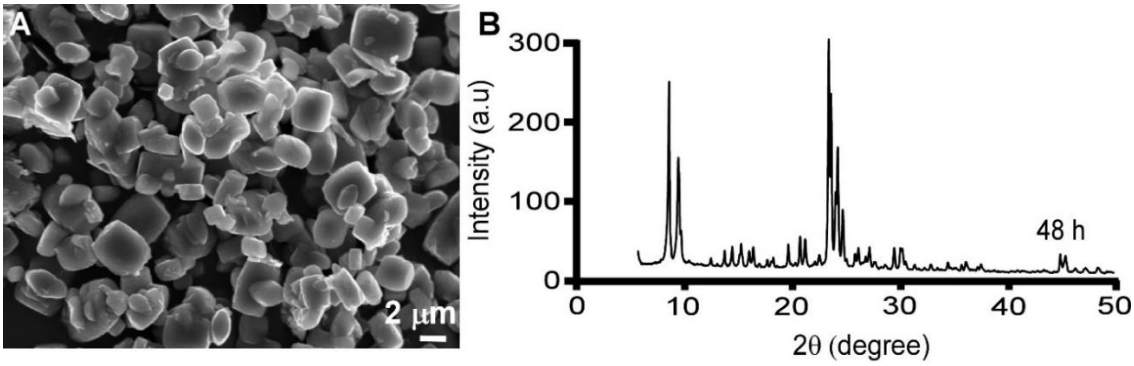


**Figure A7.** ZSM-5 crystals synthesized with TEOS as an alternative silica source. (A) Scanning electron micrograph revealing crystals grown from TEOS are larger than those from colloidal silica. (B) Powder X-ray diffraction pattern of solids extracted from a growth mixture prepared with TEOS reveals that crystallization is complete within 48 h of hydrothermal treatment.

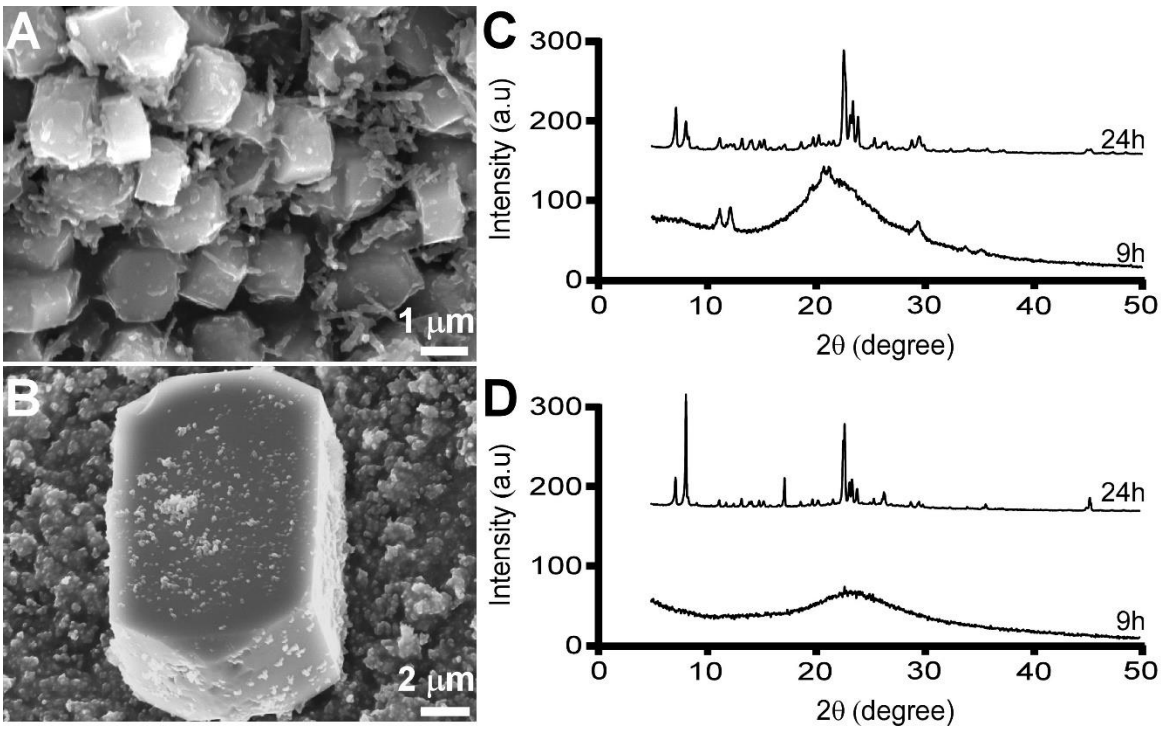


**Figure A8.** Characterization of ZSM-5 crystals synthesized using TPA as the organic SDA. (A and B) Scanning electron micrographs of ZSM-5 crystals after 72 h of hydrothermal treatment. Growth mixtures were prepared with (A) lithium and (B) cesium. (C and D) Corresponding XRD patterns of solids extracted from ZSM-5 syntheses.

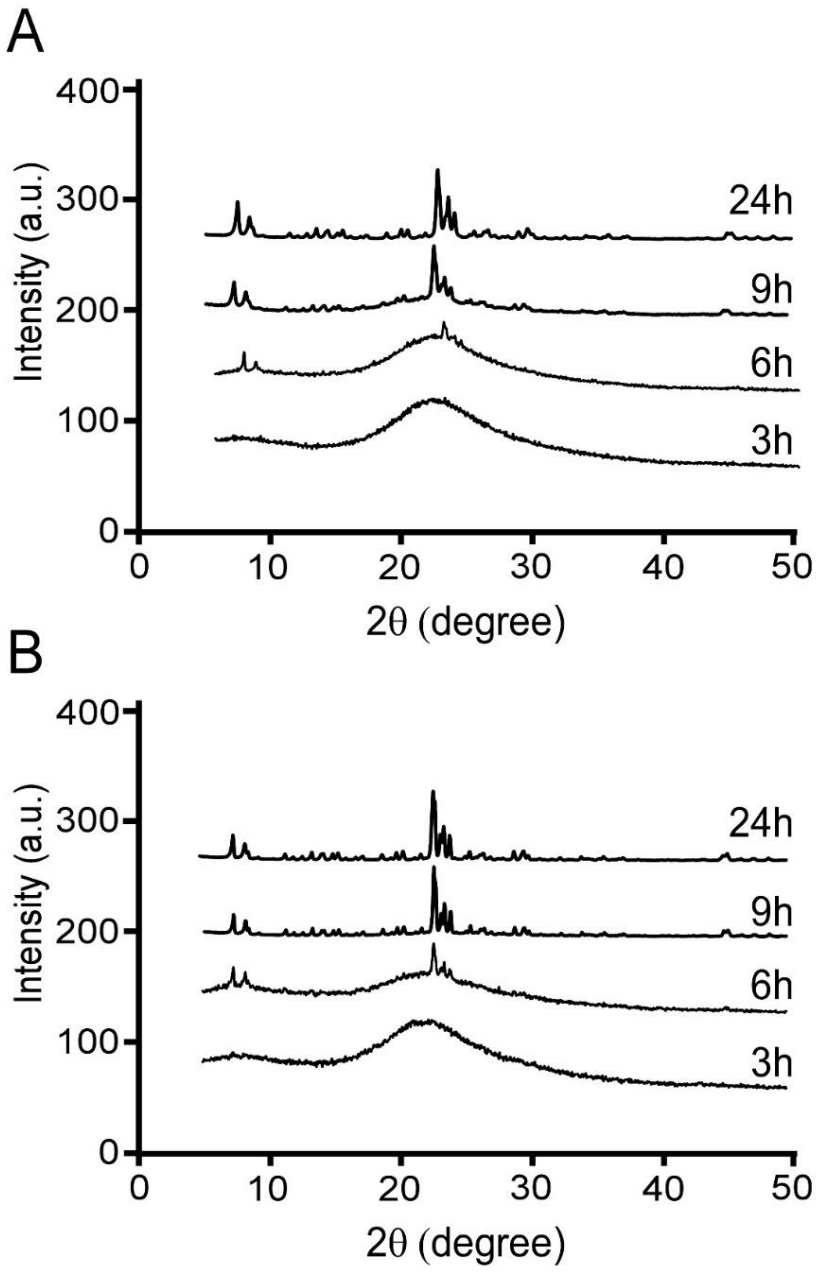


**Figure A9.** Comparison of powder X-ray diffraction patterns of solids extracted from ZSM-5 growth mixtures after specified heating times. Growth mixtures were prepared with TPA as the organic SDA and the following inorganic SDAs: (A) sodium and (B) potassium

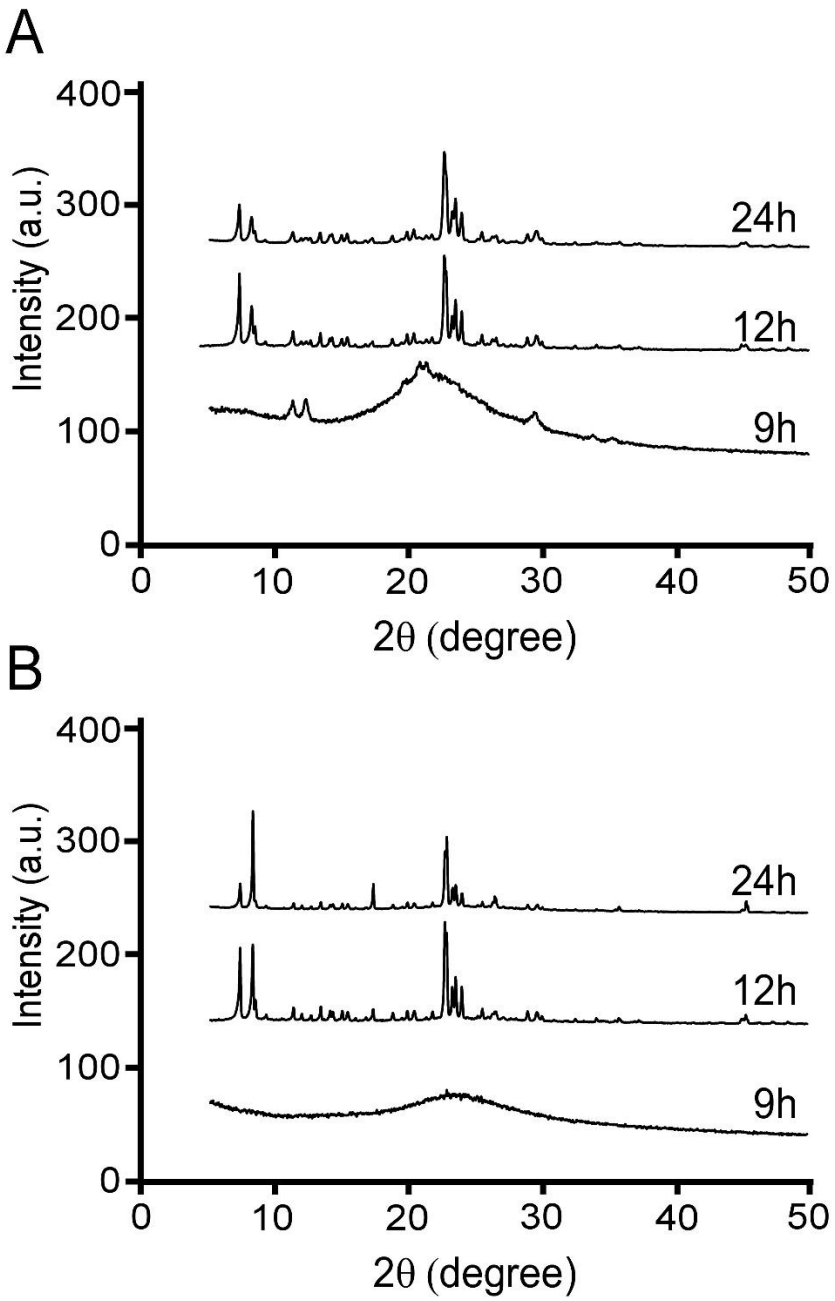


**Figure A10.** Comparison of powder X-ray diffraction patterns of solids extracted from ZSM-5 growth mixtures after specified heating times. Growth mixtures were prepared with TPA as the organic SDA and the following inorganic SDAs: (A) lithium and (B) cesium

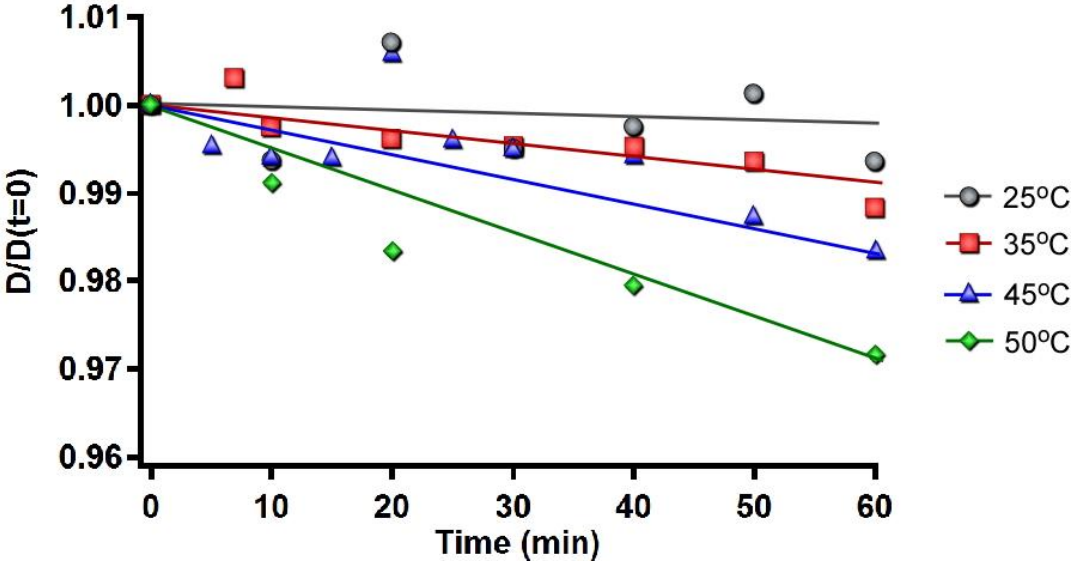


**Figure A11.** Dissolution of colloidal silica (LUDOX AS-40) in NaOH solution (pH 12) with a molar composition of 20 $SiO_2$: 0.2 NaOH: 1030 $H_2O$ at temperatures between 25 and 50 °C.

**Table A1.** t-plot analysis of ZSM-5 crystals using $N_2$ adsorption/desorption data.

| SDA Combinations | Total surface area ($m^2/g$) | Micropore surface area ($m^2/g$) | External surface area ($m^2/g$) |
|---|---|---|---|
| CTA/Na | 443 | 305 | 139 |
| TPA/Na | 398 | 311 | 87 |
| CTA/K | 450 | 316 | 134 |
| TPA/K | 423 | 346 | 77 |

**Table A2.** t-plot analysis of $N_2$ adsorption/desorption data for ZSM-5 crystals prepared with CTA/Na.

| Si Source | Total surface area ($m^2/g$) | Micropore surface area ($m^2/g$) | External surface area ($m^2/g$) |
|---|---|---|---|
| LUDOX | 443 | 305 | 139 |
| TEOS | 409 | 319 | 90 |

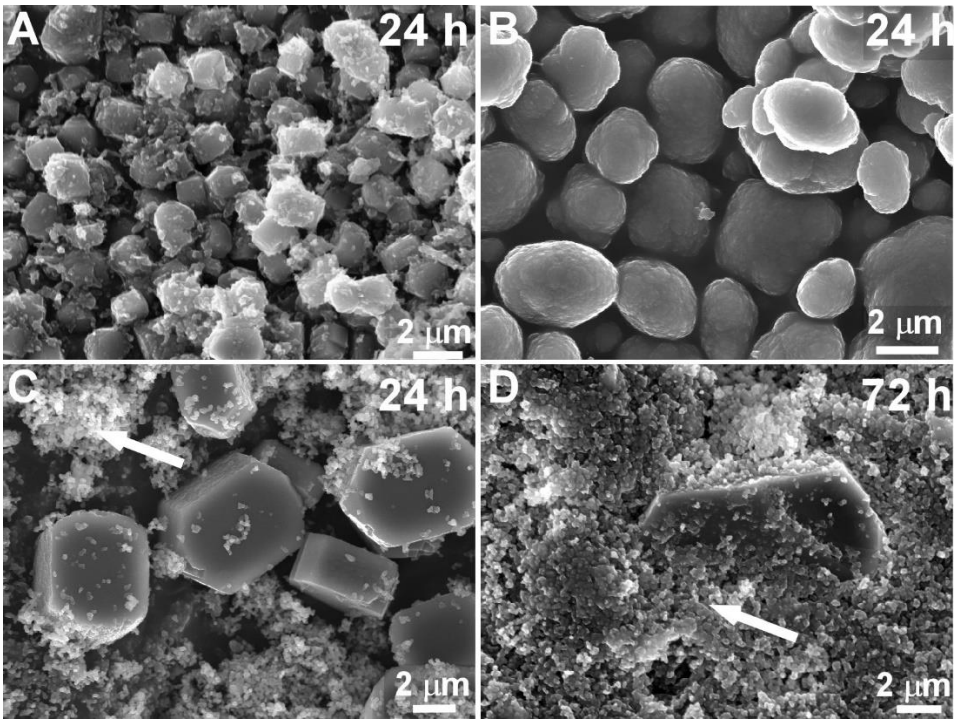


**Figure A12.** Scanning electron micrographs of ZSM-5 samples prepared with TPA as the organic SDA after specified heating times in the presence of (A) lithium, (B) sodium, (C) potassium, and (D) cesium cations.

# Appendix B

## Chapter 3 Supplementary Information

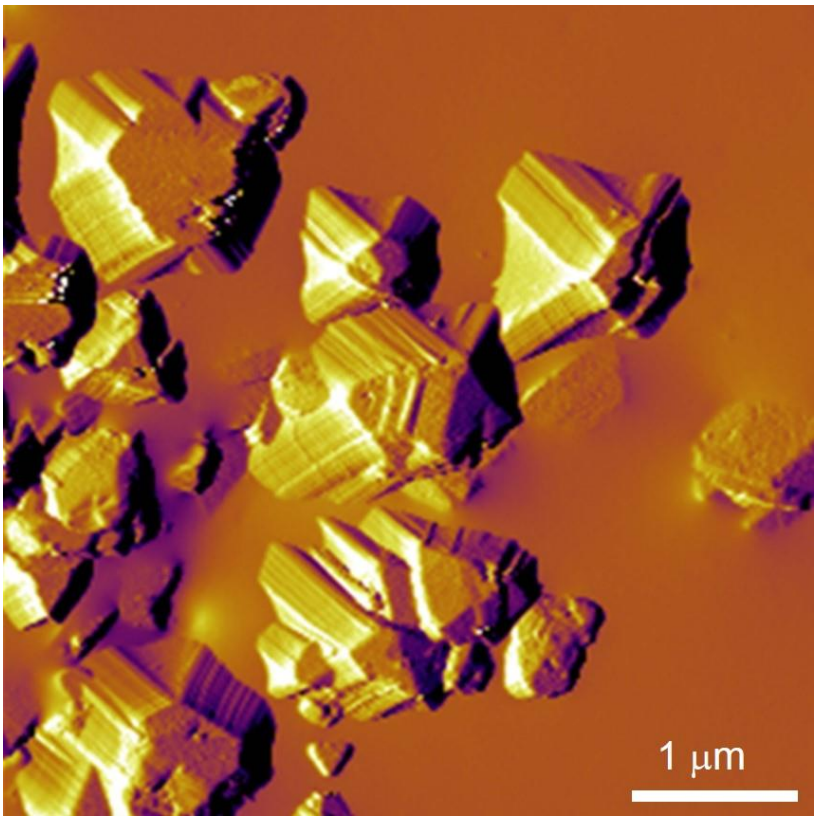


**Figure B1.** Low magnification AFM image of as received USY (CBV 780, FAU type) crystals in amplitude mode revealing rough surface protrusions and etch pits.

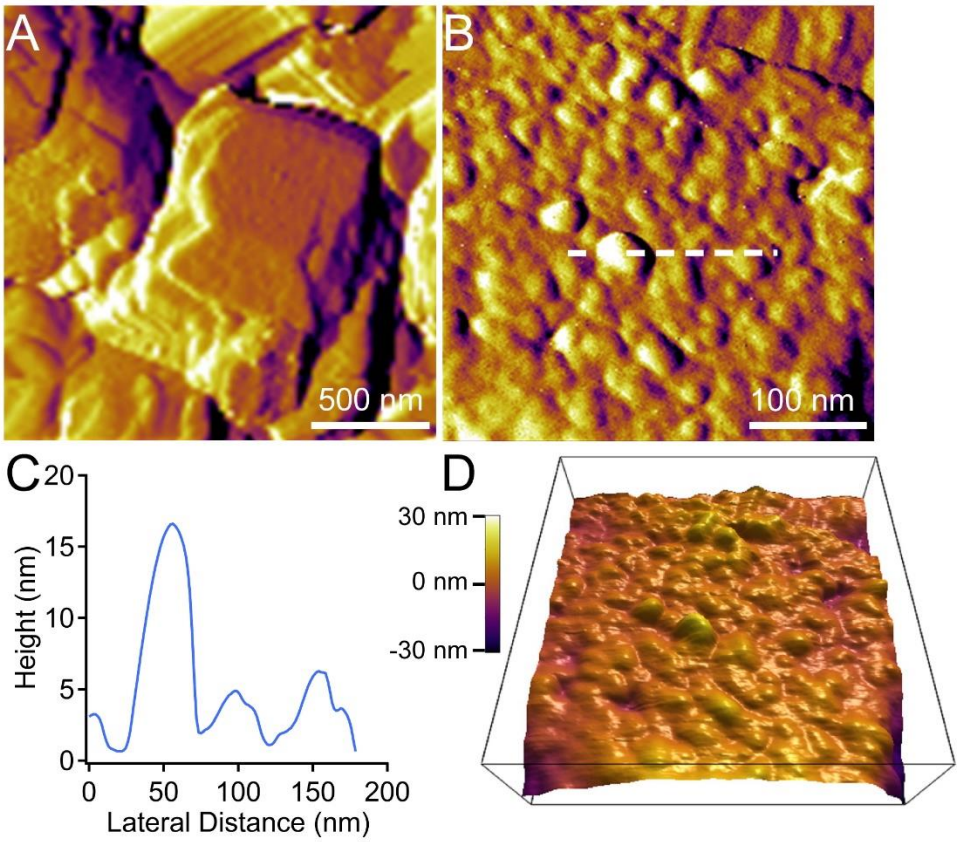


**Figure B2.** (A and B) AFM images of as received USY (CBV 780) in amplitude mode revealing rough surface protrusions. (C) Height profile along the dashed line in panel B showing a representative topography of untreated crystals. (D) 3-dimensional image of the surface depicted in panel B.

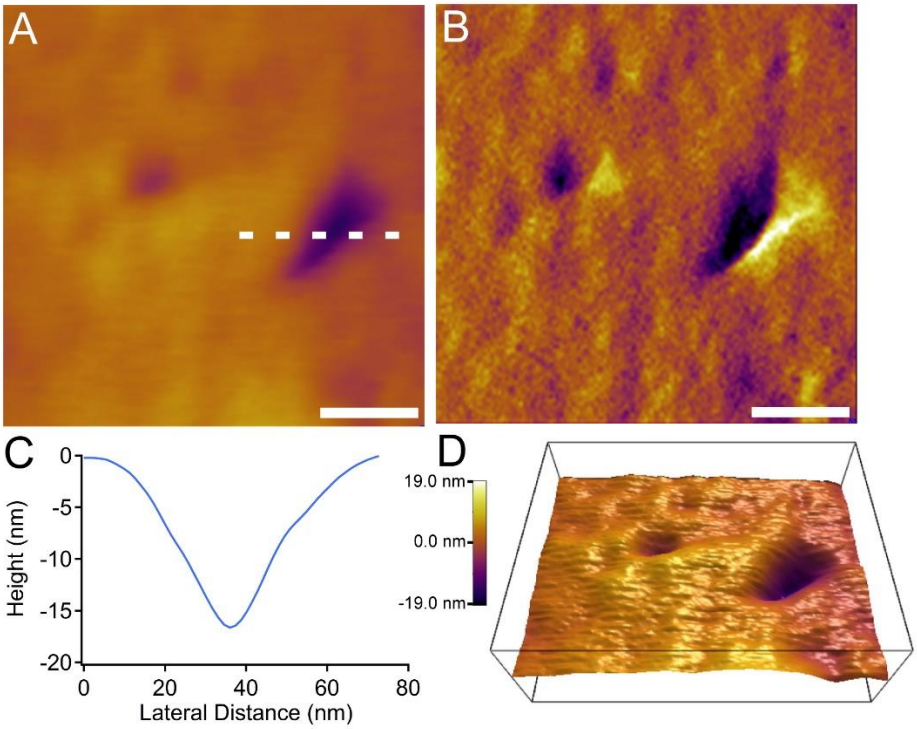


**Figure B3.** AFM images of as received (untreated) USY crystals showing the presence of etch pits on the surface in (A) height mode and (B) amplitude mode (C) Height profile along the dashed line in panel A showing a representative width of etch pits (noting that dimensions are subject to error owing to the geometry of the AFM tip). (D) 3-dimensional image of the surface depicted in panel A. Scale bars are equal to 50 nm.

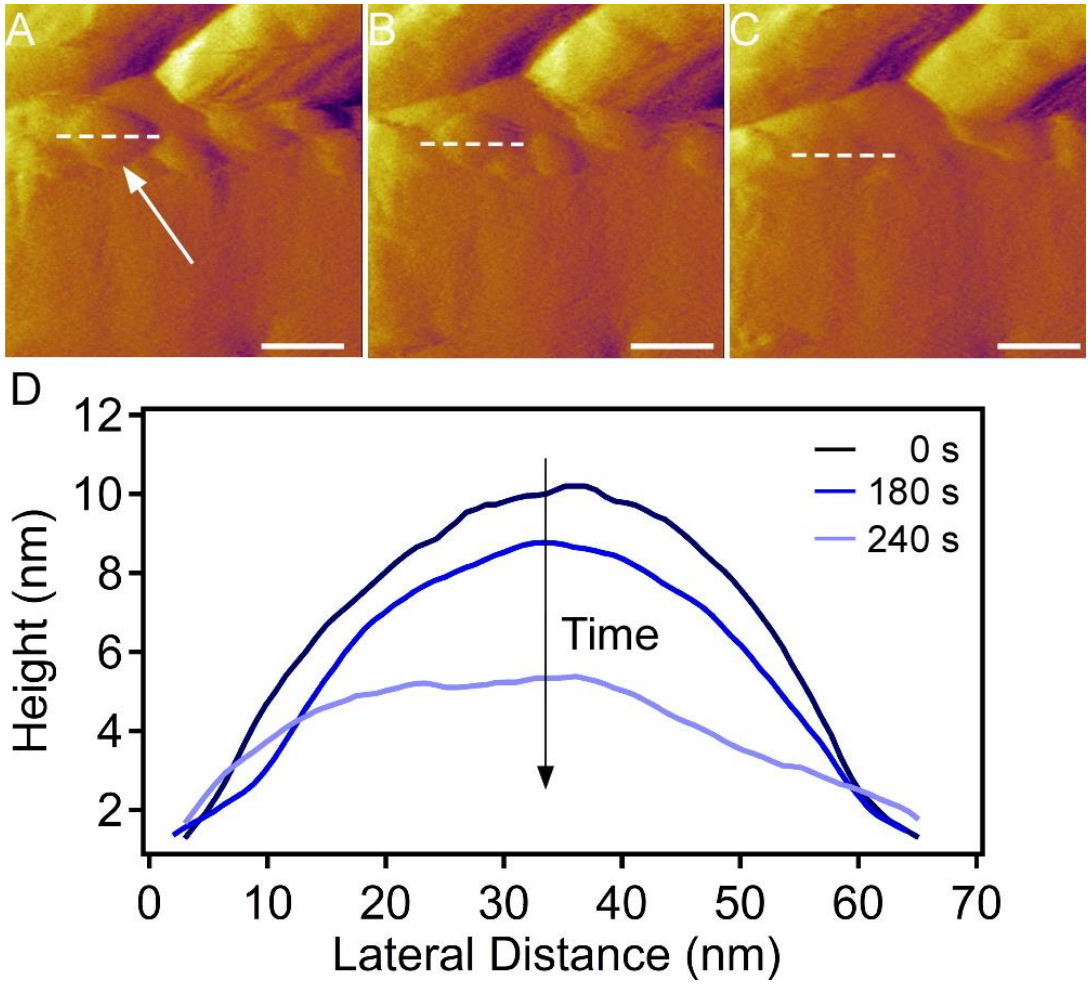


**Figure B4.** (A – C) Time-resolved in situ AFM amplitude mode images of a USY crystal treated with solution S1 at room temperature showing the disappearance of rough features (white arrow) present on the crystal surface. Images are reported in ca. 180 s intervals during continuous scanning. (D) Height profiles along the dashed white lines reveal a decrease in the height of islands (convex protrusions). Scale bars equal 50 nm.

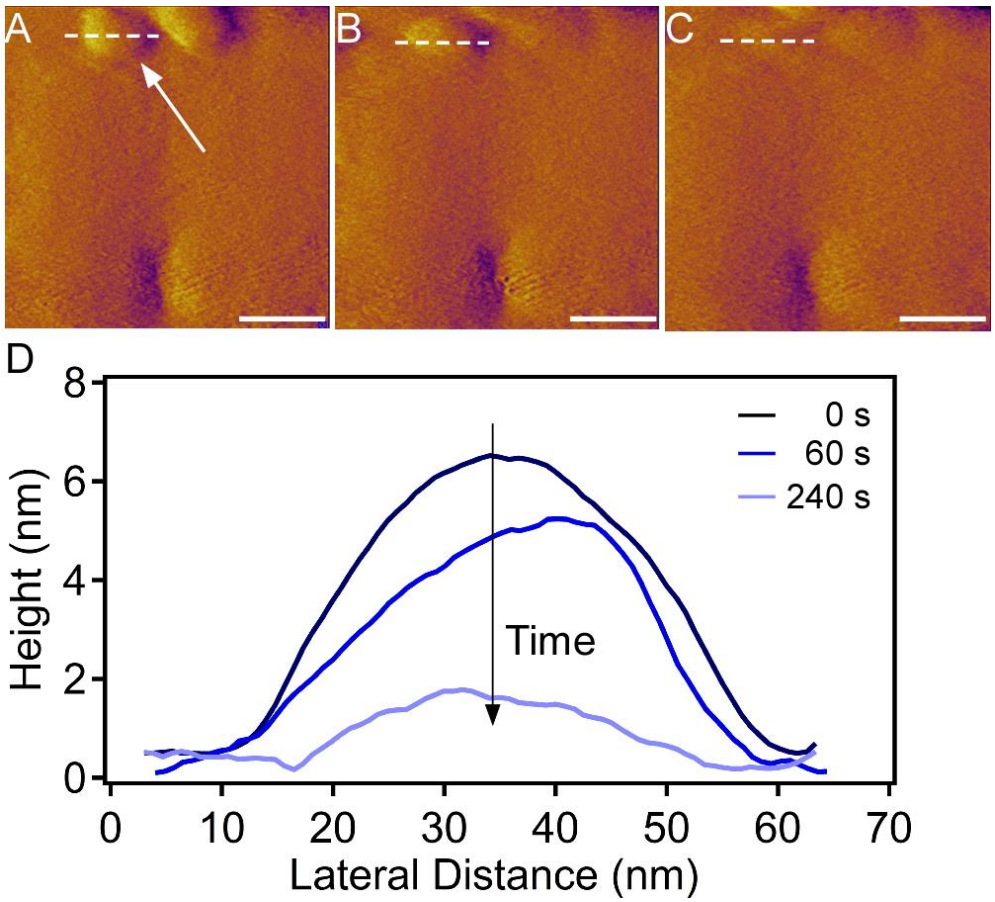


**Figure B5.** (A – C) Time-resolved *in situ* AFM amplitude mode images of a USY crystal treated with solution S2 at room temperature showing the disappearance of rough features (white arrow). Images are reported in ca. 120 s intervals during continuous scanning. (D) Height profiles along the dashed white lines reveal a decrease in the height of islands (convex protrusions). Scale bars are equal to 50 nm.

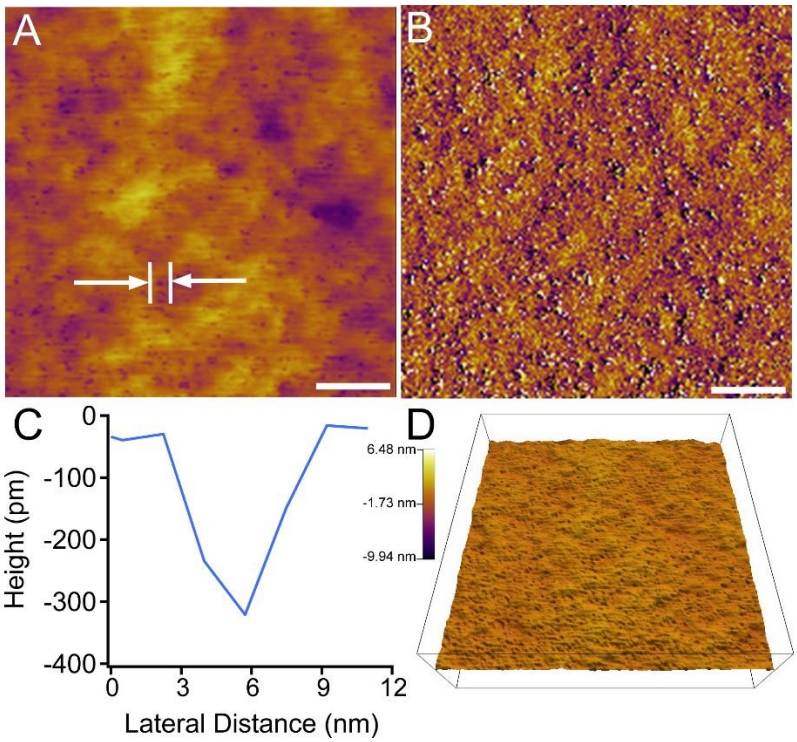


**Figure B6.** AFM images of USY crystals after 6 h of treatment *ex situ* with solution S2 at 25 °C showing the uniform distribution of mesopores in (A) height mode and (B) amplitude mode. (C) Height profile of the feature denoted in panel A (double white arrow) showing the diameter of a representative mesopore. (D) 3-dimensional image of the surface depicted in panel A. Scale bars are equal to 50 nm.

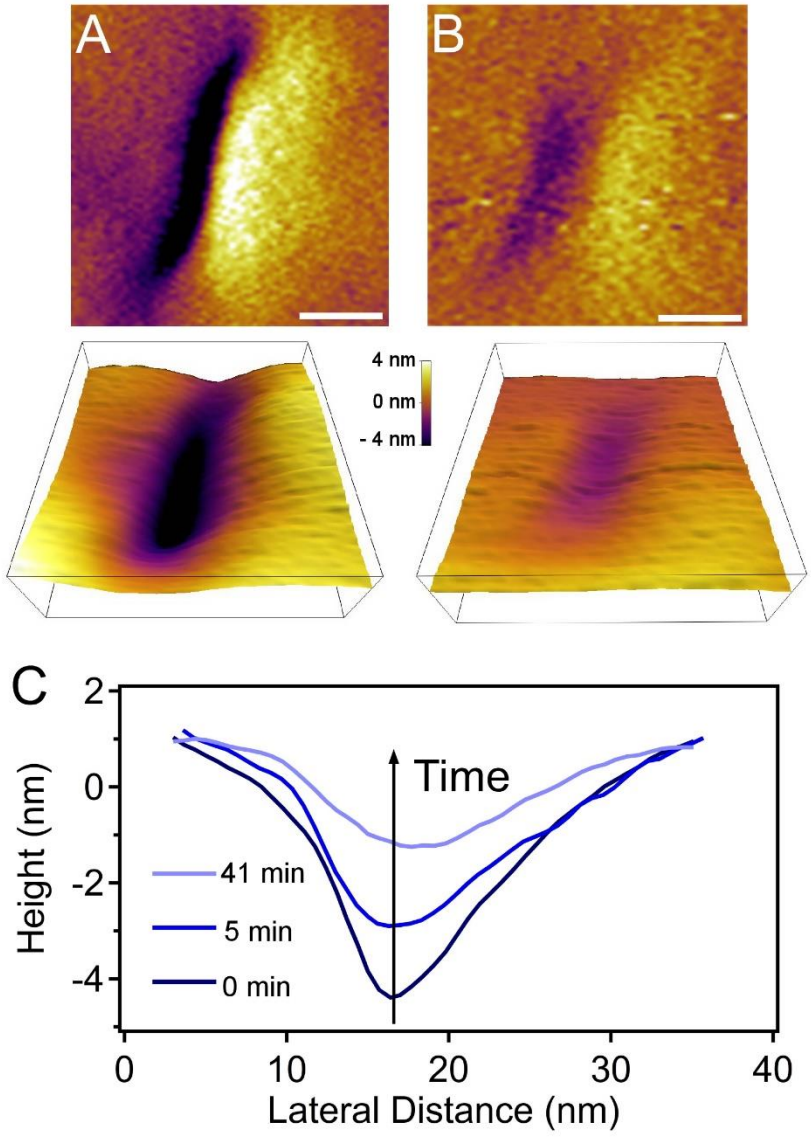


**Figure B7.** Measurements of a USY crystal showing the presence of etch pits on (A) an initial surface and (B) after 1 h treatment with solution S2 at 25°C. Corresponding 3-dimensional height profiles are shown below each image. (C) Height profiles along the dashed lines in panels A and B showing a temporal reduction in etch pit depth with increased AFM imaging time. Scale bars are equal to 20 nm.

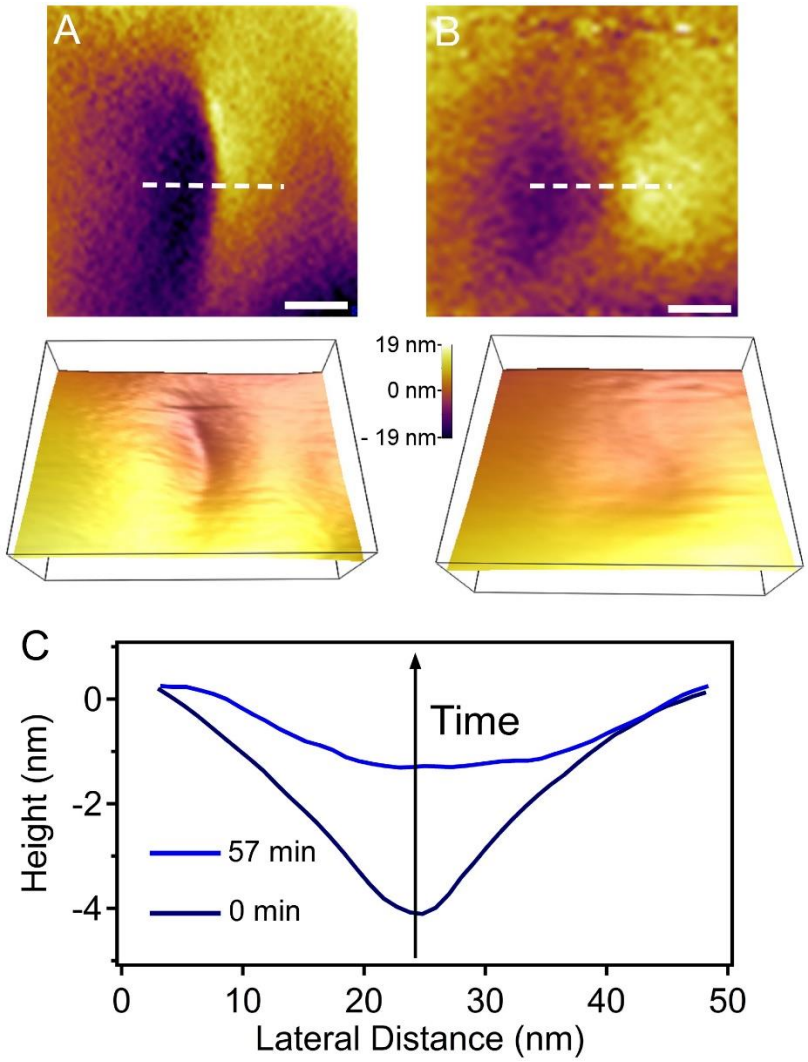


**Figure B8.** AFM images of a USY crystal showing the presence of etch pits on (A) an initial surface and (B) after 1 h treatment with solution S2 at 25°C. Corresponding 3-dimensional height profiles are shown below each image. (C) Height profiles along the dashed lines in panels A and B showing a temporal reduction in etch pit depth with increased AFM imaging time. Scale bars are equal to 20 nm.

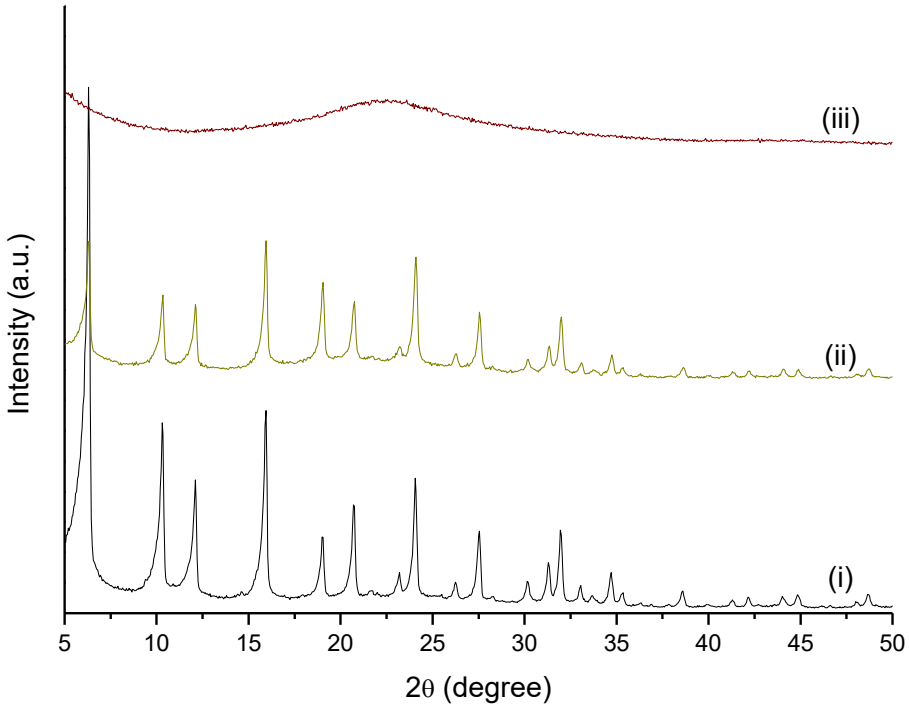


**Figure B9.** Powder X-ray diffraction patterns of (i) untreated USY (CBV 780) crystals, (ii) solids after 6 h treatment with solution S2 containing both CTAB and NaOH, and (iii) 6 h of treatment at 25°C with solution S2 containing NaOH in the absence of the surfactant. Powder XRD patterns clearly reveal the protective role of CTAB as its presence preserves the crystallinity of parent zeolite USY under basic conditions.

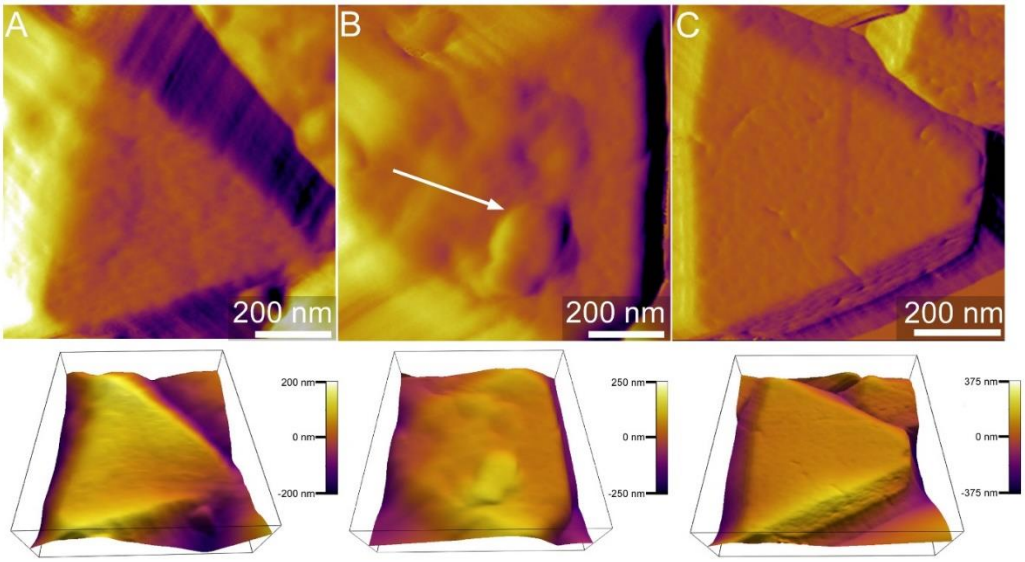


**Figure B10.** AFM images of three different USY crystals after 6 h of treatment *ex situ* with solution S1 at 25 °C showing both rough and smooth surface features. The white arrow depicts the rough surface presumably due to partial mesostructuring.

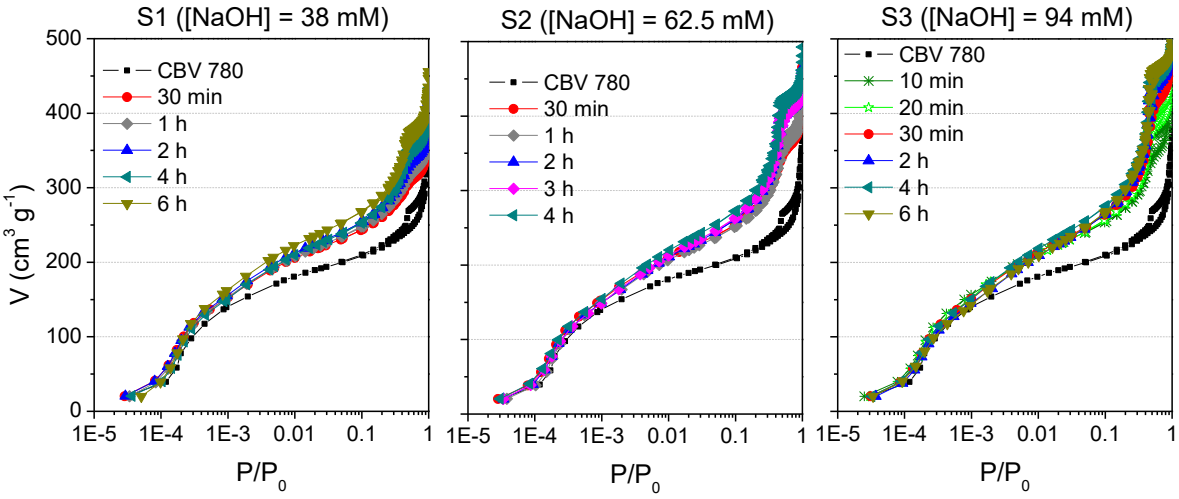


**Figure B11.** $N_2$ adsorption and desorption isotherms at 77 K (logarithmic form) for the *ex situ* surfactant-templated USY zeolites prepared using different base concentrations and treatment times at RT: 0 min (black), 30 min (red), 1 h (gray), 2 h (blue), 3 h (pink), 4 h (green), and 6 h (dark yellow).

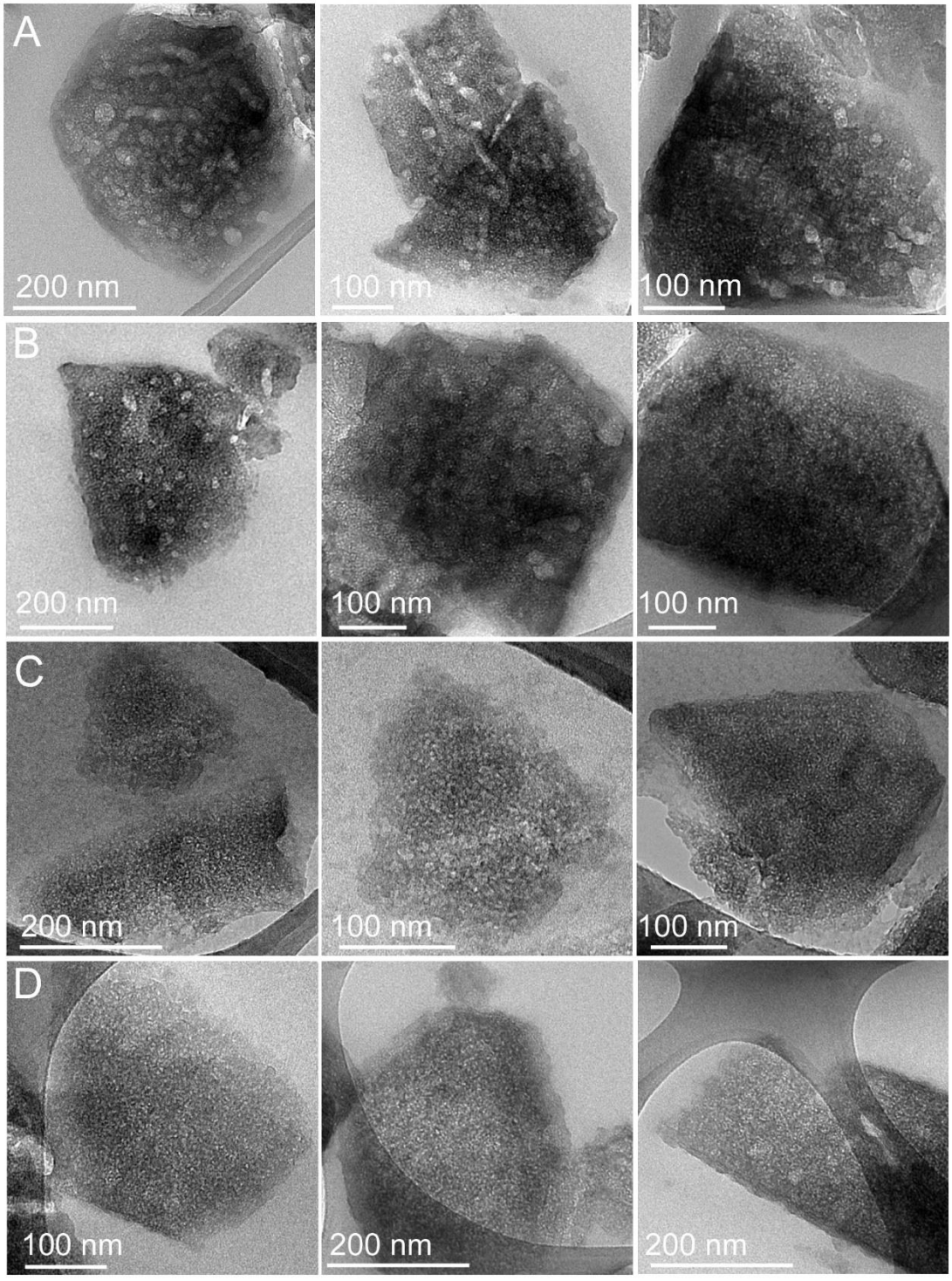


**Figure B12.** Transmission electron micrographs of surfactant-templated USY zeolites after (A) 30 min, (B) 2 h, (C) 4 h, and (D) 6 h of treatment with solution S2 at room temperature.

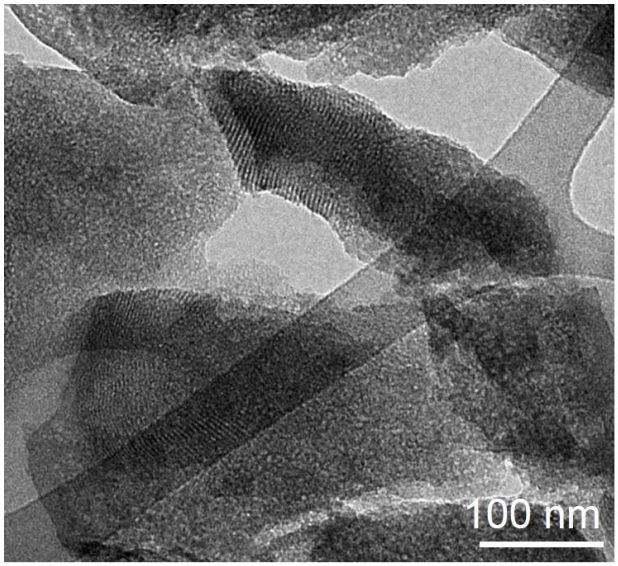


**Figure B13.** Transmission electron micrograph of a surfactant-templated USY zeolite after 6 h of treatment with solution S3 at room temperature.

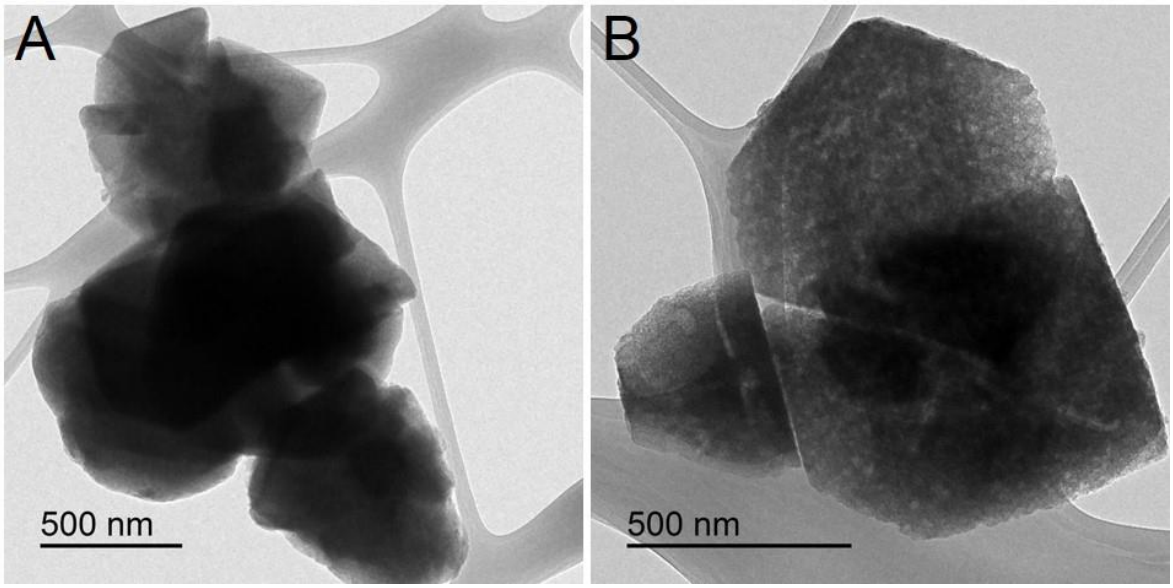


**Figure B14.** (A) Transmission electron micrographs of two different groups of crystals of a surfactant-templated USY zeolite after 6 h of treatment with solution S1. (B) The crystals are partially mesostructured, as shown for the presence of large mesoporosity due to steaming.

**Table B1.** Time-resolved evolution of the textural properties of USY with and without *ex situ* surfactant templating at three different solution conditions (pH 12.3, 12.7, and 13.0). The samples were calcined prior to $N_2$ physisorption measurements.

| pH | Time (h) | $V_{micro}$ [a] ($cm^3/g$) | $V_{meso}$ [b] ($cm^3/g$) | $V_{large\ meso}$ [c] ($cm^3/g$) | $V_{tot}$ [d] ($cm^3/g$) |
|---|---|---|---|---|---|
| CVB 780 | | 0.24 | 0.11 | 0.18 | 0.53 |
| 12.3 | 0.5 | 0.27 | 0.18 | 0.15 | 0.60 |
| | 1 | 0.26 | 0.20 | 0.15 | 0.61 |
| | 2 | 0.26 | 0.23 | 0.13 | 0.62 |
| | 3 | 0.25 | 0.21 | 0.12 | 0.58 |
| | 4 | 0.25 | 0.27 | 0.09 | 0.61 |
| | 6 | 0.26 | 0.28 | 0.11 | 0.65 |
| 12.7 | 0.5 | 0.26 | 0.26 | 0.14 | 0.65 |
| | 1 | 0.23 | 0.30 | 0.12 | 0.65 |
| | 2 | 0.23 | 0.37 | 0.07 | 0.67 |
| | 3 | 0.23 | 0.37 | 0.06 | 0.66 |
| | 4 | 0.24 | 0.39 | 0.07 | 0.70 |
| | 6 | 0.22 | 0.37 | 0.06 | 0.65 |
| 13.0 | 0.5 | 0.23 | 0.38 | 0.1 | 0.71 |
| | 1 | 0.23 | 0.40 | 0.09 | 0.72 |
| | 2 | 0.20 | 0.45 | 0.08 | 0.73 |
| | 3 | 0.23 | 0.42 | 0.08 | 0.73 |
| | 4 | 0.23 | 0.43 | 0.08 | 0.74 |
| | 6 | 0.21 | 0.47 | 0.06 | 0.74 |

[a] Micropore volume determined by NL-DFT from the adsorption branch of the isotherms shown in Figure 7; [b] Surfactant-templated mesopore volume was calculated from cumulative pore volume plot from pore size 2-7 nm; [c] Large mesopores volume was calculated by subtracting the micropore volume and surfactant-templated mesopores volume from total pore volume; [d] Total pore volume was obtained by NL-DFT at $P/P_o=0.95$.

# Appendix C

## Chapter 4 Supplementary Information

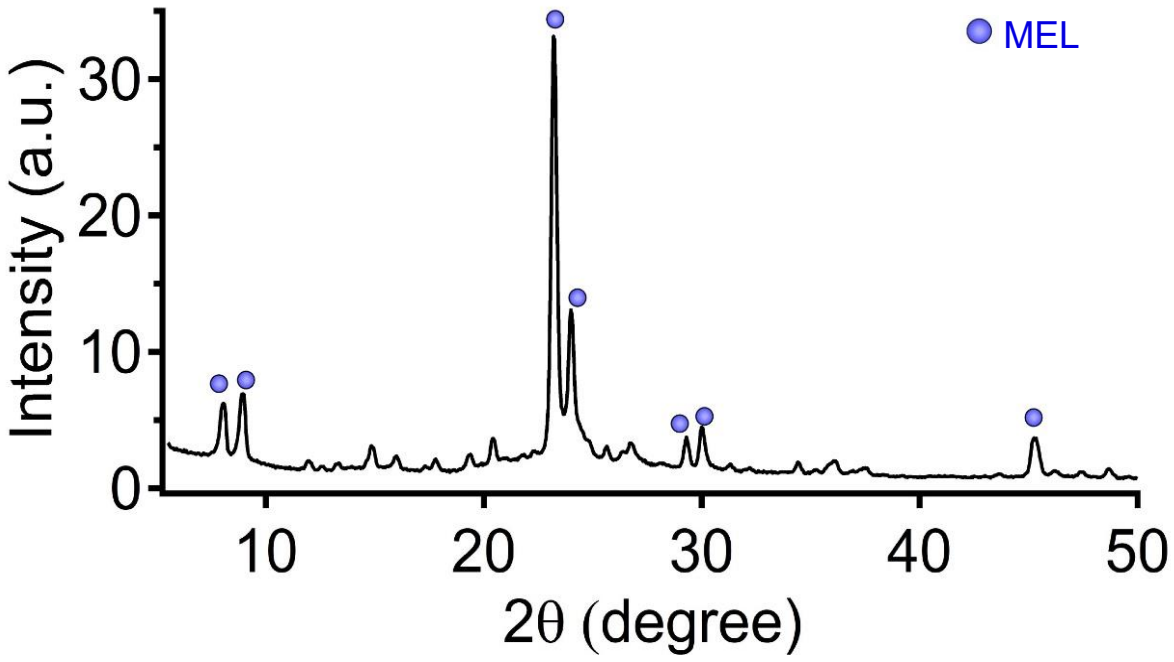


**Figure C1.** Powder X-ray diffraction pattern of silicalite-2 seeds showing phase pure MEL without any noticeable impurity of MFI.

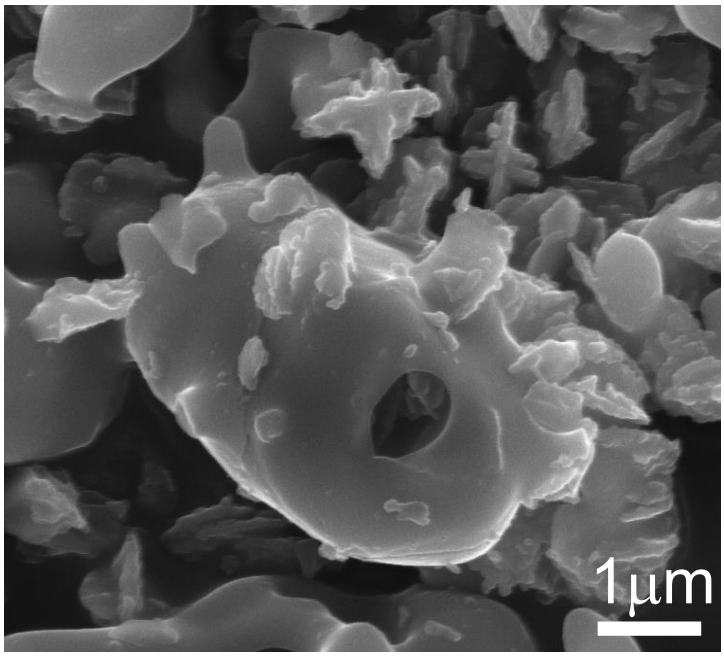


**Figure C2.** FE-SEM image of the product after 1 day of heating extracted from silicalite-2 seeded growth mixture showing the remnants of seeds.

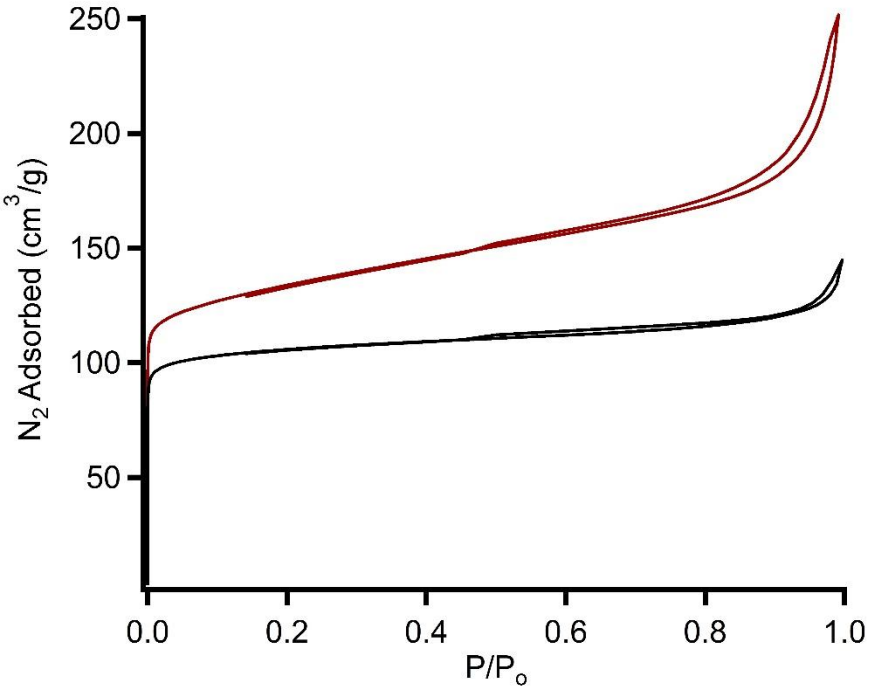


**Figure C3.** $N_2$ adsorption and desorption isotherms at 77 K of the silicaite-2 seeds (black) and hierarchical SPP crystals extracted from seeded growth mixtures containing silicalite-2 seeds (red).

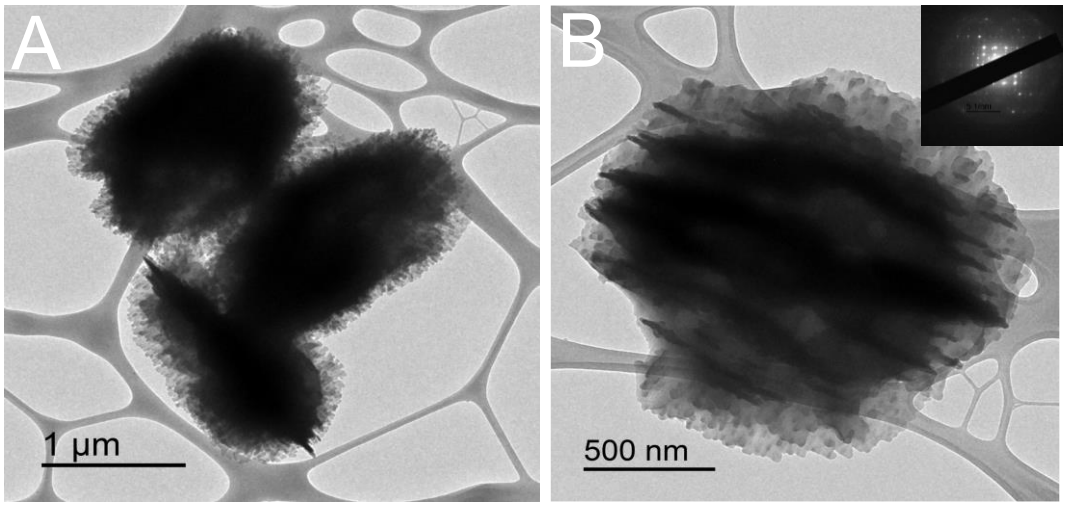


**Figure C4.** **(A)** Low resolution TEM image of hierarchical SPP crystals synthesized using silicalite-2 seeds showing the uniform intergrown morphology. **(B)** High magnification TEM image (inset: electron diffraction pattern) showing the single-crystalline nature of the particles with nanosheets exhibiting equal crystallographic registry.

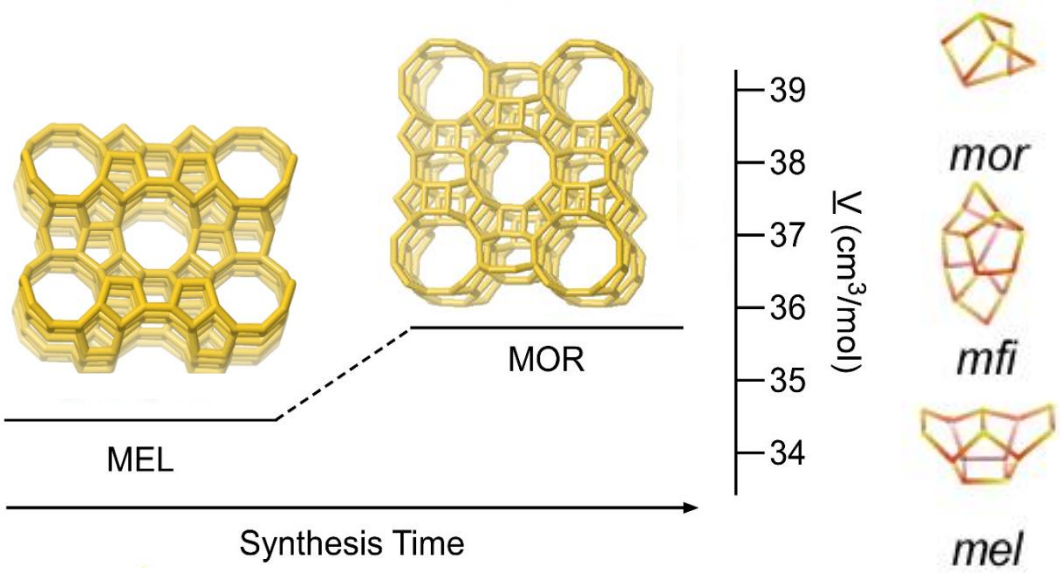


**Figure C5.** Left: Stages of zeolite phase transformation with increasing synthesis time. The molar volume for each zeolite were obtained from the International Zeolite Association Structure Database. Right: Composite building units (CBUs) of MFI and MOR framework types.

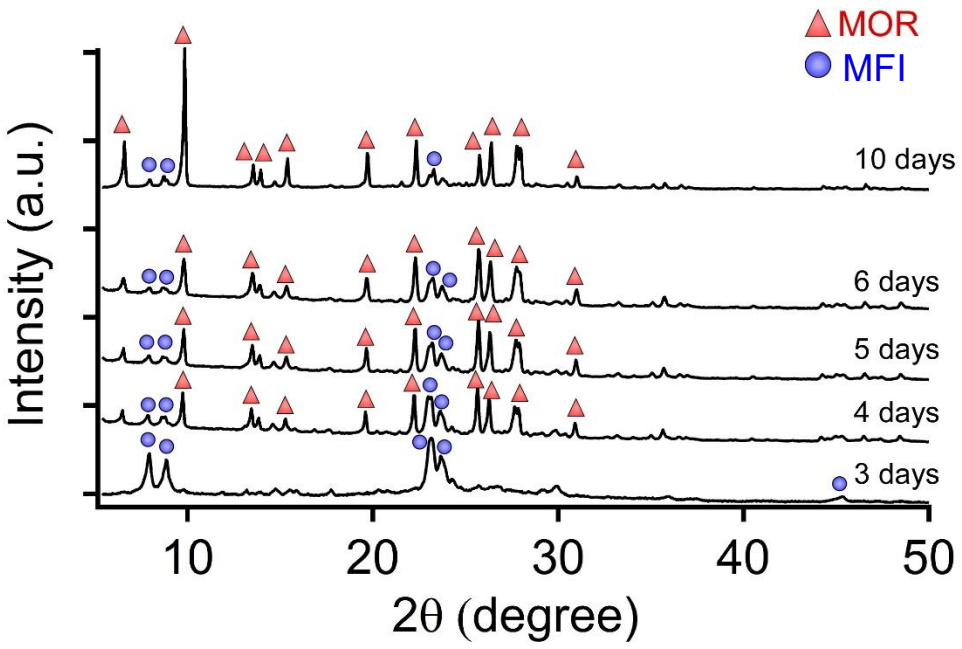


**Figure C6.** Powder X-ray diffraction patterns of solids extracted from silicalite-2 seeded growth mixture containing 10wt% silicalite-2 seeds heated at 150°C for periodic heating times (3-10 days). The powder XRD patterns are offset along the y-axis for visual clarity.

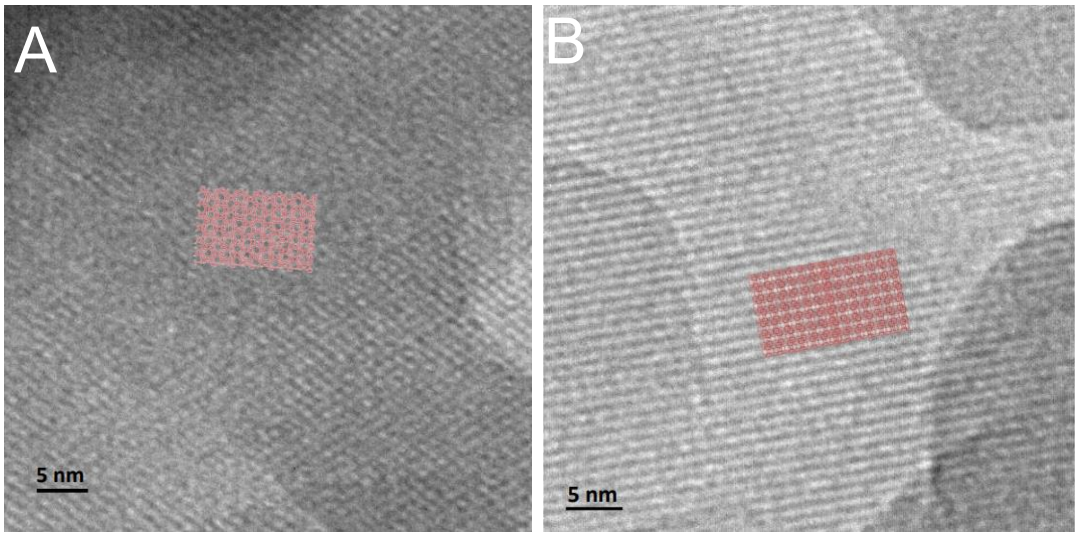


**Figure C7.** HRTEM images of hierarchical SPP crystals synthesized using silicalite-2 seeds overlaid with the MFI crystal structure along the (A) [010] axis and (B) [001] confirming the high crystallinity and orientation of nanosheets.

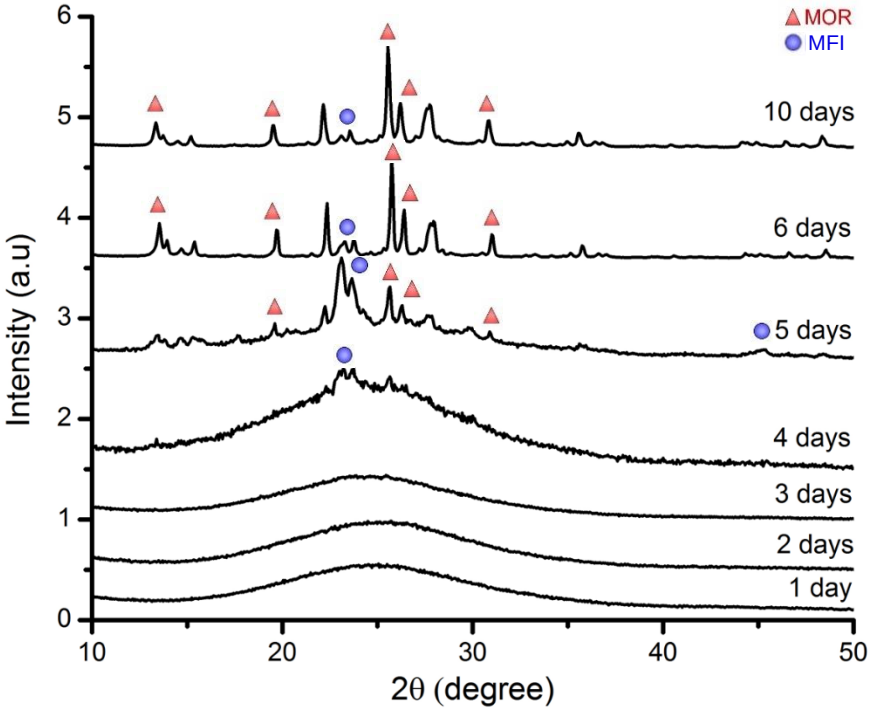


**Figure C8.** Powder X-ray diffraction patterns of solids extracted from ZSM-5 seeded growth mixture containing 10wt% ZSM-5 seeds heated at 150°C for periodic heating times (1-10 days). The powder XRD patterns are offset along the y-axis for visual clarity.

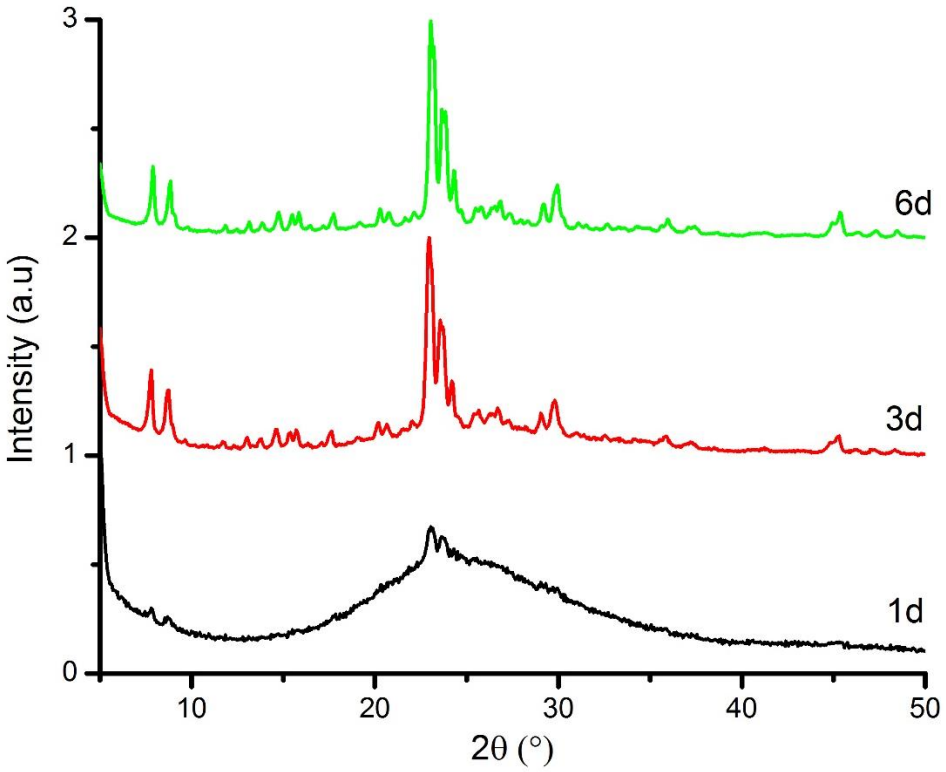


**Figure C9.** Powder X-ray diffraction patterns of solids extracted from silicalite-1 seeded growth mixture containing 10wt% silicalite-1 seeds heated at 150°C for periodic heating times (1-6 days).

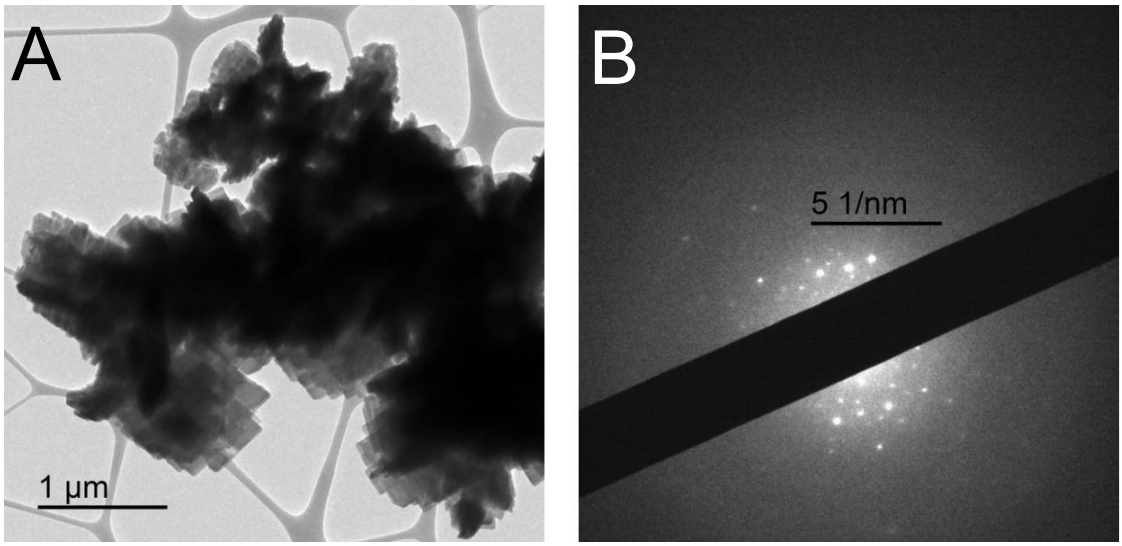


**Figure C10. (A)** TEM image of representative crystals synthesized using silicalite-1 seeds (refer to **Table C1** for textural analysis). **(B)** Electron diffraction pattern of the crystals showing the high crystallinity and confirming the MFI-type zeolite structure.

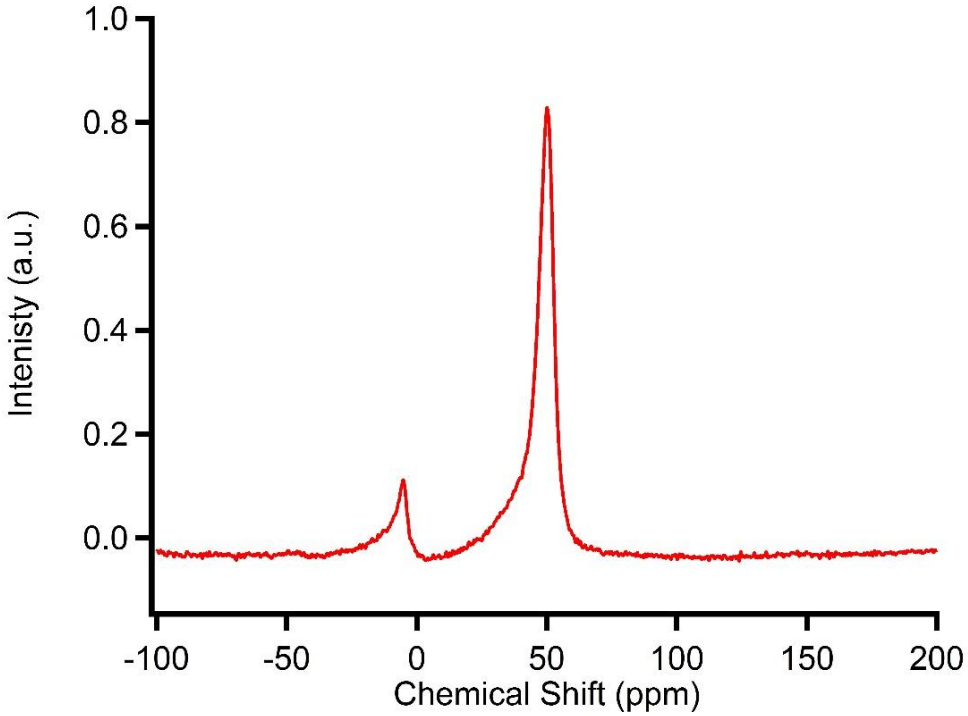


**Figure C11.** $^{27}$Al MAS NMR spectra of the hierarchical SPP crystal synthesized using silicalite-2 seeds.

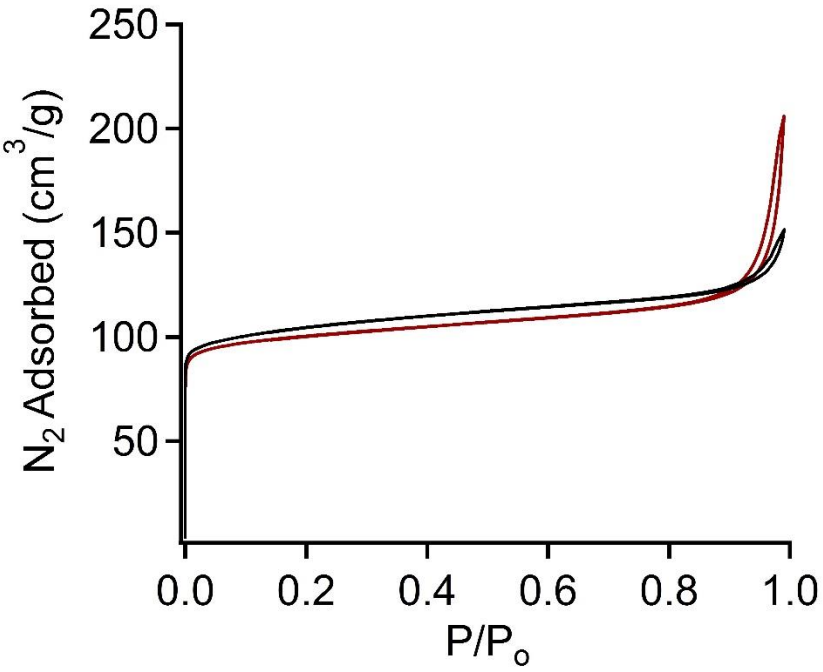


**Figure C12.** $N_2$ adsorption and desorption isotherms at 77 K of the calcined products extracted from seeded growth mixtures containing ZSM-5 seeds (red) and silicalite-1 seeds (black).

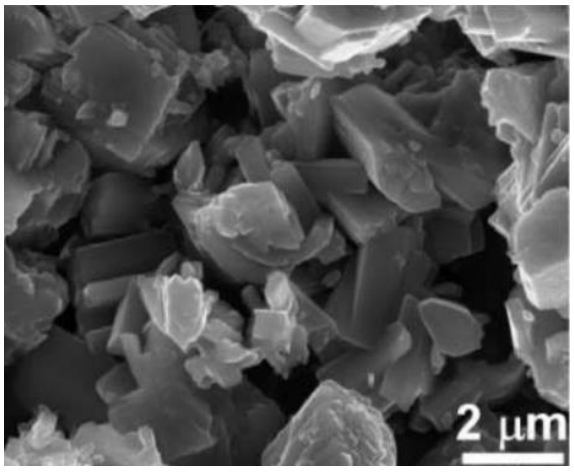


**Figure C13.** Scanning electron micrographs of mordenite crystals prepared using solution S1 with ill-defined morphology containing no seeds.

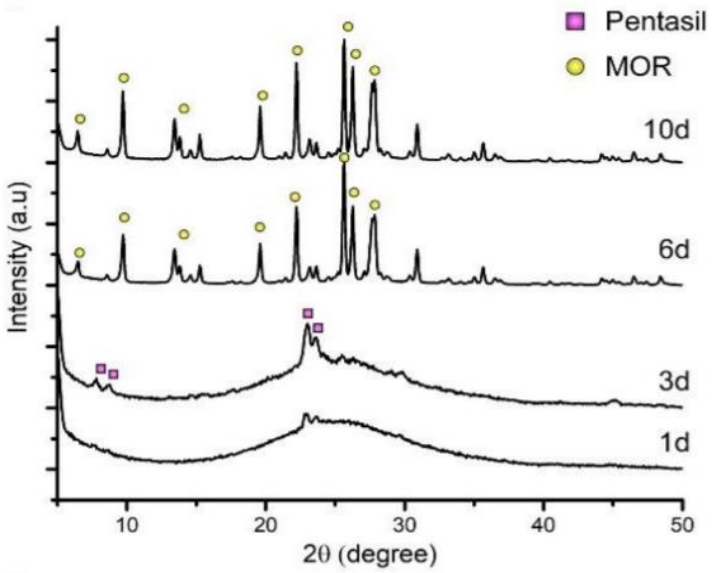


**Figure C14.** Time-elapsed powder XRD patterns for the products obtained at different time intervals by introducing ZSM-11 seeds in growth solution S1.

**Table C1.** Characterization of hierarchical SPP crystals synthesis using various seeds.

| Sample | BET $S_A$ ($m^2/g$) | $V_{micro}$ [a] ($cm^3/g$) | $V_{meso}$ [b] ($cm^3/g$) | $NH_3$-TPD (μmol/g) |
|---|---|---|---|---|
| SPP_Silicalite-2 seeds | 459 | 0.18 | 0.18 | 913.5 |
| SPP_ZSM-5 seeds | 363 | 0.13 | 0.18 | 816.4 |
| SPP_Silicalite-1 seeds | 366 | 0.12 | 0.08 | 784.9 |
| Conventional ZSM-5 | 353 | 0.11 | 0.10 | 522.8 |

[a] Micropore volume determined from the adsorption branch of the isotherms; [b] Mesopore volume was obtained by subtracting the micropore volume from the total pore volume.

# Appendix D

## Chapter 5 Supplementary Information

**Table D1.** Summary of synthesis conditions for zeolites MFI, MEL, TON, and LTL

| Molar Composition | | | | | Silica Source | OSDA | Synthesis | T (°C) | Crystal Phase |
|---|---|---|---|---|---|---|---|---|---|
| $SiO_2$ | $Al_2O_3$ | $K_2O$ | $H_2O$ | OSDA | | | | | |
| 90 | 1 | 11.9 | 3588 | 2 | Ludox AS-30 | TPA | Rotation | 160 | MFI |
| 90 | 1 | 11.9 | 3588 | 2 | Ludox SM-30 | TPA | Rotation | 160 | MFI |
| 90 | 1 | 11.9 | 3588 | 2 | Fumed silica | TPA | Rotation | 160 | MFI |
| 90 | 1 | 11.9 | 3588 | 27.3 | Ludox AS-30 | DAO | Static | 160 | MEL |
| 90 | 1 | 11.9 | 3588 | 27.3 | Ludox AS-30 | DAO | Rotation | 160 | TON |
| 90 | 1 | 11.9 | 3588 | 27.3 | Ludox AS-30 | TETA | Rotation | 160 | TON |
| 90 | 1 | 11.9 | 3588 | 27.3 | Ludox AS-30 | TEPA | Rotation | 160 | TON |
| 20 | 0.5 | 10.2 | 1030 | ----- | Ludox AS-40 | ----- | Static | 180 | LTL |
| 20 | 0.5 | 10.2 | 1030 | ----- | Ludox SM-30 | ----- | Static | 180 | LTL |
| 20 | 0.5 | 10.2 | 1030 | ----- | Fumed silica | ----- | Static | 180 | LTL |

**Table D2.** Range of silicon content in zeolite synthesis mixtures reported in literature

| **Zeolite** | **[$SiO_2$] (mM)** | **[$SiO_2$] (g/L)** |
|---|---|---|
| AEI | 1400-17000 | 84 – 1020 |
| BEA* | 1850 – 7936 | 111 – 477 |
| CHA | 1200 – 10000 | 72 – 600 |
| FAU | 175 – 2777 | 11 – 167 |
| FER | 400 – 11000 | 24 – 660 |
| GIS | 150 – 4500 | 9 – 270 |
| HEU | 8000 – 52000 | 480 – 3120 |
| LTA | 225 – 1608 | 14 – 96 |
| LTL | 793 – 5500 | 48 – 330 |
| MEL | 900 – 6000 | 54 – 360 |
| MER | 400 – 4000 | 24 – 240 |
| MFI | 35 – 1500 | 2 – 90 |
| MOR | 1234 – 7000 | 74 – 420 |
| MTT | 926 – 4273 | 56 – 256 |
| MTW | 926 – 4273 | 56 – 256 |
| MWW | 1234 – 4125 | 74 – 248 |
| RHO | 3000-9000 | 180 – 540 |
| TON | 1010 – 3704 | 61 – 222 |
| UFI | 1851 | 111 |

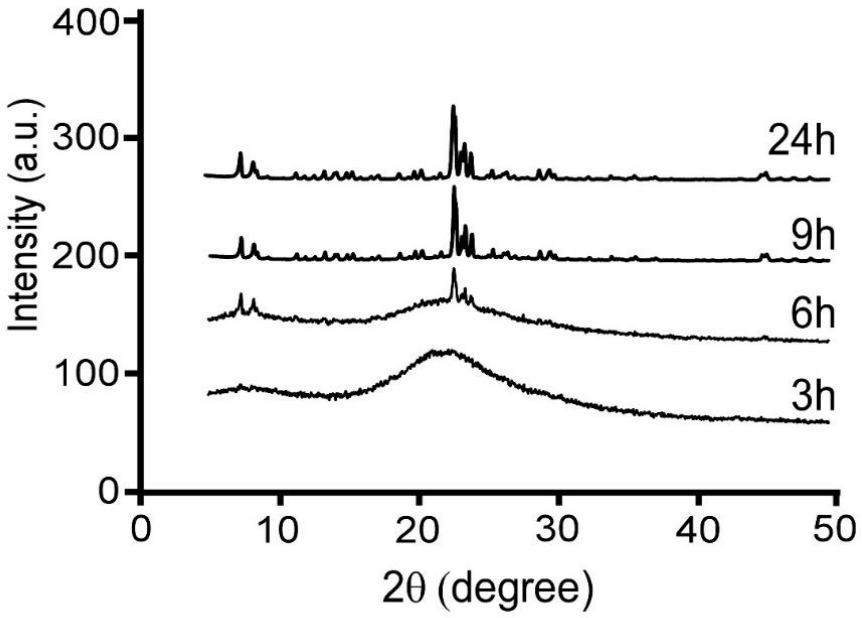


**Figure D1.** Comparison of powder X-ray diffraction patterns of solids extracted from ZSM-5 growth mixtures after specified heating times. Growth mixture with molar composition 2 TPABr: 11.9 $K_2O$: $Al_2O_3$: 90 $SiO_2$: 3588 $H_2O$ was heated at 160°C.

# Appendix E

## Chapter 6 Supplementary Information

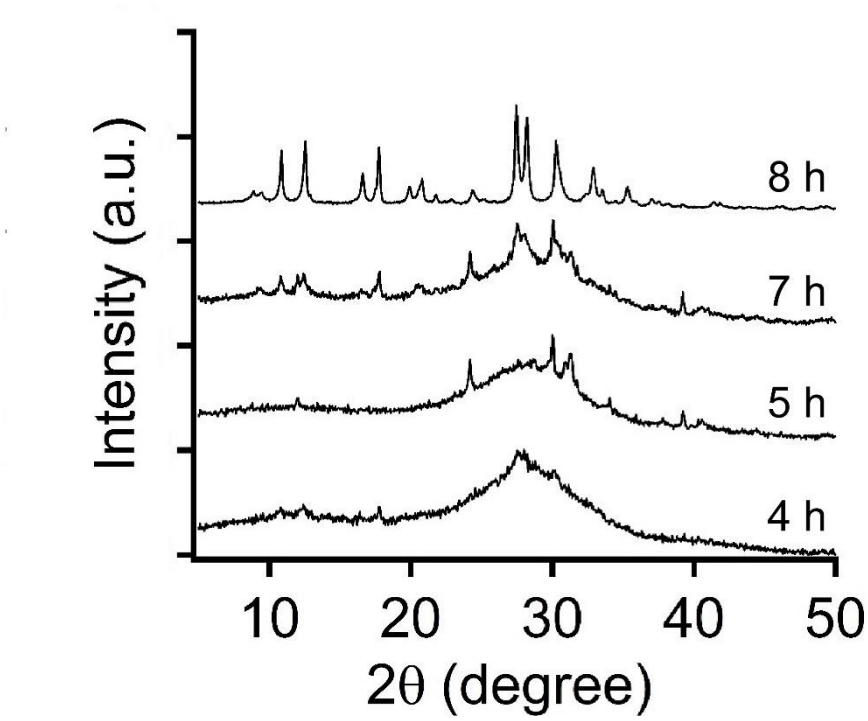


**Figure E1.** Comparison of powder X-ray diffraction patterns of solids extracted from zeolite W growth mixtures after specified heating times. The growth mixture was prepared with a molar composition of 20.4 $K_2O$: 1 $Al_2O_3$: 10 $SiO_2$: 2060 $H_2O$ that was heated at 180 °C.

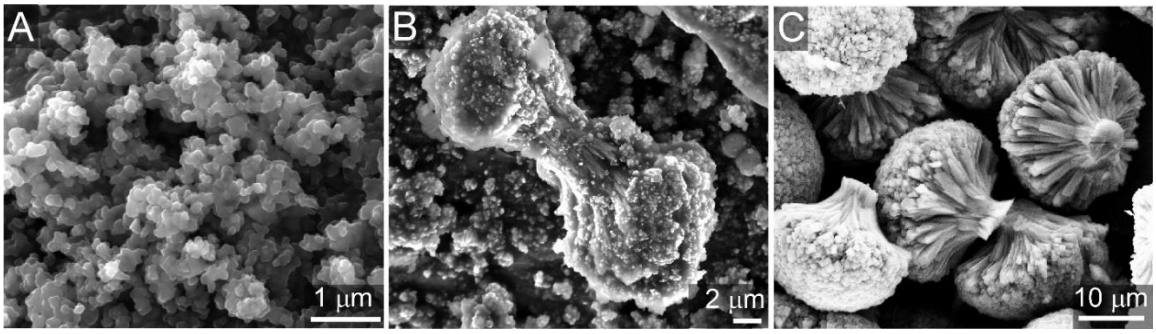


**Figure E2.** Time-resolved electron scanning micrographs of solids extracted during periodic stages of zeolite W synthesis after (A) 4 h of heating, (B) 5 h of heating, and (C) 8 h of heating.

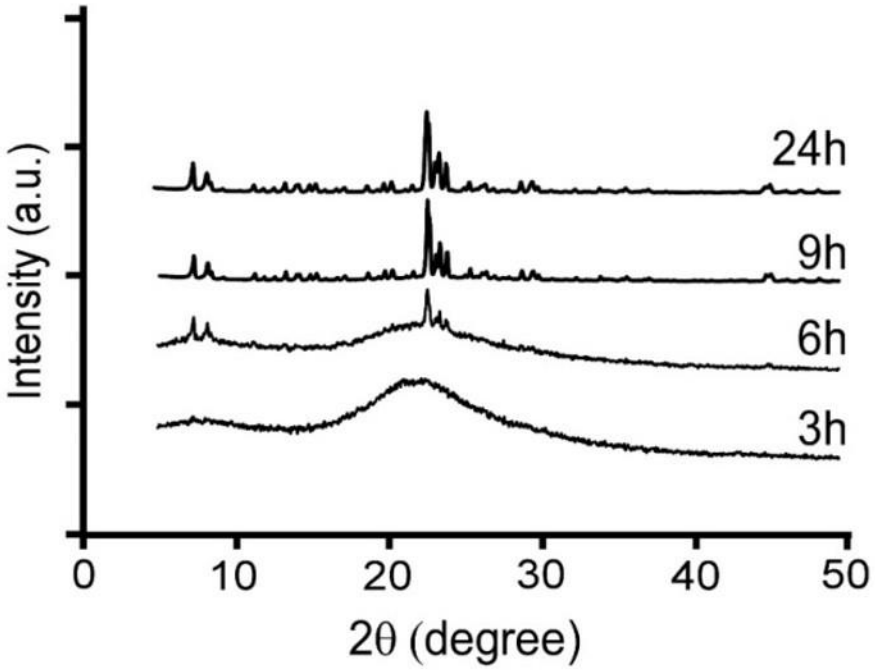


**Figure E3.** Comparison of powder X-ray diffraction patterns of solids extracted from ZSM-5 growth mixtures after specified heating times. The growth mixture was prepared with a molar composition of 2 TPABr: 11.9 $K_2O$: 1 $Al_2O_3$: 90 $SiO_2$: 3588 $H_2O$ that was heated at 160 °C.

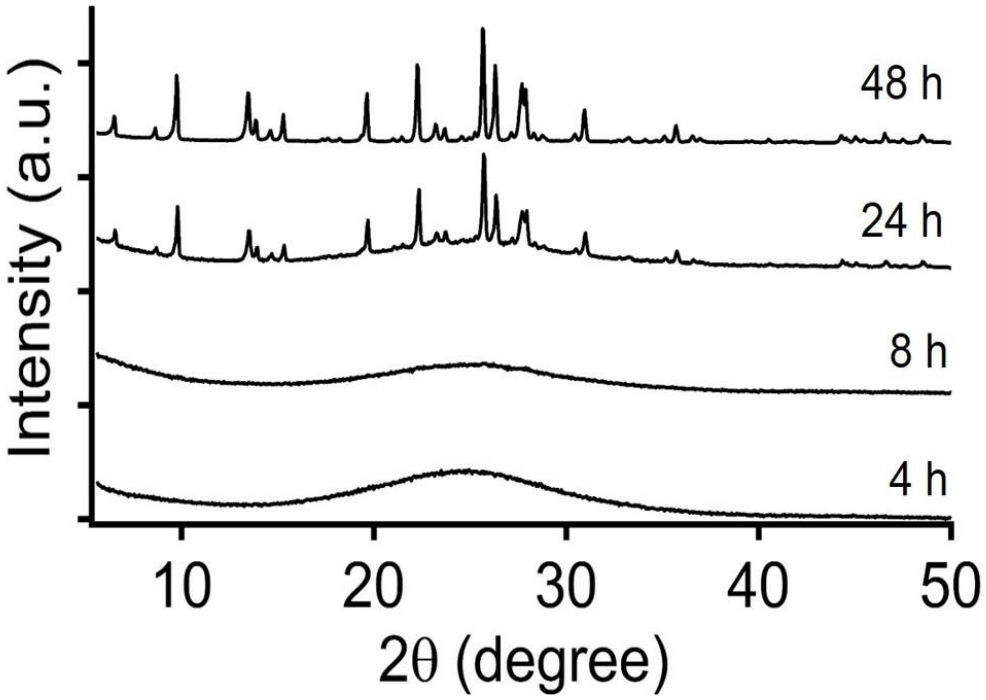


**Figure E4.** Comparison of powder X-ray diffraction patterns of solids extracted from mordenite growth mixtures after specified heating times. The growth mixture was prepared with a molar composition of 5 $Na_2O$: 1 $Al_2O_3$: 30 $SiO_2$: 780 $H_2O$ that was heated at 170 °C.

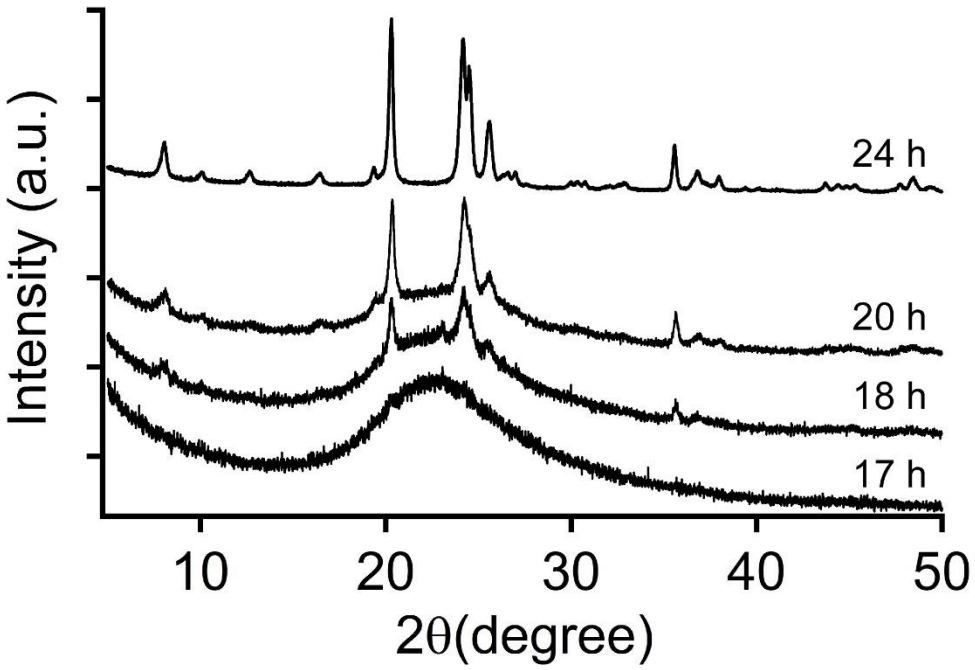


**Figure E5.** Comparison of powder X-ray diffraction patterns of solids extracted from ZSM-22 growth mixtures after specified heating times. The growth mixture was prepared with a molar composition of 27.3 DAO: 11.9 $K_2O$: 1 $Al_2O_3$: 90 $SiO_2$: 3588 $H_2O$ that was heated at 160 °C.

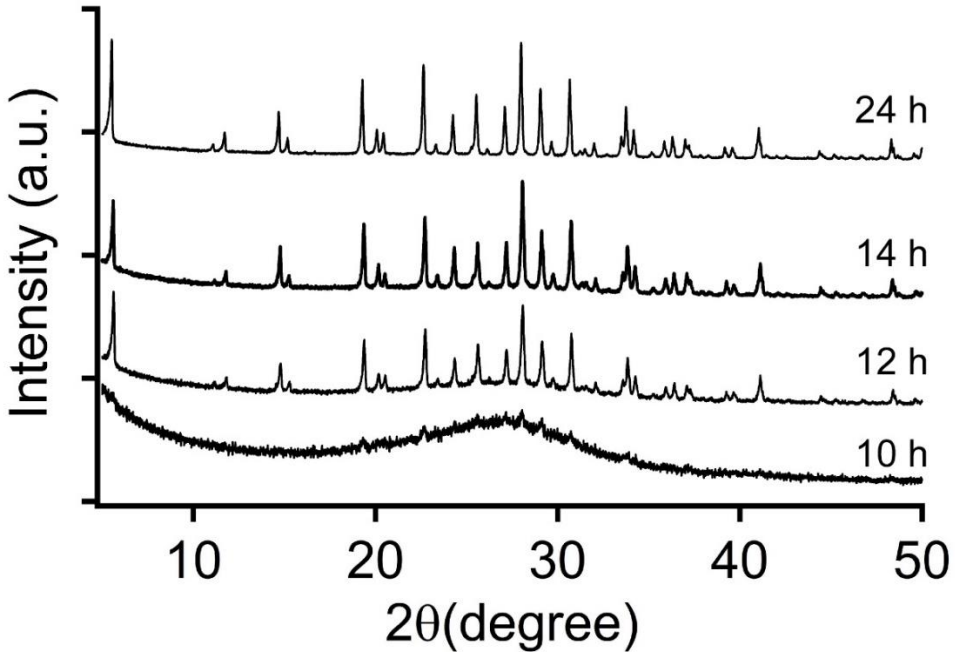


**Figure E6.** Comparison of powder X-ray diffraction patterns of solids extracted from zeolite L growth mixtures after specified heating times. The growth mixture was prepared with a molar composition of 20.4 $K_2O$: 1 $Al_2O_3$: 40 $SiO_2$: 2060 $H_2O$ that was heated at 180 °C.

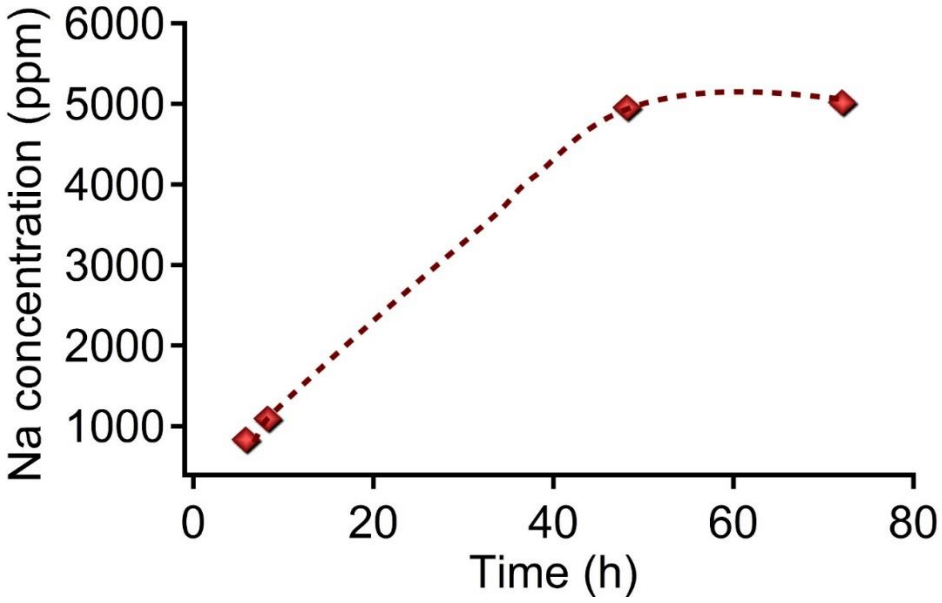


**Figure E7.** ICP-MS measurements of the concentration of sodium ions in the supernatant extracted from mordenite growth mixtures at various heating times. Dashed lines are interpolated to guide the eye.

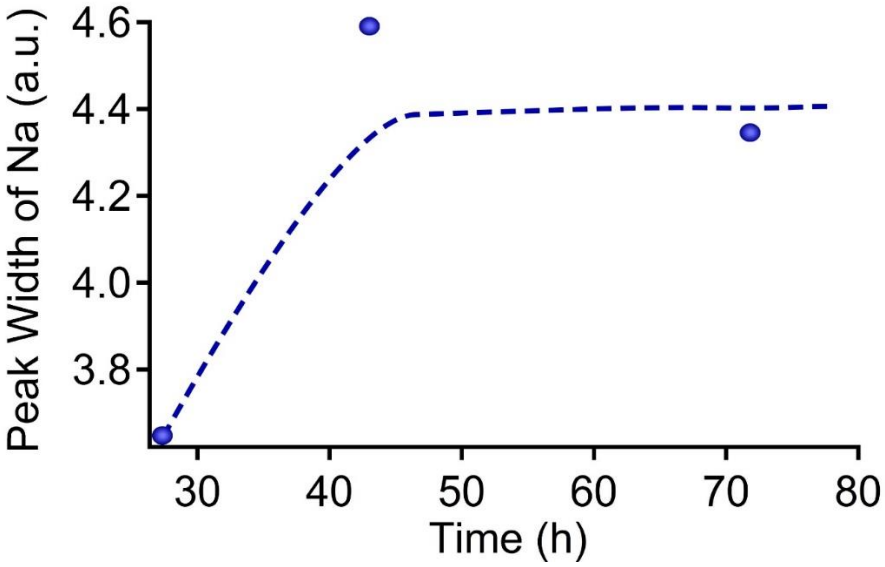


**Figure E8.** Changes in the peak area for sodium ions in the supernatants extracted from mordenite growth mixtures at various heating times measured using ex situ $^{23}Na$ NMR spectroscopy. Dashed lines are interpolated to guide the eye.

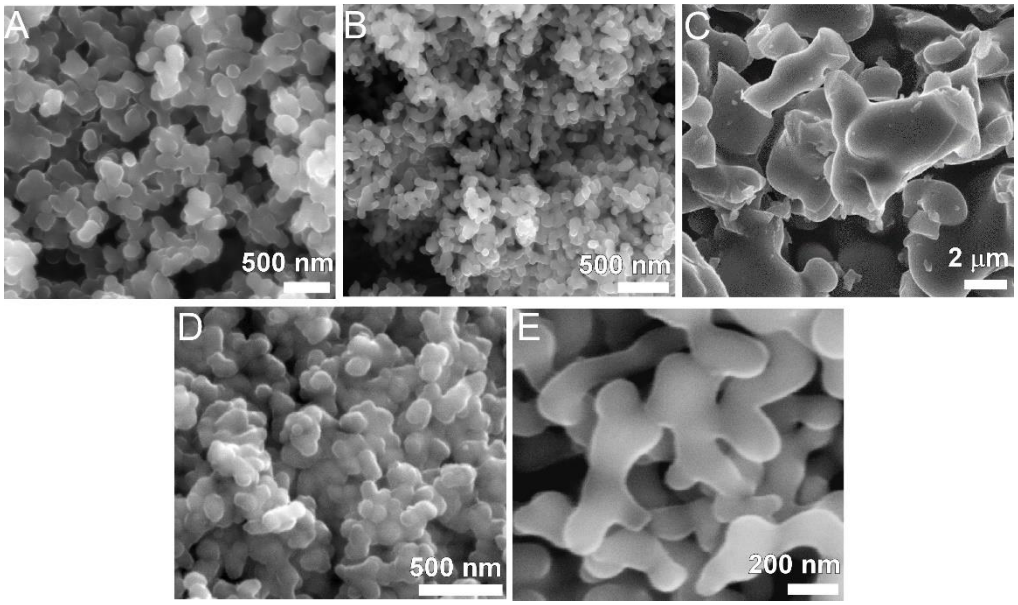


**Figure E9.** Scanning electron micrographs of amorphous precursors extracted from the growth mixtures of (A) zeolite W, (B) ZSM-5, (C) mordenite, (D) ZSM-22, and (E) zeolite L.

**Table E1.** Summary of synthesis conditions for zeolites MFI, TON, MER, LTL, and MOR

| Molar Composition | | | | | Silica Source | OSDA | Degree of Agitation | T(°C) | Crystal Phase |
|---|---|---|---|---|---|---|---|---|---|
| $SiO_2$ | $Al_2O_3$ | $M_2O$ | $H_2O$ | OSDA | | | | | |
| 90 | 1 | 11.9 | 3588 | 2 | Ludox AS-30 | TPA | Rotation | 160 | MFI |
| 90 | 1 | 11.9 | 3588 | 27.3 | Ludox AS-30 | DAO | Rotation | 160 | TON |
| 5 | 0.5 | 10.2 | 1030 | ----- | Ludox AS-40 | ----- | Static | 180 | MER |
| 20 | 0.5 | 10.2 | 1030 | ----- | Ludox AS-40 | ----- | Static | 180 | LTL |
| 30 | 1 | 5 | 780 | ----- | Silica gel | ----- | Static | 170 | MOR |

# Appendix F

Controlling crystal polymorphism is a critical aspect in areas ranging from pharmaceuticals[457] and biomineralization[458] to food industry[459] and catalysis[358]. Crystal polymorphism has been studied for a number of materials such as polymers[460], minerals[458], metal-organic frameworks[461], and zeolites[462], among others. Polymorphs of a crystalline material have distinct properties which can either be desirable or deleterious in certain instances.[463] Zeolites are an important class of crystalline materials where the phenomenon of crystal phase transformation from one structure to another has been well documented.[464] A majority of zeolites are synthesized using OSDAs, which can significantly alter the physicochemical properties such as Si/Al ratio, crystal size, morphology, pore architecture, and surface roughness, among others; however, it is economically desirable to synthesize zeolites without using any organics owing to the costs associated with the engineering of OSDAs and recycling after post synthesis calcination.[241] Typical challenges of organic-free synthesis include low Si/Al ratio, product yield, and the formation of polymorphs.[285]

There has been a significant surge in research efforts to control phase transformations in organic-free crystallization of zeolites. This topic was first investigated nearly 45 years ago, beginning with the pioneering work by Breck and Flanigen who examined interzeolite transformations involving multiple zeolite frameworks.[465] These processes involve the crystallization of a new zeolite after the formation of an initial, less thermodynamically stable structure, and can be used to either tune chemical compositions or achieve faster crystallization kinetics.[466] This process is similar to the Ostwald rule of stages where two or more distinct transitions can occur (downhill in energy).[467] Nucleation of a new (daughter) phase often happens in the presence of the original (parent) phase, giving rise to fundamental questions pertaining to parent-daughter relationship(s) that drive these transformations.[351] Navrotsky and coworkers[468]

established a trend for siliceous zeolites where the enthalpy of formation is directly proportional to molar volume, $\underline{V}$. There are many transformations that abide by this trend[358] while other do not.[356] Thermodynamic studies by Navrotsky and coworkers also revealed very little difference in the enthalpy of formation that separates most zeolites (ca. 10 kJ/mol), which suggests that kinetic pathways play a dominant role in determining the final (or intermediate) crystal structure(s).[468] Mechanisms proposed in literature often posit that the parent and daughter share a similar CBU[14,351]; however, Gómez-Bombarelli and coworkers[13] recently reported the utilization of statistical analysis and machine learning to conclude that the common hypothesis of shared CBUs is a weak predictor (i.e., more than 65% of reported cases involve parent-daughter structures that lack structural similarity). Okubo and coworkers[469] also used machine learning tools to rationalize synthesis-structure relationships for metastable zeolites using synthesis descriptors. Despite significant efforts by several groups, the mechanism(s) underlying interzeolite transformations are complex and elusive with many fundamental questions unanswered. To this end, platforms capable of quantitively characterizing zeolite phase behavior are highly desired.

Rimer and coworkers[358] established kinetic phase diagrams based on ternary plots of Si-Al-NaOH molar compositions as a unique and facile method to simultaneously investigate the impact of various synthesis parameters on zeolite crystal structures. Herein, we employ similar methodology to quantitatively identify the regions of phase-pure and multiphase regions of numerous zeolite structures synthesized using $K^+$ as an inorganic SDA. Our findings reveal that $K^+$ leads to lesser number of zeolite phase transformations as compared to $Na^+$. One of the examples we report is a CHA-to-MER interzeolite transformation, which is consistent with the Ostwald rule of stages. Moreover, we explore the utility of ternary (kinetic) phase diagrams beyond phase transformation to highlight the impact of temperature on crystal size.

Comparisons of natural zeolites and prior literature of OSDA-free synthesis reveals that $K^+$ has the potential to direct structures such as EDI, MER, CHA, LTL, ABW, LTJ, and BPH.[470]

Motivated by these findings, we explored the design space of K-zeolite crystallization in OSDA-free media as a function of various synthesis parameters that include molar composition, temperature, and time.

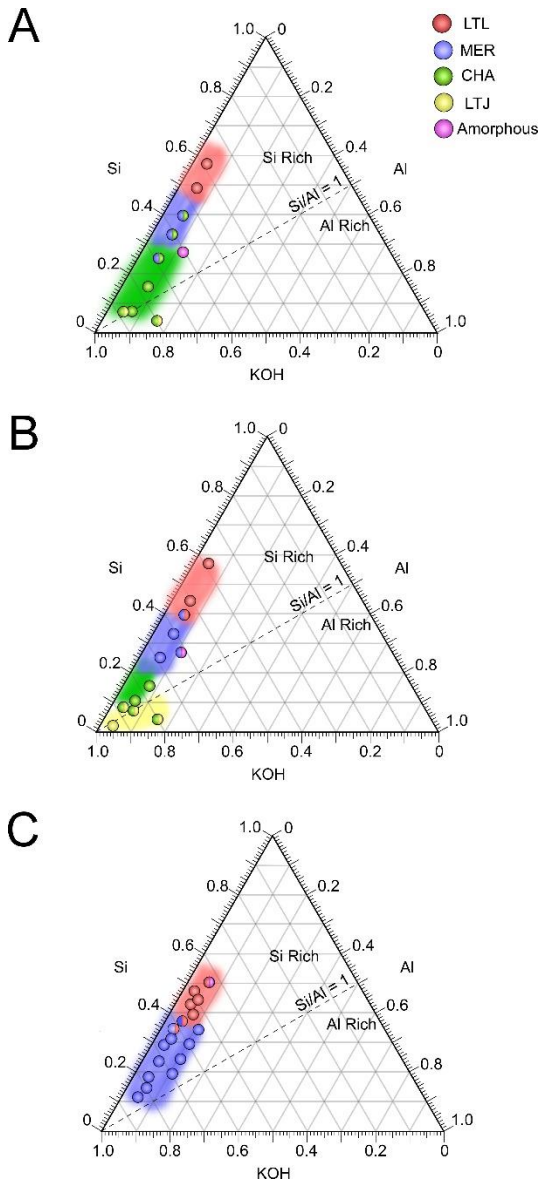


**Figure F1.** Kinetic ternary phase diagrams of zeolite structures showing single- and multi-phase (shaded) regions at increasing temperature: **(A)** CHA, MER, and LTL (85 °C, 21 days); **(B)** LTJ, CHA, MER, and LTL (120 °C, 7 days); **(C)** MER and LTL (180 °C, 3 days).

We monitored zeolite crystallization of growth solutions with gel molar ratios Si/Al> 1 and Si/OH ranging from 0.05 to 1.5. **Figure F1** compares ternary phase diagrams of K-zeolite

crystallization at three different synthesis temperatures (85, 120, and 180 °C). Colloidal silica (Ludox) and aluminum isopropoxide were employed as silica and aluminum sources, respectively. In view of the fact that metastable zeolites can undergo transformations to more thermodynamically stable structures[352,356], ternary plots in **Figure F1** are referred to as "kinetic" phase diagrams. At low synthesis temperature (85 °C), we observed the formation of three different crystal phases (CHA, MER, and LTL) and a minor impurity of LTJ at high alkalinity. CHA preferentially crystallizes around a gel Si/Al ratio of 2.5, whereas an increased silicon content dramatically shifts the phase behavior to MER and LTL crystal phases. The diagram in **Figure F1A** highlights phase pure and multiphase regions containing various crystal structures after 21 days of synthesis at 85 °C. The transition between different phases **(Figure F2A)** is evident from powder XRD patterns extracted from synthesis mixtures prepared at various molar compositions.

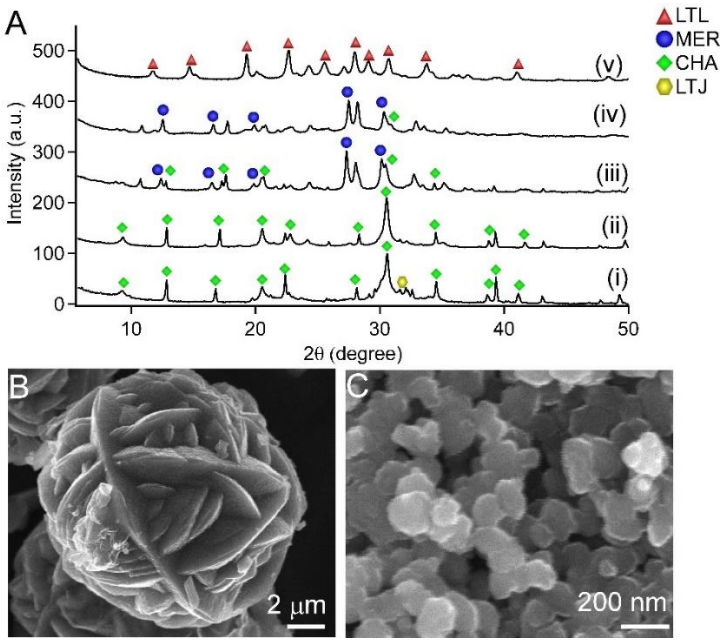


**Figure F2. (A)** XRD patterns of solids from growth solutions heated at 85 °C. Distinct zeolites were obtained using the following $Si/Al_{(liq)}$ values: (i) CHA, 1.3; (ii) CHA, 2.7; (iii) CHA-MER, 5; (iv) CHA-MER, 10; and (v) LTL, 15. Scanning electron micrographs of zeolite crystals with framework types: **(B)** CHA and **(C)** LTL.

The multiphase region consisting of MER and LTL is significantly narrower as compared to that of MER and CHA, which is a large region within the range of $5 < Si/Al < 15$. In contrast,

transition between MER and LTL regions is sharp. Interestingly, there are noticeable differences in the crystal habit of zeolites synthesized in the different regions of ternary phase diagrams. For example, CHA crystals have a star-like morphology **(Figure F2B)** indicative of intergrowths with an average diameter of 10 μm. The star-like morphology of CHA crystals closely resembles the crystal habit of Cs-CHA reported by Kirchhock and coworkers.[470,471] Micrographs of LTL crystals **(Figure F2C)** indicate sizes of around 60 nm; however, it must be noted that zeolite L (LTL) particles often appear to be clusters of smaller crystals.[472,473]

To test the effect of temperature on K-zeolite phases, we performed synthesis at 120 °C and 180 °C after heating the growth solutions for 7 days and 3 days, respectively. It is important to note that synthesis time was decreased at higher temperatures to account for an increase in the kinetics of crystallization. Powder XRD patterns **(Figure F3A)** of solids extracted at 120 °C revealed the formation of an additional phase (LTJ) at gel Si/Al < 2.5. The LTJ-CHA multiphase region in **Figure F1B** extends from 1 < Si/Al < 2.5. Moreover, we observed noticeable differences **(Figure F1B)** in the location and range of pure and multiphase regions of CHA and MER zeolite at 120 °C; there is a larger MER region and a smaller CHA region. These findings indicate that CHA is less stable at higher temperatures. Interestingly we also observe dramatic differences in the surface morphology of CHA crystals **(Figure F3C)** when increasing the synthesis temperature from 85 to 120 °C; wherein intergrowths predominantly disappear, possibly due to ripening in favor of crystals with spheroidal morphology which are less fractal in nature.

Linde Type J (LTJ) zeolite has zigzag 8-ring channel intersections and is categorized as a small-pore zeolite. Despite its early discovery, the first structural description was reported in 2011 by Kirchner and coworkers.[474] Synthesizing LTJ require unconventional reagents (e.g., rice husk and aluminum foil) which are not readily employed in commercial processes.[474] For instance, Ng et al.[475] reported the synthesis of nanosized LTJ zeolite using rice husk ash, and also demonstrated the excellent catalytic performance of LTJ in Knoevenagel reaction. Our preliminary studies

indicate that LTJ can be prepared using conventional reagents by employing a combination of longer synthesis time and low temperature. Micrographs of LTJ crystals reveal larger crystals (ca. 1μm) with a distinct rod-like morphology **(Figure F3B)** that closely resemble SEM images of pure LTJ crystals reported by Ng et al.[475]

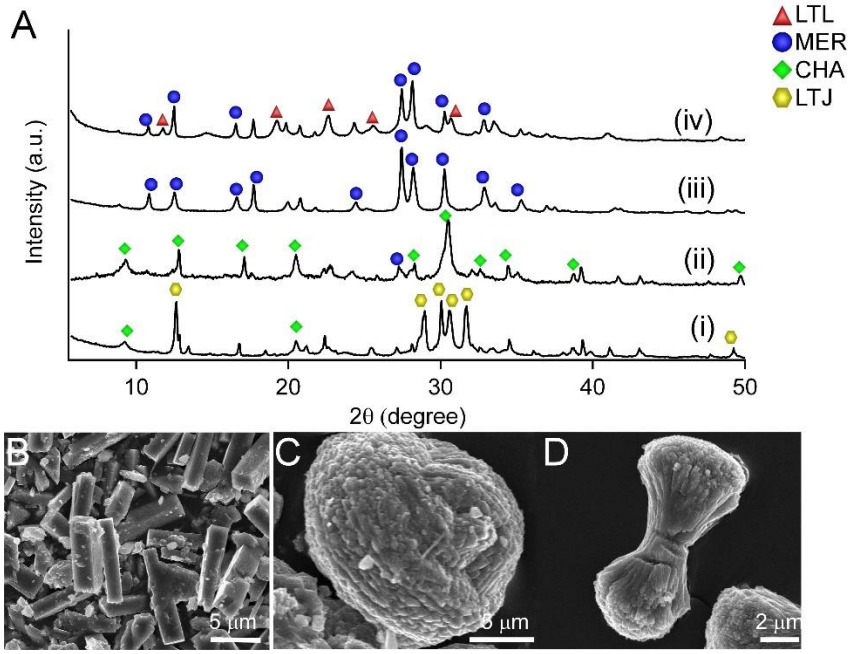


**Figure F3. (A)** XRD patterns of solids from growth solutions heated at 120 °C. Distinct zeolites were obtained using the following $Si/Al_{(liq)}$ values: (i) LTJ, 1.3; (ii) CHA, 2.7; (iii) MER, 5; and (iv) MER-LTL, 10. Scanning electron micrographs of zeolite crystals with framework types: **(B)** LTJ, **(C)** CHA, and **(D)** MER.

With further increase in the synthesis temperature to 180 °C, we observed the disappearance of CHA region **(Figure F1C)** and the expansion of MER to include the range 2 < Si/Al < 10. The phase diagram in **Figure F1C** indicates that pure MER is favored at a gel Si/Al < 10, a binary mixture of MER and LTL exists at 10 < Si/Al < 12, and pure LTL is favored at Si/Al > 12. Comparison of powder XRD patterns of solids extracted at various molar compositions after heating the growth solution at 180 °C for 3 days indicate a progressive shift in the phase behavior from pure MER to pure LTL with increasing gel Si/Al. SEM images reveal that MER crystals have a broccoli-like morphology **(Figure F4B)** with an average diameter of 5 μm, whereas LTL crystals

exhibit a cylindrical morphology **(Figure F4C)** with relatively monodisperse sizes of *ca.* 4 μm in length. The broccoli-like morphology of MER crystals closely resembles SEM images of other crystals such as zeolite offretite, ZnO, and $Al_2O_3$, among others.[476-479]

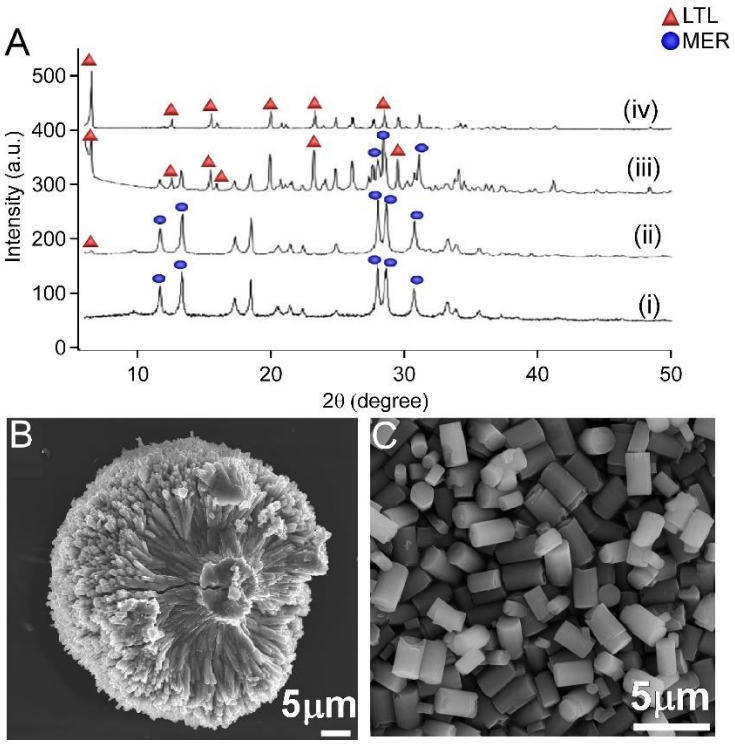


**Figure F4. (A)** XRD patterns of solids from growth solutions heated at 180 °C. Distinct zeolites were obtained using the following $Si/Al_{(liq)}$ values: (i) MER, 5; (ii) MER-LTL, 12; (iii) MER- LTL, 13; and (iv) LTL, 15. Scanning electron micrographs of zeolite crystals with framework types: **(B)** MER and **(C)** LTL

As previously mentioned, the Ostwald rule of stages is often observed in interzeolite transformations wherein metastable zeolite structures undergo a series of transformations to structures which are more thermodynamically stable. Navrotsky and coworkers[468] proposed a direct correlation between the enthalpy of formation and molar volume of purely siliceous zeolite structure, thus molar volume is often used as a descriptor to predict interzeolite conversions[358], which generally occurs in the order of increasing framework density.[191,285,358] Recent studies have demonstrated that significant differences in the chemical compositions between parent and daughter zeolites can markedly alter the thermodynamic driving force for these transformation.[356]

For instance, Gómez-Bombarelli and coworkers[13] also reported multiple examples of transformations with decreasing framework density.

The molecular level details governing the transformations between different zeolites structures are not well understood. There are two hypotheses regarding the spatial origin of interzeolite transformations: (i) epitaxial relationships between parent and daughter zeolites leading to preferential nucleation of the daughter at the surface of the parent; and/or (ii) temporal changes in the growth solution composition promoting the nucleation and growth of the daughter zeolite in the liquid phase (with concomitant dissolution of the metastable parent zeolite). We monitored the structural and morphological evolution of solids using high resolution SEM micrographs to capture the details of CHA-to-MER interzeolite transformation *ex situ*. SEM images **(Figure F5A)** after 7 h of heating, corresponding to the first appearance of CHA peaks in powder XRD patterns, show partially crystallized star-shaped particles that are putatively CHA crystals surrounded by a population of amorphous precursors. As the CHA-to-MER transformation proceeds, we observe the formation of broccoli-shaped crystals in favor of a decreasing population of star-shaped crystals. Samples extracted at a time corresponding to near complete CHA-to-MER transformation reveal what appears to be partially dissolved CHA crystals **(Figure F5C)**. After 3 days of heating, star-shaped particles predominantly disappear in favor of a single population of broccoli-shaped MER crystals **(Figure F5D)**. We postulate that incomplete dissolution of colloidal silica during the initial stages of crystallization leads to Al-rich environment that favors CHA nucleation, followed by interzeolite conversion to MER once the synthesis mixture reaches a certain composition (i.e. chemical potential) that favors nucleation of the new phase. This is consistent with the hypothesis for LTA-to-FAU intercrystaline transformation proposed by Rimer and coworkers.[358]

In this study, we also observed a CHA-to-MER transformation at elevated temperature **(Figure F5E)**, which seems to be consistent with the Ostwald rule of stages, i.e. there is a progression from low to high density structure with little change in chemical composition (Si/Al ≈

2 for both CHA and MER zeolites). Several groups have proposed that OSDA-free interzeolite conversions tend to occur when both parent and daughter zeolite share a degree of structural similarity in the form of common composite building units (CBUs); [14,351] however, Rimer and coworkers[356] provided a counter example for the OSDA-free interzeolite transformation between FAU and MFI structures, which lack common CBUs. Here it is observed that a CHA-to-MER transformation **(Figure F5B)** involves two structures with disparate CBUs, which seems to indicate that a common structural similarity is not a prerequisite for interzeolite transformations.

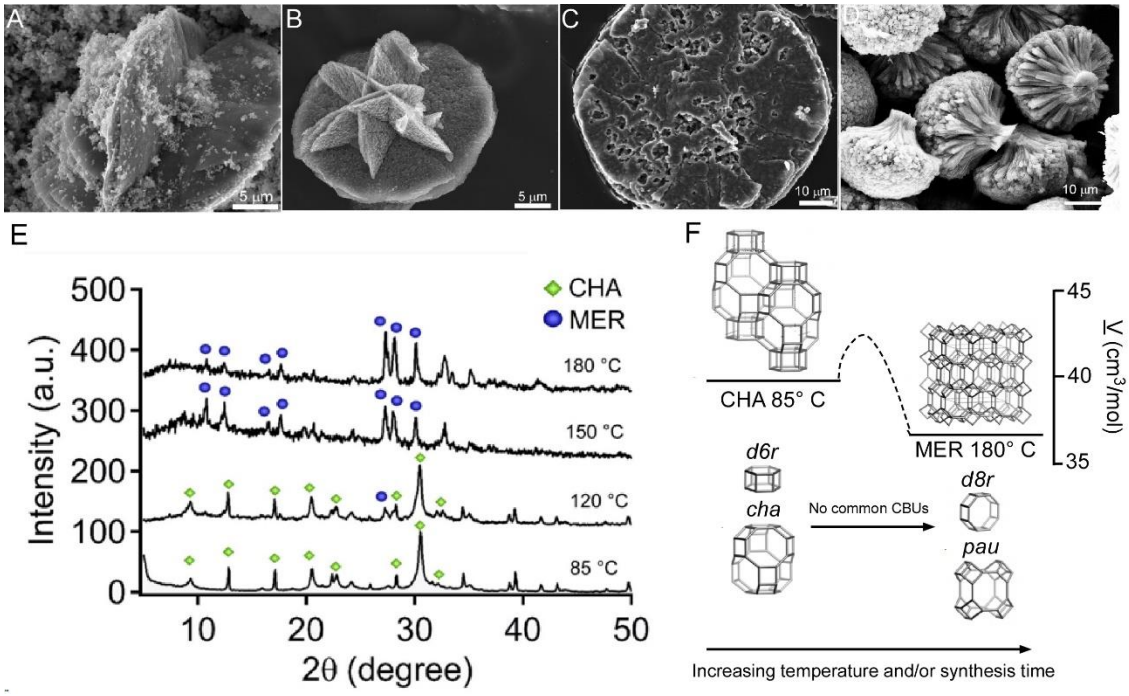


**Figure F5. (A-D)** Time-resolved SEM micrographs of solids extracted during periodic stages of CHA-to-MER transformation after **(A)** 7 h, **(B)** 8 h, **(C)** 53 h, and **(D)** 72 h of heating. **(E)** Powder XRD patterns of solids extracted from the same growth solution showing the interzeolite transformation of CHA-to-MER with increasing temperature. **(F)** Stages of K-zeolite phase transformation consistent with the Ostwald rule of stages.

Prior experimental[358] and computational studies[275,469] have reported multiple stages of zeolite phase transformation involving a wide variety of structures in organic-free Na-zeolite synthesis. Substitution of growth mixtures with $K^+$ as the inorganic SDA leads to a reduction in the number of interzeolite transformations. For instance, LTL and LTJ structures do not participate in

phase transformations under the conditions tested in our study. The interactions between zeolite precursors and inorganic SDAs that lead to significant differences in the trajectories of phase transformations are not well understood. We hypothesize that the choice of inorganic SDA could potentially influence the formation of CBUs, or alter the solvation of (alumino)silicate species in solution and/or at crystal interfaces, which can subsequently influence the addition of growth units to zeolite crystals, or display favorable packing configurations within the pores of zeolites.

It is well established that a subtle change in the synthesis conditions can markedly alter the crystal size and morphology of zeolites. For example, Mintova and coworkers demonstrated that low temperature aging[70] and the mixing of reagents at low temperature[71] is critical to control (alumino)silicate polymerization and achieve ultrasmall (10 – 100 nm) EMT and FAU zeolite crystals, respectively. Motivated by these studies, we also examined the utility of kinetic phase diagrams to control zeolite crystal size. It is commonly observed that syntheses of zeolite L produce crystals with sizes of ca. 3 μm crystals **(Figure F6C)**. Methods for producing ultrasmall zeolite L crystals often requires the use of microwave synthesis or unconventional reagents (e.g., aluminum foil and rice husk). Rimer and coworkers[480] recently showed that judicious selection of silica source in zeolite synthesis mixtures leads to ultrasmall zeolite L crystals (ca. 20 nm). Here, our findings indicate that synthesis temperature can substantially alter the crystal size of zeolite L. SEM images of zeolite L crystals extracted at various synthesis temperatures reveal a dramatic reduction in the crystal size with decreasing temperature. Specifically, zeolite L synthesis at 120 °C promotes the formation of 400 nm crystals **(Figure F6B)**, which is an order of magnitude smaller than that of crystals synthesized at 180 °C. With further reduction in the synthesis temperature to 85 °C, we observe a drastic decrease in the crystal size of zeolite L **(Figure F6A)** by another order of magnitude. To our knowledge, this is the first example of ultrasmall zeolite L (ca. 40 nm) crystals synthesized at low temperature (i.e., < 100 °C) using conventional starting reagents. Comparison of zeolite L crystal size in **Figure F6D** reveals a distinct exponential trend. The exact mechanism

of zeolite L crystallization is not well understood; however, it is reasonable to argue that low temperature drastically limits growth kinetics and Ostwald ripening, and perhaps the number of nuclei, resulting in the synthesis of ultrasmall zeolite L crystals. The high sensitivity of crystal size to temperature was only observed for zeolite L; therefore, our findings demonstrate that other zeolites (i.e., LTJ, MER, and CHA) prepared using $K^+$ as an inorganic SDA do not follow identical trends as those observed for LTL.

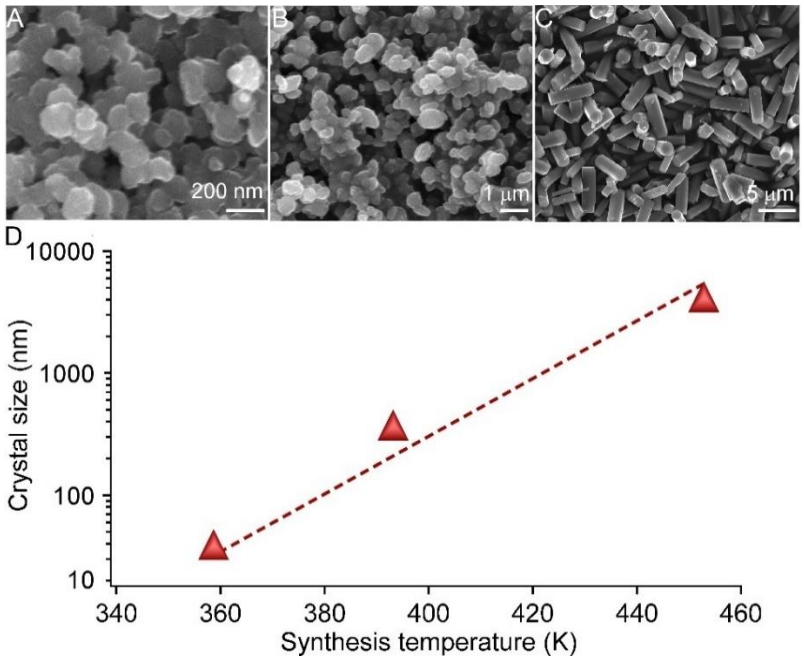


**Figure F6.** SEM images of zeolite L crystals extracted from the same growth solution heated at the following temperatures: **(A)** 85 °C; **(B)** 120 °C; and **(C)** 180 °C. **(D)** Measurements of the average LTL crystal size reveal exponential reductions as a function of decreased synthesis temperature.

In summary, we have shown that kinetic ternary phase diagrams are a unique and cost-effective approach to selectively tailor polymorphism, habit, and size of K-zeolites. This approach is another demonstration of rational zeolite design, which seeks to improve the overall economics of zeolite synthesis by eliminating the need for costly and time-consuming empirical synthesis protocols. Our findings reveal that reduced gel Si/Al ratio and intermediate synthesis temperature facilitates the formation of structures such as LTJ, which are challenging to crystallize using conventional reagents. The CHA-to-MER phase transformation observed in this study is consistent

with Ostwald rule of stages; however, these structures do not share a common building unit. We show that a decrease in the synthesis temperature is critical to enhancing the nucleation rate and facilitating the generation of ultrasmall zeolite L crystals. Our findings reveal reduced synthesis temperature does not have the same effect on all framework types; however, in select cases it may provide an alternative strategy for optimizing the physicochemical properties of zeolites. Collectively, our findings identify a facile and effective route to control the crystal polymorphism without the *a priori* knowledge of crystal phase behavior, which may prove to be more broadly applicable to other zeolites.